

ABSTRACT

Title of Dissertation: MECHANICS AND THERMAL TRANSPORT
MODELING IN NANOCELLULOSE AND
CELLULOSE-BASED MATERIALS

Upamanyu Ray, Doctor of Philosophy, 2023

Dissertation directed by: Professor Teng Li,
Department of Mechanical Engineering

Cellulose, the abundantly available natural biopolymer, has the potential to be a next generation wonder material. The motivation behind this thesis stems from the efforts to obtain mechanical properties of two novel cellulose-based materials, which were fabricated using top-down (densified engineered wood) and bottoms-up (graphite-cellulose composite) approaches. It was observed that the mechanical properties of both the engineered wood (strength~596 MPa; toughness ~3.9 MJ/m³) and cellulose-graphite composite (strength~715 MPa; toughness ~27.7 MJ/m³) surpassed the equivalent features of other conventional structural materials (e.g., stainless steel, Al alloys etc.). However, these appealing properties are still considerably inferior to individual cellulose fibrils whose diameters are in the order of nanometers. A significant research effort needs to be initiated to effectively transfer the mechanical properties of the hierarchical cellulose fibers from the atomistic level to the continuum. To achieve that, a detailed understanding of the interplay of cellulose molecular chains that affects the properties of the bulk cellulosic material, is needed. Modeling investigations can shed light on such underlying mechanisms that

ultimately dictate multiple properties (e.g., mechanics, thermal transport) of these cellulosic materials.

To that end, this thesis (1) applies molecular dynamics simulations to decipher why microfibers made of aligned nanocellulose and carbon nanotubes possess excellent mechanical strength, along with understanding the role of water in fully recovering elastic wood under compression; (2) delineates an atomistically informed multi-scale, scalable, coarse grained (CG) modeling scheme to study the effect of cellulose fibers under different representative loads (shearing and opening), and to demonstrate a qualitative guideline for cellulose nanopaper design by understanding its failure mechanism; (3) utilizes the developed multi-scale CG scheme to illustrate the reason why a hybrid biodegradable straw, experimentally fabricated using both nano- and micro-fibers, exhibits higher mechanical strength than individual straws that were built using only nano or microfibers; (4) investigates the individual role of nanocellulose and boron nitride nanotubes in increasing the mechanical properties (tensile strength, stiffness) of the derived nanocellulose/boron-nitride nanotube hybrid material; (5) employs reverse molecular dynamics approach to explore how the boron nitride nanotube based fillers can improve thermal conductivity (k) of a nanocellulose derived material.

In addition, this thesis also intends to educate the readers on two perspectives. The common link connecting them is the method of engineering intermolecular bonds. The first discussion presents a few novel mechanical design strategies to fabricate high-performance, cellulose-based functional materials. All these strategies are categorized under a few broad themes (interface engineering, topology engineering, structural engineering etc.). Another discussion has been included by branching out to other materials that, like nanocellulose, can also be tuned by intermolecular bonds engineering to achieve unique applications. Avenues for future work have been suggested which,

hopefully, can act as a knowledge base for future researchers and help them formulate their own research ideas. This thesis extends the fundamental knowledge of nanocellulose-based polymer sciences and aims to facilitate the design of sustainable and programmable nanomaterials.

MECHANICS AND THERMAL TRANSPORT MODELING IN
NANOCELLULOSE AND CELLULOSE BASED MATERIALS

by

Upamanyu Ray

Dissertation submitted to the Faculty of the Graduate School of the
University of Maryland, College Park, in partial fulfillment
of the requirements for the degree of
Doctor of Philosophy
2023

Advisory Committee:

Professor Teng Li, Chair and Advisor

Professor Hugh Bruck

Professor Abhijit Dasgupta

Professor Liangbing Hu

Professor Chunsheng Wang, Dean's Representative

© Copyright by
Upamanyu Ray
2023

Dedication

*To Baba, who read most of the chapters listed in this thesis but could not be around
to see its completion.*

Acknowledgements

A lot of people deserve to be acknowledged as I complete this professional milestone. Their support has become more imperative in the year 2023, the time of writing this dissertation. About three years ago, our world was affected by the COVID-19 pandemic. It impacted on our lives, and the way we look at life and work. As I maneuvered my research during the last stages of my PhD through these tumultuous times, many individuals helped me stay upright. Before specifically naming anyone, I want to firmly state that decades down the line, I will remember each one of them very fondly. By listing down names here, I am merely transferring my temporary perceptions of their significant contributions to caressing, long-term memory.

First and foremost, my PhD advisor Prof. Teng Li deserves countless gratitude for patiently mentoring me and allowing me to expand beyond the specific topic of doctoral research. I owe it to his farsightedness that in addition to computational research, I got the opportunity to actively learn experiments and participate in industry research collaborations. Those experiences not only enhanced my pedagogical credentials, but also made me cognizant about the bigger challenges encompassing the sustainable materials science community. Now, I feel I am in a good position to significantly contribute to this field.

My other dissertation committee members were also exceptionally helpful. I am forever indebted to Prof. Liangbing Hu for teaching me how to present research effectively over weekly meetings at his office and allowing me to conduct experiments at his laboratory. Prof. Abhijit Dasgupta was the Graduate Director during most of my PhD

stint and I am so thankful to him for always keeping his door open to provide valuable advice on almost everything. Prof. Hugh Bruck was also in my Qualifier Exam committee during the first year of PhD, and his extensive knowledge of polymer sciences has helped shape this dissertation immensely. Lastly, I thank Dean's Representative, Prof. Chunsheng Wang, for his valuable comments to improve this thesis.

My research group members became like an extended family as I gradually progressed towards the completion of my doctoral degree. I found a lifelong friend in Jian (Jerry), who, I know, will always be there if I need him. Dr. Zhenqian Pang, a friend and post-doc in my group was immensely helpful in advising me on multiple research projects and I am so happy that he is a faculty now, mentoring other young researchers. I am also grateful to Qiongyu for her friendship and help, during the later stage of my PhD.

Everyone at the Department of Mechanical Engineering in University of Maryland College Park (UMD) was extremely supportive throughout. The daunting paperwork required intermittently as I progressed towards a doctoral degree, along with help on applications for fellowships and many others, was made to look easy only because of the efficiency of Kerri, Megan, Segen and Prof. Peter Sanborn. I thank them from the bottom of my heart.

I thank Linda Macri, my boss at the UMD Graduate School Writing Center where I was a Writing Fellow for over four years. Linda and the other Fellows in the cohort were instrumental in instigating my love for writing. Revising manuscripts of professionals working in various disciplines ranging from musical history to STEM

fields polished my writing competency. This soft skill gained through those weekly, disciplined exercises of peer review have greatly rewarded my professional endeavors.

Friends of Maryland were like a family away from home. All of them, including my roomies at different points in time (Rishov, Bodhi, Devi, Sayan da, Esha di, Samarpan, Sagnik) and others (Soumyadip, Soham, Sid Pal, Jia Da, Jhila, Souvik Da, Piyana Di, Ankit, Surabhi, Bidisha, Parama, Guria, Adway, Sohini, Ahana, Darshan), made my hectic life a bit relaxed through their companionship. Also, I must specially thank Abhijit Da (Dr. Abhijit Dasgupta, now at AstraZeneca) for the stimulating discussions and help related to Python programming.

The contribution of family members is impossible to inscribe in a few lines. I am so grateful for the love and support of Didi (sister, Trina) and my brother-in-law (Rajarshi Da). The feeling of “they-are-here” made my stay in USA much easier. I received help from them with basically everything and my travels with them to different parts of the USA were always a welcome break from the mundane. Till a few years ago, Ma (mother, Sukla Ray) probably would have wanted a medical doctor in the family, but I know she will be very happy with this “not-that-kind-of-doctor” degree, too. I can never thank her enough for the upbringing I received, which led to this.

I understood the sacrifices that Baba (father, Anup Mohan Ray) made for our well-being at a much grown-up age when I started living alone, outside India. Since childhood, he aroused in me the love for basic sciences and mathematics through consistent training. The roles reversed later, when he would meticulously inquire about my doctoral research, and was probably the only one outside my research group to read

all the papers that were periodically published during my spell as a PhD student. Alas, he will not be present to read the final thesis. I miss him daily, but I know that my achievement will make him the happiest person today. That belief provided me with the hardiness to wrap this up.

Table of Contents

Dedication	ii
Acknowledgements	iii
Table of Contents	vii
List of Tables	x
List of Figures	xi
Chapter 1: Introduction and Motivation	1
1.1 Background	1
1.2 Why Cellulose?	3
1.3 Market demands and societal implications of cellulose industry	9
1.4 Experimentations driving the research motivation	12
1.4.1 Densified Engineered Wood (top-down approach)	15
1.4.2 Graphite-NFC composite (bottoms-up approach)	20
1.5 Modeling Methodology	26
1.5.1 Molecular Dynamics	26
1.5.2 Coarse-grained molecular dynamics	27
1.6 Organization of the Thesis	27
1.7 Author contributions	28
Chapter 2: State-of-the-art understanding of mechanics design in cellulose-enabled high performance functional materials	29
2.1 Introduction	29
2.2 Structural derivatives of cellulose	31
2.2.1 Wood Cellulose	32
2.2.2 Bacterial Cellulose	35
2.2.3 Cellulose nanomaterials	36
2.3 Understanding the design of high-performance cellulose materials	37
2.3.1 Role of hydrogen bonds behind the anomalous properties of nanopaper ..	38
2.3.2 Influence of structural interface on the hydrogen bonding	42
2.3.3 Effect of nanofiber diameter and orientation on fracture mechanics	43
2.4 Design of cellulose-based functional materials with superior mechanical properties	47
2.4.1 Structural alteration	47
2.4.2 Alignment	52
2.5 Understanding design of high-performance cellulose-based composites	58
2.5.1 Interface Engineering	58
2.5.2 Topology Engineering	65
2.5.3 Structural Engineering	71
2.6 Concluding remarks and challenges	76
Chapter 3: Utilizing atomistic modeling to understand the superior mechanical properties of selected cellulose-based materials	81
3.1 Role of alignment in cellulose-nanofiber enabled 3D printing of carbon nanotube microfiber network	81
3.1.1 Background	81
3.1.2 Molecular simulation methodology	84
3.1.3 Discussion of the role of alignment in the microfiber	85

3.1.4 Summary	89
3.2 All-wood hydrogel with durable elastic compressibility	90
3.2.1 Background	90
3.2.2 MD simulation methodology	93
3.2.3 Role of water on the deformation behavior of the elastic wood hydrogel ..	95
3.2.4 Conclusions and extended research	97
Chapter 4: A scalable coarse-grain modeling scheme to study the interplay of fibers in cellulose-based materials	98
4.1 Introduction	98
4.2 Detailed development of the bottoms-up, scalable CG modeling scheme	101
4.3 Validation of the CG model	110
4.4 Mechanical response of cellulose fibers under shearing and opening loads ..	112
4.5 Failure mechanism in a random network of cellulose fibers as found in a nanopaper	115
4.6 Summary and possible future work using the bottoms-up CG scheme	120
4.7 Application of the developed CG scheme to explain superior mechanics of hybrid, cellulose-based, biodegradable straws	121
4.7.1 CG modeling studies supporting experimental data qualitatively	122
4.7.2 Limitations and Outlook	125
Chapter 5: Investigating thermal transport and mechanical properties in BNNT/NFC hybrid material	127
5.1 Introduction	127
5.2 Molecular Dynamics Methodology	129
5.3 Results and Discussions	131
5.4 Conclusion	145
Chapter 6: Summary and significance of conducted research	147
6.1 Overview	147
6.2 Novelty of the experimental research presented in Chapter 1	147
6.2.1 Engineered wood (Super Wood) fabricated using top-down approach ...	148
6.2.2 Cellulose-graphite hybrid made using bottoms-up approach	148
6.3 Significance of state-of-art mechanics design strategies presented in Chapter 2	149
6.4 Novelty of the research on cellulose-based materials using MD simulations included in Chapter 3	150
6.5 Novelty of the multi-scale coarse-grained model listed in Chapter 4	151
6.6 Novelty of research presented in Chapter 5	152
6.7 Importance of the future work suggested in the following Chapter 7	153
Chapter 7: Possible avenues for future work: Utilizing intermolecular bonding to obtain high-performance materials with programmable physical properties	155
7.1 Introduction	155
7.2 Material design strategies leveraging intermolecular bonding	162
7.3 Influence of intermolecular bonding on the material physical properties	164
7.3.1 Thermal Stability	164
7.3.2 Mechanical Properties	171
7.4 Applications	185
7.5 Challenges and future perspectives	190

Appendices.....	195
Appendix I: List of publications	195
Appendix II: Python code to generate the random network model of Figure 4.6	198
Appendix III: Stepwise preparation of cellulose-graphite slurry.....	205
Step 1: TEMPO-Oxidation treatment	205
Step 2: Filtration and Homogenization	206
Step 3: Ultrasonication and centrifugation to obtain cellulose-graphite slurry	207
Appendix IV: Author Biography	208
Bibliography	212

List of Tables

Table 4.1. CG force field potential parameters.....	109
Table 4.2 Comparison of the cellulose nanopaper properties as predicted by the devised CG model with previous experimental results.....	118
Table A.3.1 Ingredients used in the TEMPO-oxidation chemical treatment.....	205

List of Figures

Figure 1.1 A few sources of cellulose such as (a) wood, (b) bacteria, and (c) algae....	3
Figure 1.2 Hierarchical structure of wood biomass and the characteristic of cellulose fibrils.....	4
Figure 1.3 Applications of cellulose-based materials.....	5
Figure 1.4 Ashby plot of specific modulus vs. specific strength showing superiority of cellulose in comparison to most engineering materials.....	6
Figure 1.5 Anomalous scaling law of strength & toughness of cellulose nanopaper....	7
Figure 1.6 Envisioned molecular-level toughening mechanism of cellulose nanopaper.	8
Figure 1.7 Preliminary life cycle analysis of cellulose-graphite composite.....	11
Figure 1.8 Selected experimental equipment used.....	13
Figure 1.9 Schematics and Digital Image of the air-gun ballistic tester.....	14
Figure 1.10 Photographs and compositions of natural and engineered wood.....	16
Figure 1.11 Processing and mechanical performance of engineered wood.....	17
Figure 1.12 Snapshots of ballistic testing.....	18
Figure 1.13 Ballistic test details.....	19
Figure 1.14 Cross-sectional SEM image of a graphite-NFC (1:1 wt.%)	22
Figure 1.15 Photographs showing peeling graphite-NFC composite from substrate...	22
Figure 1.16 Photographs showing the graphite-NFC film retain morphology before and after bending.....	22
Figure 1.17 Mechanical properties of graphite-NFC composite.....	23
Figure 2.1 Hierarchical structure of cellulose from plant wood and bacteria.....	35
Figure 2.2 Multiscale analysis of cellulose mechanics.....	46
Figure 2.3 Structurally tuning mechanical properties of cellulose materials.....	51
Figure 2.4 Manipulating alignment of cellulose fibers.....	57
Figure 2.5 Interface engineering in cellulose composites.....	60
Figure 2.6 Schematic of topology engineering in cellulose composites.....	66
Figure 2.7 Designing topology in cellulose composites to boost mechanical performance.....	68
Figure 2.8 Structural engineering in cellulose composites.....	75
Figure 3.1 Schematic to show the CNT-NFC microfiber network formation through 3D printing.....	83
Figure 3.2 MD simulations showing why alignment between CNT and NFCs favors mechanical properties.....	87
Figure 3.3 Graphical illustration of the comparison between natural wood and elastic wood hydrogel.....	92
Figure 3.4 Images showing the recovery of the elastic wood hydrogel.....	93
Figure 3.5 Role of water in elastic wood under compression.....	95
Figure 4.1 Level-1 Coarse-Grained modeling scheme.....	104
Figure 4.2 Level-2 and Level-3 Coarse-Grained modeling scheme.....	105
Figure 4.3 Non-bonded interactions in neighboring Level-1 beads.....	108
Figure 4.4 Validation of the Level-1 CG model.....	111
Figure 4.5 Simulations of shearing and opening between two fiber models.....	113
Figure 4.6 CG modeling and mechanical behavior of cellulose nanopaper films.....	117
Figure 4.7 Image of biodegradable straws, made of microfibers and nanofibers.....	122
Figure 4.8 CG modeling complimenting the experiments.....	123

Figure 4.9 Schematic representation of the simulation models for cellulose nanofibers, microfibers, and hybrid fibers.....	124
Figure 4.10 Stress versus the pulling-out displacement results predicted by the CG models.....	125
Figure 5.1 Thermal conductivity of a cellulose molecule and its vibrational density of states.....	133
Figure 5.2 Thermal conductivity of a boron nitride nanotube and its vibrational density of states.....	135
Figure 5.3 Comparison of thermal conductivity of comparable cellulose, boron nitride nanotube and the derived hybrid material.....	138
Figure 5.4 Comparison of vibrational density of states of comparable cellulose, boron nitride nanotube and the derived hybrid material.....	141
Figure 5.5 Mechanical properties of equivalent cellulose nanofiber, boron nitride nanotube and their hybrid.....	143
Figure 7.1 Comparison between primary bonds and intermolecular bonds.....	158
Figure 7.2 Role of intermolecular bonds in improving the thermal stability of hydrogels, aerogels, and composite films.....	169
Figure 7.3 Role of intermolecular bonding in elevating the mechanical properties of hard materials such as nanosheets, fibers, and artificial nacre.....	177
Figure 7.4 Role of intermolecular bonding in elevating the mechanical properties of soft materials such as hydrogels and aerogels.....	183
Figure 7.5 A few selected applications fostered by the enhanced material properties when the material structure is subjected to a greater degree of intermolecular bonding.....	189
Figure A.3.1 Images showing necessary ingredients (Na_2CO_3 , NaHCO_3 , NaBr , Pulp, TEMPO) for preparation of the buffer solution before starting the TEMPO-oxidation.....	206
Figure A.3.2 TEMPO-oxidation treatment images.....	206
Figure A.3.3 Images after TEMPO treatment involving vacuum filtration, followed by homogenization.....	206
Figure A.3.4 Images showing the steps of ultrasonication and centrifugation to obtain the final cellulose-graphite slurry.....	207
Figure A.4.1 A snapshot including some details of the Writing Fellow cohort.....	210

Chapter 1: Introduction and Motivation¹

1.1 Background

The quest of both strength and toughness is perpetual in advanced material design; unfortunately, these two mechanical properties are generally mutually exclusive.¹ While strength measures a *stress* denoting a material's resistance to irreversible deformation, *toughness* characterizes a material's resistance to fracture and thus measures the energy needed to cause fracture. Toughness requires a material's ability to dissipate local high stress, e.g., by enduring deformation. Consequently, hard materials tend to be brittle (less tough); lower strength materials, which can deform more readily, tend to be tougher.^{2,3} For example, for metals and alloys, their toughness is usually inversely proportional to their strength.⁴ As a result, in practice, the design of strong and tough materials is inevitably a compromise.

Despite the consensus on mutual exclusiveness of strength and toughness, a significant gap exists between engineering practice and scientific considerations. For applications as large as nuclear reactor vessels and as small as cardiovascular stents, catastrophic failure of their structural materials is never acceptable. Therefore, it is not unusual that materials used in most safety-critical engineering structures are rarely super strong

¹ The experimental findings related to densified engineered wood and cellulose-graphite composite included in this chapter have been published as: **A)** Y. Zhou, C. Chen, S. Zhu, C. Sui, C. Wang, Y. Kuang, **U. Ray**, D. Liu, A. Brozena, U. H. Leiste, N. Quispe, H. Guo, A. Vellore, H. A. Bruck, A. Martini, B. Foster, J. Lou, T. Li, L. Hu, "A printed, recyclable, ultra-strong and ultra-tough graphite structural material", *Materials Today*, 30, 17-25, 2019 & **B)** J. Song, C. Chen, S. Zhu, M. Zhu, J. Dai, **U. Ray**, Y. Li, Y. Kuang, Y. Li, N. Quispe, Y. Yao, A. Gong, U. H. Leiste, H. A. Bruck, J. Y. Zhu, A. Vellore, H. Li, M. L. Minus, Z. Jia, A. Martini, T. Li, L. Hu, "Processing bulk natural wood into a high-performance structural material", *Nature* 554 (7691), 224-228, 2018.

materials without appropriate fracture resistance, but rather materials with comparatively low in strength but high in toughness. Acknowledging the necessary compromise between strength and toughness, one would expect that research on advanced material design would be focused on achieving an optimum combination of these two properties. Unfortunately, a great deal of research efforts in materials science are still too focused on pursuing higher strength, with rather limited corresponding regard for toughness.⁵⁻¹⁰ One example is the enthusiasm sparked by the discovery of carbon nanotubes (CNT), which exhibit remarkably high strength. However, it still remains uncertain how such a strong material can be incorporated with bulk materials to benefit from its high strength without sacrificing toughness.

Aiming to shed new insight on the long-sought strategy addressing the conflict of strength versus toughness, this research stems from the encouraging results from previous results of our group,¹¹ in which is unveiled a highly desirable but hard-to-achieve scaling law of mechanical properties of cellulose-based nanopaper that is anomalous to conventional understanding: *both the strength and toughness of the nanopaper increase simultaneously (40 and 130 times, respectively) as the size of the constituent cellulose building blocks decreases (from a diameter of 27 μm to 10 nm).* These stimulating results suggest the promising potential toward a new and highly desirable scaling law: *the smaller, the stronger AND the tougher.* This study on cellulose-based nanopaper reveals a fundamental bottom-up strategy generally applicable for other material building blocks as well. There are abundant but largely unexplored opportunities to utilize the fundamental bottom-up strategy to design a novel class of multifunctional materials that are both strong and tough.

To explore these fertile opportunities, this research will combine systematic multi-scale modeling and complementary experiments to decipher the fundamental science underpinning the anomalous scaling law of strength and toughness revealed from the pilot study of cellulose-based nanopaper. This is expected to help synthesize and characterize a novel class of strong and tough materials. The research will not only offer new fundamental insight on addressing the Holy Grail of attaining mutually exclusive strength and toughness in advanced material design, but also open up fertile opportunities toward other class of materials with both exceptional mechanical properties and other highly desirable features (e.g., environmentally sustainable, multifunctional) conferred by their constituent building blocks.

1.2 Why Cellulose?

Cellulose is the most abundant biopolymer on earth and has long been used as the sustainable building block for paper. The length of the cellulose chains and the morphology vary slightly depending on the variable sources such as wood, bacteria and algae (Figure 1.1).

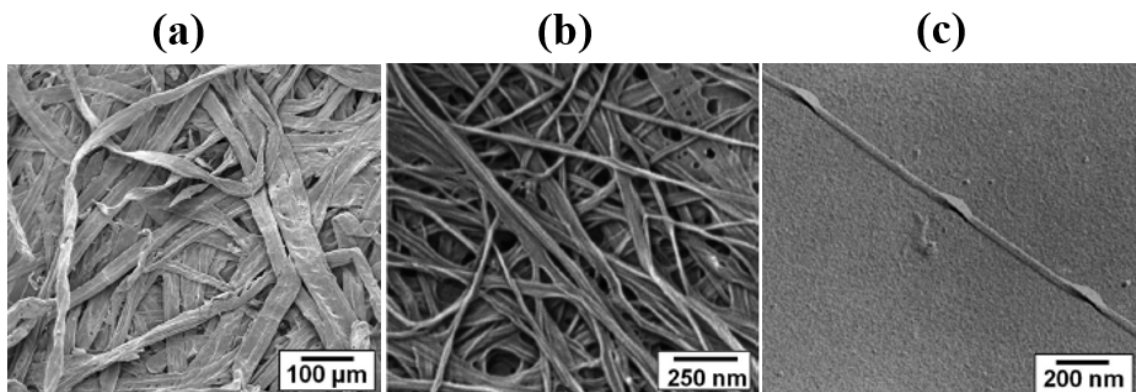


Figure 1.1 A few sources¹² of cellulose such as (a) wood, (b) bacteria and (c) algae

Wood fibers are the main natural source of cellulose and have an intrinsically hierarchical structure (Figure 1.2a). We focus on wood cellulose fibers in this thesis. A 20~50 μm thick wood fiber comprises thousands of nanofibrillated cellulose (NFC, 5-50 nm in diameter), each of which can be disintegrated into finer elementary fibrils consisting of cellulose molecular chains.¹²⁻²⁰ Cellulose molecule is a linear chain of ringed glucose molecules, with a repeat unit (Figure 1.2b) comprising two anhydroglucose rings ($\text{C}_6\text{H}_{10}\text{O}_5$) linked through C-O-C covalent bond. Rich hydroxyl groups in cellulose molecule (six in each repeat unit) enable facile formation of hydrogen bonds, both intra-chain and inter-chain. While the intra-chain hydrogen bonding stabilizes the linkage and results in the linear configuration of the cellulose chain, inter-chain hydrogen bonding among neighboring cellulose molecules plays a pivotal role in the deformation and failure behaviors of cellulose-based materials.

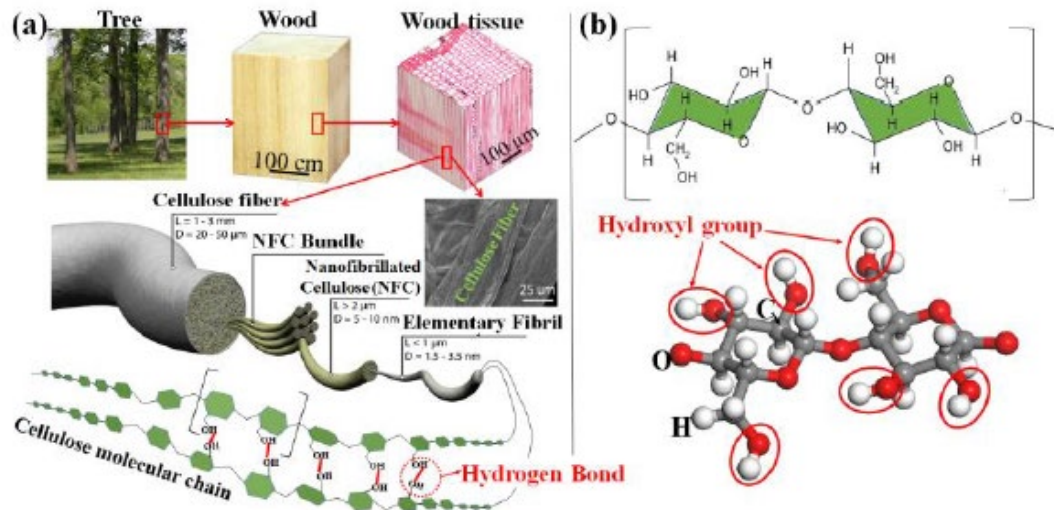


Figure 1.2 (a) Hierarchical structure of wood biomass and the characteristic of cellulose fibrils. Note the *rich inter-chain hydrogen bonds* between neighboring cellulose molecular chains.²¹ (b) Single cellulose chain repeat unit. Note the six hydroxyl groups (red solid circles) in each repeat unit.

Currently, due to its unique properties, cellulose based materials²² have multi-fold applications such as in transparent papers, organic light-emitting diode, supercapacitors, and cosmetics (Figure 1.3).

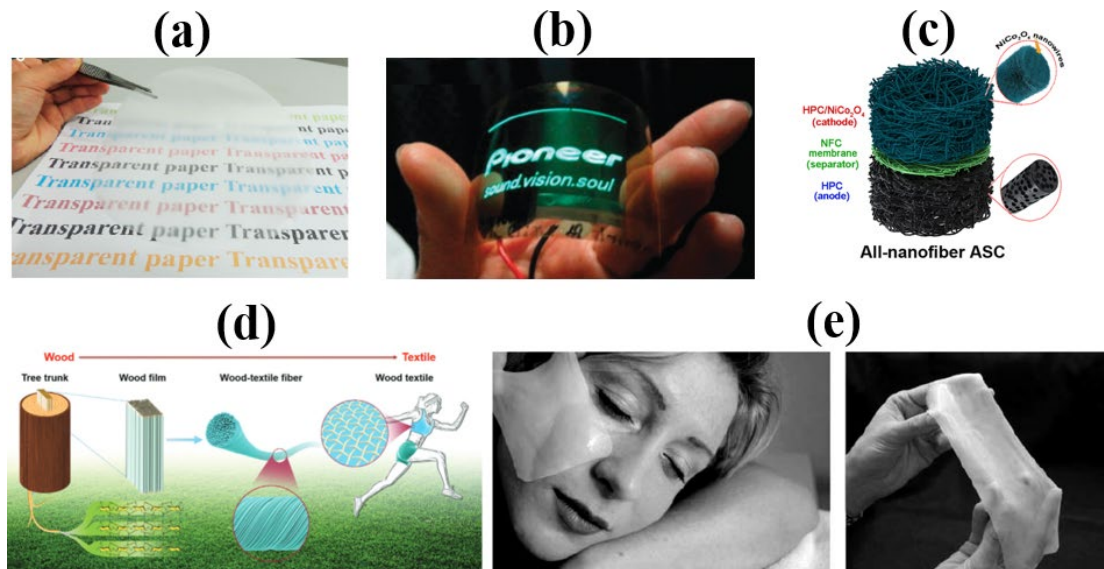


Figure 1.3 Applications of cellulose-based materials (a) Transparent paper²³ produced from wood fibers (b) Organic light-emitting diode¹² deposited onto a flexible optically transparent wood-cellulose nanocomposite (c) High-performance all-nanofiber asymmetric supercapacitor²⁴ (ASC) (d) Wood textile fiber²⁵ obtained from tree trunks used in smart textiles and wearable electronics and (e) Cosmetic applications such as NanoMasque²⁶ for skin treatment.

From a mechanistic standpoint, cellulose has appealing properties. The specific modulus and specific strength of cellulose are indeed higher than most metals and composites, and many ceramics (Figure 1.4), making it a promising building block for functional and structural materials.

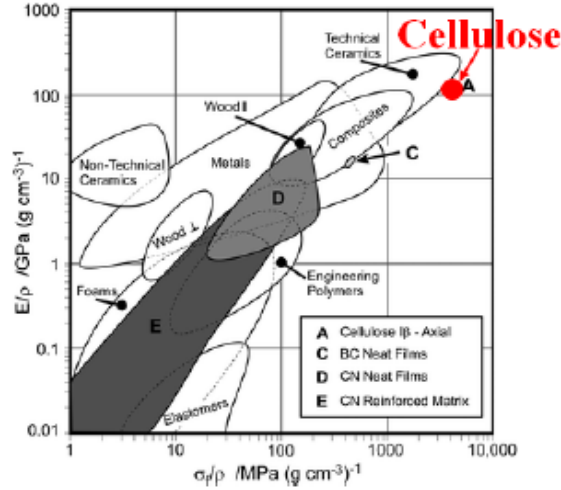


Figure 1.4 Ashby plot¹² of specific modulus vs. specific strength. Cellulose is superior to most engineering materials.

The unique molecular feature and attractive mechanical properties of cellulose is the reason why there is a simultaneous and significant increase of both the tensile strength and toughness of nanopaper as the constituent NFC diameter decreases, a highly desirable but hard-to-achieve scaling law in advanced materials design (Figure 1.5a-d). Preliminary fracture mechanics analysis suggests that the ultimate tensile strength of the cellulose nanopaper is $\sigma_{\text{uts}} = K/\sqrt{D}$, where K is a constant characterizing the resistance of an individual NFC fiber to fracture and having the same dimension of stress intensity factor and D the NFC diameter. Such a prediction is strongly supported by the experimental measurements (Figure 1.5d). To further shed insight on the anomalous scaling law of strength and toughness of the cellulose nanopaper, comparisons with CNTs were also done with diameter similar with NFC fibers (Figure 1.5e). It turns out that the strength and toughness of cellulose nanopaper are also much higher (9 and 195 times, respectively) than those of the CNT films (Figure 1.5f).

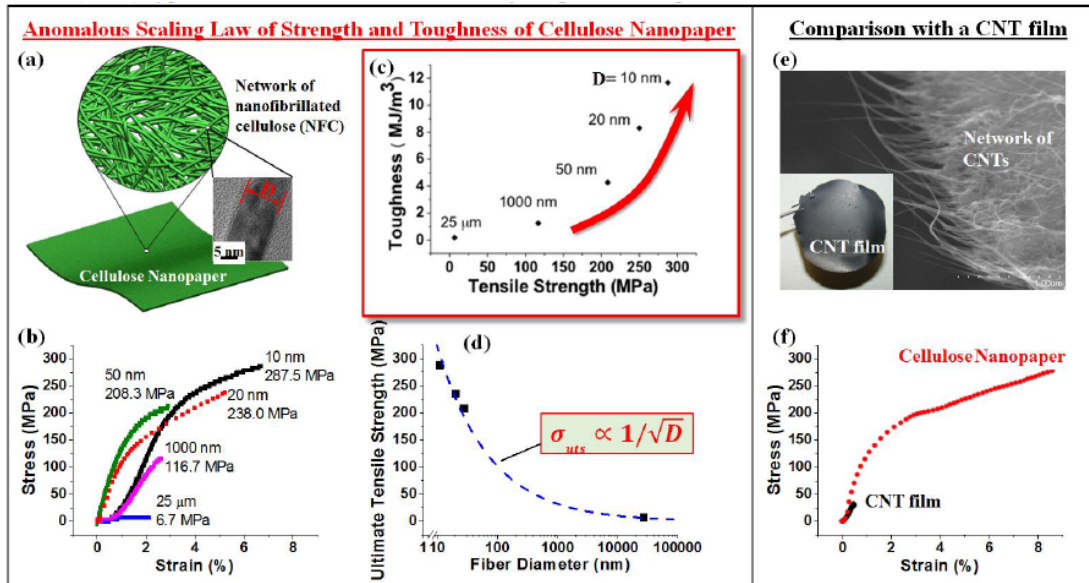


Figure 1.5 Anomalous scaling law of strength and toughness of cellulose-based nanopaper. (a) Schematic of cellulose nanopaper, made of a network of NFC. Inset shows HR-TEM image of a ~10 nm NFC. (b) Stress-strain curves of cellulose paper made of NFC of various diameters. As the NFC diameter decreases, both tensile strength and ductility of the cellulose paper increases, leading to an anomalous scaling law shown in (c): The smaller, the stronger AND the tougher. (d) Further reveals that the tensile strength scales inversely with the square root of NFC diameter. (e) Optical (inset) and SEM images of a CNT film made of network of CNTs. (f) Lack of inter-CNT hydrogen bonds, the CNT film is shown to have a much lower tensile strength and toughness than the cellulose nanopaper, although constituent CNTs and NFCs have similar diameter (~10 nm).

The study suggests the following mechanistic understanding on the exceptional mechanical properties and anomalous scaling law of cellulose nanopaper: while the increase in tensile strength of cellulose nanopaper is attributed to reduced intrinsic defect size as the constituent NFC size decreases (the smaller, the stronger); the simultaneous increase in toughness essentially results from the significant increase of hydrogen bonding among NFC fibers as their diameter decreases (and thus their surface

area increases). Figure 1.6 further clarifies the envisioned molecular-level toughening mechanism of cellulose nanopaper. Under tension, the initially entangled NFC network deflects and twists to align parallel to the tensile direction. As the load increases, the straightened cellulose nanofibers begin to slide relative to each other, and the pulling-off and fracture of such nanofibers eventually lead to the overall failure of the nanopaper.

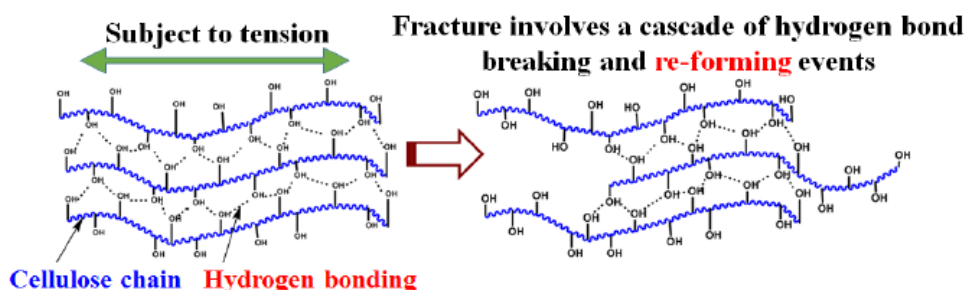


Figure 1.6. Envisioned molecular-level toughening mechanism of cellulose nanopaper: Failure involves a cascade of hydrogen bond breaking and re-forming events, which dissipate significant amount of energy, thus lead to much enhanced fracture toughness.

Due to the nature of hydrogen bonding, such a failure process involves a cascade of hydrogen bond breaking and re-forming events, which dissipate significant amount of energy, and thus result in a much-enhanced fracture toughness. By contrast, such a mechanism is lacking in a CNT film, in which inter-CNT bonding is largely van der Waals (vdW) forces, which is much weaker than hydrogen bonding. Inspired and motivated by the above underpinning mechanism, we envision a fundamental bottom-up strategy to achieve both high strength and toughness that is generally applicable for a wide range of other material building blocks. The opportunities are abundant and multi-faceted. There exist a wide variety of cellulose nanoscale building blocks with

diverse structural features that are potentially beneficial for even better mechanical properties of cellulose nanopaper. The resulting materials could be made both mechanically tough and strong but also with other highly desirable functionalities (such as exceptional electrical conductivity, electrochemical energy storage, and thermal conductivity).

Guided by the above rational, we delineate a systematic framework integrating multi-scale mechanics modeling and complementary experiments to explore the fertile opportunities that cellulose has to offer.

1.3 Market demands and societal implications of cellulose industry

To give the readers a perspective, let's start with an example elucidating on why cellulose can be a future wonder material to the materials science community. The first synthetic plastic was developed in 1907 and in over 110 years' time span, it is still impacting our daily lives. Similarly, the first nanocellulose gel was developed in 1977 and it can be expected to integrate in society and commerce within a similar timeframe. Nanocellulose global productive has almost tripled since 2000 and as predicted by USDA, the global cellulose production estimate for cellulose is expected to meet the target by 2045. The cost is also expected to decrease ($< \$2/\text{kg}$) with more effective methods of mass-production.²⁷ Right now, the industry is worth ~\$187 billion with more than 400,000 employees. This number, too, is expected to increase with advancement in relevant technology. So, the superior material properties kept aside, there are plenty of opportunities even for professional growth if we study this material.

From the academic front, the number of scientific literatures also increased over 19000% from year 2000 to 2018.²

It would be a wrong perception to assume that working with wood cellulose means cutting down trees. Around 39% of the cellulose fibers used comes from recycled paper and defective and slow growing trees.²⁸ Only 36% timber comes directly from the forest. Agriculture, palm oil, soybeans and beef cause 73% deforestation. For example, Super Wood (Section 1.4.1) is a material we invent through selective densification and lignin removal of natural wood. This technique is universally applicable on all softwoods (eg: *Oak*, *Pine*, *Cedar*) and hardwoods (eg: *Basswood*, *Poplar*). Softwood and hardwood are distinguished botanically in terms of reproduction. In general, hardwood comes from deciduous trees, and they lose its leaves annually and softwoods come from conifers, which remains evergreen throughout the year. Hardwoods are slow growing and usually denser than softwoods. Hence, using our densification technique, we can make the softwoods stronger than hardwood and being fast growing, they can be harvested in a controlled fashion. This gives us end-products with equivalent properties of hardwoods and simultaneously protects the expensive hardwoods. So, this is, in no way, aiding deforestation.

Working with cellulose will inevitably reduce the carbon footprint. It is an environmentally friendly and bio-degradable material. The paper industry contributes to only around 5% of industrial waste (27.24 billion pounds in total as of 2015). Also,

² Information obtained from the following book chapter- a) Ray, U., Zhu, S., Pang, Z., Li, T. (2023). Nanocellulose-Based Materials with Superior Mechanical Performance. In: Hu, L., Jiang, F., Chen, C. (eds) Emerging Nanotechnologies in Nanocellulose. NanoScience and Technology. Springer, Cham. https://doi.org/10.1007/978-3-031-14043-3_5

67% of all the recovered paper can be used (as of 2015), in comparison to 27% of glass, 35% of metals and 8% of plastics. The by-products of paper and pulp industry are abundant and have widespread applications. For example, (a) *bark* provides energy from a bio-mass based source, (b) *turpentine* can be used in organic synthesis, cleaning products etc., (c) *residual fibers* can be used in mulch and (d) *residual ash* can be used in concrete. Hence, this entire industry is definitely moving towards achieving self-sustainability.

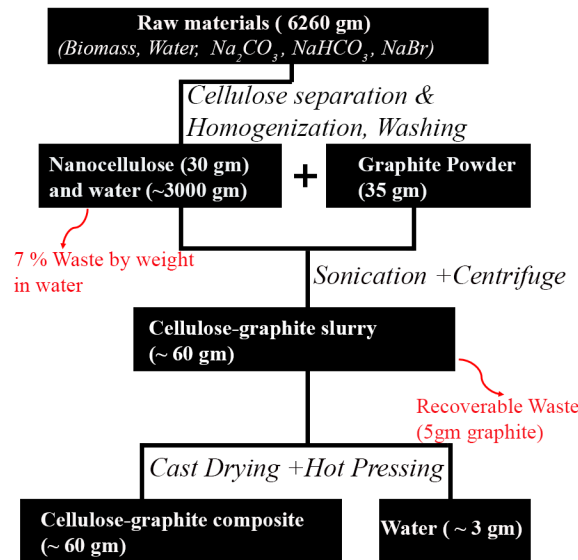


Figure 1.7 Preliminary life cycle analysis (LCA) of our cellulose-graphite composite (*section: 1.2.2*).

We performed a preliminary life cycle analysis (LCA) on the graphite-cellulose composite (*section: 1.2.2*) developed by our team. As can be seen from Figure 1.7, the only waste here is water and impurities (7%), graphite and water by evaporation. Most of the waste is recoverable. There are challenges to make our process suitable to scaled-up production, finding alternatives to using the expensive TEMPO and trying to reduce water loss by evaporation. After that is achieved, we can get a low-cost, lightweight composite that already has strength (up to 1 GPa) more than most existing materials.

Hence, the paper and pulp industry have some very well-defined goals ahead of it. Even though outside the scope of this thesis, all the challenges²⁹ can be listed as: a) utilizing the novel properties of nanocellulose at the continuum scale, b) reduce water consumption and establish a suitable drying method, c) reduce carbon emissions, d) increase the raw material yield and e) obtain a scalable but efficient manufacturing process.

Experiments integrated with computational approaches are essential to drive novel material invention, and this thesis sheds light on some of the gaps through mechanical experiments and multi-scale materials modeling.

1.4 Experimentations driving the research motivation

Some experiments were conducted on two novel-cellulose based materials, which served as a motivation for this modeling-intensive thesis. For example, cellulose fibers were fabricated cellulose fibers from bleached kraftwood pulp through TEMPO oxidation method and tensile tests were conducted using a set of equipment as shown in Figure 1.8. AFM imaging was also conducted to characterize (length and diameter) the fibers and the data was later used to validate the modeling. All of these were done with the help of Professor Liangbing Hu's (Materials Science Department, University of Maryland College Park) group.



Figure 1.8 *Selected experimental equipment used* (Location: Prof. Liangbing Hu's lab at University of Maryland, College Park).

To conduct the ballistic testing of cellulose-based materials, a sample holder for the ballistic air gun was designed. The tests were done in Dynamic Effects Laboratory at University of Maryland. The ballistic tests on engineered wood samples used an air gun, which comprises a pressure indicator frame (PIF), two cylinders filled with compressed nitrogen (N_2), a pressure chamber 127 mm in diameter and barrel-length 190.5 mm, a nozzle of length 1,156 mm and internal diameter 12.5 mm and a holder specifically designed to clamp the sample (Figure 1.9). The pressure indicator frame has dials with which we adjust the pressure inside the two N_2 cylinders. The left cylinder is used to pressurize the volume inside the barrel chamber when the projectile is fired and the right N_2 cylinder controls the pressure for the firing valve, helping it open instantaneously when fired. The chamber pressure was set to about 2.22 MPa. Once opened, the valve releases the pressure and accelerates the projectile. We

use projectiles cylindrical in shape, made of stainless steel, with a diameter of 11.85 mm, length 51.77 mm and mass 0.046 kg. The dimensions of the samples were approximately 44 mm by 44 mm by 3 mm. The whole ballistic process was captured using two Phantom v12 cameras. The Phantom Camera Control software developed for such high-speed digital cameras, captured the velocities of the projectile before and after perforating the sample. The ballistic energy absorption of the test sample is defined by the kinetic energy loss after a cylindrical steel projectile perforates the

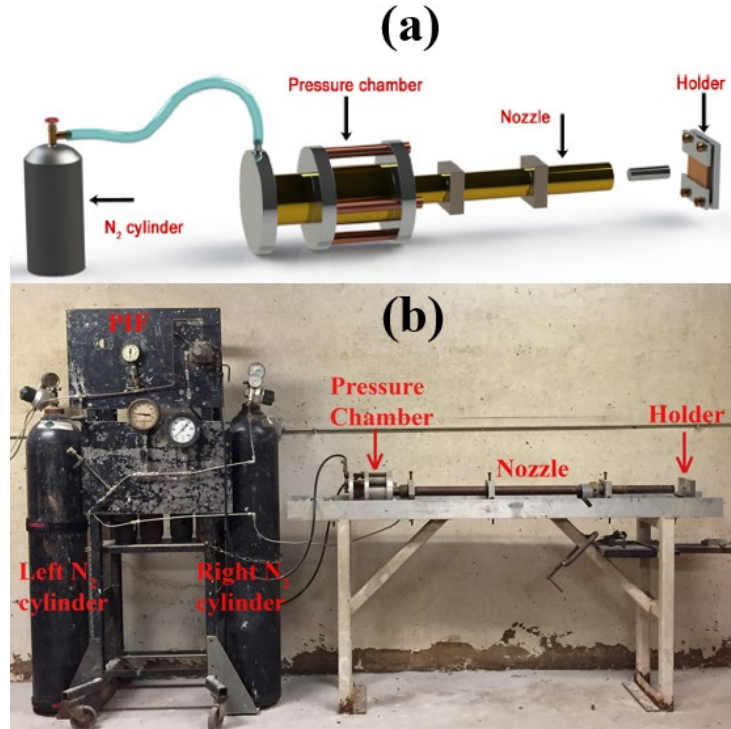


Figure 1.9 (a) Schematics of the air-gun ballistic tester³⁰ (b) Digital Image of the set-up

the sample. The equation for the ballistic energy absorption normalized by sample thickness is $m(v_1^2 - v_2^2)/2t$, where m is the mass of the projectile, t is the thickness of the sample and v_1 and v_2 are the velocities of the projectile before and after perforating the sample, respectively. The velocities of the projectile are controlled around 120

miles/hr, which is typically the velocities at which car crash occurs. This is because of our vision to use these materials in vehicle applications, with a goal to reduce the car weight by 60% and improving the fuel efficiency by over 20%.

The results of these mechanistic (tensile and ballistic) tests are included in Sections 1.4.1 and 1.4.2 where we show the superior mechanical properties of a) Densified Engineered wood and b) Graphite-NFC composite, respectively.

1.4.1 Densified Engineered Wood (top-down approach)

In top-down approach, we start with the bulk natural wood obtained from tree trunks and engineer that material to the lower length scale. Here we report a simple and effective strategy to transform bulk natural wood directly into a high-performance structural material with a more than tenfold increase in strength, toughness and ballistic resistance and with greater dimensional stability. First, natural wood blocks (typical sample dimension: 120.0 mm by 44.0 mm by 44.0 mm as in Figure 1.10a) were immersed in a boiling aqueous solution of mixed 2.5 M NaOH and 0.4 M Na₂SO₃ for 7 h, followed by immersion in boiling deionized water several times to remove the chemicals. Next, the wood blocks were pressed at 100 °C under a pressure of about 5 MPa for about 1 day to obtain the densified wood (115.6 mm by 46.5 mm by 9.5 mm as in Figure 1.10b). By adjusting the boiling times, densified wood with different degrees of lignin and hemicellulose removal can be obtained (Figure 1.10c). We found that partial lignin removal allows for the highest density of the resulting wood with the best tensile strength. Without lignin removal, it is difficult to hot-press natural wood into a completely compact wood. However, total lignin removal leads to wood that can be easily crushed during hot-pressing, probably owing to the absence of lignin as a

binder. Hot-pressing leads to the total collapse of cell walls and the complete densification of the natural wood with highly aligned cellulose nanofibers. This strategy is shown to be universally effective for various species of wood (Basswood, Oak, Poplar, Cedar and Pine). Our processed wood, named Super Wood, has a specific strength higher than that of most structural metals and alloys, making it a low-cost, high-performance, lightweight alternative. Hydrogen bonds formed between neighboring cellulose nanofibers make a pivotal contribution to the remarkably enhanced strength and toughness. The entire process schematic along with a comparison of the mechanical performance of Super Wood with other known structural materials is shown in Figure 1.11.

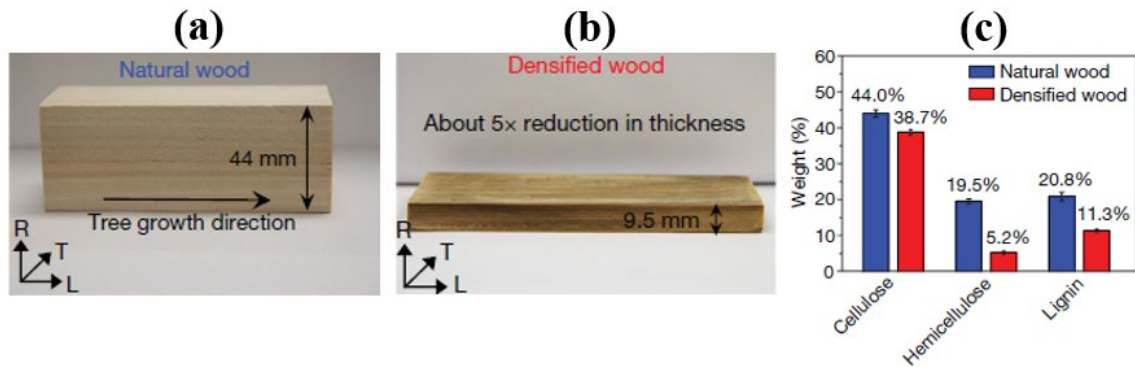


Figure 1.10 (a) Photograph of natural wood sample. (b) Photograph of densified wood. L is the tree growth direction (c) Chemical treatment leads to substantial removal of lignin (before, $20.8\% \pm 1.2\%$; after, $11.3\% \pm 0.5\%$) and hemicellulose (before, $19.5\% \pm 0.7\%$; after, $5.2\% \pm 0.5\%$) in natural wood, but only modest dissolution of cellulose content (before, $44.0\% \pm 1.0\%$; after, $38.7\% \pm 0.8\%$).

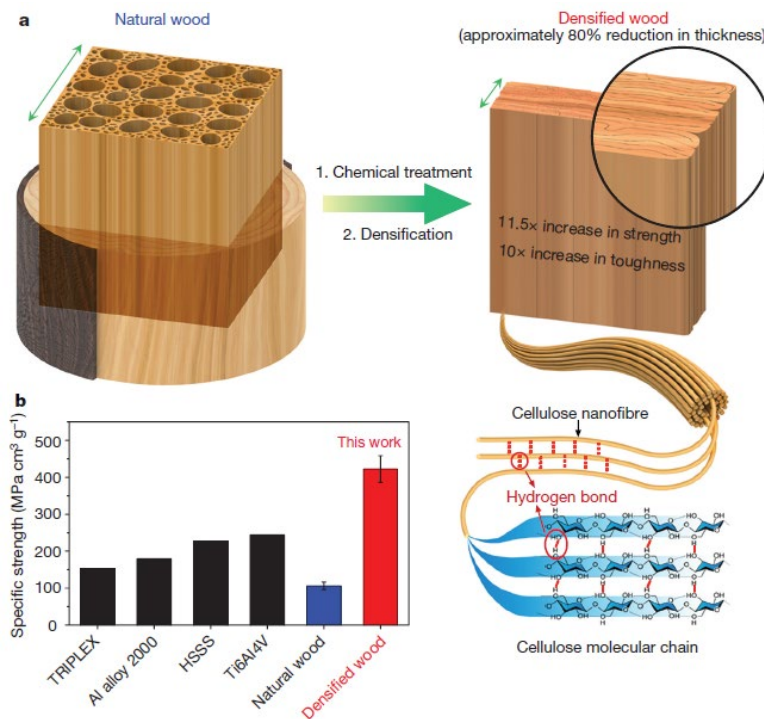


Figure 1.11 Processing approach and mechanical performance of engineered wood.³⁰ (a) Schematic of the top-down two-step approach to transforming bulk natural wood directly into super-strong and tough densified wood. Step 1, chemical treatment to partially remove lignin/hemicellulose; step 2, mechanical hot-pressing at 100 °C, which leads to a reduction in thickness of about 80%. Most of the densified wood consists of well aligned cellulose nanofibers, which greatly enhance hydrogen bond formation among neighboring nanofibers. b, Specific tensile strength of the resulting densified wood (422.2 ± 36.3 MPa cm³ g⁻¹, mean \pm standard deviation) is shown to be higher than those of typical metals (the Fe-Al-Mn-C alloy, TRIPLEX and high specific- strength steel, HSSS), and even of lightweight titanium alloy (Ti6Al4V). The tensile, bending, and compressive properties of the wood samples are measured using a Tinius Olsen H5KT tester. Error bars show standard deviation with $n = 5$ repeats.

These strong and tough yet lightweight densified woods hold promise as materials for low-cost armour and ballistic energy absorption. To demonstrate such a potential, we use the same processing approach to make a five-layer densified wood with fiber orientation alternating by 90° from layer to layer (referred to as X–Y–X–Y–X). We

name them laminated densified wood. We performed ballistic tests (Figure 1.9) on natural wood, monolayer densified wood and laminated densified wood in an air-gun ballistic tester (Figure 1.9). High-speed-camera video snapshots of the ballistic tests are shown in Figure 1.12.

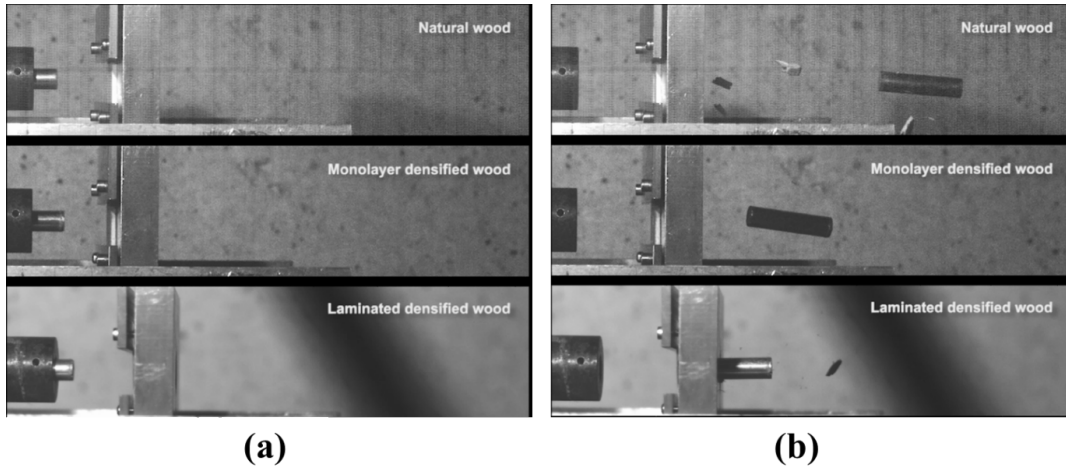


Figure 1.12 *Snapshots of ballistic testing.* (a) Initial frame when the projectile comes out of the air gun (b) Final frame after the projectile perforates the samples. Laminated densified wood was able to stop the projectile.

The ballistic energy absorption per unit sample thickness for monolayer densified wood is $4.3 \pm 0.08 \text{ kJ m}^{-1}$, a remarkable sevenfold increase from that of natural wood ($0.6 \pm 0.03 \text{ kJ m}^{-1}$). The ballistic resistance of laminated densified wood is shown to be even higher (Figure 1.13a) and more isotropic (ballistic resistance almost same along fiber alignment and perpendicular to fiber alignment direction, values being $5.6 \pm 0.2 \text{ kJ m}^{-1}$ and $6.0 \pm 0.1 \text{ kJ m}^{-1}$). The projectile can break through the laminated sample surface but is eventually trapped inside without complete perforation. The resulting ballistic energy absorption is ten times higher than that of natural wood (Figure 1.13a). Further characterization of the fractured samples (Figure 1.13b–g) reveal that in the monolayer

densified wood, the perforation opening by the steel projectile is smaller than that in the natural wood, and the wood surface is severely chapped, indicating much stronger bonding between highly packed wood cell walls and hence substantial energy dissipation during the projectile perforation. We published this research in *Nature*, 2018.³⁰

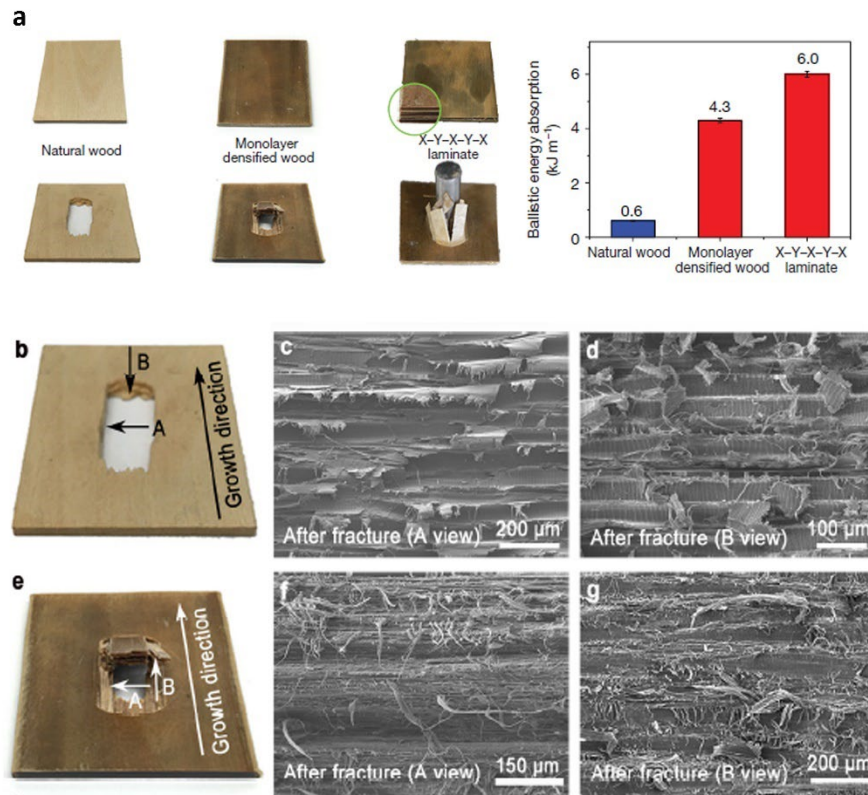


Figure 1.13 *Ballistic test details.*³⁰ (a) Comparison of ballistic energy absorption of three types of wood. Photographs of the natural wood, monolayer densified wood, and the X-Y-X-Y-X laminated densified wood before (top row) and after (bottom row) the ballistic test. (b) Photograph of natural wood after ballistic test, showing relatively smooth wood surface after the projectile perforates the wood. (c, d) SEM images of the fracture surface show that fracture takes place along the loosely bonded cell walls in natural wood. (e) Photograph of monolayer densified wood after ballistic test, showing severely chapped wood surface after the projectile perforates the wood. (f, g) SEM images of the fracture surface show

enormous numbers of wood fibers pulled out from the densely packed cell walls, suggesting substantial energy dissipation during the projectile perforating the densified wood.

1.4.2 Graphite-NFC composite (bottoms-up approach)

In bottoms-up approach, we start with the fibers at the molecular length and scale up to achieve mass-production. By dispersing graphite flakes and nano-fibrillated cellulose (NFC) in water at room temperature to form a stable and homogeneous solution with a high solid concentration (20 wt.%), we demonstrate this slurry can be scalably printed to manufacture a graphite-NFC composite that exhibits a high tensile strength and toughness, that is significantly greater than most engineering materials (e.g., steels, aluminum, and titanium alloys). This research demonstrates how hydrogen bonds between the graphite flakes and NFC play a pivotal role in the superb mechanical performance of the composite, also enabling this low-cost (\$1.5/kg in comparison to \$20/kg price of carbon fibers) material to be recyclable for an environmentally sustainable solution to high performance structural materials.

Pine, a type of softwood, was used in this study. A kraft process for conversion of wood into wood pulp was used. The kraft process entails treatment of wood chips with a hot mixture of water, sodium hydroxide (NaOH), and sodium sulphite (Na₂SO₃). Then NFC fibers are produced by (2,2,6,6-tetramethylpiperidin-1-yl) oxidanyl (TEMPO) oxidation. Commercial graphite powder (Asbury Carbons 3061) and 2 wt% NFC solution were mixed with a solid mass ratio of 1:1 for graphite to NFC. All the samples have a graphite to NFC mass ratio of 1:1. The dispersion process was performed using a Vibra-Cell ultrasonic liquid processor for 5 min, and then bath sonicated for 15 min (FS110D, Fisher Scientific). After sonication, the graphite flakes were well dispersed

in the NFC solution. The obtained graphite-NFC slurry was degassed for 20 min in a vacuum pumping system until no bubbles were observed in the slurry. The graphite-NFC slurry can be concentrated by placing it on a heating stage at 110°C with high-speed stirring to ensure the uniformity of the whole system. The graphite-NFC composites (Figure 1.14) were prepared by cast-drying the 20 wt% slurry. The final composite with 20 to 50 μm thickness and $\sim 1.2 \text{ g/cm}^3$ density was obtained after a 60 °C hot press for 24 h. For control experiments, we prepared NFC films using a similar procedure except without the addition of graphite. The graphite film was also prepared using a similar procedure except that the graphite solution was intensively washed by ZnCl_2 and water to remove NFC before pressing. All the NFC nanopapers and graphite-NFC composites used for mechanical testing were pressed at 60 °C under a force of about 50 kN for 24 h using a hot press (YLJ-HP88V-250, MTI). The NFC nanopapers and graphite-NFC composites were hot pressed before completely dry to be full densified. The applied pressure increased gradually, and usually reached 50 kN in 4 h, then kept at 50 kN for 20 h. To fabricate block materials from the single graphite-NFC composites sheet, the single sheet should not be completely dried at first. Then multiple sheets are stacked together in the hot press at 60 °C under 50 kN for 48 h. The graphite-NFC composites sheet can be easily peeled off from the substrate and can be bent as shown in Figures 1.15 and 1.16.

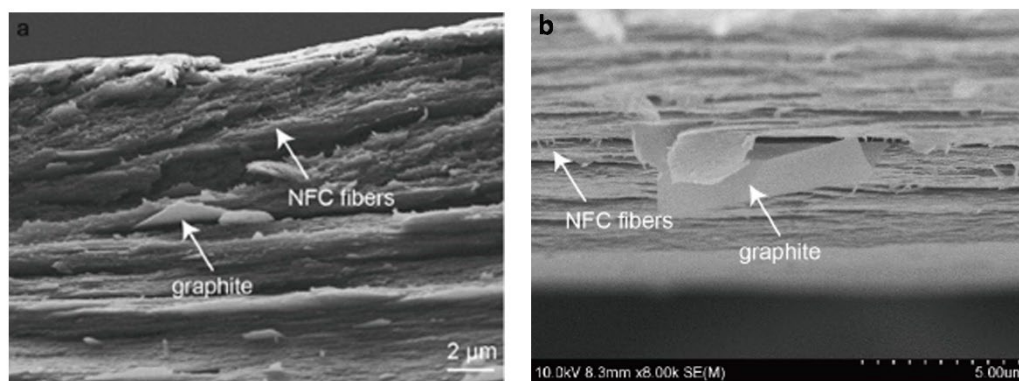


Figure 1.14 (a,b) Cross-sectional SEM image³¹ of a graphite-NFC (1:1 wt. %), wherein platelets of multilayered graphite are observed as well as NFC fibers.

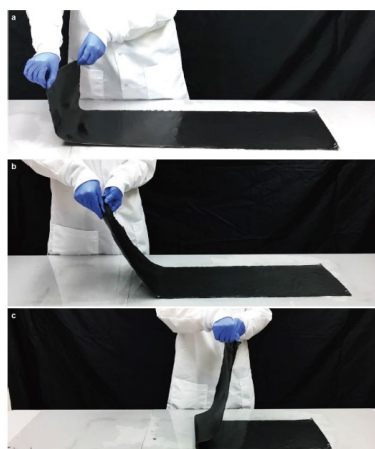


Figure 1.15 (a-c) Photographs showing peeling off graphite-NFC composite from the substrate after water evaporation.



Figure 1.16 Photographs showing the graphite-NFC film retain morphology before and after bending.

A single column tabletop model testing system (Instron, USA) was used to perform mechanical tests. Ballistic tests are performed using the same set-up as described in Figure 1.9. Figure 1.17a and b show the typical stress-strain curves and the obtained ultimate tensile strength of graphite-NFC composite, cellulose nanopaper and graphite respectively.

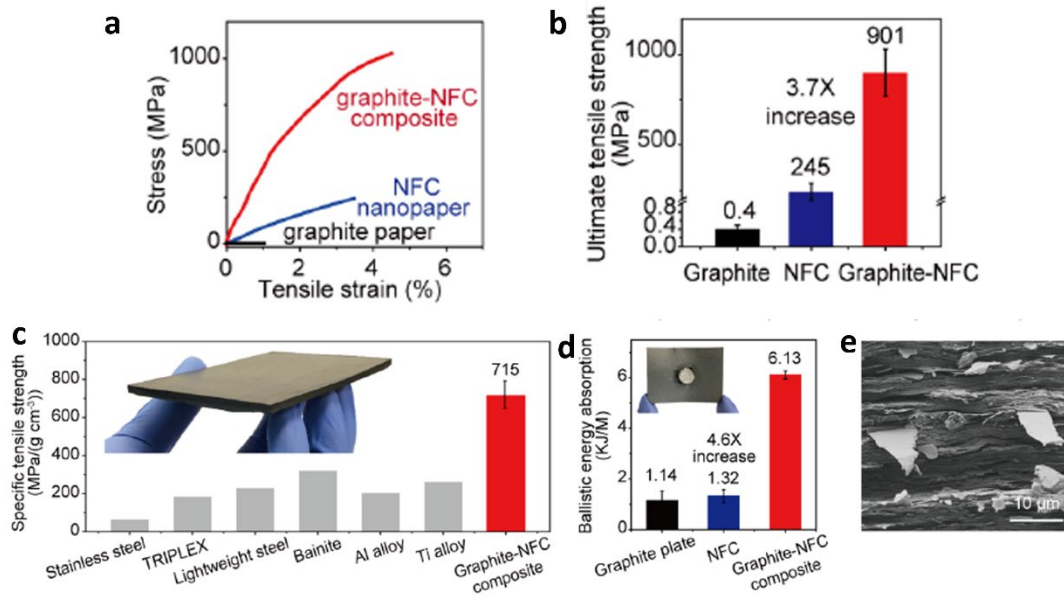


Figure 1.17 Mechanical properties of graphite-NFC composite (a) Stress-strain curves³¹ of graphite-NFC, NFC nanopaper, and graphite paper. (b) Comparison of the ultimate tensile strength of the graphite-NFC composite, NFC nanopaper, and graphite paper, respectively. (c) Specific tensile strength of the graphite-NFC composite compared with strong metallic alloys. (d) The ballistic energy absorption of the NFC, commercial graphite plate and graphite-NFC composite. Inset: Photo of the graphite-NFC composite after the ballistic test. (e) Cross-sectional SEM image of the vertically stacked multilayer graphite-NFC composite after the ballistic test.

As graphite flakes are hybridized into the NFC matrix, the ultimate tensile strength (Figure 1.17b) increases by ~ 3.7 -times, from 245 ± 47 MPa (NFC) to 901 ± 129 MPa (graphite-NFC composite). The specific tensile strength of our graphite-NFC

composite is even higher than ultra strong low-density steel and titanium alloys (Figure 1.17c). Our bottom-up processing approach provides the ability to fabricate graphite-NFC block materials by hot pressing multiple layers of the graphite-NFC composite (inset in Figure 1.17c). We performed ballistic tests on NFC nanopaper, a commercial graphite plate, and the graphite-NFC composite block (1 mm thick), in which the ballistic energy absorption of the samples is defined by the kinetic energy loss after a cylindrical steel projectile perforates the sample. When the same ballistic test is conducted using these three kinds of materials, the resulting energy absorption per unit thickness of the block graphite-NFC material was 6.13 ± 0.16 KJ/m, a remarkable 4.6- and 5.4-times increase from that of NFC nanopaper and the commercial graphite plate, respectively (Figure 1.17d). The graphite flakes, with some parts still embedded in the NFC matrix, break along the incident direction of the projectile, indicating substantial energy dissipation during the projectile perforation (Figure 1.17e). Toughness values, calculated separately in this study by computing the work of fracture, also increase which is contrary to the conventional conflict between strength and toughness.

Here strong interactions between graphite flakes and NFC fibers play a pivotal role in the high strength and toughness. The hydrophilic behavior of NFC is attributed to the hydroxyl groups that are located on the surface of the NFC fibers. The exposure of the hydrophobic C-H bonds also causes hydrophobic faces to form in the elementary fibers, which enables hydrophobic interactions with the hydrophobic plane of the graphite.

Meanwhile, the spatial gaps between the edges of the graphite flakes are filled with the flexible NFCs. A large amount of the interfaces between the graphite flake edges and NFC matrix are thus hydrogen bonded, which significantly enhances load transferring between graphite flakes. Due to the presence of the graphite hydrophobic surfaces, the hydrogen bonding networks projected along the tensile direction are densified, thus the load transferring capacity of the NFC matrix also increases. The synergistic interaction between the graphite flakes and NFC substantially increases the load resistance of the composite to failure (i.e., high strength) and the energy dissipation during composite failure (i.e., high toughness). In contrast, in a pure graphite film there are only a limited number of hydrogen bonding sites at the flake edges, and the inter-flake interactions are essentially weak van der Waals forces. As a result, pure graphite is weak and brittle. The fabrication of this composite requires relatively little energy without producing harmful waste, making it a scalable, economically feasible, environmentally friendly, and recyclable material, thus opening new opportunities for developing high-performance structural materials in a more sustainable manner. This research was published in *Materials Today*, 2019.³¹

The two experiment-driven research described in sections 1.4.1 and 1.4.2 where we obtain record-high mechanical strength and toughness of two materials (Densified engineered wood and Graphite-NFC composite) obtained by two different approaches (top-down and bottoms-up respectively), proved to be the main motivating factor to delve deeper in the cellulose system using a modeling framework. A robust modeling scheme applicable across different length scales will help shed light on the principal

mechanisms of many phenomena which cannot be explained by known experimental techniques.

1.5 Modeling Methodology

Two types of modeling techniques are implemented in this thesis. They are a) atomistic simulations (section 1.5.1) and b) coarse-grained molecular dynamics (section 1.5.2). The former is applicable in the length scale of 10^{-9} to 10^{-10} m, while the latter is a scaled-up technique to reduce the computational expenses and applicable till 10^{-6} m length scale. All the simulations are performed using the open-source package LAMMPS³² and the molecular trajectories are visualized using VMD³³ and/or OVITO.³⁴

The post-processing of all the data obtained as an output from LAMMPS (e.g.: (i) computation of bond length between coarse-grained beads and (ii) calculation of pulling force versus displacement) are done by programming in Python. Graphs are plotted using MATLAB, MS Excel and/or Grace wherever applicable. Figures are edited using Adobe Photoshop/Illustrator. The author acknowledges the University of Maryland supercomputing resources (<http://hpcc.umd.edu>) made available for conducting the research reported in this work.

1.5.1 Molecular Dynamics

Molecular dynamics (MD) is a deterministic modeling tool which can shed light on the principle understanding of many experimental phenomena, otherwise inexplicable by tools in the laboratory. Here we calculate the equations of all the atom trajectories in the system by classical Newton's laws of motions and an appropriate potential

(“negative slope” of which is force). The properties of the system evaluated in the nanoscale as a result, also helps to predict the system properties at the macroscale and thereby saves experiment time and cost. The computation generally demands high amount of parallel computing (estimated RAM usage per core - 5GB) and physical memory (estimated file space required $\sim 5000\text{GB}$), which are both far beyond the capacity of non-high performance computing setup (e.g., desktop computers). We used Deepthought2 and Zaratan available at University of Maryland, College Park for all the modeling research in this thesis.

1.5.2 Coarse-grained molecular dynamics

Fully atomic simulation is computationally prohibited at current stage. Coarse-grained molecular dynamics³⁵⁻⁴² derives its information from atomistic simulations but bridges the timescale and length-scale gap between molecular modeling and experimental techniques. Here, an all-atom described system is used as a starting point and then a coarse-grained model is derived with reduced number of degrees of freedom. Due to absence of intricate interaction details, the coarse-grained simulation can shed light on multiple useful properties in addition to requiring less time across length scales not achievable using atomistic simulations.

1.6 Organization of the Thesis

This research is undertaken to advance the knowledge of nanocellulose mechanics and understand why cellulose-based hybrid materials exhibit (1) higher mechanical strength and/or (2) thermal conductivity. To that end, the rest of this thesis is organized as follows.

Chapter 2 is a perspective on the state-of-the-art understanding related to mechanics design of cellulose based functional materials. *Chapter 3* uses atomistic MD simulations and sheds light on why certain cellulose-based hybrid materials (cellulose/carbon-nanotube fibers & elastic wood) possess superior mechanical properties. *Chapter 4* details the multi-scale coarse-grained modeling scheme developed to study the failure mechanism of cellulose nanopaper and uses that scheme to analyze why hybrid cellulose fibers present in experimentally fabricated biodegradable straws, possess better mechanical properties. *Chapter 5* discusses the reasoning behind the elevated mechanical and thermal transport properties of nanocellulose/boron-nitride nanotube composites, using MD simulations. *Chapter 6* concludes the research presented in the thesis by clearly listing the novelty of each section. *Chapter 7* presents a few avenues of possible future work using techniques related to engineering the intermolecular bonds and obtaining targeted materials possessing programable physical features such as, but not limited to, enhanced thermal stability and mechanical properties.

1.7 Author contributions

For the current chapter (*Chapter 1*), the author was primarily involved in conducting/designing the tensile/ballistic testing described in sections 1.4.1 and 1.4.2 and LCA analysis described in Figure 1.7. The author investigated, wrote, and designed the figures in *Chapter 2*. For chapters 3, 4 and 5, the author was primarily involved in the modeling efforts (Molecular Dynamics and Coarse-grained simulations). The author contributed to the investigation, writing, and creating visualizations for *Chapter 7*.

Chapter 2: State-of-the-art understanding of mechanics design in cellulose-enabled high performance functional materials³

2.1 Introduction

The steadily increasing demand for multi-functional devices possessing superior mechanical properties such as high strength, high toughness, lightweight, resistance to decay and many more, calls for high-performance materials, the desire for which has always accompanied the development of human society. The first half of the 20th century witnessed accelerated leaps in materials discovery with the invention of plastic, stainless steel, synthetic rubber, Teflon, and super alloys. This continued in the latter half of the 20th century through the invention of single-crystal silicon, carbon fibers, electrically conductive organic polymers, rare earth metals and synthetic skins, which shaped the daily human life through a wide range of consumer products. Then year 1990 onwards, with the incorporation of nanotechnology, materials engineering by manipulation at the atomic and molecular levels entered a new paradigm. In the 21st century, with the further advancement of nanotechnology, focus on inventing green nanomaterials using nature-inspired renewable sources has gained increasing prominence to mitigate the detrimental effects on the environment that fossil fuel-based materials generate. To this end, cellulose has emerged in the arena of materials innovation.¹⁻⁸

³ This chapter has been modified from the article that has been published as: **U. Ray**, S. Zhu, Z. Pang, T. Li, “Mechanics design in cellulose-enabled high performance functional materials”, *Advanced Materials* 33 (28), 2002504, 2021.

Cellulose is abundantly available from diverse natural sources such as plants, bacteria, tunicates and algae, which makes it a green polymer to be used in sustainable materials engineering. Cellulose nanofibers have a high aspect ratio with diameters of around 5-10 nm and fibril length ranging from nanometers to microns depending on the source. There exist six hydroxyl groups per repeating unit of a cellulose molecule. The massive distribution of such hydrogen bonding sites (i.e., hydroxyl groups) along the free fibril surface makes cellulose nanofibers extremely compatible for reinforcement and functionalization through secondary bonding. On the other hand, cellulose suspension with surface modification can uniformly disperse the composite solution in an aqueous medium.⁹⁻¹⁴ Such dispersion is crucial for augmenting the designing space of the reinforced material to the maximum performance. However, the fabrication of cellulose-based materials poses certain bottlenecks. The most significant one of them is the difficulty to convey the nanoscale properties of cellulose to the macroscale level of the bulk material.^{9,15-19} For instance, cellulose nanocrystals isolated from feedstock are highly crystalline ($\sim 88\%$ crystallinity)²⁰ and possess a high strength of $\sim 1.6-7.7$ GPa.^{21,22} and stiffness of ~ 150 GPa.²³⁻²⁵ However, natural wood, the primary portion of which is comprised of cellulose, has a much lower tensile strength (<100 MPa) and stiffness (several GPa).¹⁸ Therefore, there exist fertile yet largely unexplored opportunities to significantly enhance the performing indices of cellulose-based functional materials.

Capable of reducing the carbon footprint and initiating the advent of a much-needed circular economy,²⁶ the incorporation of cellulose into functional applications such as structural materials, additive manufacturing, flexible electronics, energy storage,

thermal management and biomedical devices, has recently attracted tremendous attention. In this progress report, the fundamental understanding of multiscale structure-mechanics relationships in cellulose and the operating design principles in cellulose-enabled functional materials, are outlined and reviewed. The origin and structure of cellulose are described in Section 2.2. Section 2.3 discusses various mechanics design techniques of pure cellulose-based materials via bottom-up (e.g., cellulose nanopaper) or top-down (e.g., densified wood) manufacturing strategies. Section 2.4 discusses the mechanics design implemented to obtain high-performance cellulose based functional materials through various strategies such as interface and topology engineering. Section 2.5 concludes with general remarks on the applications of cellulose functional materials, supporting these mechanics design principles.

2.2 Structural derivatives of cellulose

Natural cellulose structure varies in shapes and sizes across diverse sources, such as in wood, bacteria, cotton, bamboo, hemp, jute, algae, tunicates, etc.²⁷ The structural form of cellulose nanomaterials is dependent on processing techniques. The structural aspect of cellulose in all these multiscale materials is extremely important as it directly affects their mechanical properties. This section mainly discusses typical structural forms as found in wood fiber, bacterial cellulose nanofiber, nanofibrillated cellulose, and microfibrillated cellulose.

2.2.1 Wood Cellulose

The primary source of cellulose on Earth is naturally occurring plants, such as trees, bushes, and grass. For example, there are more than three trillion mature trees on Earth²⁸ and the content of cellulose in wood is around 45%.²⁹ Wood cell wall possesses a hierarchical structure as shown in Figure 2.1A. The primary cell wall is formed during the early stages of plant growth. As the plant cell matures and reaches a conclusive size, a secondary cell wall (thickness $\sim 4\ \mu\text{m}$) is formed inside the primary wall. The secondary wall can further be sub-divided into three concentric layers S1, S2 and S3 (Figure 2.1A)³⁰ where the content and distribution of cellulose microfibrils (MFs) vary. The thinnest S1 layer ($\sim 0.1\text{-}0.3\ \mu\text{m}$ thickness) constitutes around 5-10 % of the cell wall thickness and the cellulose microfibril angle (MFA), defined as the angle (ϕ in Figure 2.1A) made by the microfibril relative to the wood fiber axis, is around 60° to 80° . The S2 layer ($\sim 1\text{-}10\ \mu\text{m}$ thickness) represents around 75% to 85% of the cell wall thickness with the MFA ranging from 5° to 30° in the absence of external stress. The S3 layer ($\sim 0.5\text{-}1.1\ \mu\text{m}$ thickness) contains MFs in parallel orientation (with MFA $\sim 60^\circ\text{-}90^\circ$) and consists of $\sim 5\%$ of the total cell wall thickness. The lumen forms the hollow center. An additional G layer may also be present in between the S3 layer and lumen of some angiosperms, containing only cellulose with MFA almost equal to 90° .³⁰ Most of the MFCs are present in the secondary layer, which contains millions of cellulose MFs, each with diameters ranging from 5-10 nm and lengths reaching more than $2\ \mu\text{m}$.^{31,32} These MFs can further be broken down into elementary fibrils (EFs) (diameter: 1.5-3.5 nm and length $< 1\ \mu\text{m}$)³² which consist of cellulose nanofibers, the fundamental building block of wood cell wall (Figure 2.1A). Each cellulose molecule

contains rich hydroxyl (-OH) groups capable of forming hydrogen bonds within (intra) the same molecule, thus stabilizing the nanofibers and with the neighboring (inter) molecules, thus promoting a parallel chain stacking. The MFA substantially influences the mechanical properties of the bulk cellulosic fibers (length of ~15mm – 65 mm, diameter of ~ 45 μ m – 205 μ m). Previous studies have shown that lower MFA and higher cellulose content³³ lead to a higher wood fiber strength; whereas, higher MFA and lower cellulose content dictate a higher fiber ductility.^{34,35} Cellulose is an organic polysaccharide with the general formula $(C_6H_{10}O_5)_n$, where n is the degree of polymerization (DOP) varying with different sources. A molecular representation of cellulose is shown in Figure 2.1B. Two anhydroglucose rings, each rotated by 180° relative to the other and connected by β 1-4 glycosidic bond ($-C-O-C-$), form one repeating unit of the cellulose molecule which is linear in nature. The inter-layer spaces of the cell-walls in between wood fibers are filled by amorphous hemicellulose (~25%), ‘glue’- like lignin (~25%) and other trace elements. Hemicellulose³⁶ and lignin³⁷ form the matrix in which cellulose fibrils are embedded. Hemicellulose is a polysaccharide similar to cellulose, but it has a shorter cross-linked chain structure (DOP ~200³⁸) in comparison to the longer (DOP ~10000-15000³¹) and straight-chain molecular arrangement of crystalline cellulose.⁴⁰ Also, cellulose is made of glucose monomers only whereas hemicellulose is comprised of several monomers such as glucose, galactose, xylose, mannose, arabinose and rhamnose. Hemicellulose is one of the key components responsible for cross-linking with the cellulose and lignin by hydrogen bonds and strengthening the cell wall.⁴¹⁻⁴³ Lignin is a phenolic polymer⁴⁴ with three main aromatic sub-units (p-coumaryl alcohol, coniferyl alcohol, and sinapyl alcohol as

shown from left to right under “Lignin” in Figure 2.1B) cross-linking with each other in multiple possible complex formations, generally dependent on the specific isolation techniques. Lignin has a much higher degree of cross-linking than hemicellulose and is responsible for imparting the elasticity and mechanical strength to the wood.^{45,46} Cellulose from plants needs to be isolated from this hierarchical wood assembly by removing the hemicellulose and the lignin for various uses. This is done by manipulating mechanical processes^{47–49} and/or TEMPO (2,2,6,6-tetramethyl-piperidiny-1-oxyl radical) oxidation⁵⁰ or enzyme^{51,52} or acid treatments^{53–56} to obtain the desired final cellulosic materials such as MFCs, NFCs and nanocrystalline cellulose or cellulose nanocrystals (CNC).⁵⁷

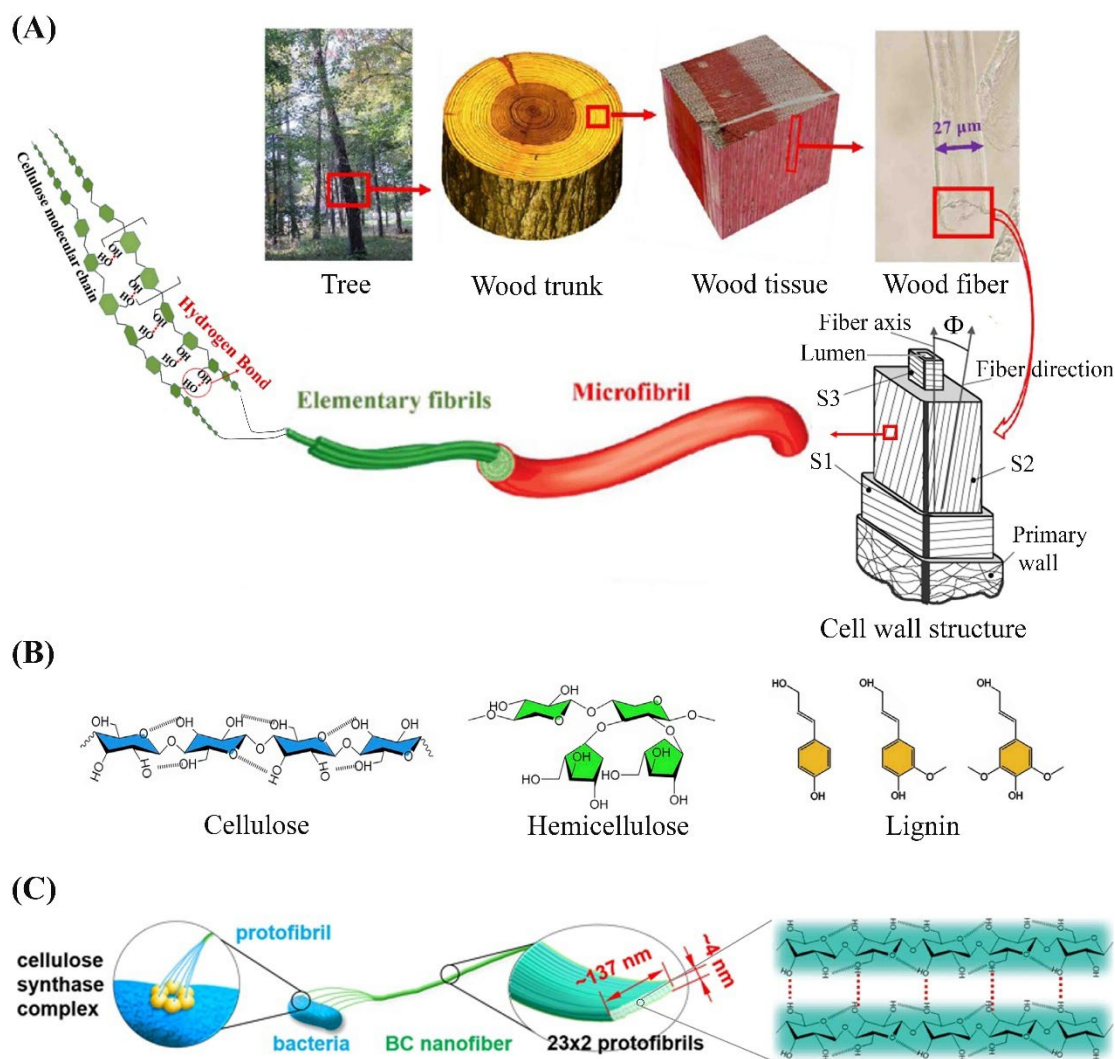


Figure 2.1. Hierarchical structure of plant wood with cellulose as the fundamental building block and bacterial cellulose. (A) The top-down hierarchical structure of wood.^{79,102,186} (B) Molecular structures of cellulose, hemicellulose and lignin, the three primary components of plant cell wall.¹⁸⁷ (C) The schematic illustration of bacterial cellulose biogenesis and cellulose fibril formation.¹⁰⁹

2.2.2 Bacterial Cellulose

Another predominant source of cellulose is from bacteria. A common source of bacterial cellulose (BC) nanofibers is *Acetobacter xylinum* (*A. xylinum*, strain ATCC 1765).^{58–60} Other bacteria of the genera *Sarcina ventriculi* and *Agrobacterium* can also

produce BC nanofibers by a microbial fermentation process.⁶¹ The interior of the bacterial cell possesses nozzles or “cellulose synthase complex” (Figure 2.1C) which spins out protofibrils (~2 nm by ~ 6 nm in cross section). The protofibrils can be bundled into BC nanofibers which are randomly entangled in the three-dimensional gel network. This synthesis process is cost-effective, environmentally friendly and has the potential to be scalable. BC nanofiber is 100% pure cellulose and thereby the time-consuming and expensive mechanical and chemical treatments of removing hemicellulose and lignin are not required. The DOP of BC nanofiber is typically high (~ 8000⁶²), whereas the DOP of cellulose extracted from plants reduces significantly (~ 500-2500²⁰) during processing. The BC nanofiber can be made in large amounts (tons day⁻¹) making its production industrially feasible. Presently, using BC nanofibers in high-performance cellulose enabled materials is a rising field with emerging potential applications.^{63,64}

2.2.3 Cellulose nanomaterials

Different materials processing techniques can result in a novel class of materials which possess particle types or building blocks in the length scale intermediate between cellulose derivatives and the wood fibers. Such materials, termed as cellulose nanomaterials (CNs),^{65–68} is characterized by ordered parallel stacking of cellulose chains and can be isolated from the cellulosic source by implementing combinations of various extraction techniques. Generally, extraction techniques initiate with pretreatment steps involving purification and homogenization so that the source material responds to the subsequent treatments appropriately.⁶⁵ This is followed by a second step of refinement, commonly accomplished by mechanical treatment

(homogenization, ultrasonication, grinding, etc.) or acid hydrolysis using sulfuric, hydrochloric, maleic, or phosphoric acid. Different types of CNs having varied morphology are obtained when diverse isolation techniques are adopted.

A CN type, termed as the microfibrillated cellulose (MFC) is obtained when very purified wood fibers are subjected to mechanical refinement to produce pure cellulose particles, comprised of both crystalline and amorphous zones.⁶⁷ If the refinement step during the extraction process uses a higher shear to cleave the cellulosic source, highly flexible nanofibrillated cellulose (NFC) or cellulose nanofibrils⁶⁸ are obtained, which comprise both crystalline and amorphous domains. NFCs are structurally like MFCs, with the primary difference being the diameter of the particle type is much smaller in NFCs due to the modified fibrillation process. Cellulose nanocrystals⁶⁶ are another type of stiff, spindle-like CNs obtained by refining the pretreated cellulosic material by acid hydrolysis. They are highly crystalline, straight with limited chain folding and contain minimal defects. Cellulose nanocrystals are synonymously referred to as cellulose nanowhiskers or nanorods.⁶⁵ Different pretreatment processes such as TEMPO-mediated oxidation⁶⁷ followed by homogenization, can result in TEMPO-NFCs, possessing surface chemistry different from the NFCs as TEMPO selectively oxidizes the -OH group in the glucose ring to -COOH groups. The different structural aspects of each of the CNs influence the overall mechanics design of the bulk material in a distinctive way, as will be discussed in the following sections.

2.3 Understanding the design of high-performance cellulose materials

This section discusses the role of hydrogen bonding that is instrumental behind the anomalous scaling law of increased strength and toughness in a cellulose nanopaper is

discussed along with the dependence of structural interfaces on the spatial hydrogen bond density. The effect of nanofiber size and orientation on the fracture toughness are also discussed. Then various experimental approaches such as structural alteration and nanofiber alignment that enables these multiscale mechanics techniques towards cellulose based high-performance materials are reviewed.

Section 2.3.1 discusses the role of hydrogen bonds in a cellulose nanopaper under tensile deformation, which results in the simultaneous increase of the two generally mutually exclusive properties of strength and toughness. Section 2.3.2 analyzes the effect of hydrogen bonds across the different interfaces of the crystalline cellulose structure using studies based on molecular simulations. Section 2.3.3 reviews continuum models shedding light on how the reduction in cellulose fiber diameter and/or increasing fiber alignment result in increasing the spatial hydrogen bond density, thereby enhancing the interfacial energy dissipation and thus, leading to superior fracture toughness. Finally, a map that can guide the design of cellulose nanopaper possessing desirable mechanical properties are discussed.

2.3.1 Role of hydrogen bonds behind the anomalous properties of nanopaper

An idea to develop materials with higher strength is to use smaller material structures. For example, the smaller grain size in metals restricts dislocation motions, leading to a higher strength.^{69–74} However, such “go smaller” treatments could suppress possible mechanisms (e.g., crack-tip blunting) to relieve local high stress, resulting in a lower toughness, since toughness is an indicator of a material’s ability to dissipate local high stress by enduring deformation. In fact, strength and toughness are two properties that

generally contradict each other.^{75–78} Such observations can be termed as the conventional scaling law- the smaller, the stronger, but not tough, which is a ubiquitous challenge in engineering material design.

Nevertheless, the unconventional scaling law “the smaller, the stronger and the tougher” was observed in the cellulose nanopaper, synthesized by Zhu *et al.*⁷⁹ The transparent cellulose nanopaper (Figure 2.2A), microscopically containing a dense random network of entangled NFCs, was fabricated using bleached softwood (pine) pulp as a source material, followed by TEMPO mediated oxidation and homogenization. Homogenization under different pressures was performed to reduce the NFC mean fiber diameters. The cellulose nanopaper having NFCs with smaller fiber diameters was found to possess superior strength (obtained from tensile tests⁸⁰) and toughness (obtained from fracture toughness tests using a method developed by Rivlin and Thomas^[81]). As the cellulose fiber diameter decreased from 27 μm to 11 nm, the strength (Figure 2.2B) and toughness (area under the stress-strain curve until failure) of the nanopaper increased around 40 times and 130 times respectively. This work depicting the simultaneous increase of these two properties with decreasing fiber diameter gave rise to an anomalous scaling law of “*smaller (fiber diameter), stronger and the tougher*”⁷⁹ for cellulose. Control experiments were also performed on thin films of carbon nanotubes (CNTs), in which the diameter of constituent building block (bundles of single-walled CNTs) is processed to be comparable to the fiber diameter as in the cellulose nanopaper (~ 11 nm). Although individual CNT is in principle much stronger than NFC, the measured stress-strain curves (Figure 2.2C) showed that the CNT films had an ultimate strength and toughness that were significantly inferior to

those of cellulose nanopaper, whose ultimate strength and toughness were found to be 9 and 281 times higher than that of the CNT film, respectively. Scanning electron microscope (SEM) images for cellulose nanopaper and CNT films showed the individual fibers aligning itself to the loading direction before the final fracture, thus suggesting a similar deformation mechanism. The toughness of the cellulose nanopaper (16.9 MJ m^{-3}) was found to be even around two orders of magnitude higher than that of the CNT film (0.06 MJ m^{-3}). The experimental evidence of the increase in toughness along with the strength suggested the anomalous scaling law, which may prove to be a well-sought strategy for designing high-performance materials.

The highly desirable unconventional scaling law of cellulose nanopaper could be understood from multiscale mechanics modeling. As the cellulose fibers become *smaller* with a reduction in diameter, pre-existing intrinsic natural defects in the fibers decrease in size and content. The improved strength for the smaller cellulose fibers was found to be inversely proportional to the square root of the fiber diameter, which can be derived from fracture mechanics using dimensional analysis.⁷⁹ This increase in strength (*stronger*) in the cellulose nanopaper formed by smaller fiber diameters gave rise to the conventional scaling law of *smaller* and *stronger*, which was also established in other materials.^{75–78} Nevertheless, the mystery lies in the simultaneous increase of toughness, the understanding of which requires investigating at molecular scales. Because of the ultra-high strength on the individual NFC fibers, failure of the cellulose nanopaper is expected to occur by inter-fiber sliding. Atomistic simulations of inter-fiber sliding of cellulose nanofibers (Figure 2.2D) reveal the interfacial energy variation profile relative to the sliding displacement. It is found that the local energy

extremum is correlated with the breaking and reformation of hydrogen bonds. The local energy maxima correspond to the stretched hydrogen bonds formed between the sliding interfaces. The subsequent decrease of energy corresponds to the breaking of hydrogen bonds, but the local energy minimum indicates the formation of new hydrogen bonds. Then the subsequent sliding initiates another cycle of breaking and reforming of hydrogen bonds. This series of events continues until the entire chain is pulled out, giving rise to the zigzag profile of the energy curve. The repeated cost of energy during the breaking and reforming of hydrogen bonds contributes to the toughness. The more the breaking and reforming events occur due to this self-healing nature of hydrogen bonds, the more the dissipation of energy to fracture the fibers and the higher is the toughness.

Molecular simulations for CNT fiber bundles show an absence of the salient zig-zag nature when compared with an analogous curve as obtained from cellulose models (Figure 2.2E). This is due to the absence of hydrogen bonding in CNTs. Only weak vdW forces of interaction exist between the CNT fiber bundles for sliding against each other. Hence it can be coherently envisaged through control experiments and modeling, that with reduction of mean fiber diameter, the spatial density of hydrogen bonds that take part in the interfacial sliding increases. Therefore, energy dissipation is much more enhanced due to the repeated energy cost of breaking and reforming of a larger amount of hydrogen bonds at the interface. This facile reformation of hydrogen bonds plays a major role in the anomalous mechanical scaling law of strength and toughness (Figure 2.2F) for the cellulose nanopaper.

2.3.2 Influence of structural interface on the hydrogen bonding

The spatial hydrogen bond density that is instrumental in influencing the strength and toughness of cellulose nanopaper is also structural interface dependent. The effect of hydrogen bonds is dominant across the (110)-(110) interface of the crystalline cellulose 1 β structure, which is the most common polymorph of cellulose found in plants.⁸² Sinko *et al.*⁸³ constructed an atomistic model of such a (110)-(110) interface involving two cellulosic fibrils, where each fibril contained 36 cellulose chains arranged in a hexagonal pattern (Figure 2.2G), to study the shearing at the designated interface. During continuous shearing at the (110)-(110) interface, the –OH groups were sometimes aligned (location 1 and 3 of Figure 2.2H) and sometimes misaligned (location 2 of Figure 2.2H). When the cellulose chains were aligned across the interface, it corresponded to the local minima of the system energy contour and involved the maximum number of hydrogen bonds formed at the interface (location 1 and 3 as in Figure 2.2I). As the shearing transited from location 1 to 2, a few cellulose chains were aligned and few misaligned. In this scenario, a few hydrogen bonds (blue in Figure 2.2H) break and some (red in Figure 2.2H) begin to form, resulting in a decrease in the number of completely formed hydrogen bonds (location 2 of Figure 2.2I) in the system. This breaking and reforming of hydrogen bonds aided in the resistance to failure and with continuous sliding, fewer hydrogen bonds were involved due to the reduction in cellulose fibril overlap length with increasing shearing distance separation. Other interfaces such as (200)-(200) which lacked involvement of sufficient hydrogen bonds exhibited a more stick-slip behavior in the energy landscape instead of

this continuous sliding probably due to the presence of polar or non-polar barriers present along the interface.

2.3.3 Effect of nanofiber diameter and orientation on fracture mechanics

The influence of cellulose nanofiber size (diameter) on the fracture toughness has also been explained theoretically by Meng *et al.*⁸⁴ using a microstructure-based crack-bridging model of cellulose nanopaper consisting of randomly oriented nanofibers. The model contained a crack-bridging zone behind the crack-tip, while the rest of the nanopaper was assumed to be an isotropic solid of elastic nature. Given a constant length (1.5 μ m) of cellulose nanofibers, the fracture toughness of the nanopaper was found to increase with decreasing radius of the nanofiber (Figure 2.2J). This was because, for a fixed volume, reduction in nanofiber diameter resulted in increasing the spatial hydrogen bond density which consequently magnified the interfacial energy dissipation. A higher energy barrier was needed to overcome the facile reformation of hydrogen bonds undergoing deformation, thus delaying the failure and enhancing the fracture toughness. The results of fracture toughness held in good quantitative agreement with experimental results,⁷⁹ facilitated by the proposed hydrogen-bonding mechanism.

The orientation of nanofibers was also found to play a prominent role in the fracture toughness of the cellulose nanopaper (Figure 2.2K). The crack-bridging model incorporated a distribution parameter A , to quantitatively understand the effect of nanofiber orientations on the fracture toughness. A value of A around 0 indicated random nanofiber orientations, while positive (~ 100) and negative (~ -100) values of

A signified nanofibers parallel (aligned) and perpendicular (misaligned) to the loading direction respectively. When A was increased from 0 to a larger positive value, the nanofibers became more aligned to each other and could support a larger force along the deformation direction, maximizing their ability to hinder the crack opening and bridge the crack propagation. Therefore, the toughening effect was enhanced and thus the fracture toughness. Using a similar crack-bridging model, Meng *et al.*^{85,86} connected the fracture toughness and the various material parameters such as nanofibril radius (R) (Figure 2.2L) and length (l) by proposing a unified scaling law between bridging-toughening ratio and the microstructural parameters of the nanopaper. The toughening ratio (TR) was defined as the ratio of the ability of the microstructure to bridge stresses in the crack-opening zone to the natural fracture toughness of the nanopaper, which is directly related to the crack-opening displacement. The higher the toughening ratio, the better was the bridging effect. Keeping radius constant, TR increased with the increase in nanofiber length, which revealed that longer nanofibers will strengthen the toughening mechanism due to a longer crack-bridging zone. Keeping length constant, TR increased with the decrease in nanofiber radius. It was because thinner nanofibers could offer an enhanced interfacial surface area in the crack-bridging zone leading to an increased toughness. This study helped create a map (Figure 2.2L) which can guide the design of cellulose nanopaper with targeted mechanical properties.

Many other relevant research contributions related to cellulose mechanics also exist. The increase in strength and elongation at break with increasing degree of polymerization (DOP) of cellulose on nanofibers,⁸⁷ film^{88,89} and nanopaper obtained

from various sources⁹⁰ such as bamboo, softwood and hardwood that have been discussed. Experimental evidence indicates that there may be an influence of the amorphous regions on the toughening mechanism⁹¹ and elastic modulus of the nanopaper.⁹² Other significant multi-scale computational strategies such as finite element modeling⁹³ and coarse-graining⁹⁴ addressed the effect of bonded and non-bonded interactions and bending of crystalline cellulose bundles along with practical understanding of interfacial failure in real-world architectures such as Bouligand structures which is commonly used in many biomaterials. All these strategies underpinning the inelastic behavior of cellulose nanofiber⁹³ and different failure mechanisms across the nanofiber interfaces,⁹⁴ combined with experimental design techniques described above, enrich the molecular cellulose mechanics.

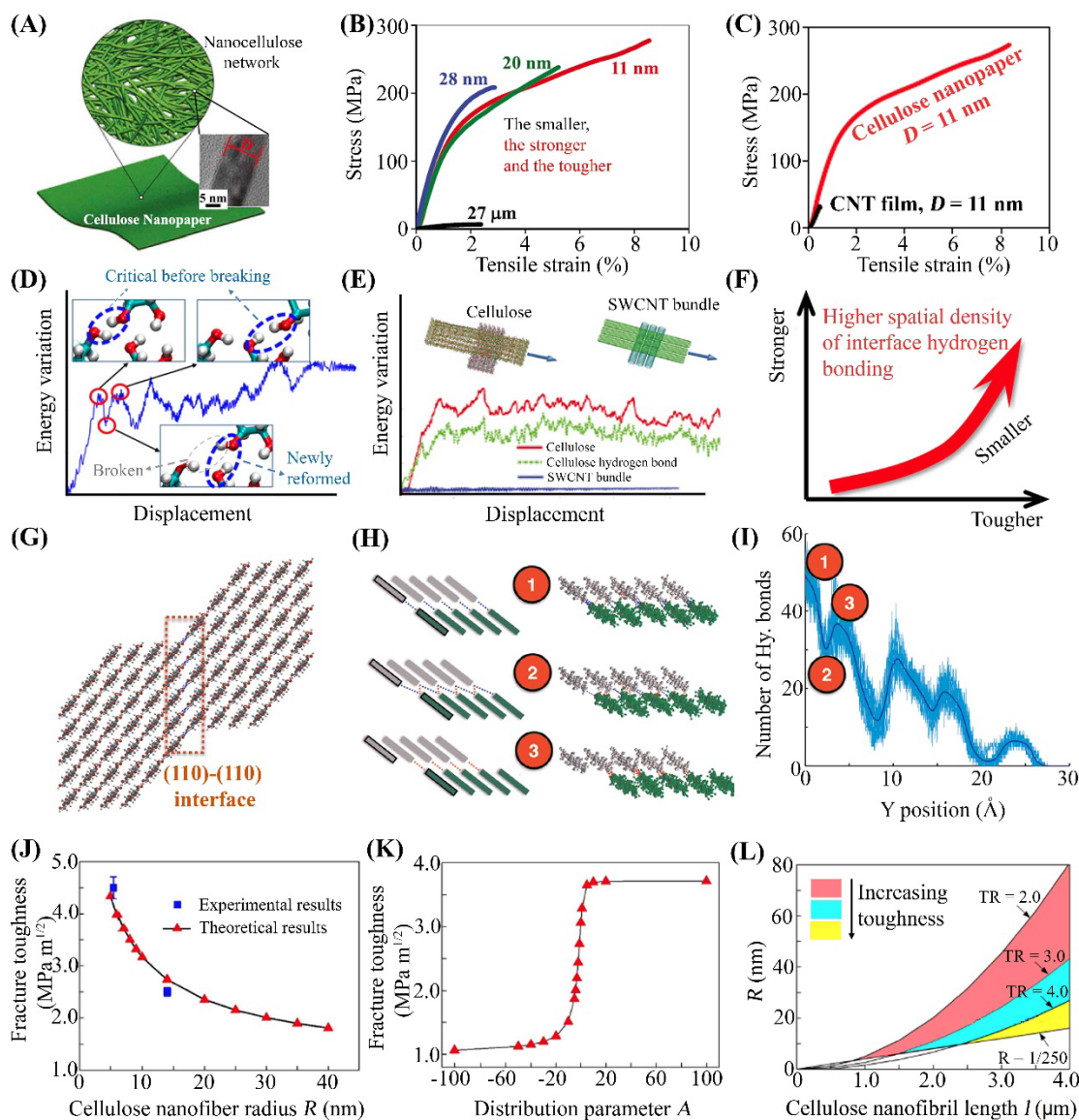


Figure 2.2. Multiscale analysis of mechanics of cellulose. (A) Schematic of cellulose nanopaper. Inset shows an SEM image of cellulose fiber (~11 nm in diameter) in the nanopaper. (B) Experimental stress-strain curves of cellulose nanopaper with decreasing fiber diameters. (C) Comparison of stress-strain curves of films made of cellulose and carbon nanotubes, each having comparable fiber diameter of ~11 nm. (D) Variation of energy during hydrogen bonds breaking and reforming, as obtained from molecular simulations. (E) Variation of potential energy with respect to sliding between interfaces of cellulose nanopaper and carbon nanotube film, as obtained from molecular simulations. (F) Schematic showing the relation of spatial hydrogen bond density with the strength and toughness of the cellulose based nanopaper. (A-F)⁷⁹ (G) Schematic of a (110)-(110) interface in a cellulose 1 β structure dominated

primarily by hydrogen bonding. (H) Change of hydrogen bonding networks during sliding between the (110)-(110) interface. (I) Change in number of hydrogen bonds during sliding along the (110)-(110) interface. (G-I)⁸³ (J, K) Variation of fracture toughness of the cellulose nanopaper with (J) fiber radius and (K) orientation. (J-K)⁸⁴ (L) A design map based on the crack-bridging toughening ratio (TR) relative to fiber length (l) and radius (R).⁸⁵

2.4 Design of cellulose-based functional materials with superior mechanical properties

In this section, several experimental techniques towards high-performance cellulosic materials that support the above mechanics insights are summarized. In Section 2.4.1, methods of structural alteration for tuning the mechanical properties of cellulosic materials are reviewed. Under this design technique, densification of wood fibers after full/partial lignin removal and collapse of wood cell wall to fabricate a cellulose based transparent paper are discussed. In Section 2.4.2, methods of manipulating structural alignment are summarized.

2.4.1 Structural alteration

To enhance the functionality of cellulose derived materials such as wood, structural alteration (lignin removal, densification etc.) is a possible avenue by which the hydrogen bonding of the nanofibers can be tuned. Frey et al.⁹⁵ fabricated a cellulose bulk material from natural wood (spruce) through stepwise delignification of hydrogen peroxide and acetic acid treatment, followed by densification using a combined approach of compression by applying a pressing force coupled with lateral shear (Figure 2.3A). Delignification resulted in complete lignin removal from the cell walls, which imparted the much-needed flexibility. Densification was applied to remove the

larger defects in addition to preserving the natural directionality of the wood fibers in the final product.⁹⁶ The two-step approach to densification resulted in cell walls that compressed more smoothly with minimal gaps between them. In contrast, if lateral shear was not applied, the cell walls were more wrinkled and uneven. The material was observed to possess an elastic modulus (~ 35 GPa) and strength (~ 270 MPa) at high relative humidity ($\sim 95\%$) (Figure 2.3B). Higher humidity ($\sim 95\%$) resulted in a more compact structure in comparison to the delignified wood pressed at a much lower humidity ($\sim 65\%$), leading to an increase in strength in the former. The cell walls came in closer proximity to each other due to the stepwise protocol of delignification and densification in the processing approach. The strength of native wood and only densified wood that was obtained without delignification exhibited much inferior mechanical strength. After delignification, the modified bulk material with moisture content could be easily molded into arbitrary shapes (Figure 2.3C) without the use of an adhesive, in addition to retaining the directionality of the wood fibers. This shaping processability demonstrated that it was a significant step forward in integrating the densified wood in many applications, thereby further amplifying the multipurpose capacity of wood derived cellulosic materials.

Meticulous control of the delignification process before densification is the key to refining the mechanistic design approach and maximize the mechanical properties of wood cellulosic materials. The demonstration of how to cause the maximum densification by removing optimum portions of lignin and hemicellulose and amplify the mechanical performance was achieved by Song et al.¹⁸ Here, bulk natural Basswood (Tilia) was modified through a novel yet simple, top-down, two-step process to obtain

a high-performance densified wood. A natural wood block of density $\sim 0.43 \text{ g cm}^{-3}$ was immersed in a boiling solution of sodium hydroxide (NaOH) and sodium sulfite (Na_2SO_3) and then washed in boiling deionized water solution. This was followed by hot-pressing at 100°C (pressure - 5 MPa; time - 1 day) which led to complete collapse of the cell walls to obtain densified wood with approximately 80% reduction in thickness (density = 1.3 g cm^{-3}). The schematic of the entire processing approach is shown in Figure 2.3D. Variation of the boiling time resulted in different degrees of lignin and hemicellulose removal. The decrease in cellulose content (original: 44.0 %, final: 38.7 %) was mild but the corresponding decrease was quite large for lignin (original: 20.8 %, final: 11.3 %) and hemicellulose (original: 19.5 %, final: 5.2 %). This was because the stability of these components varies when subjected to the chemical treatment (NaOH/ Na_2SO_3). The resulting cell walls, after the partial lignin/hemicellulose removal, became less rigid and porous and more amenable to further modifications (e.g., hot pressing). This resulted in the superior mechanical properties (strength $\sim 586.6 \text{ MPa}$, work of fracture $\sim 4.0 \text{ MJ m}^{-3}$) of the densified wood shown in Figure 2.3E and it was found to be 12 times higher than natural wood ($46.7 \pm 4.5 \text{ MPa}$). Without any removal of lignin/hemicellulose, densification of the wood involving the subsequent cell wall collapse was not possible to achieve the desired dimensions. The lignin/hemicellulose matrix in the wood cell walls hindered the interaction between the cellulose-cellulose fibrils and as a result, the primary material design goal of exploiting the inter-hydrogen bonding between neighboring cellulose chains was severely restricted. Furthermore, full removal of lignin/hemicellulose suggested the absence of a binder for the cellulose fibrils and that type of chemically

treated wood was crushed during hot-pressing which led to failure to densify. The finding that partial lignin and hemicellulose removal allowed maximum densification by the total collapse of cell wall and yielded the optimum mechanical properties, that are key factors to consider for mechanics-based design in wood based cellulose materials.⁹⁷⁻¹⁰¹ Additionally, the work of fracture, a measure of toughness, also increased 10 times ($3.9 \pm 0.2 \text{ MJ m}^{-3}$) than that of natural wood after densification. Hence densified wood also defeated the conflict between two mutually exclusive properties, strength and toughness. Upon densification, the cell walls become closely packed due to their collapse, in contrast to their natural wood counterpart where hollow lumina were present. The spatial density of the interfacial hydrogen bonds significantly increased, and capable of dissipating a tremendous amount of energy, which resulted in much higher toughness for the densified wood. The hot-pressing not only reduced the defects but also improved the wood fiber alignment, leading to enhanced strength. Even under a relative humidity of 95%, there was a modest drop in strength ($\sim 493.1 \text{ MPa}$), probably because of the inability of water to diffuse through the densified microstructure. The specific strength ($422.2 \pm 36.3 \text{ MPa cm}^3 \text{ g}^{-1}$) of the densified wood was found to be higher than most structural metals and alloys such as TRIPLEX, Al alloy 2000, high-specific strength steel (HSSS) and lightweight Titanium alloys (Ti6Al4V) as shown in Figure 2.3F. The superior mechanical properties of enhanced strength and toughness were found to be applicable for other hard (oak, poplar) and soft (cedar, pine) densified woods, thus validating the universality of the processing approach.

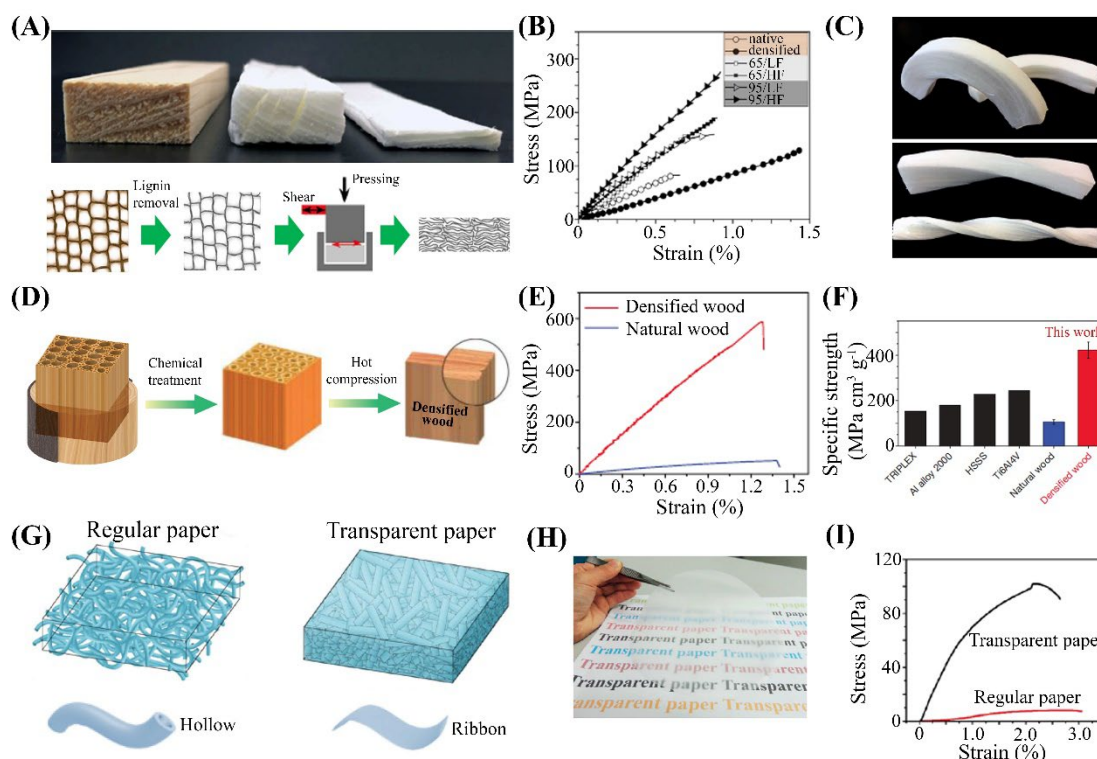


Figure 2.3. Structural alteration to tune mechanical properties of cellulose-based materials. (A) Images and processing approach of wood based cellulosic bulk material obtained by complete delignification and two-fold densification approach. (B) Stress-strain curves showing the tunability of mechanical properties of delignified and densified wood at different processing conditions. (C) Images showing the feasibility of the obtained material to mold into arbitrary-shaped objects. (A-C)⁹⁵ (D) Schematic showing the processing approach of densified wood, obtained by partial lignin/hemicellulose removal of bulk natural wood. (E) Comparison of stress-strain plots of the densified wood with natural wood. (F) Comparison of the specific strength (MPa cm³ g⁻¹) of densified wood with respect to known structural materials. (D-F)¹⁸ (G) Schematic of regular and TEMPO-oxidized paper. The hollow structure of fibers in regular paper is processed into ribbon-like structure, increasing the packing density. (H) A digital image of the transparent paper. (I) Experimental stress-strain curves of regular and TEMPO-oxidized paper. (G-I)¹⁰²

Analogous to the collapse of wood cell walls, a similar structural alternation could also be realized in cellulose based transparent paper. This was possibly achieved by

processing the original wood fibers by TEMPO oxidation, which unzips the tubular pulp into a more ribbon-like structure,¹⁰² thus morphologically ensuring improved packing density among hydrogen bonding interfaces. The transparent paper (Figure 2.3G, H) was obtained using such a treatment. Due to significantly enhanced interfibrillar surface area of contact that leads to the increased spatial density of interfacial hydrogen bonds, both the mechanical strength and toughness of the TEMPO-oxidized transparent paper were superior to the regular paper. The strength of the transparent paper increased more than 13 times than that of the regular paper as shown in Figure 2.3I. The toughness of the transparent paper also increased more than 12 times when compared with the regular paper.

2.4.2 Alignment

Cellulose nanopaper,⁷⁹ containing randomly entangled nanofibers, can be relevant in many emerging areas where isotropic (independent of the direction) mechanical properties are essential. However, tuning cellulose nanofibers to initiate anisotropy and thus introducing aligned fibers in the bulk material can be crucial for some applications.^{103–105} Techniques such as hot-pressing in wood can increase the alignment of the constituent wood fiber, and thus anisotropy. To this end, Zhu *et al.*¹⁰⁶ devised a tunable approach and fabricated a transparent film with highly aligned EFs (Figure 2.4A) from wood. Using Basswood and Pine as starting raw material, natural wood blocks were cut in different cutting angles (angle θ between the natural wood growth direction and the cutting direction as in Figure 2.4B) at the beginning. This was followed by chemical treatment leading to lignin removal and hot mechanical pressing. Lowering the cutting angle (Figure 2.4C) produced films with higher degree of wood

fiber alignment (angle between the wood fibers and direction of film surface) and it was found to possess high mechanical strength (~ 350 MPa, around 3 times of isotropic film) along the wood fiber axis direction, whereas increasing the wood fiber alignment to $\sim 45^\circ$ decreased the anisotropy resulting in films with much reduced strength (~ 190 MPa). In comparison, the transparent anisotropic film possessed much diminished strength (~ 23.2 MPa) in a direction perpendicular to the wood fiber alignment. The spatial density of hydrogen bonds actively participating in the deformation mechanism is more in aligned films as they offer increased parallel interfaces between the wood fibers and this led to greater energy dissipation, a feature considerably reduced when the wood fibers are not aligned.

Procedures such as wet-drawing^{107,108} could further loosen up the entangled cellulose fibers and make them longer and narrower, thus introducing anisotropy. When coupled with wet twisting (Figure 2.4D), it could further stimulate the anisotropy, leading to the formation of BC macrofibers, which had a diameter of around $300\ \mu\text{m}$ and consisted of long ($\sim 1\text{-}9\ \mu\text{m}$) and aligned BC nanofibers, as demonstrated by Wang *et al.*¹⁰⁹ The wet-drawn and twisted fibers were reported to possess a high strength (826 MPa) and stiffness (~ 65.7 GPa). In the absence of wet drawing, the corresponding strength and modulus were much lower at 114.8 MPa and 3.5 GPa, respectively. The scalable design of tuning anisotropy, capitalizing the large length of the BC macrofiber, was the major underlying reason behind these superlative mechanistic properties. Zhu *et al.*¹¹⁰ fabricated mechanically strong fibers by induced alignment of the regenerated cellulose suspension by wet-spinning and a multi-step drawing process (Figure 2.4E). Here, the regenerated cellulose obtained from cotton pulp was dissolved in

NaOH/LiOH/urea/H₂O solution followed by wet spinning. The extruded suspension through the spinneret was treated in a bath of phytic acid and sodium sulfate to remove the existing alkali-urea shell. The alignment induced in the nanofibers by spinning was further intensified by a two-step drawing process using rollers. The resulting fibers were observed to contain nanofiber having remarkable alignment as verified by diffraction patterns and possessed a high strength. Fibrillation causing nanofiber swelling, making it vulnerable to mechanical abrasion, was also reduced by this novel environmental-friendly design thus aiding the self-assembly of nanofibers, a property which strongly authenticated its successful future application potential in textile engineering. Yao *et al.*¹¹¹ demonstrated the design of long BC fibers of length ~15 μm having aligned nanofibers (length ~15-40 nm) by a stepwise treatment of TEMPO oxidation of the cellulosic suspension, followed by wet-spinning and stretching under high humidity (Figure 2.4F). This was found to be an energy efficient process avoiding intensive homogenization of pulp since BC nanofibers were already found to be much finer than that obtained from plant sources.¹¹² The obtained fibers were found to exhibit high strength and modulus of 248.6 MPa and 16.4 GPa respectively. The process was further modified by introducing infiltration of multivalent ions such as Fe^{3+} or Cu^{2+} . This increased both strength and modulus to 357.5 MPa and 22.9 GPa, respectively. Remarkably, the treatment showed high wet strength and modulus of 262.2 MPa and 15.9 GPa respectively of the BC fibers. The technique of wet-stretching may serve to be an effective method of aligning longer nanofibers, which can be difficult to align during wet-spinning due to entanglement of fibrils at high extrusion speeds.

Designing a double flow focused device to ensure hydrodynamically induced self-assembly and alignment of NFCs, enabling an almost linear chain arrangement of NFCs in the final cellulosic filament, was also one unique approach as addressed by Håkansson *et al.*¹¹³ Using bleached softwood pulp as the starting material, NFC suspension was prepared by a sequence of steps involving enzymatic treatment, homogenization, sonication and centrifugation. The flow-focusing device (Figure 2.4G), where the prepared NFC suspension was then injected, contained a tapered central channel where Na^+ ions were added in the form of NaCl from the top (blue arrows in Figure 2.4G). When the cellulose suspension was first injected in the core channel, NFC alignment was poor due to extensive Brownian diffusion (a) in Figure 2.4G). With the core flow further accelerated along the tapered center channel, a temporary hydrodynamically induced alignment (b) in Figure 2.4G) in the stretched NFCs occur, which simultaneously prevented the suspension to stick to the channel walls. With the flow further accelerating along the long channel, Brownian motion stills exists (c) in Figure 2.4G) as the fibers are aligned. Simultaneously, the electrostatic repulsions were also minimized in the ongoing flow ((e)-(h) in Figure 2.4G) possibly due to protonation of carboxyl groups leading to the formation of $-\text{COO}-$ ions or increased Na^+ concentration. Then, with continual flow downstream along the channel, the NFC suspension slowly immobilizes which arrests the Brownian motion (d) in Figure 2.4G), and the resulting gel was manually removed and air-dried. The aligned filaments obtained as a result were found to have a strength (490 MPa) higher than most of the previously reported filaments, a modulus of 17.6 GPa and a failure strain of 6.4%. In terms of mechanical performance, this surpassed most of the strong pure

cellulosic filaments having similar nanofibril orientation as reported before. This was possible probably because this distinctive flow-focusing alignment strategy formed continuous filaments having a uniform cross-section and densely stacked NFCs.

Other strategies such as the application of electric and magnetic fields can also be devised to align the NFCs. Due to their negative diamagnetic and positive dielectric anisotropy, partial alignment of NFCs was previously possible perpendicular¹¹⁴ and parallel¹¹⁵ to the magnetic and electric field respectively. Kim *et al.*¹¹⁶ envisioned a design strategy by application of both electric and magnetic fields to better align the NFCs and fabricate a long cellulosic fiber. Here the NFCs isolated from hardwood bleached kraft pulp were subjected to TEMPO oxidation followed by wet spinning. Since the wet fibers disperse well in water, to maximize the alignment both electric and magnetic were simultaneously applied using a high voltage power system and a DC magnet respectively. Initially, the NFCs are randomly oriented. Application of magnetic and electric field helps attain conjoined NFCs aligned to each other as shown in Figure 2.4H. Effective drying at room temperature disposed the excess water molecules between the NFC chains and helped form strong hydrogen bonds. The aligned long fiber achieved as a result had high strength and toughness of 289.9 MPa and 11.8 MJ m⁻³ respectively with a failure strain of 5.7%. In comparison, the fiber obtained without the application of any field had a much lower strength (127.8 MPa) and toughness (3.7 MJ m⁻³). Efforts of remolding anisotropy such as this may have the potential to open routes towards multiple applications if it can be scaled up suitably. For example, innovations will be possible if liquid transport can be channeled in one direction in micro/nanofluidics¹¹⁷⁻¹¹⁹ or if transparent cellulose substrates can guide the

light in the desirable direction required for unique display applications¹²⁰ in optoelectronic devices.

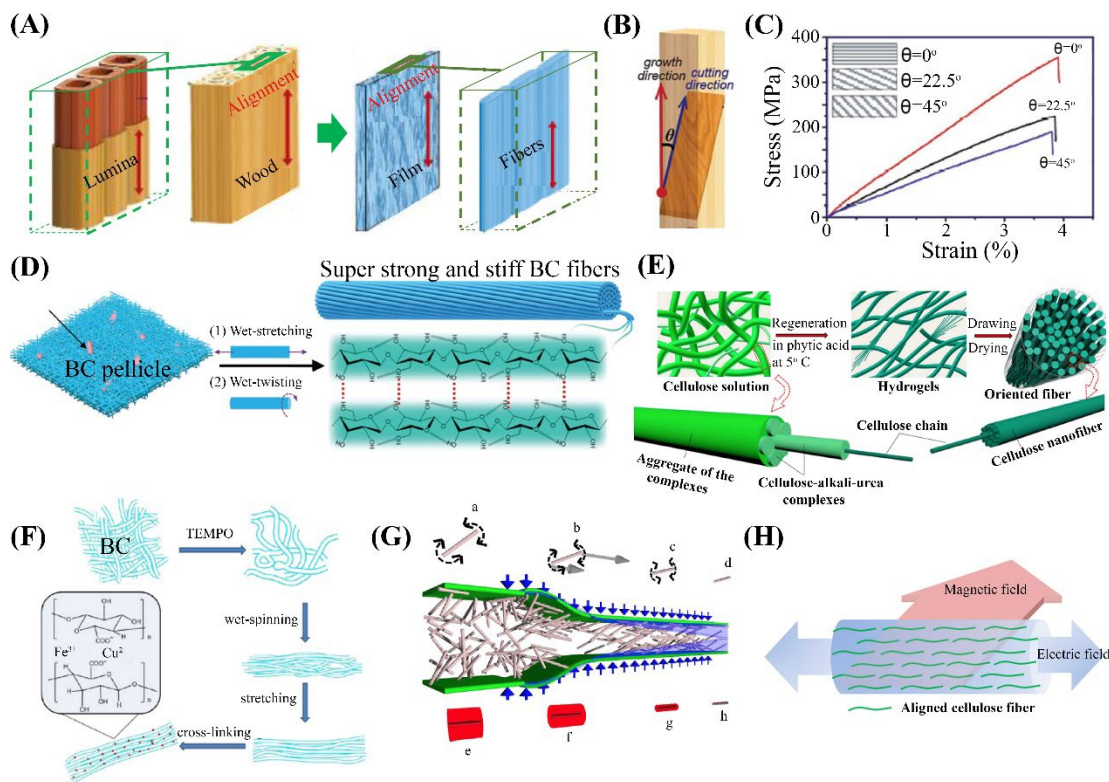


Figure 2.4. *Manipulating alignment of cellulose fibers.* (A) Schematic showing fabrication of anisotropic film from anisotropic natural wood structure. (B) Schematic to obtain tunable anisotropy of the film by varying the wood cutting directions (θ). (C) Experimental stress-strain curves of cellulose films having tunable mechanical properties with respect to alignment. (A-C)¹⁰⁶ (D) Schematic showing transformation of bacterial cellulose suspension to super strong and stiff bacterial cellulose fibers by applying wet-drawing and twisting.¹⁰⁹ (E) Schematic to obtain strong cellulose fibers by wet-spinning and drawing.¹¹⁰ (F) Schematic showing alignment of bacterial cellulose nanofibers involving wet spinning, stretching and ion infiltration.¹¹¹ (G) Schematic illustration of alignment mechanism using a flow-focused assembly device.¹¹³ (H) Schematic showing the alignment strategy of cellulose nanofibers under the simultaneous influence of electric and magnetic field.

2.5 Understanding design of high-performance cellulose-based composites

Given its excellent mechanics attributes at multiple scales, cellulose could also play an active role in achieving high-performance composite functional materials. This section extends the understanding of cellulose mechanics to the composite realm and summarizes various experimental approaches applicable. The section starts with the interface engineering (Section 2.5.1) where the hydrogen bonding between cellulose nanofibers and other materials, such as graphite or graphene oxide, are exploited to increase the binding at the interfaces to develop a high-performance structural material. Then the methods of topology engineering (Section 2.5.2) are discussed where physical or chemical cross-linking or a combination of both helps in tuning the mechanical performance of the composites. Finally in Section 2.5.3, the design procedure of structural alteration is summarized which involves aligning the cellulose nanofibers within the composite matrix by processing methods such as drawing, 3D printing and fabrication of helical macro fibers to elevate the mechanics design of the cellulose composites.

2.5.1 Interface Engineering

Cellulosic hydrogen bonds can be exploited to enhance interfacial binding, thus improving the mechanical properties of the composites. For example, a bottom-up approach to fabricating an ultra-strong and tough graphite-NFC composite was demonstrated by Zhou *et al.*⁹ Here, commercially available graphite powder and NFC suspension were mixed followed by dispersion, sonication, cast-drying, and hot-pressing. The final graphite-NFC composite (Figure 2.5A) of thickness 20-50 μm , in which the diameter of NFC was ~ 2 nm and the lateral size of graphite stack was ~ 11

μm . Upon experimental mechanical testing, the work of fracture (30.0 MJ m^{-3}) and ultimate tensile strength ($901 \pm 129 \text{ MPa}$) of the graphite-NFC hybrid were found to far superior to NFC films (5.9 times and 3.7 times higher respectively), that defeat the existing traditional conflict of the mutually exclusive strength and toughness properties. The specific strength ($794 \text{ MPa gm}^{-1} \text{ cm}^{-3}$) of the composite (density 1.2 gm cm^{-3}) was observed to be much superior to conventional structural materials such as alloys (Al alloys, Ti alloys, TRIPLEX, Bainite) and stainless steel.

The tensile deformation investigated through molecular simulations (Figure 2.5B, C) showed a similar trend (Figure 2.5D). Engineering stress-strain plots (Figure 2.5D) generated from the simulations were qualitatively comparable with experimental data. The results show that due to the increased the interfacial hydrogen bonding density between the NFCs and the edges of the graphite flakes, graphite became a much better load transferring agents, since the contribution of graphite in the stress-strain curve of the composite (cyan lines of Figure 2.5D) can be observed up to a prolonged deformation range, which is absent in pure graphite film and with earlier fracture. Pure graphite, due to empty gaps between flakes and sparsely distributed hydrogen bonding sites at the edges, primarily depended on weak vdW forces to sustain the applied deformation and was much weaker and brittle. The simulations results were further supported by *in situ* AFM pulling out tests which showed that binding between edges of graphite flakes to the NFC matrix was very strong. This innovative strategy of hybridization of one-dimensional cellulose with two-dimensional graphite may have the potential of scaling up for mass production to provide a cost-effective alternative to current non-biodegradable structural materials, thus enabling a much-needed paradigm

shift from petroleum-based products to a novel material with the restricted carbon footprint.

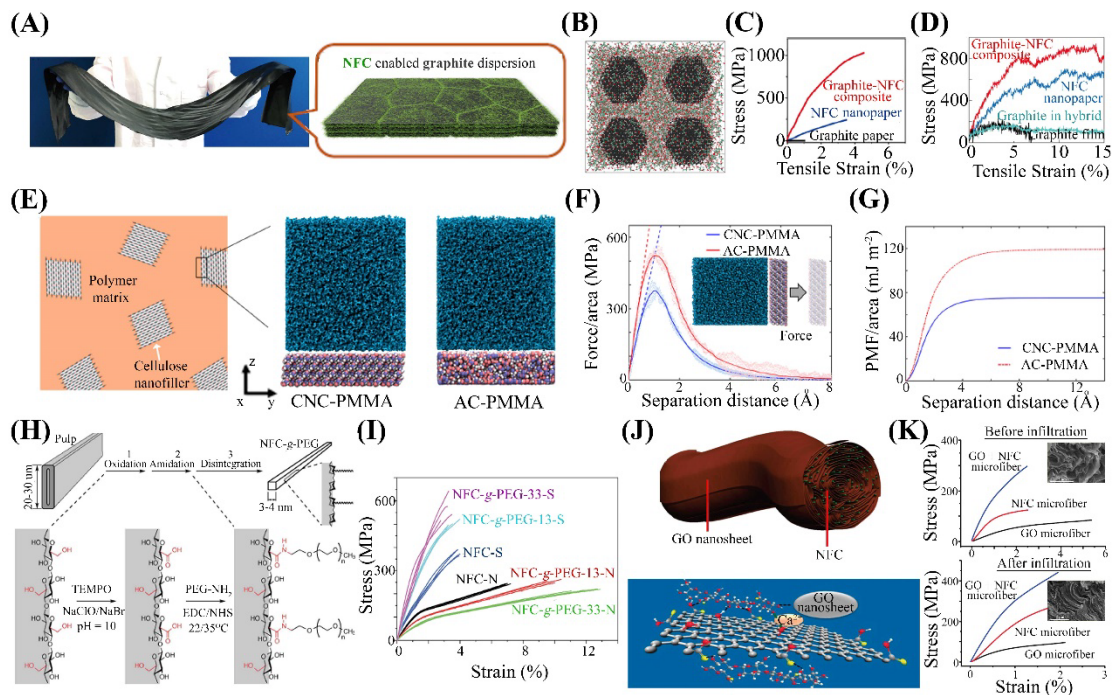


Figure 2.5. *Interface engineering in cellulose composites to tune the mechanical performance.* (A) Digital image of the NFC-graphite bulk material and a schematic illustrating the uniform dispersion of NFC (in green) on graphite flakes (dark grey) to form the graphite-NFC composite. (B) An atomistic model of NFC embedded in the graphite matrix. (C) Experimental stress-strain plots of graphite-NFC composite (red), NFC nanopaper (blue) and pure graphite film (black). (D) Simulated stress-strain curves of graphite-NFC composite (red), NFC nanopaper (blue), graphite film (black) and contribution of graphite (cyan) in the composite to the entire stress-strain curve. (A-D)⁹ (E) Atomistic models for interfaces in CNC (under layer, crystalline)-PMMA (top layer), and in AC (under layer, amorphous)-PMMA (top layer). (F) Plots of driving force versus the separation distance of the CNC/AC and PMMA layers. (G) Plots of potential of mean force (PMA) per unit area versus the separation distance. (E-G)¹²¹ (H) Schematic illustration of the polymer grating using PEG on the NFCs. (I) Stress-strain curves showing the effect of grafting on the mechanical performance of the composite macroribbon. (H-I)¹²² (J) Pictorial representation of hybridization of graphene oxide (GO) and NFC fibers. (K) Stress-strain plots

of the composite fiber, pure GO and pure NFC fiber before (top) and after (below) ion infiltration. (J-K)¹²³

The NFCs filling up the gaps between the graphite stacks are assuming a rather amorphous configuration. It would be interesting to see if an interface of disordered distribution of the NFCs within a composite was indeed helping in strengthening the interfaces in composite materials. To this end, Xia *et al.*¹²¹ constructed two atomistic models involving crystalline cellulose (CNC) and amorphous cellulose (AC), and each of them embedded in a matrix of poly(methyl methacrylate) (PMMA) as shown in Figure 2.5E. The models are defined as CNC-PMMA and AC-PMMA (Figure 2.5E). For both the models, molecular dynamics simulations were performed to separate the layer of cellulose (CNC or AC) from the PMMA to shed light on the fundamental understanding of the dependence of interfacial adhesion on the crystallinity of CNC. The (110) surface characterized the interface between CNC and PMMA. With increasing separation distance, the applied driving force (Figure 2.5F) increased linearly at the beginning and then reached a maximum value, which denoted the interfacial adhesive strength before the full separation. Both the stiffness (initial linear slope) and the adhesive strength in AC-PMMA were observed to be greater than that in CNC-PMMA. The potential of mean force (PMA), assessing the average work required to separate the layers from initial adhered state to final separated state, was calculated from the area under the force-separation distance curve as shown in Figure 2.5G. The interfacial adhesion energy, calculated from the plateau of the PMA per unit area versus the separation distance profile (Figure 2.5G), was much higher for the AC-PMMA interface. This proved that the hydrogen bonding between the randomly

arranged –OH groups of the AC with the –COOH groups of PMMA was much denser and stronger than that in the CNC-PMMA. The higher spatial density of hydrogen bonds in AC-PMMA also created free room for other –OH groups in the cellulose to strengthen the interfacial adhesion. In separate simulations, surface energy of the AC-AC interface was found to be much lower (210.3 MJ m^{-2}) than the CNC-CNC interface (360.4 MJ m^{-2}) which proved a higher dispersion ability of the AC as nanofillers in the AC-PMMA interface.

Strategies such as polymer grafting where different polymers are added onto the surface of the main polymer backbone have also been effectively applied to engineer the cellulose-polymer interface and improve the strength of the final composite. Tang *et al.*¹²² fabricated a cellulose-based ribbon where polyethylene glycol (PEG) was grafted on the NFCs to obtain a composite ribbon named here as NFC-g-PEG-*x*, where *x* denotes the wt. fraction % of the grafted PEGs. Here, the cellulose pulp was TEMPO-oxidized, followed by grafting the amine group from the amino-terminated PEG on the –COOH group of the TEMPO-treated pulp (Figure 2.5H). The suspension was then defibrillated by mechanical treatment and sonication. The resulting suspension was stretched (-S) to 40% strain to induce alignment in the nanofibers and then dried by clamping to obtain the macroscale ribbons. The non-stretched ribbons (-N) were just dried without stretching. The mechanical performance of the PEG grafted cellulose ribbons was found to be much superior with increasing content of grafting (Figure 2.5I). The strength of NFC-g-PEG-33 was higher (576 MPa) in comparison to that of NFC-S (388 MPa). The corresponding modulus of NFC-g-PEG-33 also increased to 32.3 GPa from 17.2 GPa in NFC-S. This was because the increasing grafting content

intensified the aligned orientation of the crystalline cellulose present in the ribbon by preventing agglomerations and maximizing the stress transfer mechanism along with the stretched interface. However, the toughness for the grafted –N ribbons was found to be quite higher (maximum 17 MJ m^{-3}) than that in the –S ribbons (maximum 10.9 MJ m^{-3}) which probably because of the presence of soft matrix PEG layer enhancing the nanoscale interface lubrication and thus elevating the extensibility of the ribbon. In terms of enhanced strength and modulus, this work achieved commendable results and could be used in structural applications or in biofouling where increased strength is necessary.

In addition to reinforcement in composite sheets/filaments, NFCs can also be utilized to fabricate strong hybrid fibers such as long ($\sim 20 \text{ mm}$) and flexible NFC-graphene oxide (GO) nanosheet based microfibers (1:1 mass ratio) as demonstrated by Li *et al.*¹²³ (Figure 2.5J, top). NFCs, prepared by TEMPO oxidation and GO nanosheets, prepared by Hummer's method, were mixed to form a hybrid suspension, which was then wet-spun by extrusion¹²⁴ manually and dried while applying tension. The drying method by the application of pulling ensured alignment between the GO sheets and NFCs, while simultaneously reducing the fiber diameter from $80 \text{ }\mu\text{m}$ to $\sim 10 \text{ }\mu\text{m}$, thus increasing the fiber aspect ratio. This, in turn, increased the NFC/GO interfacial surface area. The number of –OH groups available to enhance the interface mechanics by increasing the spatial hydrogen bond density, increased manifolds. Here, the synergistic interaction between NFCs and GO boosted mechanical performance. Besides standard hydrogen bonding between the sandwiched NFCs and GO sheets, additional hydrogen bonding sites opened because of the bridging effects of the larger

GOs linking the NFCs. The augmented resistance fostered therein implied overcoming an additional cascade of hydrogen bond breaking and reforming during sliding of the hybrid fiber layers under tension, thereby delaying the mechanical failure of the system. Experimental stress-strain plots (Figure 2.5K, top) validated the effectiveness of the design by demonstrating much higher strength (~ 274 MPa) and elastic modulus (20.6 GPa) than individual NFC microfibers (strength: ~ 139.1 MPa, elastic modulus: ~ 15.5 GPa) and GO microfibers (strength: ~ 84.0 MPa, elastic modulus: ~ 2.3 GPa). The mechanical performance of these hybrid fibers could further be tuned by Ca^{2+} ion infiltration in the inter-layer spaces. This was performed by immersing the dried composite fibers in CaCl_2 suspension, a schematic of which is shown in Figure 2.5J (bottom). After infiltration, the strength and elastic modulus of the fiber further increased to ~ 416.6 MPa and ~ 31.6 GPa as displayed in Figure 2.5K (bottom). Infiltration brought the NFCs and the GOs in closer proximity forming better ordered GOs resulting in a structure with higher packing density, as revealed by the SEM image of the fiber cross-section after infiltration (bottom inset of Figure 2.5K).

Other investigations have reported many methods¹²⁵ related to interface engineering demonstrating how the incorporation of cellulose at the interface can boost the mechanics design. For example, a filament based on single-walled CNT (SWCNT) and NFCs^[126] was found to possess higher strength and modulus than most NFC based films, membranes, microfibers and nanopapers.^{127–132} Another film¹³³ based on a fluorinated CNT (FCNT) and NFC exhibited how to achieve superior toughness by tuning the strong hydrophobic-hydrophobic interaction between NFC and FCNT, the role of which is suggested by the Fourier transform infrared (FTIR) spectroscopy data,

which is very intriguing given that traditional NFC are hydrophilic and thus should inspire further mechanism study. These kinds of films can have a wide range of applications where usage will involve considerable bending and folding such as sensors. In one interesting study,¹³⁴ a newly discovered material called MXenes¹³⁵ belonging to family of transitional metal carbide/nitrides, was combined with NFCs to obtain fibers having novel mechanical properties due to the presence of oriented NFCs, in addition to electrical or photonic properties instigated by the presence of MXenes. This clearly implied the wide range of beneficial properties that can be obtained by tuning the interface mechanics design for cellulose functional materials.

2.5.2 Topology Engineering

Topology engineering is a design procedure frequently used to fabricate high-performance cellulose functional materials. It involves physical and chemical cross-linking. Physical cross-linking is formed by ionic interactions or hydrogen bonding (dominate case for crystalline cellulose) and is reversible in nature, i.e., they can be dissociated or associated depending on the external stimulus (e.g., heat). Structural morphology of a cellulosic material may be designed in such a way that hydrogen bonding between neighboring cellulose chains is effectuated, and this gives rise to physical cross-linking, a schematic of which is shown in Figure 2.6. When cellulose chains are involved in sliding relative to each other during tensile loading (as described in Figure 2.2D), it involves breaking and reformation of physically cross-linked bonds. It is comparatively weaker than chemical cross-linking.^{136,137} is an approach frequently used where molecules (cross linkers) consisting of multiple reactive ends attach to the functional groups of neighboring polymeric molecules, thus

introducing a covalent bond between them. They are much more stable and form a tight network (Figure 2.6) by reducing the mobility of the chemically cross-linked molecular chains, which makes it difficult to sever the linked bonds. It is to be noted that chemical cross-linking can also have significant effects in elevating the wet strength of cellulosic materials. This was because enforcing chemical cross-linking reduces the water uptake

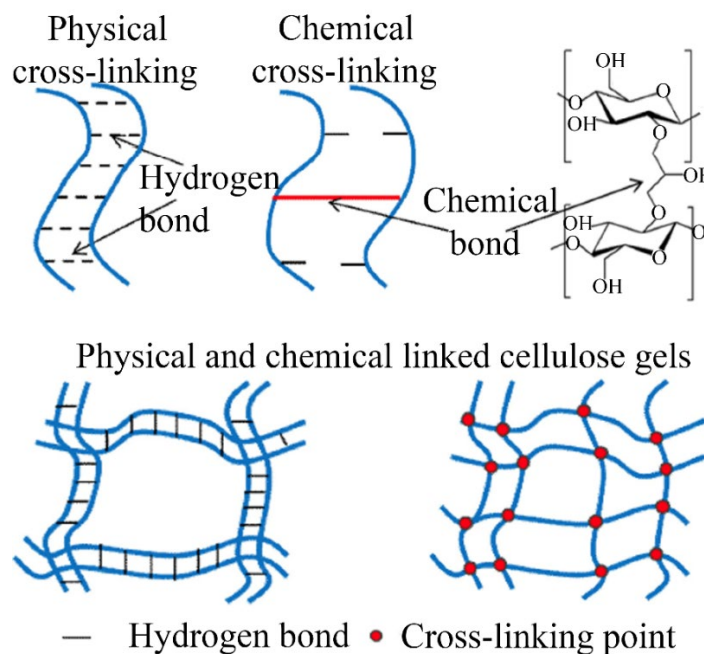


Figure 2.6. *Topology engineering of cellulose composites.* A schematic illustration of physical and chemical cross-linking.^[188]

capacity of the material due to the interfibrillar spaces being occupied by strong chemically cross-linked covalent bonds. The entry of water molecules was considerably blocked, thus restricting them to act as a plasticizer.¹³⁸ The strong covalent bonds maximized the interfacial stress transfer, thereby increasing the strength. On the contrary, if there was only physical cross-linking present, in this case, the existing hydrophilic $-OH$ groups will have more affinity towards water, thus

promoting plasticity and extensibility and thereby reducing the wet strength. These modification strategies may be coupled to cause dual cross-linking which involves a combination of both physical and chemical cross-linking.

Recently a novel design demonstrating dual cross-linking network was shown by Ye *et al.*¹³⁹ through their investigation of an anisotropic cellulose film possessing high strength and record high toughness. Here, regenerated cellulose, which was obtained from cotton linter pulps, was dissolved in a pre-cooled aqueous solution of LiOH/Urea and followed by adding dropwise epichlorohydrin (EPI) which act as chemical linkers to initiate the cross-linking (Figure 2.7A). Then air bubbles were removed by centrifugation and the suspension was poured into handmade molds for gelation.¹⁴⁰ The resulting cross-linked gel was washed with sulfuric acid to terminate the chemical cross-linking reaction and removal of the alkali/urea. Then the chemically cross-linked gel was stretched to induce alignment by physical cross-linking facilitated by the hydrogen bonds, followed by densification using air-drying which evaporated the water and formed an anisotropic cellulose film (ACF). The ACF, fabricated using this dual linking approach was observed to possess a high strength (Figure 2.7B) of 253.2 MPa and work of fracture (Figure 2.7C) of 41.1 MJ/m³.

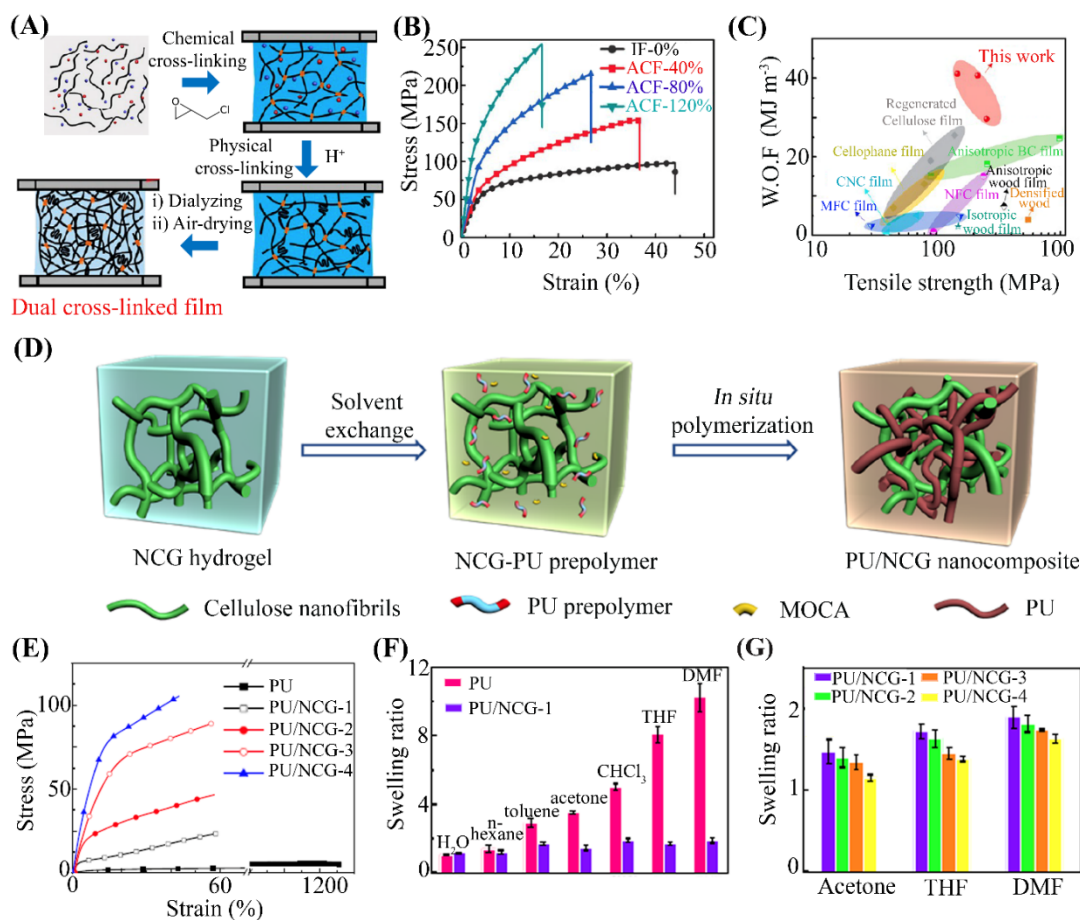


Figure 2.7. Designing topology in cellulose composites to boost the mechanical performance. (A) Schematic showing the dual-cross linking on anisotropic cellulose films (B) Comparison of stress-strain curves of isotropic (IF) and anisotropic (ACF) films. (C) Comparison of the work of fracture (W.O.F) of the ACF obtained in this work with other cellulose based films and densified wood. (A-C)¹³⁹ (D) Schematic showing the formation of double network of PU-NCG composite. (E) Stress-strain curves of pure polyurethane (PU) and PU-nanoporous cellulose gel (NCG) composites. (F) Bar diagram showing the swelling ratios of PU and PU-NCG composites in different solvents. From PU/NCG-1 to PU/NCG-4, the weight content of NCG increases. (G) Bar diagram showing the swelling ratios of PU-NCG composites with varying contents of NCG. (D-G)¹⁴²

The mechanism behind the superior mechanical performance of the ACF described above can be explained as follows. Chemical cross-linking temporarily aligned the cellulose fibrils, that helped improve its connectivity and amplified the stress transfer

mechanism. However, the network was still porous, which resulted in the presence of more defects.¹⁴¹ Further applying physical cross-linking by stretching the chemically cross-linked gel reduced the defects by formation of a much more compact structure with densely stacked aligned or interlocked fibrils. The chemical cross-linking process of the dual strategy gave rise to available additional amorphous region, which enhanced the extensibility of ACF, and was responsible for causing large energy dissipation under deformation, thus being the dominant factor in increasing the toughness (Figure 2.7C). The physical cross-linking minimized the internal defect size in the film and promoted increased cellulose fibril alignment, primarily leading to the enhancement of mechanical strength. The synergistic interactions facilitated by this novel dual cross-linking approach were responsible to extenuate both strength and toughness of ACF.

Chemical cross-linking by different functional groups in sequence could establish a double network in the cellulosic dispersion which may constitute an effective path for engineering the topology of the composites. Li *et al.*¹⁴² applied a nanoporous cellulose gel (NCG) as a precursor material, which was solvent-exchanged with acetone and tetrahydrofuran (THF) (Figure 2.7D) at first. This was sequentially followed by an *in situ* polymerization reaction to infuse the mixture with polyurethane (PU) and 3,3-dichloro-4,4-diamino-diphenylmethanethiol (MOCA). This resulted in a double-network PU-NCG composite. In general, PU based elastomers have a three-dimensional structure. The NCG enriched that structure by acting as a nanofiller because its –OH groups could form urethane linkages with the –NCO groups of the PU. Different PU/NCG composites were fabricated with increasing NCG and the

mechanical properties of these double network PU/NCG composites which were compared with a pure PU sample fabricated using the same procedure in a control experiment (Figure 2.7E). Firstly, due to reinforcement effects of NCG, the strength of the double-network was found to increase from 5.5 MPa to 105 MPa, which was found to be higher than most PU based nanocrystals and composites whose strength varied from 6 MPa to 27.7 MPa. Secondly, it is clear from Figure 2.7E, that the failure strain was arrested within ~60% for the composites in contrast to the 1100% for the pure PU sample possibly because of the linkages forged by the NCGs in realizing this robust gel network. The volumes before (v_0) and after (v) immersing the composite in the water/solvents give the swelling ratio (v/v_0), which indicates the capacity of the material to absorb a solvent. The swelling ratio was found to be stable (1.2 to 1.9) for the composite (PU/NCG-1) in contrast to pure PU sample (1.4 to 10.2) (Figure 2.7F). This low swelling indicated a higher resistance to solvent penetration and was due to the enhanced stiffness of the cellulose gel structure because of the interconnected composite network.^{140,143} In addition, the swelling ratio of various composites (PU/NCG-1 to PU/NCG-4) was found to decrease with increasing NCG weight content (Figure 2.7G). It suggested that the NCGs can be used in creating additional cross-linking by spatially densifying the hydrogen bonds effectively, thus increasing the solvent resistance of the network. The network interconnectivity imparted by the NCGs was directly responsible for the improved reinforcement effects of the composite as evidenced by the superior mechanical strength (Figure 2.7E), making these gels very suitable for applications as sensors or in biomedical engineering.

2.5.3 Structural Engineering

Like pure cellulose materials, alignment can constitute an effective course of action to enhance the mechanical performance for composites. A study on the influence of various degrees of alignment on the mechanical properties of cellulose composites was reported by Wang *et al.*¹⁴⁴ Here a composite film based on cellulose nanocrystals (CNC) and carboxymethyl cellulose (CMC), was formed by solution casting (Figure 2.8A). This was followed by drawing form Film 1 (Figure 2.8A), which was used to test the effect of various drawing ratios ($DR = \text{stretched length}/\text{unstretched length}$) on the mechanical performance of the composite films (Figure 2.8B). It was observed that due to the fiber alignment, the strength of the composite film increased dramatically from around 93 MPa in disordered or misaligned films to around 175 MPa in the aligned film ($DR = 2.5$) as shown in Figure 2.8B, which was also confirmed by both SEM imaging and diffraction patterns. The stiffness (~ 15 GPa) of the aligned film was also found to increase two-fold than that in the disordered film. Surprisingly, the work of fracture for the aligned film (10 MJ m^{-3}) was found to be comparably unchanged from that of the disordered film (11.8 MJ m^{-3}). This indicated that a similar deformation mechanism culminating in failure, which was dominated by hydrogen bonding interactions at the CNC/CMC interface occurred for both and did not sacrifice the toughness to a great extent. This procedure may have the potential to be very fruitful in fabricating high strength functional materials without sacrificing toughness. Additionally, Film 1 as shown in Figure 2.8A, was subjected to multivalent ion infiltration (e.g., Na^+ , Cu^{2+} , Fe^{3+}) to obtain Film 2. The latter was used to study the capacity of the ion infiltration technique to improve the wet strength of the composite

film. In comparison to dry state, the strength of Film 1 reduced considerably from ~220 MPa to ~40 MPa at wet state. This is due to the water weakening the interfacial interactions in the CNC/CMC matrix. However, with Film 2 subjected to ion infiltration, an increasing trend of wet strength was observed. For treatment with multivalent ions such as Na^+ , Cu^{2+} and Fe^{3+} , the wet strength increased to 42 MPa, 128 MPa and 140 MPa respectively. The stiffness of wet Film 2 also increased around 10-fold from 1.3 GPa to 11 GPa when Na^+ and Fe^{3+} infiltrated respectively. The interaction with water is a pertinent problem to tackle while designing high-performance cellulose materials and this study provided an avenue to handle that problem.

Wet spinning combined with drying could also be an effective strategy of structural engineering by inducing alignment and raising the mechanical performance of cellulose functional materials. Li *et al.*¹⁰ demonstrated a hybrid composite microfiber have well aligned CNT–CNF nanofibers. Here, NFC acted as a good dispersing agent and produced a homogenous mixture of NFC-CNT without agglomerations. The mixture was then extruded through a small syringe which aligned the building blocks of NFC and acid-treated CNT along the longitudinal axis of the microfiber (Figure 2.8C). This was followed by a solvent exchange which transformed the mixture to a gel fiber. The gel fiber was then manually pulled out and dried under tension which further enhanced the alignment (Figure 2.8D) in the NFC and CNT structural building blocks. The process was fast and scalable. The spatially dense hydrogen bonding between the aligned –COOH groups of CNT and –OH groups of NFCs helped obtain a microfiber with high strength of ~247 MPa as shown in Figure 2.8E. Significant interfacial area overlap among well-aligned nanofibers, connected by strong hydrogen bonds, implied

the demand for a substantial amount of energy to overcome the facile hydrogen bond reformation while driving the microfiber failure. Since most of the energy required to cause the fiber failure dictated by inter-fiber sliding that originated from the hydrogen bonds, an isotropic film devoid of aligned nanofibers or a CNT film with reduced inter-hydrogen bonding connectivity was observed to possess much lower strengths of 156 MPa (blue line in Figure 2.8E) and 31 MPa respectively, suggesting the fruitfulness of leveraging the anisotropic cellulose mechanics design.

Applying a bio-inspired design to helically coil smaller fibers to form larger macrofibers can also be an insightful approach for structural alteration as reported by Gao *et al.*¹⁴⁵ In this work, an aqueous dispersion was formed between BC nanofibers and a sodium alginate (Alg) matrix because of expected additional hydrogen bonding interactions between the abundant –COOH groups of Alg with the –OH groups in BC nanofibers. The suspension was then subjected to wet spinning where the local shear forces inside the nozzle facilitated the alignment of the BC nanofibers in the matrix (Figure 2.8F, middle panel), resulting in the formation of a uniaxial oriented gel filament. Two, four and eight such gel filaments were then wet-twisted only to initiate a multilevel helical design in obtaining Helical-2, Helical-4 and Helical-8 macrofibers respectively. The (+) and (–) signify filaments whose twist directions were the same and opposite respectively to form the composite macrofibers as shown in Figure 2.8F. After drying, the final macrofibers were densified and revealed very few voids due to the water film binding the individual filaments by surface tension and mobile polymer components of one filament migrating into other filaments and reinforcing the interface. The mechanical strength of the dried single BC filament increased from ~310

MPa to ~430 MPa when the BC content was increased from 10 wt.% to 40 wt.% respectively, validating the strengthening effect provided by the strong hydrogen bonding interactions among unidirectional nanofibers in the network. Further, by applying the helical design strategy, better mechanical properties can be obtained. In comparison to the strength of one dried filament (~420.4 MPa), the strength for Helical-2 (+) and Helical-4 (+) increased to 494 MPa and 504.2 MPa respectively. The strength of Helical-4 (–) was slightly higher at 535.4 MPa, possibly due to different rotational deformation before straightening out under tensile loading. In comparison, the analogous macrofiber (parallel), which had no helical design due to fabrication done by only spinning and no twisting, had a much lower strength (~394.2 MPa). Toughness also increased consistently with higher levels of hierarchy. This is evidenced by the observation that a parallel macrofiber had a toughness value of 8.3 MJ m^{-3} , whereas the corresponding value was 44.8 MJ m^{-3} for Helical-8 macrofiber. The multilevel deformation mechanism involving interfacial sliding of filaments at each hierarchy for the higher-level fibers under tension would dissipate enhanced energy due to increased facile reformation of hydrogen bonds, thus delaying the failure, and increasing the toughness. To add to the phenomenal mechanical properties of increased strength and toughness, the failure strain was also found to increase from 7.5% (for parallel) to 16.2% (for Helical-8). Such nature-inspired helical design to fabricate high-performance macrofibers have the potential to be used in future applications such as textiles.

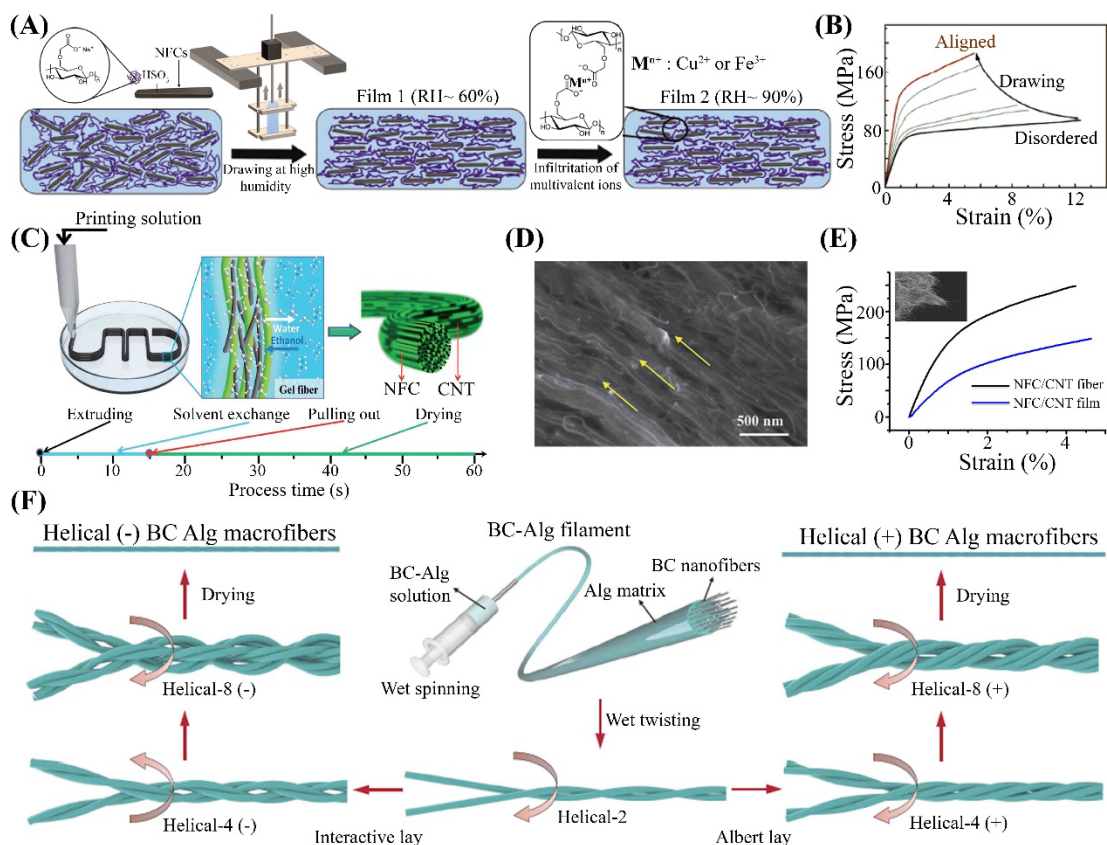


Figure 2.8. *Structural engineering in cellulose composites.* (A) Schematic showing the manipulation of nanofiber alignment in composite cellulose (CNC/CMC) films by drawing and infiltration. (B) Stress-strain curves showing how alignment enhances mechanical performance. (A-B)¹⁴⁴ (C) Schematic showing how 3D printing is used to align NFCs and fabricate a carbon nanotube (CNT) based composite microfiber. (D) SEM image showing the aligned NFCs in the microfiber. (E) Stress-strain curves of the NFC/CNT microfiber (black) and NFC/CNT isotropic film (blue). Inset showing the aligned NFCs after the tensile tests. (C-E)¹⁰ (F) Schematic showing the fabrication of helical macrofiber based on bacterial cellulose (BC) and Sodium alginate (Alg). Albert lay (+) and Interactive lay (-) designate lower-level filaments having same and opposite twist direction respectively in forming the macrofiber. In Helical-y, the number y denotes number of filaments twisted to form the macrofibers.¹⁴⁵

2.6 Concluding remarks and challenges

In summary, this chapter delineated various mechanics design tactics that form the core understanding of the superior mechanical performance of cellulose based functional materials. The chapter commenced with a detailed description of the cellulose's origin and structure features, the understanding of which was essential for connecting its structural traits to engineered mechanical properties. Multiscale mechanics analysis on the mechanical performance of cellulose derived materials emphasized the key role of interfacial hydrogen bonds. Detailed evidence from both experimental and theoretical investigations is offered to help explain the underlying mechanics. This was followed by elucidating ongoing efforts which aims to adapt the molecular engineering of the “nano” level to fabricate novel materials with remarkable mechanical properties. Methods of structural alteration in cellulose-based materials by lignin removal, densification and collapse of cell walls are reported with a focus on how these design techniques in effect elevate the mechanical properties. Fiber alignment design strategies enforced by stretching, twisting, applying flow-focused self-assembly and imposing electric as well as magnetic fields, that resulted in modifying the mechanical performance are discussed. The report also summarized the different mechanics design strategies of cellulose-based composites such as interface engineering by tuning cellulose-polymer matrix interactions, topology engineering involving physical and/or chemical cross-linking in cellulosic gels, and structural engineering administered by wet-spinning, drawing and twisting based techniques.

Despite the innovative mechanics scheme already implemented, there are a few challenges that need to be addressed in future. For example, the DOP (degree of

polymerization) of the cellulose breaks from tens of thousands in plants to ~1000-2500 during isolation of cellulose fibers from raw feedstock.^{20,87,146} An effective DOP protection strategy can increase the chain length and since DOP is directly correlated with strength.^{87,89,146} it may enhance the mechanical performance of the bulk material. TEMPO-mediated oxidation, a common method used to isolate TEMPO-NFCs from plants, is expensive thus impeding low-cost product development. To address that, enzymatic treatments^{51,147} may be used along with novel computational techniques driven by machine learning algorithms^{148,149} to minimize the experimental cost in materials design and optimization. Furthermore, the studies to tune the mechanical performance of cellulose-based materials by overcoming its hydrophilicity and reaching a high value of wet strength are still limited.^{150,151}

To date, emerging applications arise where cellulose is playing a pivotal role in functional materials, such as hydrogels, aerogels, membranes, and fibers. A combination of multiple factors such as strong hydrogen bonding between cellulose and the polymer matrix along with the mechanical wrapping of the long nanofibers with the matrix material to stabilize the composite network become crucial for exploiting the maximum advantage of the reinforced material in myriads of applications. For example, hydrogels, a representative class of soft materials,^{152–154} have demonstrated superior mechanical performance like compressibility and stress retention, where creative design schemes on interface¹⁵⁵ and topology^{156,157} as well as structural alteration induced by anisotropy¹⁵⁸ are in effect. This opened many possible avenues for the application of cellulose in hydrogels. For example, cellulose fibers served as a stiff filler material in a polymer matrix to form complex viscoelastic

hydrogel ink.¹⁵⁹ During 4D printing, the extruded fibers were aligned which caused increased elastic modulus along the longitudinal direction. The obtained filaments swelled on immersion in water and such accurate local control of cellulose fibril orientation may impact the field of shape shifting architectures. A hydrogel containing TEMPO oxidized cellulose carried a large capacity of water due to the presence of densely distributed hydrophilic –COOH groups in their molecular chain, thereby helping in soilless agriculture.¹⁶⁰ Using hydrogel as precursor materials, ice-templating techniques such as freeze-drying can be applied to replace its aqueous gel phase (water) with air to form aerogels. For cellulose-based materials such as wood, chemical treatment destroyed the thin cell walls, and the freeze-drying enabled the broken thin cell walls to attach to the thicker walls forming an interconnectivity between the thicker layers. The lamellar lattice structure in the original wood evolved to a curved stacking of porous, thick cellulosic layers. Aerogels having such unique morphology were reported to be extremely lightweight and demonstrated minimal plastic deformation after repeated loading/unloading cycles along with high fragility resistance and compressibility.^{24,161–163} Research evidence such that even paper waste¹⁶⁴ can be used to manufacture aerogels and they can serve as excellent fire resistance materials,¹⁶⁵ that make their usability more appealing. Incorporating cellulose nanocrystals with functionalized nanomaterials such as polypyrrole nanofibers was reported¹⁶⁶ to result in novel aerogels which could be inserted inside supercapacitor cells. The pores inside the aerogel offered a path for smooth electrolytic diffusion ensuring an efficient overall performance of the supercapacitor. Sophisticated 3D, an interdigitated energy storage device¹⁶⁷ using cellulose nanocrystal aerogel as a substrate, was observed to possess

remarkable electrolytic stability, which is a key advantage accentuating their use as electronic materials such as battery and supercapacitor. In a separate study, due to superior functionalization capabilities, cellulose nanofibers of aerogel could be tuned to be both hydrophobic and oleophilic after treatment with copper nanoparticles.¹⁶⁸

This resulted in ultralight aerogels allowing oils (both immiscible and in emulsions) to pass through but repelling the water, thus validating their uses as membranes separating oil and other pollutants from wastewater and help preserve the natural ecology. In addition to hydrogels and aerogels, the presence of cellulose has strengthened the versatility of other functional materials such as films/membranes too. Traditional films based on plastic and glass which have a transparency of over 90%, exhibited haze less than 20%. Other materials such as tracing paper having a high haze over 50%, possessed low transparency (<80%). Transparency and haze are two mutually exclusive properties in general, but a cellulose based transparent paper,¹⁰² as already described in section 2.4.1 (Figure 2.3G), was reported to have a high haze (~60%) along with high transparency (~96%). The enhanced haze effect was responsible for increasing the photocurrent and the power conversion efficiency of the embedded organic photovoltaic device (OPV), demonstrating the enhanced light harvesting quality of the transparent paper. Superior light harvesting photovoltaic devices can be used in solar windows or roofs as key green building materials of the future so that they are operational even when ambient light was less on any given day. Another transparent wood,⁹⁸ reported to possess high haze (~85%) and high transmittance (~90%), also helped enhance the short circuit and overall current density of a GaAs solar cell, enabling their use in various optoelectronic devices. Sensors to detect strains using a

SWCNT/NFC filament¹²⁶ were able to lift a load around 520 times its own weight and detect different types of muscular contractions through fractional changes in the electrical resistance values. These strain sensors may have phenomenal uses in the field of therapeutics for monitoring patients.

The list of cellulose based functional materials used in high-performance applications is constantly expanding. Additional investigations reporting cellulose tuning the properties of either hydrogel, aerogel, films/membranes or modified wood have also been performed which demonstrate their innovative uses in many diverse areas related to drug delivery,¹⁶⁹ electronic skin and sensing,^{170,171} tissue engineering¹⁷² and electrically conductive materials,¹⁵⁸ insulating materials,^{161,173} water sensing,¹⁷⁴ smart textiles,^{99,175} soft robotics,¹⁷⁶ micro and nanofluidics,^{105,177–179}, packaging,¹⁸⁰ carbon sequestration,^{181–184} thermal management^{12,133,185} and structural materials in future green buildings.⁹⁷ The immense breadth of appealing efficacy that cellulose based high-performance functional materials, motivated by the well-crafted mechanics design, entitles it with the epithet of a next-generation material.

Chapter 3: Utilizing atomistic modeling to understand the superior mechanical properties of selected cellulose-based materials⁴

3.1 Role of alignment in cellulose-nanofiber enabled 3D printing of carbon nanotube microfiber network

3.1.1 Background

Flexible, stretchable, and wearable electronics are attracting increasing scientific and industrial interest in recent studies.¹⁻⁶ Conductive fiber, serving as an important component in wearable electronics,^{7,8} has gained tremendous attention by virtue of their high flexibility, knittability and light weight.^{9,10} Three-dimensional (3D) printing is a prototyping technology that enables transferring conductive ink into fibers and fiber-based 3D network structures. Successful demonstrations include 3D printed batteries,¹¹ embedded electronic sensor,¹² embedded circuits,¹³ and supercapacitors.¹⁴ Superb mechanical properties together with good electrical conductivity are necessary in order to meet the requirements for flexibility and performance under severe deformation.¹⁵ Carbon nanotubes (CNTs) have been intensely studied as the building blocks to make mechanically strong and highly conductive microfibers due to their impressive mechanical properties and electrical conductivity.^{16,17} The elastic modulus and strength

⁴ The main findings included in this chapter have been published as: **A)** Y. Li, H. Zhu (co-first), Y. Wang (co-first), **U. Ray (co-first)**, S. Zhu, J. Dai, C. Chen, K. Fu, S-H. Jang, D. Henderson, T. Li, L. Hu, “Cellulose-Nanofiber-Enabled 3D Printing of a Carbon-Nanotube Microfiber Network”, *Small Methods* 1(10), 1700222, 2017 & **B)** C. Chen, J. Song, J. Cheng, Z. Pang, W. Gan, G. Chen, Y. Kuang, H. Huang, **U. Ray**, T. Li, L. Hu, “Highly elastic hydrated cellulosic materials with durable compressibility and tunable conductivity”, *ACS Nano*, 14 (12), 16723-16734, 2020.

of single walled CNTs and multi-walled CNTs are on the order of 1.0 TPa and 50 GPa, respectively, and their electrical conductivity reaches 10^6 S cm^{-1} and $3 \times 10^4 \text{ S cm}^{-1}$, respectively.^{18,19} However, such excellent properties cannot be fully employed when they are assembled into micro-scale structures due to the poor dispersion quality and alignment of the building blocks, and the unsatisfied load-transfer between CNTs and a matrix.^{20,21} Dispersing CNT bundles into stable single CNTs in liquid is a challenge for 3D spinning process due to the severe agglomeration driven by the strong van der Waals forces among CNTs. Covalent modifications can help disperse CNTs.^{22,23} However, it usually destroys the electronic structure of CNTs, leading to lower conductivities, and increased cost.²¹ Nanofibrillated cellulose (NFC) with diameters in the nanoscale and lengths in the microscale is a promising polymer that can be used as a surfactant due to its amphiphilicity.^{24,25} Hamedi *et. al.*²⁵ successfully demonstrated CNT dispersion using carboxy-methylated NFC through bath sonication. Indeed, NFC possesses dimensions similar to CNTs, excellent mechanical properties, large surface area, and a low density.²⁶ These properties make NFC an excellent building block to fabricate lightweight and strong materials suitable for structural applications^{27,28} and substrates for energy storage devices.^{29,30}

Using NFC as a dispersant for CNT dispersion is also easy to scale up and holds more advantages than CNT dispersion through chemical modification. Firstly, NFC can be extracted from abundant cheap resources, such as wood, cotton, and wheat straw. It is also bioactive because the NFC is biocompatible and organic solvent can be avoided. This makes the dispersion suitable for applications in life science and the disposal is sustainable. Secondly, the dispersion of CNT is mainly based on absorption or

wrapping between CNT and NFC. Thus, the electronic structure and conductivity of individual CNT is preserved compared with dispersion by chemical modification. In addition, the NFC remaining in the dispersion is an excellent building block to make strong, lightweight CNT nanocomposites.

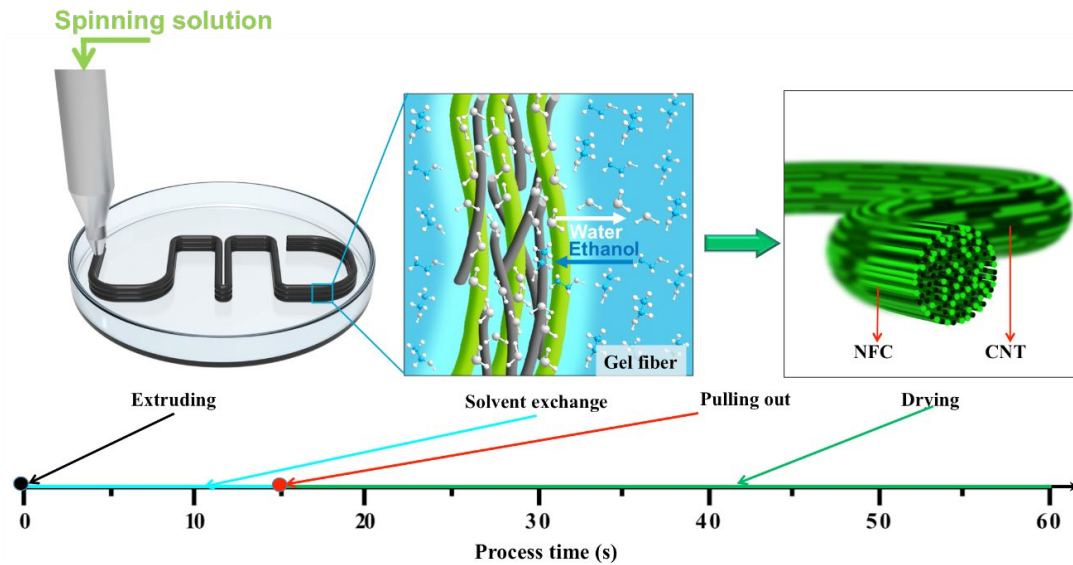


Figure 3.1 Schematic to show the CNT-NFC microfiber network formation through 3D printing. Solvent exchange was performed once the CNT-NFC solution was extruded into the coagulation bath of ethanol, leading to the formation of a stable gel fiber. A dry CNT-NFC microfiber can be obtained after pulling the gel fiber out to dry under tension for tens of seconds. During the process, all the building blocks are highly aligned along the fiber direction due to shear force. The alignment of both CNT and NFC in microfibers leads to the combination of excellent mechanical strength and electrical conductivity.

Because of its excellent properties, NFC was applied as a surfactant to disperse CNTs into water to form strong, conductive microfibers through a 3D printing process as shown in Figure 3.1. When the CNT-NFC solution is extruded out from the head with shear rate, the random network CNT and NFC fibers will get aligned along the microfiber direction. If the CNT-NFC microfibers get highly aligned after being

extracted from the ethanol bath, will the mechanical property of the hybrid fiber increase? If it does, its potential to be a lucrative candidate in smart textile and wearable electronics applications, get enhanced. Here, molecular dynamics (MD) are utilized to shed light on why composites designed with aligned CNT/NFC fibers may acquire more mechanical strength than the ones comprised of randomly arranged (non-aligned) constituent fibers. MD modeling studies like this have the potential to design smart materials with targeted applications.

3.1.2 Molecular simulation methodology

The molecular simulations were performed using the open-source package Large-Scale Atomic/Molecular Massively Parallel Simulator (LAMMPS) and the potential used was the ReaxFF potential³¹ which has been developed based on first principle and is appropriate for carbon-carbon interactions and hydrocarbon oxidation. This potential can model the chemical bonding contributions to potential energy by bond-order functions based on distances and can break down the total potential energy contribution into several sub-categories including an explicit expression for hydrogen bonding. A (5, 5) CNT with length of 5 nm was used in our model. To model the acid treated CNTs, -COOH functional groups were attached to each side of CNTs throughout, that is 6 number of -COOH groups on one face of a CNT and 6 more on the diametrically opposite face. One NFC chain in our model has 5 periodic units. The NFCs in the experiment are TEMPO treated. To model that, we replace the -CH₂OH group at C6 position by -COOH group such that one -CH₂OH group in every periodic unit is replaced by -COOH. We use 2 models in total and each one of them comprises of 3 layers - top, middle and bottom. In the CNT-NFC-CNT aligned model, it is the top

layer with 3 CNT-COOH structures, the middle layer with 3 NFC chains parallel to the CNTs, and the bottom layer with 3 CNT-COOH structures. Bottom and top layer are the same. The CNT-NFC-CNT not aligned model is occupied by CNTs in the top and bottom layers as before but the NFCs in the middle layer are arranged perpendicular to the longitudinal axis of the CNTs. In the atomistic models, the vertical separation distance (in $-y$ direction) between each layer is kept constant for all cases and is equal to 0.5 nm. The distance between CNTs center (in $-z$ direction) is also kept constant for all cases and equals to 0.1 nm. A time-step of 0.5 fs was used throughout to make the simulations stable. Total energy and hydrogen bond energy data points were sampled after 200 time-steps. The groups in all the layers were modelled as rigid bodies. Pulling was applied to the top and bottom layers at a constant translational velocity of 0.001 Å/fs in the x - direction while the entire structure in the middle layer was kept fixed. It is modelled as interactions between rigid structures and the explicit total energy and hydrogen energy values were obtained from the atomistic simulations.

3.1.3 Discussion of the role of alignment in the microfiber

To provide fundamental insight on the role of aligned CNT/NFCs for mechanical property improvement in the microfiber, we carry out systematic atomistic modelling as detailed below. In our material system, the CNTs are decorated with carboxyl groups (-COOH) due to partial acid treatment. CNTs are well dispersed by NFC and the CNT-NFC fiber shows strong alignment due to the shear force during extruding and the tension applied during drying. To understand the deformation and failure mechanics of the resulting microfiber, we construct an aligned CNT-NFC-CNT simulation model as shown in Figure 3.2a. Three single-walled CNTs in the top layer and three single-

walled CNTs in the bottom layers are aligned (Figure 3.2a and 3.2b) with three cellulose molecular chains in the middle layer, respectively. To check the role of alignment we also construct a control simulation model consisting of two layers of CNTs (3 CNTs in each layer) in the top and bottom layers along with three cellulose molecular chains in the middle layer but in a direction perpendicular to the longitudinal axis of the CNTs, as illustrated in Figure 3.2c and 3.2d. This model is termed CNT-NFC-CNT not aligned model. Hydrogen bonds can form between the hydroxyl groups (-OH), carboxyl groups (-COOH) of the NFCs and the carboxyl groups (-COOH) present in the CNT layers. Given that each repeating unit of cellulose molecule contains 6 hydroxyl groups, it is expected that in the CNT-NFC-CNT aligned model, significant amount of hydrogen bonds can form in between neighboring CNTs and NFCs, much more than those in the CNT-NFC-CNT not aligned model (Figure 3.2c, 3.2d). Given the ultrahigh strength of individual CNT and NFC, the tensile failure of the microfiber is expected to result from the relative sliding between neighboring CNTs and NFC along the length direction. We simulate such a failure mechanism by sliding the two CNT layers relative to the NFC layer along the length direction in the CNT-NFC-CNT aligned model. For comparison, we also simulate the sliding of the top and bottom CNT layers relative to the middle NFC layer in the CNT-NFC-CNT not aligned model. Recent studies on tensile failure of cellulose nanopaper (made of a network of NFC nanofibers) reveal that, due to the facile formation nature of hydrogen bonds, the inter-fiber sliding involves a cascade of events of forming, breaking, and reforming of hydrogen bonds in between neighboring NFC nanofibers. Each hydrogen bond breaking dissipates energy. In sum, significant energy is needed to fracture the

nanopaper by inter-fiber sliding (i.e., high toughness of the nanopaper). It is expected that the similar toughening mechanism holds in the CNT/NFC microfiber. Figure 3.2g

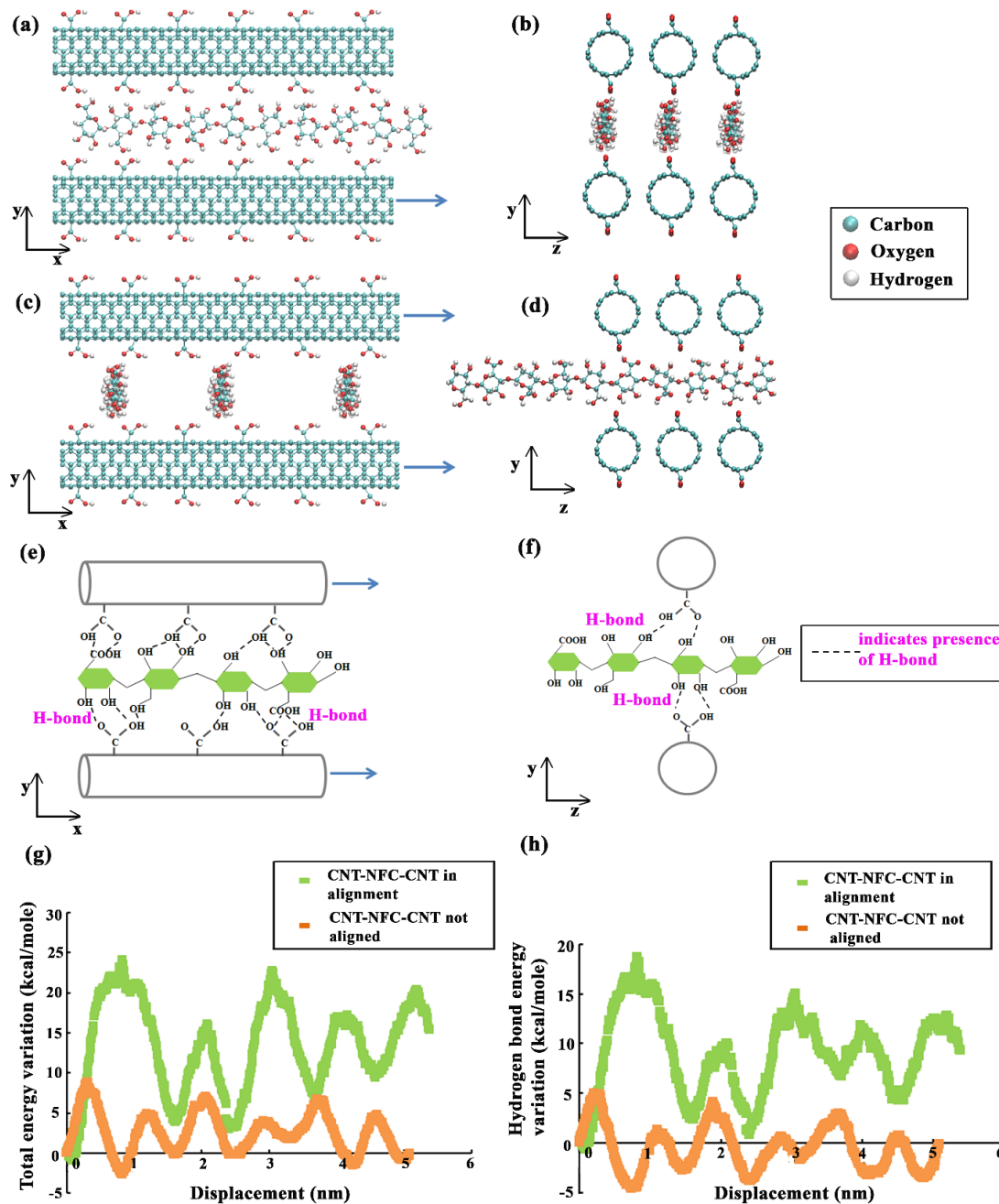


Figure 3.2 MD simulations showing why alignment between CNT and NFCs favors mechanical properties (a, b) Side view and end view of molecular simulation model made of 3 layers: the top and bottom layers contain 3 CNTs each, the middle layer contains 3 NFC chains. All CNTs and NFC chains

are parallel to each other. This model is termed as the aligned CNT-NFC-CNT model. (c, d) Side view and end view of the CNT-NFC-CNT not-aligned model: the 3 NFC chains in the middle layer are perpendicular to the CNTs in the top and bottom layers. (e, f) Schematic illustrations showing more facile hydrogen bond formation in the CNT-NFC-CNT aligned model (e) than in the CNT-NFC-CNT not aligned model (f) due to interactions of rich hydroxyl groups in NFC interacting with the greater number of -COOH groups in CNTs for the aligned model. (g, h) Variations of potential energy (g) and hydrogen bond energy (h) as a function of sliding displacement for the two models: CNT-NFC-CNT aligned model (green) and CNT-NFC-CNT not aligned model (orange) clearly demonstrate the effect of alignment on the superb toughness and strength of CNT/NFC microfibers. The zigzag nature of the curve (g) in addition to the significant difference in hydrogen bonding energy between the two models in (h) reveal the molecular level toughening and strengthening mechanisms in aligned CNT/NFC microfibers.

plots the variation of potential energy during the sliding process for the above two simulation models. Both curves feature a highly zigzag nature, which corresponds to a cascade of events of hydrogen bond forming (curve rising), breaking (curve dropping) and reforming (curve rising again), similar with that in the case of cellulose nanopaper and thus indicating the similar molecular-level toughening mechanism. The amplitude of the zigzags for the CNT-NFC-CNT aligned case is significantly larger (around 3 times) than that for the CNT-NFC-CNT not aligned case, showing clear evidence of the effect of NFC on facilitating hydrogen formation and thus toughening in the CNT/NFC microfiber. Figure 3.2h plots the variation of hydrogen bond energy variation magnitude during the sliding for the two simulation cases. From the difference in amplitude of zigzags in the hydrogen bond energy plots, it is evident that the NFC fibers in the aligned model undergoes significantly larger amount of breaking and reforming of hydrogen bonds and this substantially increase the resistance to sliding-induced mechanical failure of the microfiber, which finds its origin in the facile

hydrogen formation due to rich hydroxyl groups in cellulose molecules. As a result, aligned CNT/NFC microfibers are effectively strengthened as well. In the CNT-NFC-CNT not aligned model this breaking and reforming of hydrogen bonds is significantly lower. This can be readily understood as the significantly enhanced interfacial area in between neighboring CNTs and NFC chains if they are well aligned, which in turn leads to facile formation of hydrogen bonds between the neighboring CNTs and NFC chains. In other words, a microfiber with well aligned CNTs and NFCs can dissipate much more energy and require much higher stress during sliding-induced mechanical failure than a microfiber without CNT/NFC alignment, resulting in the high toughness and strength of the microfiber with well alignment. Also, if Fig. 3.2(g) and (h) are observed closely, both the energy and the hydrogen energy variation of each of the two models are very much equivalent. This indicates that for each model, the majority of the energy to withstand the tensile failure from sliding induced loading indeed stems from the hydrogen bonding. The greater the density of hydrogen bonds, the greater the breaking, reforming of hydrogen bonds and better the mechanical performance of the material.

3.1.4 Summary

Hybridizing CNT with NFCs has numerous advantages. One of them is that NFC can serve as an excellent dispersion agent to disperse CNTs in solution. Here, molecular dynamics modeling is used to understand why incorporation of NFC, when aligned with CNT microfibers lead to excellent mechanical strength/toughness. Designing composite fibers following the approach predicted by molecular modeling has the potential to obtain a hybrid microfiber, which consequently also demonstrated a high

electrical conductivity. This dual combination of beneficial properties makes the microfiber an excellent enabling material for use in wearable electronics.

3.2 All-wood hydrogel with durable elastic compressibility

3.2.1 Background

Hydrogel gains surging interest due to its unique properties such as high-water containing capability, biocompatibility and porous structure for cell growth, designable structure with aligned channels, with an array of potential applications in tissue engineering, biomedical, microfluidics, soft robots, energy storage, and water purifications. For certain applications (e.g., tissue engineering, microfluidics, and energy storage), an anisotropic structure with well-aligned building blocks and/or macro-/nanoscale channels is highly desirable either for anisotropic tissue formation or for fast transport of mass and ions. In addition to anisotropic structure, mechanical robustness, especially anti-fatigue property plays another vital role in dynamic devices that require material to be compressed for numerous cycles. Tremendous efforts have been dedicated to developing various kinds of anisotropic hydrogels for multifunctional applications. Bottom-up approach has been a popular fabrication strategy with various nanomaterials as building blocks, such as cellulose nanofibers, graphene oxide, poly (N54 Isopropylacrylamide), liquid crystal and silk nanofibers. Despite the advantages such as precise control of the hydrogel structure and capability of hybridizing with various additional components, the bottom-up approach usually involves complex multi-step fabrication process with unsatisfactory fabrication efficiency and suffers from relatively high cost and energy consumption as well as the use of toxic chemicals. Besides, most man-made anisotropic hydrogels fail to meet the requirement of

mechanical robustness (e.g., anti-fatigue property), leaving a huge gap between synthetic hydrogels and nature-made hydrogels (e.g., muscles, gristle). These drawbacks have become the major obstacle toward scalable manufacturing of robust anisotropic hydrogel, thus limiting its potential applications.

Anisotropic structures are ubiquitous in biological materials. For example, the structure of a tree features many channels (i.e., lumina and vessels) along the tree growth direction for mass (mainly water and nutrients) and ion transport. These channels are formed by wood cell walls, which consist of highly aligned fine cellulose fibers. Such a hierarchical material structure of tree renders the intrinsic anisotropic properties of natural wood. Another typical example comes from muscle, which is the core actuation system for driving motion of animal body. The muscle sarcomere has a liquid-crystalline anisotropic structure that contains actins and myosins. Such an anisotropic structure offers a high mechanical strength along the fibril direction of muscle, as well as excellent anti-fatigue mechanics for millions of times of movements in the whole lifetime of animals. Here, we report a facile and scalable top-down approach to fabricating elastically compressible anisotropic hydrogel directly from natural wood. The chemical treatment of natural wood using a mixed solution of NaOH/Na₂SO₃ partially removes lignin/hemicellulose and thus softens the wood cell walls. Furthermore, the chemical treatment as well as the ice-templating during freeze-drying causes the formation of interconnected cellulose fiber networks inside individual wood channels (Figure 3.3).

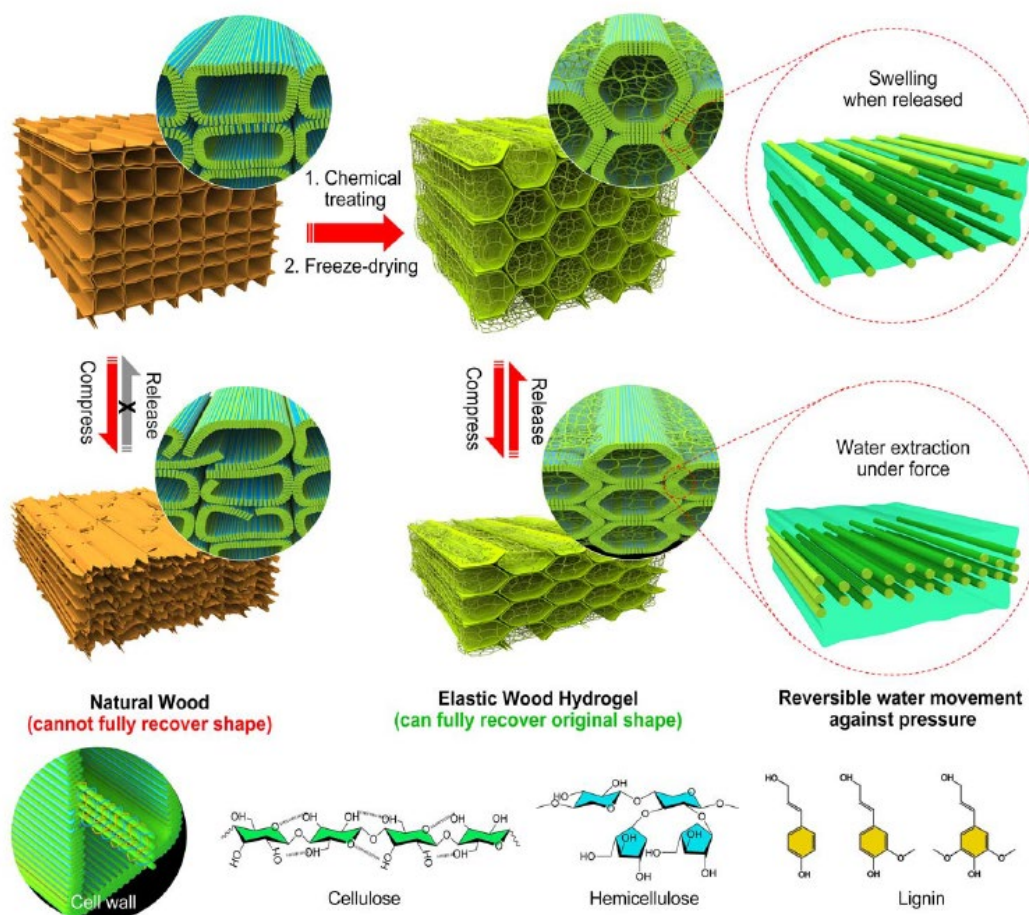


Figure 3.3 Graphical illustration of the comparison between natural wood and elastic wood hydrogel.

Natural wood can be compressed to a large strain (e.g., 70%) due to its high porosity, yet is easy to fracture and cannot fully recover to its original state. By contrast, wood hydrogel can fully recover to its original state even if compressed to a large strain (e.g., 70%) owing to the reversible water movement between the hydrophilic cellulose fibril-based cell walls and internal gel inside the lumina.

Subject to severe compression perpendicular to the wood channel direction, natural wood undergoes structural damage and cannot fully recover its shape upon releasing the compression. By contrast, it is shown that the wood hydrogel with a honeycomb structure and hydrated interconnected cellulose network (i.e., inner gel) inside the wood channels can sustain large compression (up to 70% reduction of thickness) and recover

its original shape without appreciable structural damage after repeated compression (up to 10,000 times), as shown in Figure 3.4.

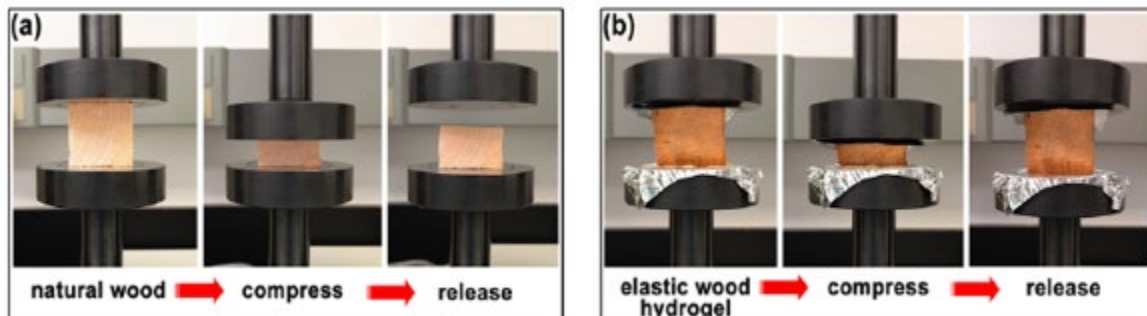


Figure 3.4. Images showing the recovery of the elastic wood hydrogel. (a) Photo images of the natural wood block before compressing, under compression and after releasing, respectively. (b) Photo images of the elastic wood hydrogel block before compressing, under compression and after releasing, respectively.

The atomistic modeling described in the following section (Sections 3.2.2 and 3.2.3) elucidates how the peculiar material structure of the wood hydrogel enables free and reversible movement of water from wood cell walls to the interconnected cellulose fiber network in channels, when subject to compression. On releasing the compressive force, the molecular water acts as the driving force of the fast (within a few seconds) structure recovery.

3.2.2 MD simulation methodology

The full atomistic simulation using ReaxFF potential implemented in the Large-Scale Atomic/Molecular Massively Parallel Simulator (LAMMPS) simulation package is performed to determine the atomic interaction between fibers and water. ReaxFF potential can be widely used to describe chemical bonds and weak interaction, such as

hydrogen bonds. There are 16 fibers aligned as cubic arrangement (4×4) in our simulations. A Nose-Hoover thermostat is used to maintain the NPT and NVT ensembles at 300K in the process of relaxing and compression, respectively. The timestep is set as 0.5 fs and the periodic boundary conditions are applied in both x-, y- and z-directions for all the models. All the calculations are relaxed using the conjugate gradient (CG) algorithm to minimize the total energy of the system until the total atomic forces are converged to less than 10^{-9} eV/Å. We first equilibrate the structures at room temperature (300K) and external pressure with 0Pa for 5ps. In this process we can relax the models sufficiently and define the size of the models in y-direction as original (O) length (L_{original}). Considering the interaction between water and cellulose, the cellulose will be adhered tightly by water. Thus, the size of model with water which is about 60 Å * 41 Å * 30 Å is much smaller than that without water (72 Å * 80 Å * 80 Å). The displacement loading applied to y-direction is indicated by green arrows in the end views of Fig 3.5. After compressing the models for 25ps, we set the models in zero pressure environment for 25ps to release the internal stress sufficiently. For visual clarity, we show the snapshot of section view of the cellulose molecular chains only (water molecules are not shown). The percentage (%) of compression (C) is calculated by $(L_{\text{compressed}} / L_{\text{original}}) * 100$, where $L_{\text{compressed}}$ is the compressed length of the models kept along y direction. The percentage (%) of recovery (R) is calculated by $(L_{\text{recovered}} / L_{\text{original}}) * 100$, where $L_{\text{recovered}}$ represents recovered length of the model (along y-direction) after loading is released and the model is allowed to recover. The water content (wt%) is defined by $(M_{\text{water}} / M_{\text{water+cellulose}}) * 100$, where the $M_{\text{water+cellulose}}$ is the total mass of model and M_{water} is the mass of water in the system. Comparing the water

content of wood hydrogel (65 wt%), we calculated the model with the water content about 60 wt.%.

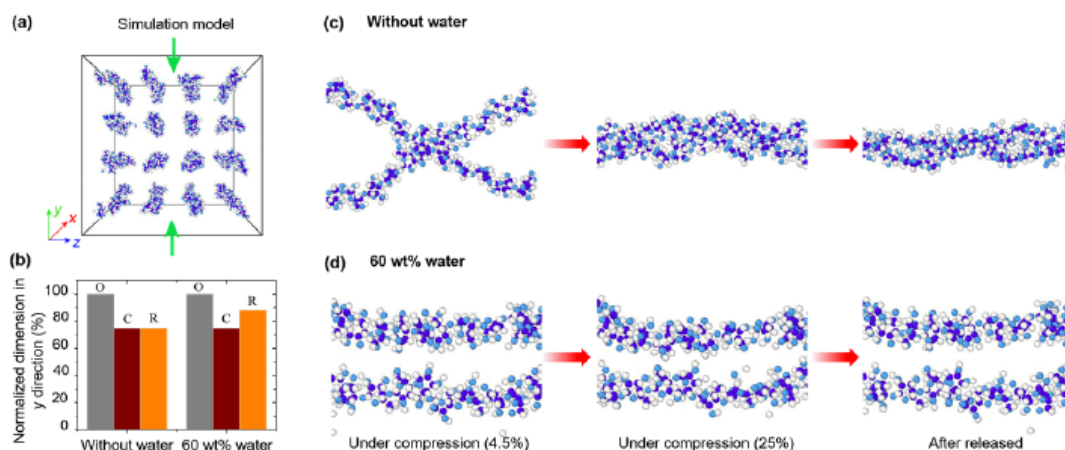


Figure 3.5. Mechanistic understanding of the role of water in elastic wood under compression. (a-d) atomistic simulation of the influence of water on the deformation behavior of wood: (a) the simulation model; (b) normalized dimension of the models in y-direction before compression (O), after compression (C) and after release of the compression (R); (c, d) the morphological derivation of cellulose without (c) and with 60wt%(d) water in the process of compression and releasing. For visual clarity, only the cellulose chains are shown. The comparison of two cases (i.e., with and without water) clearly reveals the effect of retained water on the shape recovery of cellulose fiber network.

3.2.3 Role of water on the deformation behavior of the elastic wood hydrogel

To offer mechanistic understanding of the superb elastic compressibility of wood hydrogel, we carry out mechanics modeling at two different length scales to reveal the deformation behavior of the wood hydrogel under compressive loading and its shape recovery upon release of the loading. The cellulose fiber network inside channels of the wood hydrogel helps retain water in the channels, which in turn plays a key role in the shape recovery of the wood hydrogel. The molecular scale understanding using

atomistic simulations described here bridges the gap that finite element simulations cannot explain from the continuum level.

To this end, we perform a full atomistic simulation using ReaxFF potential to reveal the effect of retained water on the shape recovery of cellulose fiber network after compressive loading is released. Figure 3.5a depicts the atomistic simulation model containing sixteen cellulose molecular chains in parallel. Simulation models consider two different scenarios: (1) without retained water (Figure 3.5c) and (2) with water molecules retained in the space in between the cellulose molecular chains (Figure 3.5d, 60 wt% of water. For visual clarity, water molecules are not shown.). The simulation model is first compressed along y direction up to a compressive strain of about 25%. Next the compressive strain is released, and the percentage of recovery is calculated.

Figure 3.5b compares the percentage of recovery of the simulation models in two scenarios, and clearly demonstrates the critical role of retained water content on the shape recovery of cellulose fiber network. Without retained water, the cellulose fiber network recovers its thickness only marginally after the release of compression. This can be understood as follows. The cellulose molecular chains are rich in hydroxyl group (6 per repeat unit). Subject to compression, the cellulose molecular chains are forced to come close to each other. As a result, a significant amount of hydrogen bonds form in between hydroxyl groups in proximity on the neighboring cellulose molecular chains, as shown in Figure 3.5c. These hydrogen bonds hold the cellulose molecular chains together and prevent the chains from recovering their original spacing upon the release of compression (Figure 3.5c), leading to a low percentage of recovery. By contrast, when water is retained in the cellulose fiber network, the water molecules

limit the amount of hydrogen bonds formed in between neighboring cellulose molecular chains (Figure 3.5d). Upon releasing of compression, the water molecules further help push the cellulose molecular chains back to their original relative spacing (Figure 3.5d), leading to a substantially enhanced shape recovery. The above results offer molecular scale mechanistic understanding of the shape recovery of the cellulose fiber network with retained water, which in turn is shown to be one driving force for the elastic compressibility of the wood hydrogel.

3.2.4 Conclusions and extended research

The atomistic modeling approach described here reveals that the unique internal structure along with free movement of water between the cell walls enables the fast and reversible shape recovery of the elastic wood hydrogel. However, the deformation behavior of the entire hydrogel is not possible due to the length-scale restrictions of the atomic simulations. This is because honeycomb-like microstructure of elastic wood, containing numerous open channels (i.e., lumina and vessels) has a much larger pore size ($\sim 20\ \mu\text{m}$ vs. $\sim 40\ \mu\text{m}$), as characterized using Scanning Electron Microscopy. So, the deformation study of the entire microstructure of wood hydrogel, containing innumerable interconnected fibrils, was extended using finite element modeling. In conclusion, both the honeycomb-like interconnected structure and trapped water were found to be responsible for achieving excellent compressibility and the fast, reversible recovery of the elastic wood.

Chapter 4: A scalable coarse-grain modeling scheme to study the interplay of fibers in cellulose-based materials⁵

4.1 Introduction

Cellulose is gaining increasing attention due to a multitude of desirable properties such as high stiffness, strength and toughness, low density, and sustainability^{1–6}. Given the environmental issues related to high carbon footprint and emissions that exist in the 21st century, significant research efforts are invested in green, nature-inspired materials. The fact that cellulose is abundantly available from diverse natural sources such as plants, bacteria, tunicates, and algae, makes it a desirable bio-based polymer for utilization in sustainable materials engineering. Currently, cellulose-based materials have been used in applications such as high-performance structural materials^{7–10}, additive manufacturing^{11,12}, smart textiles¹³, flexible and wearable electronics^{14,15}, energy storage^{16–18}, thermal management¹⁹, microfluidics²⁰, biomedical devices²¹, tissue engineering^{22,23} and thermal management²⁴. In many of these applications such as high-performance structural materials, the importance of the fundamental insights offered by detailed mechanics-based studies^{6,25,26} is paramount.

To address the structure-performance relation of cellulose materials from a bottom-up perspective where experimental characterization is difficult, molecular dynamics (MD) simulations are extensively used to study in the nanoscale and envision macroscale

⁵ The main findings of this chapter have been published as: **A) U. Ray**, Z. Pang, T. Li, “Mechanics of cellulose nanopaper using a scalable coarse-grained modeling scheme”, *Cellulose* 28 (6), 3359-3372, 2021 and **B) X. Wang**, Z. Pang, C. Chen, Q. Xia, Y. Zhou, S. Jing, R. Wang, **U. Ray**, W. Gan, C. Li, G. Chen, B. Foster, T. Li, L. Hu, “All Natural, degradable, rolled-up straws based on cellulose micro- and nano-hybrid fibers”, *Advanced Functional Materials*, 30 (22), 1910417, 2020.

predictions ²⁷⁻³¹. A recent study ³² uses MD simulations to reveal that the anomalous but desirable scaling law of simultaneous increase of the two conflicting mechanical properties of cellulose nanopaper (i.e., strength and toughness) is due to the facile breaking and reformation of hydrogen bonds between the neighboring molecular cellulose chains. In separate studies, MD simulations have complemented experiments to shed mechanistic insights on various material systems such as oxidized wood fibers ³³, cellulose/carbon nanotube macrofibers ¹², cellulose/graphene-oxide microfibers ³⁴, bacterial cellulose microfibers ^{35,36}, wood films ³⁷ and cellulose-graphite composites ¹⁰. However, despite the advantages against experimental characterization, there are limitations in using MD simulations as a modeling tool.

MD simulations, usually effective at the nanometer length scale and at the time scale up to nanoseconds, are severely restricted to model material systems at the length scale comparable to experimental specimen because of the prohibitive computational expenses. Hence coarse-grained (CG) modeling schemes are desirable to bridge the gap between the nanoscale properties with continuum ^{7,38}. Several CG models with variable mapping degrees have been developed in the past for mechanics studies, such as predicting strategies for improving the mechanical strength of cellulose nanopapers ³⁹ or capturing the elastic properties of the cellulose nanocrystals ⁴⁰. But these existing CG models are either unable to differentiate between smaller nanofibrils and larger microfibers or may not be able to model random network of cellulose probably due to modeling approximations. Another study ⁴¹ uses a non-scalable CG scheme to model a highly porous percolative network representative of cellulose based hydrogels. This model captures the value of elastic modulus for a single cellulose fibril close to

experiments but the reported strength of fibrils (~ 700 MPa) is order of magnitudes lower than the previous estimated fibril strength of 6-10 GPa^{42,43}. Other random network modeling for cellulose based systems⁴⁴⁻⁴⁶ uses finite element modeling (FEM) at continuum length scales, which cannot consider the interactions among cellulose fibers, the key to understanding the deformation behaviors of cellulose based materials. Hence, a CG modeling scheme of cellulose materials to study the deformation and failure mechanism of cellulose-based materials with insight of the interplay among cellulose building blocks at different length scales, starting from molecular chain, to nanofiber, and finally to microfiber scales is essential.

Here, we present a bottom-up, scalable CG scheme based on atomistically informed MD simulations to study the response of cellulose fibers under various representative loading, such as shearing and opening. In addition, we devise a random network model of cellulose fibers, mimicking cellulose nanopaper as fabricated in experiments, and demonstrate the relation of strength and stiffness with respect to various cellulose fiber lengths. The depiction of cellulose film fracture, otherwise impossible by lower-level atomistic MD simulations, can also be effectively captured by the CG simulations.

Our scalable CG scheme consists of three levels, ranging from Level-1 (smallest fiber diameter), Level-2 to Level-3 (maximum fiber diameter) (Section 4.2). The present CG model has the scope to be extended to further complex material systems, such as hybrid cellulose fibers having variable diameters by using⁴⁷ different CG beads at Level-1, Level-2 and Level-3 as the fundamental building blocks. The potential energy of constructed fibers can be obtained as $E(new) = \sqrt{E(a) \times E(b)}$, through the customary Lorentz-Berthelot mixing rules⁴⁸, where $E(a)$ and $E(b)$ are the potentials

obtained in Level-1, Level-2 or Level-3. This chapter is a comprehensive discussion on the development of the CG model and utilizing the scheme to study the behavior of cellulose fibers under representative loads of shearing and opening (Section 4.4), along with an investigation of the failure mechanism of a random network of cellulose fibers as found in a nanopaper (Section 4.5). This is followed by an application of the CG model to study the mechanical properties of experimentally fabricated biodegradable straws (Section 4.7). Thus, the CG model presents multifaceted opportunities in the mechanics design of novel cellulose-based materials.

4.2 Detailed development of the bottoms-up, scalable CG modeling scheme

The CG modeling scheme starts from one molecular chain of cellulose and uses data from atomistic simulations is devised step by step to scale up to lengths reaching micrometers. To design the first level of the CG model (Fig. 4.1a), referred to as Level-1 CG hereafter, we represent the assembly of 21 carbon, oxygen and hydrogen atoms present in one anhydroglucose monomer ($C_6H_{10}O_5$) unit of a molecular cellulose chain by a single CG bead. This bead was chosen so as to minimize the risk of artificial reduction of conformational degrees of freedom due to its much softer torsion potential³⁸. To evaluate the equilibrium bond length (R_o) (Fig. 4.1b), bond angle (θ_o) (Fig. 4.1c) and the dihedral angle (Φ_o) (Fig. 4.1d) between the Level-1 CG beads, we construct three separate atomistic models consisting of 2, 3 and 4 glucose units of cellulose, respectively, in a water simulation box³⁸ with dimensions of 36 Å by 20 Å by 20 Å. The initial parametrization (Level-1) of the CG model thus considers the effect of bound water. After model relaxation using the conjugate gradient algorithm to minimize the total energy of the system until the total atomic forces are less than 10^{-10}

eV/Å, we apply canonical ensemble (NVT) at 300K to equilibrate the system with time and calculate the center of mass ⁴⁹ of each glucose unit from the atomic trajectories. Each of the bond length (R), bond angle (θ) and dihedral angle (Φ) terms are obtained as the system evolves with time towards equilibration, by averaging 50 trajectories of an equilibrated configuration, for each of Fig 4.1b-d. The bond length, bond angle and dihedral angle data obtained from these all-atom simulations were then superposed to represent the bonded interactions of the Level-1 CG model. When each curve stabilizes (Fig. 4.1b-d), we obtain the equilibrium parameters of R_o (0.546 nm), θ_o (163.27°) and Φ_o (171.42°). The timestep in our simulations is set as 0.25 fs. A larger timestep is expected to yield coincidental results of the elastic region in the stress-strain plot but can mitigate the important features of oscillations in the plot and thus avoided here.⁵⁰ We employ the REAX potential ⁵¹ known to effectively capture force interactions in cellulose models to run our simulations.

The bonded interactions (U_{bond}) in a molecular chain to incorporate the stretching, bending, and twisting ⁵² is captured by three terms: two-body bond energy term, three-body angle energy term and the four-body dihedral energy term:

$$U_{bond} = \sum k_{bond}(R - R_o)^2 + \sum k_{angle}(\theta - \theta_o)^2 + \sum k_{dihed}(1 + \cos(\Phi - \Phi_o)) \quad (1)$$

To compute each bonded force parameter (k_{bond} , k_{angle} and k_{dihed}), we stretch, bend and apply torsion to atomistic single cellulose chain models with 2, 3 and 4 glucose units, respectively, and compare the potential energies of the atomistic models with the corresponding analytical equation (1) representing the Level-1 CG model. The force acting on one Level-1 CG bead is matched with the reference forces, as proposed by

(Izvekov S, Voth GA (2005)), acting on 21 carbon, oxygen and hydrogen atoms obtained from atomistic simulations. The CG bonded parameters are evaluated as $k_{bond}=90.283 \text{ kcal mole}^{-1} \text{ \AA}^{-2}$, $k_{angle}=111.5109 \text{ kcal mole}^{-1} \text{ deg}^{-2}$ and $k_{dihed}=8.409 \text{ kcal mole}^{-1}$, which compare well with previous literature literature ($k_{bond}=89.86 \text{ kcal mole}^{-1} \text{ \AA}^{-2}$, $k_{angle}=106 \text{ kcal mole}^{-1} \text{ deg}^{-2}$ as in ³⁸). We model the non-bonded interactions between beads of the adjacent chains (U_{inter}) by

$$U_{inter} = 4u_{o_inter}[(r_{o_inter}/r)^9 - (r_{o_inter}/r)^6], \quad (2)$$

where r is the separation distance between the beads at any given time, and the non-bonded energy parameters u_{o_inter} and r_{o_inter} characterize the depth of the potential well and the equilibrium position of the pair potential, respectively, which are derived from the explicit hydrogen bond energy term of the REAX potential at the atomistic level. Equation (2) is known to capture non-bonded interactions, ⁵³ designated by wider potential wells, between neighboring chains. Furthermore, we represent the non-bonded interactions between beads in the same chain (U_{intra}) by

$$U_{intra} = 4u_{o_intra}[(r_{o_intra}/r)^{12} - (r_{o_intra}/r)^6], \quad (3)$$

where u_{o_intra} and r_{o_intra} are of similar meaning as u_{o_inter} and r_{o_inter} , respectively. To evaluate U_{inter} and U_{intra} , we vary the distance between two glucose units representing two CG beads to obtain the non-bonded interaction energies relative to the separation distance r as shown in Fig. 4.1e and 4.1f, respectively, and then calculate the non-bonded parameters (u_{o_inter} and r_{o_inter} , u_{o_intra} and r_{o_intra}) by curve fitting as shown in Figs. 4.1e-f.

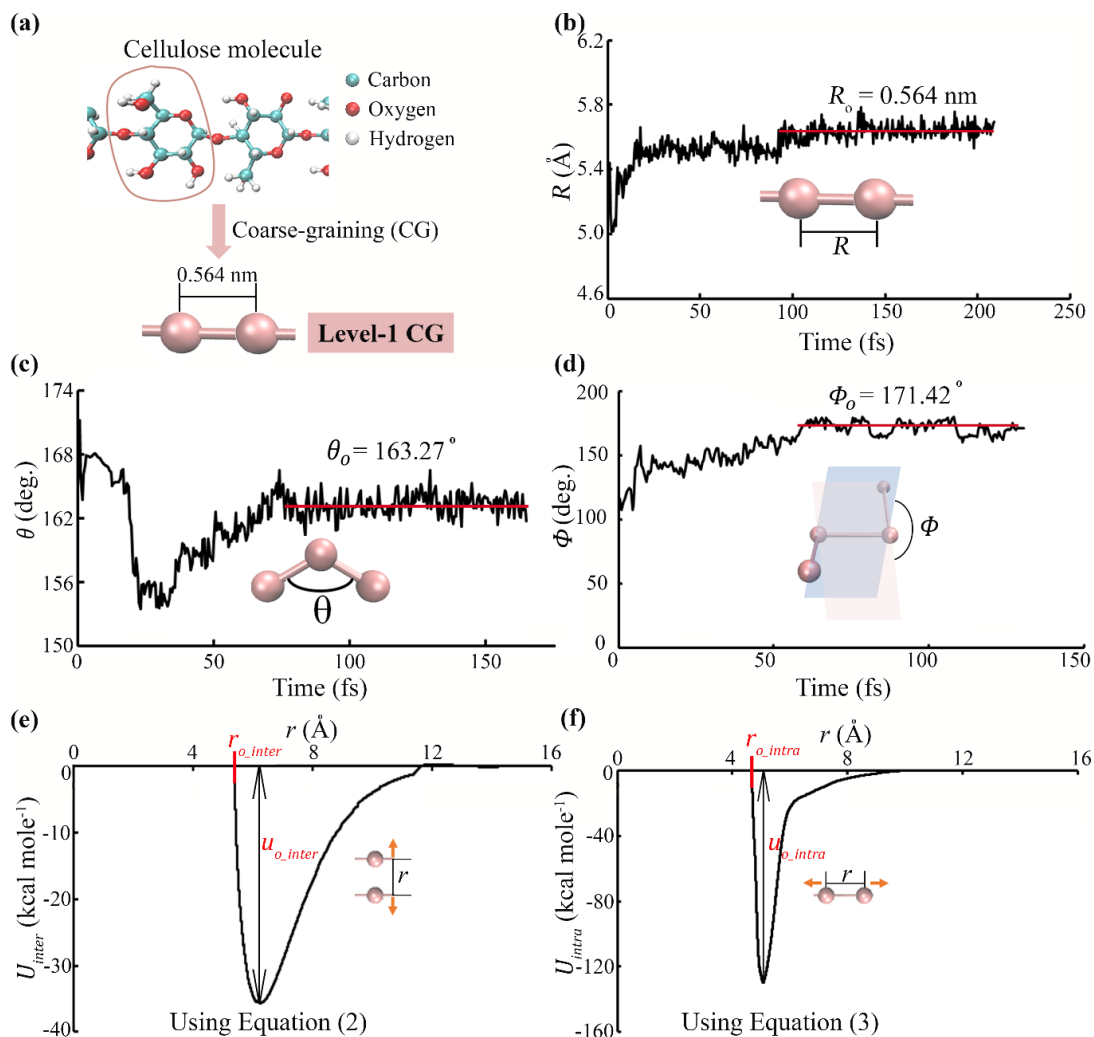


Figure 4.1 (a) *Level-1 CG scheme*. Each glucose unit of the molecular cellulose chain is mapped as one Level-1 CG bead of cellulose. (b-d) Evolution of the (b) bond length (R), (c) bond angle (θ) and d) (dihedral angle (Φ) versus time (fs) obtained from atomistic simulations. The equilibrated bond length R_o , bond angle θ_o and dihedral angle Φ_o , are computed as 0.546 nm, 163.27° and 171.42°, respectively. (e) Plot of non-bonded interaction energy between beads of neighboring chains U_{inter} (kcal/mole) versus the distance of separation (r) of the beads for evaluation of the non-bonded parameters for Level-1 of the CG scheme. (f) Plot of non-bonded interaction energy between beads of the same chain U_{intra} (kcal/mole) versus the distance of separation (r) of the beads for evaluation of the non-bonded parameters for Level-1 of the CG scheme.

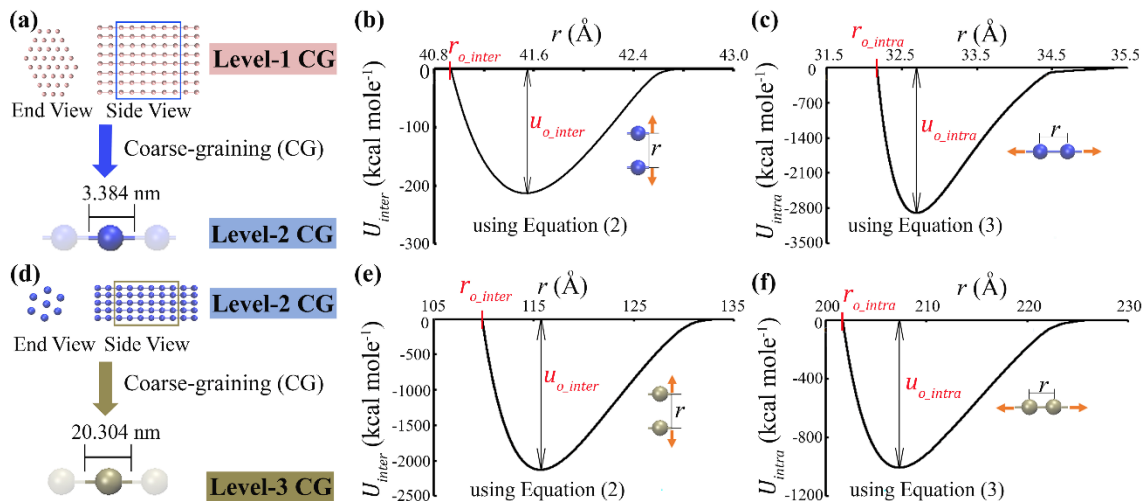


Figure 4.2 (a) *Level-2 CG scheme*. Here, 36 chains, each comprising of six Level-1 CG beads are mapped to form one Level-2 CG bead as shown in the schematic. The bond length between two Level-2 CG beads is 3.384 nm. (b-c) Plots of non-bonded vdW interaction energy (b) between beads of the adjacent chains U_{inter} (kcal/mole) and (c) between beads of the same chain U_{intra} (kcal/mole) versus the distance of separation (r) of the beads for evaluation of the non-bonded parameters (r_o and U_o) for Level-2 of the CG scheme. (d) *Level-3 CG scheme*. Here, 7 chains, each comprising of six Level-2 CG beads are mapped to form one Level-3 CG bead as shown in the schematic. The bond length between two Level-2 CG beads is 20.304 nm. (e-f) Plots of vdW interaction energy with (e) neighboring beads of different chains U_{inter} (kcal/mole) and (f) adjacent beads of the same chain U_{intra} (kcal/mole) versus the distance of separation (r) of the beads for evaluation of the non-bonded parameters for Level-3 of the CG scheme.

For representing the Level-2 CG scheme (Fig. 4.2a), we construct a model that comprises of 36 Level-1 beaded chains based on the crystalline structure of cellulose 1 β , commonly found in plants⁵⁴. Each chain contains 6 Level-1 CG beads. The CG bead length for Level-2 is ~ 3.384 nm. To evaluate the bonded force parameters of the Level-2 from Level-1, we assume periodic conditions so that each bead is connected to two other beads on its two sides. Also, since the cellulose structures show self-

similarity in one direction (self-affine) ⁵⁵⁻⁵⁸, we use the techniques of comparing the parametric bonded force parameter equations of corresponding CG levels for scaling up as used in previous other literatures (Zhu *et al.* 2014b). For example, since 36 chains each comprising of six beads form one bead of the Level-2, the equation of bond energy of two connected beads of Level-2 ($L2$) is given by

$$U_{bond_L2} = k_{bond_L2} b_{i+1} c_{i+1} [6(R - R_o)]^2 \quad (4)$$

where b_{i+1} and c_{i+1} stands for the number of bonds and chains, respectively, formed at CG Level- $(i+1)$. When $i=1$, it represents parameters from Level-1 and hence $(i + 1)$ denotes parameters of Level-2. From our calculations, $b_{i+1} = 2$ and $c_{i+1} = 1$. The bond energy equation of the corresponding Level-1 ($L1$) beads is given by

$$U_{bond_L1} = k_{bond_L1} b_i c_i [(R - R_o)]^2 \quad (5)$$

where $b_i = 12$ and $c_i = 36$ represents the number of bonds and chains, respectively, formed by Level-1 CG beads, respectively, to scale up to the CG Level-2. Comparing the equations (4) and (5) ($U_{bond_L2} = U_{bond_L1}$), we have

$$k_{bond_L2} = 6k_{bond_L1} \quad (6)$$

The angle energy term of the corresponding Level-1 beads forming three Level-2 CG beads is given by

$$U_{angle_L1} = k_{angle_L1} b_i c_i (\theta - \theta_o)^2 \quad (7)$$

where $b_i = 18$ represents the number of bonds from beads and $c_i = 36$. The corresponding angle energy term of the Level-2 beads is given by

$$U_{angle_L2} = k_{angle_L2} b_{i+1} c_{i+1} (\theta - \theta_o)^2 \quad (8)$$

where $b_{i+1} = 3$ and $c_{i+1} = 1$ represents the number of bonds and chains, respectively, formed by Level-2 beads. Comparing (7) and (8), we get

$$k_{angle_L2} = 216 k_{angle_L1} \quad (9)$$

Similarly, comparing the two dihedral energy terms, we obtain

$$k_{dihed_L2} = 216 k_{dihed_L1} \quad (10)$$

To evaluate the non-bonded interactions between different (U_{inter}) and same chains (U_{intra}), the Level-1 structures as shown in Fig. 4.2a are energy minimized and equilibrated following similar procedure as before and then modeled as rigid bodies to restrict the natural twisting of the cellulose bundle⁵². The non-bonded force parameters (U_{inter}) and (U_{intra}) are evaluated by fitting the corresponding energy versus separation distance curve as shown in Figs. 4.2b and c, respectively, to obtain the non-bonded force parameters u_{o_inter} , r_{o_inter} , u_{o_intra} and r_{o_intra} . It is to be noted that the structure in Fig. 4.2a has a non-symmetric hexagonal shape with three different interfaces. The non-bonded interaction energies per unit area relative to the separation distance r , across three different interfaces are computed (Fig. 4.3). The magnitudes of the normalized potential well in the three plots are observed to be almost identical. This suggests that non-bonded interaction energies per unit bead are relatively constant irrespective of the interface. Hence, the maximum inter-bead distance bound is used here to parametrize non-bonded interaction energy while scaling up from Level-1 to Level-2. This is a reasonable choice to avoid the overlap of the fibers at higher levels of the developed CG scheme and thereby simplify the modeling scheme without loss of generality.

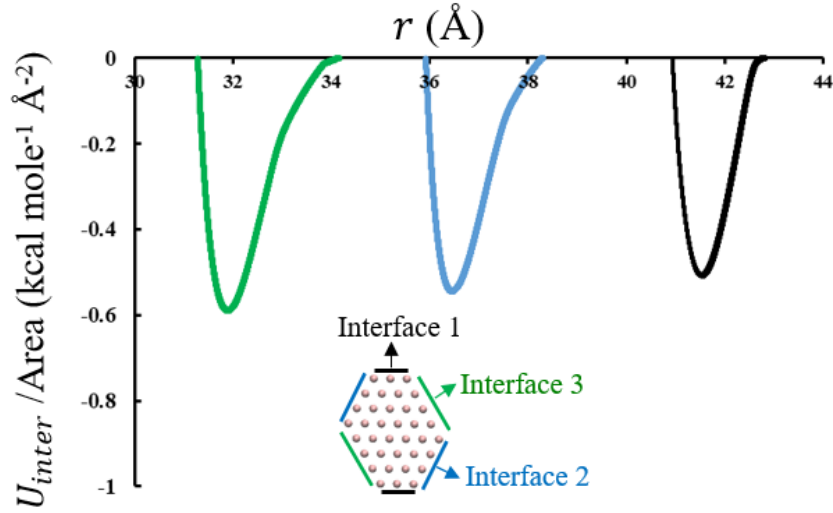


Figure 4.3. The non-bonded interaction energies, between neighboring chains comprised of Level-1 beads, per unit area relative to the separation distance r , across three different interfaces. The areas of Interface 1, Interface 2 and Interface 3 are 419.56 Å^2 , 629.83 Å^2 and 839.4922 Å^2 , respectively. The structure shown here is used to scale up from the Level-1 the assembly to a Level-2 CG bead.

For Level-3 CG (Fig. 4.2d), we construct the beads of crystalline cellulose with 7 Level-2 beaded chains, each containing 6 Level-2 beads, to model a micron-scale cellulose fibril having a diameter of 10.98 nm, in accordance with experimental observations ($\sim 10\text{-}15 \text{ nm}$ as in ¹⁴⁶⁰). The CG bead length for Level-3 is $\sim 20.304 \text{ nm}$. We use a similar procedure as in Level-2 to compute the bonded force parameters for Level-3 ($L3$). For denoting parameters of $L3$, the subscript $(i+2)$ is used following the usual notations as before. Here, we obtain

$$k_{bond_L3} = 7/6 k_{bond_L2} \quad (11)$$

Similarly, the angle parameter at Level-3 is calculated

$$k_{angle_L3} = 42 k_{angle_L2} \quad (12)$$

Also, the dihedral parameter at Level-3 is calculated following the same equation and is represented as

$$k_{dihed_L3} = 42 k_{dihed_L2} \quad (13)$$

The non-bonded interactions between different (U_{inter}) and same chains (U_{intra}) are evaluated by fitting the corresponding energy versus separation distance curve of Level-2 beads forming corresponding Level-3 beads as shown in Figs. 4.2e-f, respectively, to obtain the non-bonded force parameters of Level-3. We carry the CG simulations in LAMMPS⁶¹. All CG force field parameters values evaluated across Level-1 to Level-3 are listed in Table 4.1.

Table 4.1. CG force field potential parameters

	Level-1	Level-2	Level-3
R_o	0.564 nm	3.384 nm	20.304 nm
k_{bond}	90.28 kcal mole ⁻¹ \AA^{-2}	541.69 kcal mole ⁻¹ \AA^{-2}	631.98 kcal mole ⁻¹ \AA^{-2}
k_{angle}	111.51 kcal mole ⁻¹ deg ⁻²	24086.35 kcal mole ⁻¹ deg ⁻²	1011626.88 kcal mole ⁻¹ deg ⁻²
k_{dihed}	8.41 kcal mole ⁻¹	1816.34 kcal mole ⁻¹	76286.45 kcal mole ⁻¹
u_{o_intra}	129.10 kcal mole ⁻¹	2895.42 kcal mole ⁻¹	1004.87 kcal mole ⁻¹
r_{o_intra}	0.47 nm	3.22 nm	20.17 nm
u_{o_inter}	34.77 kcal mole ⁻¹	212.97 kcal mole ⁻¹	2128.43 kcal mole ⁻¹
r_{o_inter}	0.537 nm	4.093 nm	10.983 nm

4.3 Validation of the CG model

Here, a cellulose bundle with seven molecular chains, each having 8 repeat units (8 glucose monomer units) and length 4.38 Å as shown in Fig. 4.4a (top panel). An equivalent Level-1 CG model consisting of 7 chains, each containing 8 repeat units (Level-1 beads) is also constructed (Fig. 4.4a, bottom panel). The simulations mimic inter-fiber sliding of the cellulose chains in the fiber bundle and the middle chain (inset of Fig. 4.4a) is pulled out. We compare the variation of total potential energy (Fig. 4.4b) during the sliding process for the above two (AM and CG) simulation models. The results from the AM model are obtained from Ref. ³². The pulling is initiated by applying a velocity of 0.001Å/fs in the first glucose unit and the first CG bead of the AM and CG models, respectively. The initial increase of both curves results from the tension of cellulose chains. At the initial stages of pulling out of middle chain in the CG simulations, the applied tension is transferred stepwise starting at the pulled end and slowly transmitted to the other end of the chain. During the initial stages before the advent of inter-fiber sliding, the energy variation in the CG simulations is captured by the bond energy incorporated within equation (1). This equation developed using the coarse-graining methodology is an approximate form of the bond energy described by the REAX potential, developed using first-principle calculations in atomistic simulations. The lag in the energy variation curve obtained through CG modeling is mainly because of the energy drop due to the approximations while formulating the CG scheme. When the whole chain slides, both curves of the energy variation versus pulling displacement feature the zigzag nature, indicating the cascade of hydrogen bond forming (curve rise till the local peak), breaking (curve drop from local peak to local

trough) and reforming (curve rising from the trough to the next peak), a representative feature of the relative sliding between cellulose chains. The similar tendency and amplitude of the zigzags in both curves show that the CG model is accurate enough to the parameterization of bond and non-bond interaction. The maximum amplitude of the CG model (corresponding to displacement ~ 1.5 nm - 4.8 nm) is within 1.6% tolerance to that predicted by the atomistic model. Since the maximum energy dissipated while sliding is an indicator of the extent of breaking and reformation of the hydrogen bonds before final failure, the accuracy of median energy and amplitude of curve suggests that the developed CG model can effectively capture the failure modes in cellulose fibers. This proves that our CG model can capture reasonably well the hydrogen bond breaking and reforming of the molecular cellulose, a deformation mechanism dissipating a significant proportion of energy while the cellulose fibers are undergoing interfacial sliding.

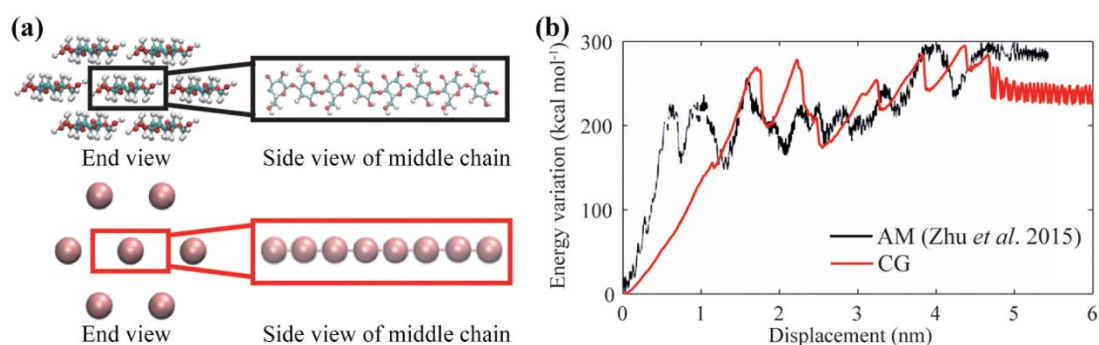


Figure 4.4 Validation of the Level-1 CG model with an atomistic model (AM) from previous literature

³². Here, the atomistic model consists of seven molecular cellulose chains, each having 4 repeat units (eight glucose units, as illustrated in the zoom-in view). The middle chain is pulled out of the surrounding six neighboring chains. To verify our scheme, we built an analogous CG based model to mimic the pulling out simulation. The potential energy variation (kcal mole^{-1}) with respect to the pulling

displacement (nm) is plotted and the energy variation matches well with the atomistic simulation results for ref.³²

4.4 Mechanical response of cellulose fibers under shearing and opening loads

Figure 4.5 plots the mechanical response of the cellulose fibers under two representative loadings such as shearing and opening. In shearing loading, two fibers, each 1.22 μm long, comprised of 60 Level-3 CG beads, slide (red arrows in Fig. 4.5a) against each other parallel while in opening loading, the same two fibers are opened by pulling the left most beads (red arrows in Fig. 4.5c) away from each other. For the shearing mode, the pulling is initiated by applying a velocity of 0.0001 $\text{\AA}/\text{fs}$ to the end beads. The temperature is controlled around 5K to reduce the thermal noise while undergoing shearing. For the opening mode, fibers are separated by applying a velocity of 0.0001 $\text{\AA}/\text{fs}$ to the leftmost beads (red arrows in Fig. 4.5c). The other ends of the fibers undergoing deformation by opening are allowed motion only along x- and y-direction (wiggly lines in Fig. 4.5c schematic) to execute pure opening deformation modes in our model. Both the shearing and opening simulations are performed under microcanonical ensemble with a timestep of 0.25 fs and the energy data points are collected after every 5000 timesteps. For both deformation modes, we plot the average the averaged potential energy (kcal mole^{-1}) versus the pulling displacement (microns) (Figs 4.5a-b).

The energy variation versus pulling displacement plot (Fig. 4.5a) of the shearing simulation shows an initial linear profile symbolizing immense bending of the chains initially starting to slide relative to each other. This is accompanied by non-bonded interactions between one bead of the first chain and the adjacent bead of the

neighboring chain. As the resistive force imposed by the non-bonded energy between the beads of the neighboring chains trying to restrict the shearing increases, the beads are stretched to the maximum extent as shown in Fig. 4.5b (labelled 1 in blue) corresponding to the first peak of Fig. 4.5a (labelled 1). As the shearing continues, the same bead reaches an equilibrium position (local minima) by aligning itself with the next bead of the neighboring chain as depicted by the schematic corresponding to the first trough (labelled 2 in Fig. 4.5b). This stretching of beads of adjacent chains followed by energy stabilization continues with further progress of shearing resulting in the zigzag amplitude of the energy profile. The curvy nature stems from the hydrogen bonding originating from the molecular level cellulose chains. The facile breaking and reformation of hydrogen bonds cause resistance to the sliding chains, which results in tremendous dissipation of energy. The cascading effects of strong inter-fiber non-bonded energy continue until the whole chain is pulled out, which indicates failure.

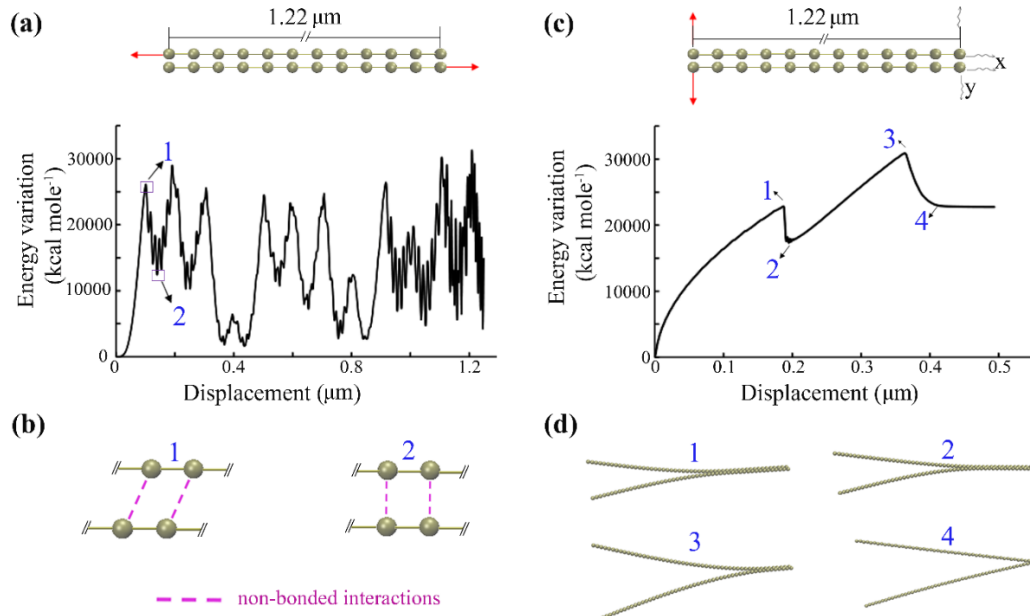


Figure 4.5 Simulations of shearing and opening between two fiber models built using Level-3 beads from the devised CG scheme. Each of the two fibers have a length of 1.22 μm. (a) Potential energy

variation (kcal mole^{-1}) versus the pulling displacement (μm) as the fibers slide relative to each other, indicating shearing. (b) Schematic showing the beads under shearing deformation causing the peaks (first peak labelled 1 in blue) and troughs (first trough labelled 2 in blue) in Fig. 4.5a. (c) Potential energy variation (kcal mole^{-1}) versus the opening displacement (μm) as the fibers bend relative to each other. (d) Snapshots of the bending deformation corresponding to the peaks and troughs (labelled 1, 2, 3 and 4 in blue) of Fig. 4.5c. The directions of shearing and opening are indicated by red arrows.

Figure 4.5c shows the energy profile of two fibers opening relative to each other. Here, in the first part of the potential energy variation versus the pulling displacement (displacement from 0 to $0.175 \mu\text{m}$), the fibers bend and move away from each other while trying to resist the opening deformation. The simulation snapshot (labelled as 1 in Fig. 4.5d) demonstrates the initial phase of the bending process corresponding to the first peak of the energy profile (Fig. 4.5c). As further opening is imposed, there is a steep drop in the energy profile. It is mainly because the remaining part cannot resist the bending and relax the potential energy suddenly by partial separation (corresponding to the label 2 of Fig. 4.5d) and adjusting their orientation (right end of snapshot 2 (Fig. 4.5d) goes down). With the further increase of opening deformation, the energy profile rises again until it reaches a global maximum in the energy profile (labelled as 3 in Fig. 4.5d), corresponding to the further bending. When the remaining part cannot maintain the bending again, the curve drops suddenly due to stopping of the bending and release of energy as the fibers straightened (snapshot 4 in Fig. 4.5d). Due to the length of fiber in our simulations, such an energy variation appears twice until the two chains separate from each other (labelled as 4 in Fig. 4.5d).

4.5 Failure mechanism in a random network of cellulose fibers as found in a nanopaper

Furthermore, the CG modeling scheme is applied to study the mechanical properties of a random network of cellulose fibers, which is a reasonable estimate of the material structure of cellulose nanopaper in experiments³². Such a simulation is crucial for revealing the deformation and failure mechanisms of cellulose nanopaper that are challenging, if not impossible, to capture in experiments, and cost prohibitive for fully atomic simulations. To investigate the effect of cellulose fiber length on the mechanical properties of cellulose nanopaper, three random network models with a fiber length of 0.9 μm , 1.2 μm and 1.5 μm , respectively, are constructed. The total number of Level-3 CG beads in each of the three models are 29,508 ($\pm 0.005\%$ tolerance) corresponding to 267,696,576 atoms. Fully atomistic simulations of such a model size are prohibitive. Experimental tensile tests are usually performed by cutting thin strips of specimens from the bulk sample which may result in broken fibers at the edges. To accurately reproduce the experiments, randomly oriented fibers are placed into a simulation box of size 6 μm by 1.5 μm by 0.1 μm and fibers are cut if they protrude the simulation box. The minimum length of the remaining small fiber is set to be larger than 0.1 μm for the convergence of simulations. Each CG model is relaxed using the conjugate gradient algorithm to minimize the total energy of the system by decreasing the total atomic forces less than 10^{-15} eV/ \AA , thus releasing the internal stress sufficiently. After a relaxation with canonical ensemble, the left and right ends (~ 1.5 μm from each end) are set as rigid bodies to incorporate the effect of clamps in a tensile testing machine. Uniaxial tension is applied by pulling the right end (red arrows in Fig. 4.6a) at a

constant velocity of 0.001 Å/fs using a timestep of 0.25 fs under microcanonical ensemble, while the other (left) end is kept fixed. Stress is calculated by computing the sum of stress components of the mobile segment of the model along the tensile loading direction.

Figure 4.6a shows the deformation of one model of randomly distributed cellulose fiber network where the maximum length of each fiber is 1.2 μm. The initial structure before application of tensile loading (strain = 0%) is shown in Fig. 4.6a (top panel). The random network is modeled on the hypothesis that thicker cellulose fibers having diameter in the range of 10-20 nm, as present the current CG model are relatively shorter and straight, as evidenced by experimental characterization in separate investigations⁶². Three deformation snapshots of the model under tensile loading are labeled (I), (II) and (III) in Fig. 4.6a, corresponding to strains of 0.34%, 5% and 15%, respectively. When uniaxial tension is applied, the randomly oriented cellulose fibers start to slide apart from each other and non-bonded interactions, mainly arising from hydrogen bonding among the neighboring fibers, resist the sliding in between the cellulose fibers until the stress-strain plot reach the global maximum (label I). As the tensile strain increases, the cellulose nanopaper elongates in tensile direction and contracts in the perpendicular direction, until cracks initiate at the edges which lead to stress concentration and thus localized deformation in the nanopaper (label II). Upon

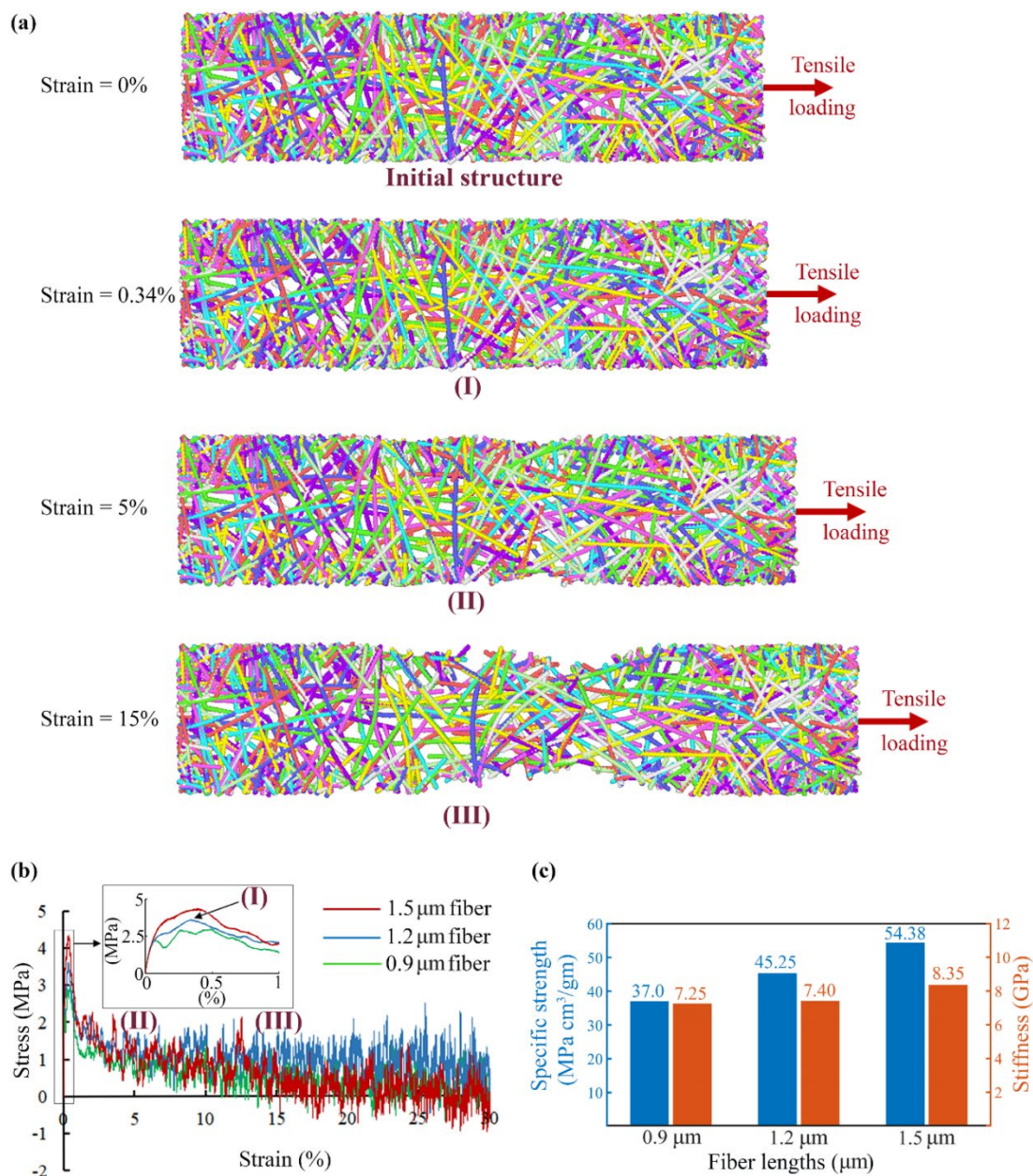


Figure 4.6 CG modeling and mechanical behavior of cellulose nanopaper films. (a) Deformation snapshots of a random network of cellulose fibers made of Level-3 CG beads. The deformation snapshots of the model, consisting of fibers having a maximum length of 1.2 μm fiber, under tension (red arrows) is shown here. The initial structure before deformation is shown in the top panel. The snapshots corresponding to variable strains of 0.34%, 5% and 10% are labeled (I), (II) and (III), respectively. (b) Engineering stress (MPa) versus the strain (%) plots for the random networks with different fiber lengths: 0.9 μm (green), 1.2 μm (blue) and 1.5 μm (red). Inset shows the magnified stress-strain plots at strains

ranging from 0 to 1% to clearly display the peak stress values for the three models. (c) Comparisons of the specific strength (MPa cm³/gm) and stiffness (GPa) for all three models with varying fiber lengths (0.9 μm, 1.2 μm and 1.5 μm).

further tensile loading, the localized deformation causes the cellulose fibers in the severely deformed region to be more aligned with the tensile direction. The failure of the cellulose nanopaper occurs when the cellulose fibers slide off from each other in the localized deformation region. It is to be noted that no breakage of cellulose fibers is observed in the simulations, which asserts on the understanding that failure in cellulose nanopaper is mainly due to inter-fiber sliding instead of individual cellulose fiber fracture, largely due to the superb mechanical properties of individual fibers (up to 7.5 GPa of tensile strength) ⁶³. Similar deformation and failure behaviors are also observed in the other two sets of CG modeling, with a cellulose fiber length of 0.9 μm and 1.5 μm, respectively.

Table 4.2. Comparison of the cellulose nanopaper properties as predicted by the devised CG model with previous experimental results

Properties	This work by CG modeling	Experimental results from literature	Reference
Specific Strength (MPa cm ³ /gm)	~ (37.0 - 54.38)	~ (24.15 - 41.66)	Sehaqui H <i>et al.</i> (2011), ⁶⁴ Yousefi H <i>et al.</i> (2013), ⁶⁵ Motamedian HR <i>et al.</i> (2019) ⁶⁶
Stiffness (GPa)	~ (7.25 - 8.35)	~ (7 - 11)	Sehaqui H <i>et al.</i> (2011), ⁶⁴ Zhu H <i>et al.</i> (2015) ³²

Figure 4.6b plots the stress-strain curves of the three models obtained from CG simulations, from which the tensile strength and stiffness of the corresponding cellulose

nanopapers can be determined, as compared in Fig. 4.6c. The specific strength of the cellulose nanopaper increases as the cellulose fiber length increases, e.g., 37.0 MPa cm³/gm, 45.25 MPa cm³/gm, 54.38 MPa cm³/gm, for fiber length of 0.9 μm, 1.2 μm and 1.5 μm, respectively. It is acknowledged that a fair comparison is difficult because the diverse processing conditions may result in a final cellulose nanopaper with a broad range of fiber lengths as well as fiber diameters. Our specific strength values (37.0-54.38 MPa cm³/gm) agree reasonably well with various experimental samples in previous literature⁶⁴⁻⁶⁶, as included in Table 4.2. Such a fiber length dependence of tensile strength of cellulose paper can be attributed to the fact that increasing degree of polymerization or length of a cellulose fiber allows for more non-bonded interactions between neighboring cellulose fibers, which in turn lead to higher energy dissipation during the tensile deformation and failure of the cellulose nanopaper. In other words, longer cellulose fibers can resist more tensile deformation as a higher energy is required to fail the random network of cellulose fibers, which corresponds to a higher tensile strength with increasing cellulose fiber length. This is well aligned with previous multi-scale crack bridging models which emphasize that the absence of hydrogen bonding is the primary factor in reducing the fracture toughness drastically, thus leading to accelerated failure in the cellulose nanopaper⁶⁷. The oscillation of the stress-strain curves after the tensile stress peaks results from the cascade of events of hydrogen bond formation, breaking and reformation, as the cellulose fibers in the nanopaper model slide relative to each other with the increase in the tensile strain. Such oscillations from positive to negative stress values at large strains (~12-30%) can be observed in studies related to atomistic and coarse-grained models³¹⁴⁰²⁹ but hard to be observed in the

experimental test samples, due to length scale effects. The stiffness of the cellulose nanopaper increases modestly as the cellulose fiber length increases, e.g., 7.25 GPa, 7.40 GPa, 8.35 GPa, for fiber length of 0.9 μm , 1.2 μm and 1.5 μm , respectively, which can be attributed to the higher non-bonded interactions (e.g., hydrogen bonds) between neighboring cellulose fibers. The range of stiffness of cellulose nanopapers is well in line with the experimental measurements ($\sim 7 - 11$ GPa as in Table 4.2)^{32,64}. The dependence of tensile strength and stiffness of cellulose nanopaper on the constituent cellulose fiber length revealed by the CG simulations can serve as a quantitative guideline for designing cellulose nanopaper with desirable mechanical properties.

4.6 Summary and possible future work using the bottoms-up CG scheme

In summary, we design a bottom-up, scalable CG scheme that enables modeling of cellulose fibers ranging from nanometers to microns at a low simulation cost, a much-sought capability in understanding the deformation and failure mechanisms of cellulose nanopaper that is otherwise impossible by fully atomistic simulations. The CG scheme is validated by fully atomistic simulations and employed to investigate the behavior of cellulose fibers under representative mechanical loads. Furthermore, a random network of cellulose fibers in micron-scale in the plane under tensile deformation is simulated by CG scheme, a simulation task prohibitive for atomistic modeling. The CG simulation of such a random network of cellulose nanofibers offers crucial insights on the in-situ deformation and failure mechanisms of cellulose nanopaper under tensile loading, which are challenging to observe in experiments. Parametric study using CG simulations reveals the dependence of tensile strength and stiffness of cellulose nanopaper on the length of constituent cellulose fiber and offers quantitative design

guidance of cellulose nanomaterials. The bottom-up and scalable nature of the CG scheme presented in this study might suggest its broader applicability in simulating cellulose-based materials with various feature sizes of material building blocks, which in turn may facilitate the design of cellulose materials with desirable mechanical properties. Incorporating additional functional groups as separate beads at Level-1 of the presented CG scheme to include the effects of other molecules such as hemicellulose and/or considering different ambient conditions (e.g. humidity⁶⁸), and scaling it up till Level-3 may also form a basis for prospective research which may aid in analyzing mechanistic behavior of composite cellulose nanopapers and other cellulose based bulk structural materials⁶⁹, providing us the much needed guidance into design of cellulose based functional materials.

4.7 Application of the developed CG scheme to explain superior mechanics of hybrid, cellulose-based, biodegradable straws

The CG scheme that is described above, was used to study why hybrid straws comprised of nano and micro cellulose fibers possess superior mechanical properties when compared to straws made of only nanofibers or microfibers.⁴⁷ Here, the nanofibers were experimentally characterized and found to be of length ~ 130 nm with 5 nm diameter. Similar length and diameter of the microfiber were ~ 2 -3 mm and 13 μ m, respectively. The following subsection (Section 4.7.1) sheds light on how modeling qualitatively compliments the experimentally obtained mechanical properties), followed by a discussion on what limits the model to predict accurate quantitative values.

4.7.1 CG modeling studies supporting experimental data qualitatively.

The biodegradable straw was made from microfibers from Bagasse which as obtained as a by-product of sugarcane waste, and nanofibers (length - 130 nm, diameter 5 nm), from wood chips (Fig. 4.7). Since this is made from a mixture of both nano and microfibers, the nomenclature of “hybrid fiber” is used. The dimensions of the nanofiber obtained separately by experiments closely match our CG scheme for Level-2. We use that CG level to model nanofibers. The experimental dimensions of the microfiber (order of millimeters) are difficult to model using CG simulations due to constraints in computational resources. So, we use Level-3 scheme to model them and draw a qualitative understanding. The aspect ratio of the fibers matches both the experiments and the model.

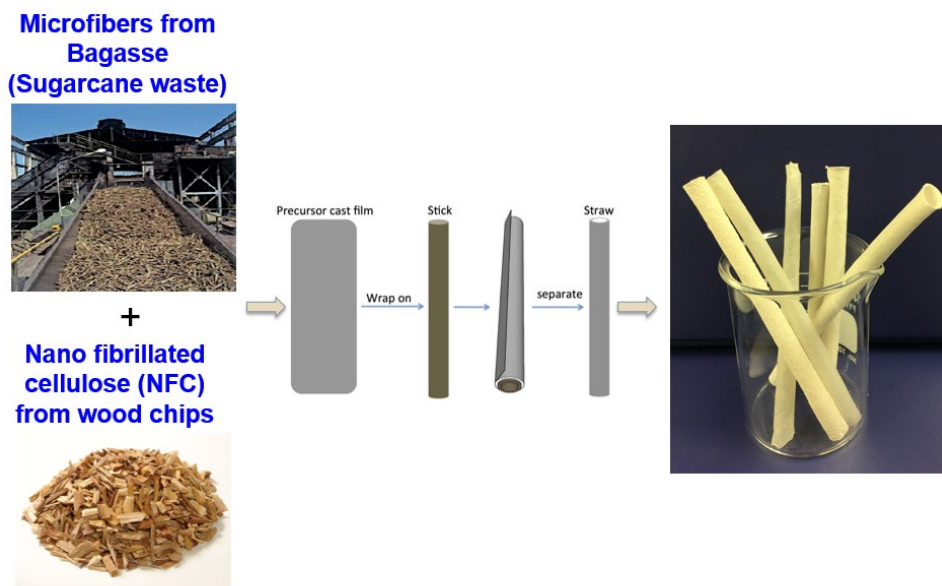


Figure 4.7. Digital image (right panel) of biodegradable straws, made from microfibers and nanofibers (left panel).

In the experiments, the mechanical strength of the nano fibers (~ 57 MPa) is much higher than that of microfibers (~ 5 MPa) (Fig. 4.8a). However, the hybrid fibers (1:1) possessed a higher strength than both the individual fibers (~ 80 MPa). The CG model predicted values of normalized fracture energy which are aligned with the experimental observations (Fig. 4.8b). The specific modeling details along with the explanation of this phenomenon are discussed below.

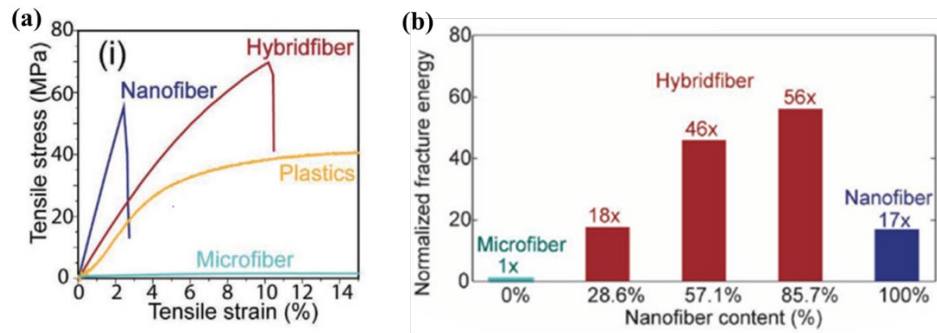


Figure 4.8. CG modeling complementing the experiments (a) Tensile tests of nanofiber, microfiber and hybrid fiber (nano: micro = 1:1 by mass) (b) Modeling plots of normalized fracture energy w.r.t various nanofiber weight %, shedding a qualitative insight of why hybrid fibers possess superior mechanical strength.

The three models (Fig 4.9) are developed using Level-2 and Level-3 of the developed CG scheme, as shown in Fig. 4.9. Here, the key to the modeling is to help understand why the 1:1 (microfibers: NFC) hybrid fiber is mechanically stronger than the straw made only out of Bagasse (micro-fiber) or a straw made only out of NFCs. The length of the “Nano” model fibers is 131.9 nm, and the length of the “Micro”/ “Hybrid” model fibers is 2.010 μm . The hybrid model is built same as micro, but the surrounding fibers are used from the nano model. Non-periodic boundary conditions are applied in all directions and the center fiber is pulled from each of the models. The force of the

pulling fiber versus the pulling displacement are obtained and from there the stress on each of the models are computed.

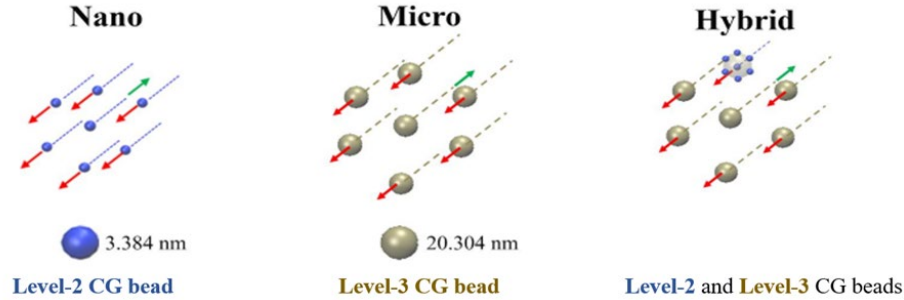


Figure 4.9. Schematic representation of the simulation models for cellulose nanofibers (Level-2 CG beads), microfibers (Level-3 CG beads) and hybrid fibers (combination of Level-2 and Level-3 CG beads).

We obtained the results for nano, micro and hybrid models as in Figure 4.10. We get the maximum strength of nano (Figure 4.10a) and micro (Figure 4.10b) fibers to be around ~ 320 MPa and ~ 100 MPa respectively. The strengths for the three hybrid models (Fig 4.10c) increase with the increase in nanofiber content. We propose that in the nanofibers, there is more density of hydrogen bonds than in micro. So, the breaking and reforming of H-bonds with the pulling out of fibers increase in nano fibers, thus delaying their failure. This phenomenon occurs much less in microfibers because of the less H-bonds interactions happening among neighboring fibers due to size effects. Thus, for hybrid fibers, their strength can be tuned with incorporation of more nanofibers. It is this mechanism that renders the hybrid mechanically stronger than pure nano and micro-fibers.

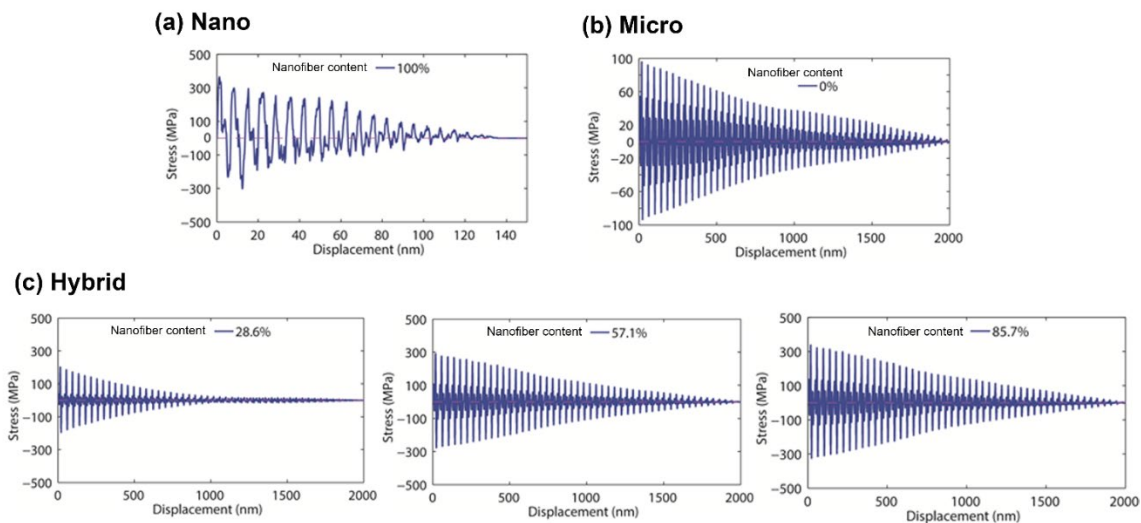


Figure 4.10. Stress (MPa) versus the pulling-out displacement (nm) results predicted by the CG models.

(a) shows the nano model, (b) shows the micro model and (c) shows the hybrid models with varying % of nanofibers

4.7.2 Limitations and Outlook

The CG modeling scheme possesses limitations, which restricts its accuracy for predicting results that are quantitatively comparable to experimental measurements. The reason is as follows. There are a lot of factors in the real experiments that should be put into consideration in computational studies, to enable a condition-matching estimate. For example, the sizes of cellulose microfibrils in the experiment are 2~3 orders of magnitude larger than those in the CG simulation model. In addition, given the limitation of computation expense, the timescale simulated in the model is also very short (in the order of nanosecond), whereas in real experiments, the mechanical properties are measured over the timescale of seconds or minutes. These intrinsic difficulties and complexities related to modeling need to be overcome to completely match with the experimental conditions. Nevertheless, the qualitative understanding

delineated by the model in Fig. 4.10 suffices in revealing the fundamental understanding of the strengthening mechanism in hybrid straws.

Chapter 5: Investigating thermal transport and mechanical properties in BNNT/NFC hybrid material⁶

5.1 Introduction

Cellulose, the widely available renewable biopolymer, has recently emerged as an exceptionally promising candidate in sustainable materials design.¹⁻⁶ Nanomaterials based on cellulose nanofibers (NFCs) display an anomalous scaling law of simultaneous increase in strength and toughness,⁷ two mechanical properties which conventionally conflict each other. The reason behind this superior mechanical properties in NFC based nanomaterials stems from its unique morphology that can offer numerous bonding sites (hydrogen bonding and other non-covalent interactions) for functionalization.^{8,9} However, the thermal conductivity (k) of NFCs^{10,11} is relatively low (~ 1.45 W/mK), although it still surpasses that of conventional polymers by approximately six times.¹² Enhancing the thermal conductivity of NFC based materials¹³⁻¹⁵ through noncovalent functionalization may open up opportunities to develop composites possessing appealing thermo-mechanical properties.

On the contrary, single-walled boron nitride nanotubes (BNNTs)¹⁶⁻¹⁸ hold great potential as fillers for developing advanced thermal management materials due to their high thermal conductivity (~ 400 W/mK) and thermal stability up to temperatures around 800°C. However, reproducing the remarkable properties of BNNT to bulk is the primary challenge. Recent advancements have overcome some initial obstacles in

⁶ The main findings of this chapter are listed here for archival publication and a manuscript describing these findings has been submitted (as in October 2023) to a peer-reviewed journal.

fabricating pure BNNT films through novel methods such as gram-scale fabrication promoters¹⁹ and scalable techniques involving dissolving BNNTs in acids.²⁰ Nevertheless, bulk form of BNNT films still exhibits relatively low values of k at 18 W/mK.²¹ Furthermore, hybridizing BNNTs with polymers to fabricate composites continues to yield values of k less than 5 W/mK,^{22,23} which might be insufficient for applications requiring high thermal conductivity.

The primary challenge to achieve high thermal conductivity in BNNT filler-based polymer composites is overcoming the interfacial thermal resistance between adjacent BNNTs, which may lead to aggregate formation. Research efforts have been undertaken to address this issue by functionalizing BNNTs with polymers such as PVA,^{24,25} ether imides,²⁶ and epoxy resins.²⁷ To this end, NFCs have emerged as a potential biopolymer to effectuate non-covalent hybridization with BNNT fillers and enhance the thermal conductivity of the resulting material. For instance, in NFC/BNNT based materials, k was found to increase significantly to approximately 20.9 W/mK, representing an improvement of around 14.3 times compared to conventional polymers.²⁸ In a separate study, a BNNT/NFC based nanocomposite was found to demonstrate high value of k (~ 21.39 W/mK)¹² due to reduced interfacial resistance facilitated by the strong interactions between NFCs and BNNTs. However, there is currently no systematic study explaining why the incorporation of BNNTs into NFC-based materials increase k ; this gap may be attributed to the difficulty in conducting characterization experiments at length scales below 10^{-10} m. A modeling-driven research approach could bridge this gap and is therefore the focus of our present investigation.

In this study, molecular dynamics (MD) simulations are employed to investigate the thermal conductivity enhancement in nanocellulose-based materials due to the incorporation of BNNTs. Reverse non-equilibrium molecular dynamics (RNEMD) technique is utilized to compute k , while the vibrational density of states (DOS) analysis helps in identifying the phonon modes responsible for efficient heat transfer. Furthermore, the synergistic combination of NFCs and BNNTs increasing the mechanical properties in derived hybrid structures, is explored. This modeling-based approach aims to inspire sustainable materials design for NFC/BNNT composites with exceptional mechano-thermal properties.

5.2 Molecular Dynamics Methodology

The MD simulations reported in this article have been carried out using the parallelized, open-source package LAMMPS.^{29,30} The empirical reactive force field ReaxFF^{31,32} that can capture the atomic interactions of complex reactions through bond-order details has earlier been found suitable for Boron-Nitride/Cellulose based systems,³³ and hence applied in this study. Periodic boundary conditions are imposed in all directions. The time step for all the simulations is 0.5 fs. All the models are built in a way that the unsaturated dangling bonds at the boundaries are terminated by adding -H atoms. Equilibration of the models are performed to achieve a global temperature of ~300K and pressure ~1 atm using Nose-Hoover isothermal-isobaric (NPT), canonical (NVT) and microcanonical (NVE) ensembles for a total time of 3.5 ns, in absence of any external constraints.

The thermal conductivity (k) is computed using the RNEMD method proposed by Müller-Plathe.³⁴ The equilibrated model is numerically divided into spatial bins along their length L , which is also the heat transport direction ($-z$ axis). Kinetic energies are swapped every 150 fs between the “hot” (middle) bin and the “cold” (two ends) bins, as a result of which a temperature gradient is imposed on the model along $-z$ axis. This continues for a total time of 5 ns to ensure that the system has reached steady state. The energy exchanges are further continued for an additional 1 ns performing time averages every 50 fs to assess the total energy transferred, along with the thermal temperature gradient. The latter is subsequently used to compute k as per the equation:³⁴

$$k = \frac{m \sum v_1^2 - v_2^2}{2t A \frac{dT}{dz}}$$

where the numerator outputs the total kinetic energy exchanges through the simulated structure, t is the total time spent in the energy exchanges, A is the cross-sectional area and $\frac{dT}{dz}$ is the average temperature gradient obtained from the simulations. The cross-sectional area ($-xy$) of the simulation box perpendicular to the heat transfer direction is used to determine A . The temperature gradient ($\frac{dT}{dz}$) along the thermal transport ($-z$) direction is obtained from the arithmetic mean of the two linear regimes in every inverted “V” shaped temperature profile of a simulated model.

To calculate the vibrational density of states (DOS), the simulations are performed after equilibration for an additional 1 ns under the canonical ensemble at 300 K, with atomic trajectories every 50 ps. Each sampled trajectory is then extended by an additional 5 ps, and the atomic velocities are recorded every 0.001 ps. The data is utilized to

compute the time-translation invariance of the mass-weighted velocity autocorrelation function (VACF). The correlation time is set as 4.5 ps. A Fourier-transformed of the overall average VACFs yields the DOS spectra, as described by the following equation:

$$P(\omega) = \frac{1}{\sqrt{2\pi}} \int_0^\infty e^{i\omega t} \left[\sum_{j=1}^N m_j v_j(t) \cdot m_j v_j(0) \right] d\omega$$

where the frequency of vibration is represented by ω , and the mass and velocities of atom j are represented by m_j and v_j , respectively. The resolution of the obtained DOS spectra is 0.061 THz.

The results of the mechanistic studies are obtained by deforming the periodic, equilibrated simulation box at a tensile engineering strain rate of 10^{10} s^{-1} . In the engineering stress-strain plots that are shown, the reported stress is the normal stress component on the simulation box along the tensile loading direction. The entire deformation simulation was carried out for 50 ps with time averages of the engineering stress-strain values performed every 1.0 ps.

5.3 Results and Discussions

To investigate the effect of increasing length (L) of a single NFC molecular chain (Fig. 5.1a) on k , six models of single-chain NFC molecules are constructed with values of $L = 10 \text{ nm}$, 20 nm , 30 nm , 35 nm , 40 nm and 50 nm . A representative temperature profile for the model with $L = 20 \text{ nm}$, obtained by employing RNEMD calculations, is shown in Fig. 5.1b. The cross-sectional area (A) used to compute k is determined as 0.33 nm^2 , which closely matches previous results¹⁴ (0.32 nm^2) obtained from non-equilibrium

MD simulations for a single NFC chain, thus validating the adopted method and force-field. Additionally, the calculated values of k for all NFC molecules are between 0.8 W/mK to 1.69 W/mK, aligns with experimental studies measuring in-plane thermal conductivity values of nanocellulose within the range of 0.6 to 2.5 W/mK.³⁵ On observing the trend of change in thermal conductivity for the six models with varying L (Fig. 5.1c), it is observed that k values increase with an increase in length. The rate of increase tends to decrease after reaching a certain length (~ 35 nm). The enhancement of k with increase in L can be attributed to the phonon scattering. Phonons, that are discrete lattice vibrational elastic waves, serve as major carriers of thermal transport in nanostructures. With an increase in the chain length, phonon transport and scattering increase, raising its mean free path and resulting in the increase of k . To further explore this phenomenon, the vibrational density of states (DOS) (Fig. 5.1(d-f)) is calculated for two NFC chains having $L = 10$ nm (black lines) and 40 nm (red lines). Fig. 5.1d, Fig. 5.1e and Fig. 5.1f denote the total phonon DOS along in-plane heat transport direction ($-z$), out-of-plane $-x$ and out-of-plane $-y$ directions, respectively. First and foremost, all the plots in each direction follow similar pattern indicating similar phonon properties for different lengths of the NFC molecular chains. In a spectrum, low-frequency waves have a higher wave number, and thus a longer range. So, low-frequency peaks (here, ~ 0 -20 THz) are monitored as they represent the dominant vibrational models that cause the change in thermal conductivity. The low-frequency peaks of the vibrational spectra being distributed across 0 THz to 20 THz for NFC molecules have been observed in previous literature.¹⁴ Here, it is observed that the first prominent peak in the low frequency of spectra along the heat transport ($-z$) direction,

occurs at approximately 5.49 THz (Fig. 5.1d) ($1 \text{ THz} = 10^{12} \text{ Hz}$) and 6.04 THz (marked by red arrow in Fig. 5.1d) for NFCs with $L=10 \text{ nm}$ and $L= 40 \text{ nm}$, respectively. This spectral shift towards higher frequency indicates an increase in energy carrying capacity of the phonons as NFC molecule lengths increase, resulting in an enhanced k . Similarly, although less conspicuous, a shift in frequency from low to high with increasing lengths of NFCs is also observed consistently for $-x$ and $-y$ directions that are perpendicular to thermal transport (Fig. 5.1e and Fig. 5.1f).

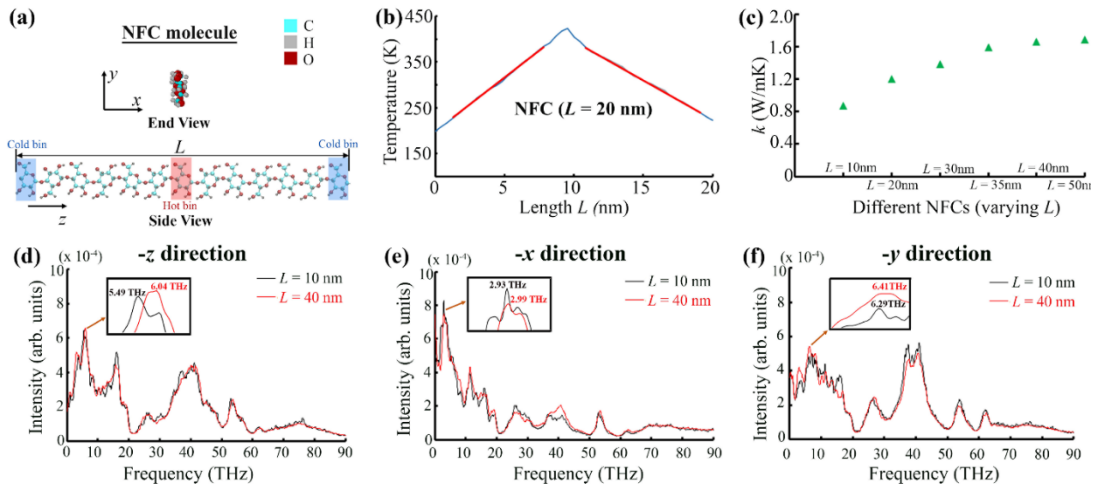


Figure 5.1 (a) Initial model of a cellulose (NFC) molecular chain of length L . Thermal conductivity (k) values of six models with varying L are calculated; (b) Temperature profile (K) of an NFC molecular chain along $-z$, the thermal transport direction. For this profile, $L = 20 \text{ nm}$. The two red lines are the linear temperature gradients, the arithmetic mean of which is used to compute k by RNEMD method; (c) Variation of k (W/mK) with increasing lengths ($L = 10 \text{ nm}$, 20 nm , 30 nm , 35 nm , 40 nm , 50 nm) of NFC molecular chain models; (d-f) Comparison of vibrational density of states (DOS) for two NFC molecular chain models with $L = 10 \text{ nm}$ (black) and 40 nm (red), along the (d) heat transport (z) direction, and the out-of-plane (e) $-x$ and (f) $-y$ directions. All the spectra in (d-f) contains frequency (THz) along X axis and Intensity (arbitrary units) along Y axis.

In addition to individual NFC molecular chains, the variation of k in single-walled BNNTs with increasing nanotube length (L) (Fig. 5.2a), is also investigated. BNNTs are constructed with chirality (10, 10) and different values of $L = 10$ nm, 20 nm, 30 nm, 40 nm, 50 nm and 60 nm. The temperature profile obtained from RNEMD simulation of the BNNT having $L = 20$ nm, is shown in Fig. 5.2b. It is observed that the k in BNNTs increases with the increase of L (Fig. 5.2c), but the increase rate diminishes beyond a certain L (~ 40 nm). Furthermore, for a BNNT with $L = 20$ nm, the calculated k value is found to be approximately equal to 98.47 W/mK, which reasonably matches well with the range of 110-130 W/mK predicted by previous MD simulations³⁶ for a BNNT(10, 10) at 300 K. To identify the vibrational modes influencing thermal transport in BNNTs of variable lengths, total phonon DOS spectra along three perpendicular directions are compared for two BNNTs with $L = 10$ nm (black lines in Fig. 5.2(d-f)) and $L = 40$ nm (red lines in Fig. 5.2d-f). The DOS spectra of these nanotubes along thermal transport (-z) direction and out-of-plane transverse directions (-x and -y) are shown in Fig. 5.2d, Fig. 5.2e and Fig. 5.2f, respectively. Each spectrum along a specific direction (-z or -x or -y) exhibits a reasonably comparable shape for BNNTs with increasing lengths. This indicates similar phonon properties along directions having similar morphology. It is also to be noted that for BNNTs the phonon spectra along -x and -y directions are also closely similar to each other, an observation absent in NFCs discussed in Fig. 5.1. This is probably because for the NFCs, the cross-sectional directions (-x and -y as in Fig. 5.1a) are not alike. However, for BNNTs, the -x and -y directions represent the two perpendicular axes across the nanotube circular cross-section (-xy plane) that are indistinguishable from each other. Hence, the atom vibrations driving the thermal

transport across those two planes are comparable. The discrete lattice waves (phonons) because of those vibrations are thereby similar. For the BNNTs, the in-plane vibrational modes along heat transfer ($-z$) direction are distributed across at a relatively high frequency in the range of 26.4 THz to 37.1 THz (Fig. 5.2d) and thus contribute less to thermal transport. For the BNNTs, the dominant, low-frequency peaks representing the out-of-plane transverse vibrational modes are illustrated by black (for BNNT with $L = 10$ nm) and red (for BNNT with $L = 40$ nm) fonts in Figs. 5.2(e-f). For the BNNT with $L = 10$ nm, low-frequency peaks are at 13.3 THz along $-x$ (Fig. 5.2e) and at 12.8 THz (Fig. 5.2f) along $-y$ directions. The corresponding peaks for the BNNT with $L = 40$ nm are 13.9 THz along $-x$ and 13.1 THz along $-y$. A comparison of the DOS plots of the two BNNTs along $-x$ and $-y$ directions when the nanotube length increases from 5 nm to 40 nm, thus clearly reveals a spectral shift towards high frequency. A shift to higher frequency in the vibrational spectra implies increased phonon energy carrying capacity. This indicates greater phonon-phonon scattering which is responsible for amplifying the value of k as the L in BNNTs increase.

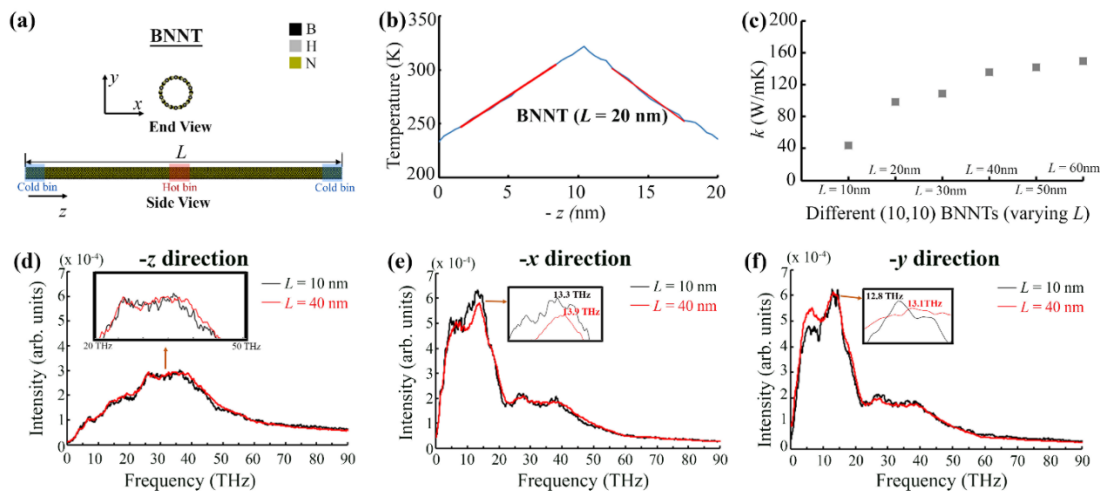


Figure 5.2 (a) Initial snapshot of a (10,10) BNNT model having length L . k values for different models

with increasing L is computed; (b) A plot of a temperature profile (K) of a BNNT model having $L = 20$ nm along its length, which is also along $-z$, the heat transport direction. The two red lines are the linear temperature gradients, and their mean is used to compute k by RNEMD method; (c) Variation of k (W/mK) in BNNT models having different lengths ($L = 10$ nm, 20 nm, 30 nm, 40 nm, 50 nm, 60 nm); (d-f) Comparison of vibrational density of states (DOS) (intensity (arbitrary units) along Y axis and frequency (THz) along X axis) in two BNNT models having lengths $L = 10$ nm (black) and 40 nm (red)} along the (d) heat transport (z) direction, and the out-of-plane (e) $-x$ and (f) $-y$ directions.

After the evaluation of k in pure NFC molecule and pure BNNT, the study is extended to a hybrid-based NFC/BNNT, to investigate the effect of incorporation of BNNT on k values of NFC based materials. To achieve this, three molecular models with similar combined weight content of NFCs and BNNTs are constructed for comparison. Each NFC chain and BNNT in the three models have lengths of approximately 38 nm and 40 nm, respectively, due to the diminished increase of the rate of k beyond those lengths, as previously demonstrated in Fig.5.1 and Fig. 5.2. The models are labeled as “100% NFC”, “0 % NFC” and “50% NFC”, where “ X ” in “ X % NFC” denotes the weight content of NFC in the model. The “100% NFC” model consists of 14 aligned NFC molecular chains, with its end (top panel) and side (bottom panel) views shown in Fig. 5.3a. The “0% NFC” model comprises two aligned (10, 10) BNNTs and their end (top panel) and side (bottom panel) views are displayed in Fig. 5.3b. Lastly, the “50% NFC” model consists of the hybrid, where one middle BNNT is surrounded by seven NFC molecular chains, as demonstrated in Fig. 5.3c (end view - top panel; side view - bottom panel). The “100% NFC”, “0% NFC” and “50% NFC” models contain 22358, 12880 and 17619 atoms, respectively. The temperature profiles, obtained from RNEMD simulations, for each of the “100% NFC”, “0% NFC” and “50% NFC”

models are shown in Fig. 5.3d, Fig. 5.3e and Fig. 5.3f, respectively. The lowest value of k is observed for pure NFCs ("100% NFC model") at 0.746 W/mK (Fig. 5.3g). It is noteworthy that k for a single NFC molecular chain was higher ~ 1.66 W/mK, as discussed in Fig. 5.1c. However, when NFC molecules with identical lengths form a bundle (Fig. 5.3a), k decreases due to the higher phonon scattering between the neighboring molecular chains, which has been previously observed in cellulose¹⁴ and other polymers.³⁷ On the other hand, the highest value (~ 68.29 W/mK) is obtained for the pure BNNT ("0% NFC" model), as shown in Fig. 5.3g. Interestingly, it can be concluded that enhancing thermal transport in NFC-based materials by taking advantage of the high individual thermal conductivity values exhibited by BNNTs is indeed possible. This is because introducing BNNT into the NFC structures increased k from 0.746 W/mK ("0% NFC" model) to 24.38W/mK ("50% NFC" model) (Fig. 5.3g).

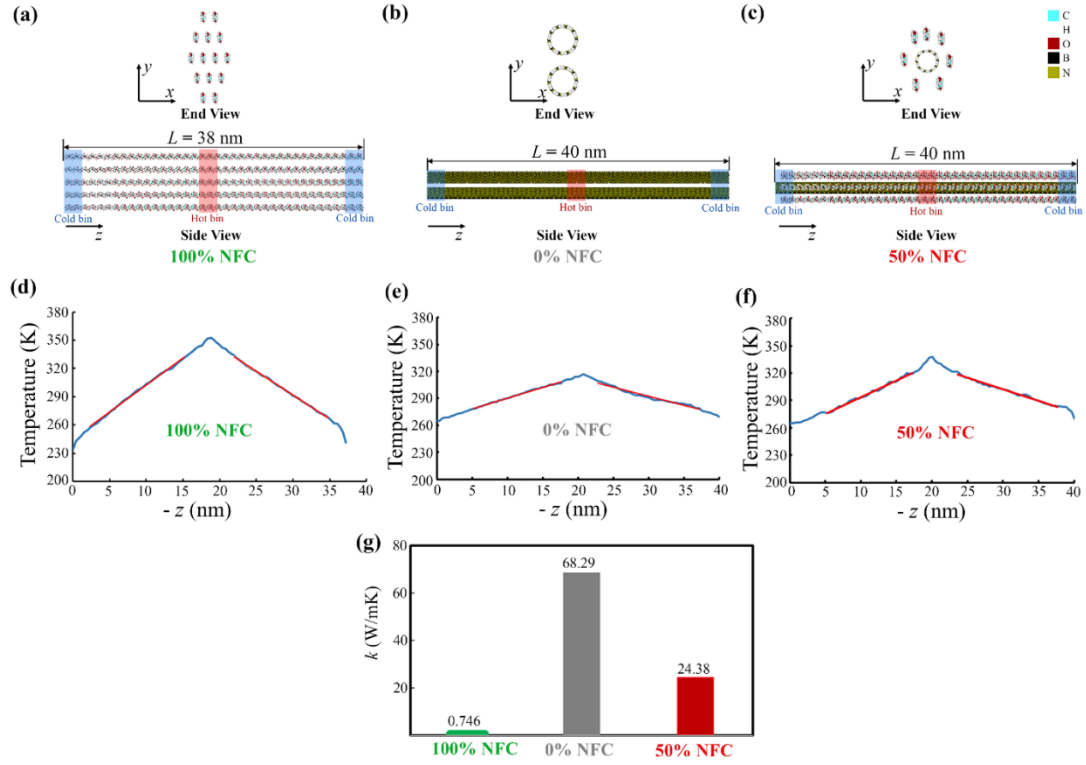


Figure 5.3 Comparison of k (W/mK) in three different models (“100% NFC”, “0% NFC” and hybrid (“50% NFC”)) having similar weight content; (a) Initial snapshot of a pure cellulose model (“100% NFC”) that is used to compute k by plotting the (d) temperature profile (K) along (here, $L = 38$ nm) the thermal transport ($-z$) direction; (b) Snapshot of a pure BNNT model (0% NFC) used to compute k by plotting the (e) temperature profile (K) along (here $L = 40$ nm) the heat transfer ($-z$) direction; (c) Initial snapshot of a hybrid NFC-BNNT model with $\sim 50\%$ weight content of BNNTs (“50% NFC”) and (f) its temperature distribution (K) along the thermal transport ($-z$) direction ($L = 40$ nm); Two red lines in each of the plots (d-f) are the linear temperature gradients used to compute k by RNEMD method (g) Comparison of k for the three different models {“100% NFC” (green), “0% NFC” (gray) and “50% NFC” (red)} elucidating the effect of addition of BNNT on the thermal transport of the NFC-BNNT hybrid.

To elucidate the phonon modes responsible for the increase in k upon incorporating BNNT into NFC-based materials, the vibrational density of states is computed for three models: “100% NFC”, “0% NFC” and “50 % NFC” models. The DOS spectra were

calculated along perpendicular directions ($-x$, $-y$, $-z$), as depicted in Fig. 5.4a (“100% NFC”), Fig. 5.4b (“0% NFC”) and Fig. 5.4c (“50% NFC”). Fig. 5.4d shows the DOS spectra of the three models along the thermal transport direction ($-z$), while the spectra across the out-of-plane directions are shown in Fig. 5.4e ($-x$ direction) and Fig. 5.4f ($-y$ direction). Consistent color coding is employed for plot lines representing different models (green for “100 % NFC”; gray for “0% NFC” and “red” for “50% NFC”). On comparing the DOS plots along each direction, it is evident that pure BNNTs (“0% NFC” model) facilitate thermal transport through transverse, out-of-plane vibrational modes ($-x$ wise and $-y$ wise). This can be attributed to their low frequency (~ 0 -20 THz) phonon modes which significantly influence k ; these modes exhibit peaks at approximately 14.3 THz (Fig. 5.4e) along $-x$ and around 14.2 THz (Fig. 5.4f) along $-y$ directions, respectively. It is plausible that these two out-of-plane modes predominantly contribute to enhancing k values in BNNTs. However, in the case of pure NFCs (“100% NFC” model), the thermal transport is governed by in-plane ($-z$ wise) vibrational modes, as evidenced by the low-frequency spectral peak at ~ 6.17 THz (Fig. 5.4d). On incorporation of BNNT into NFCs, the corresponding peak shift from 6.17 to 7.14 THz for the hybrid, as indicated by the red line in Fig. 5.4d. This shift towards high energy and frequency denotes higher phonon energy carrying capacity in the hybrid, that ultimately bolsters their k value. When comparing the transverse directions of the three structures to assess the impact of incorporating BNNT, it is observed that the analogous low-frequency peaks exhibit a subdued intensity. The maximum intensity is observed for BNNTs, while the minimum intensity is observed for NFCs, with the hybrid peak intensity in between. For instance, upon examining Fig. 5.4f, it can be noted that the

low-frequency peak for NFC occurs at approximately 11.2 THz with an intensity of around 3.41×10^{-4} units. The hybrid exhibits a peak at a similar frequency (~ 13.8 THz) with a relatively higher intensity of 4.29×10^{-4} units. In comparison, the BNNT peak at ~ 14.2 THz demonstrates a maximum intensity of ($\sim 5.62 \times 10^{-4}$ units). The same phenomenon is also observed prominently in other lower frequency vibrational crests (~ 20 THz) along both $-x$ (Fig. 5.4e) and $-y$ (Fig. 5.4f) directions. For the pure NFCs, the spectral intensity is diminished due to the mobility and sliding of NFC molecular chains along all degrees of freedom when heated, resulting in a higher state of disorder in the molecular domain. The introduction of crystalline BNNTs into NFCs leads to a reduction in this disorder. This explains why the corresponding spectral peak for the hybrid material is higher than that observed in pure NFCs. Furthermore, the peak intensity in BNNT is the highest due to their crystalline nature, which helps mitigate disorder compared to other materials. This, combined with the enhanced energy-carrying capacity of phonons, could potentially account for the increase in thermal conductivity when incorporating BNNTs into NFC structures.

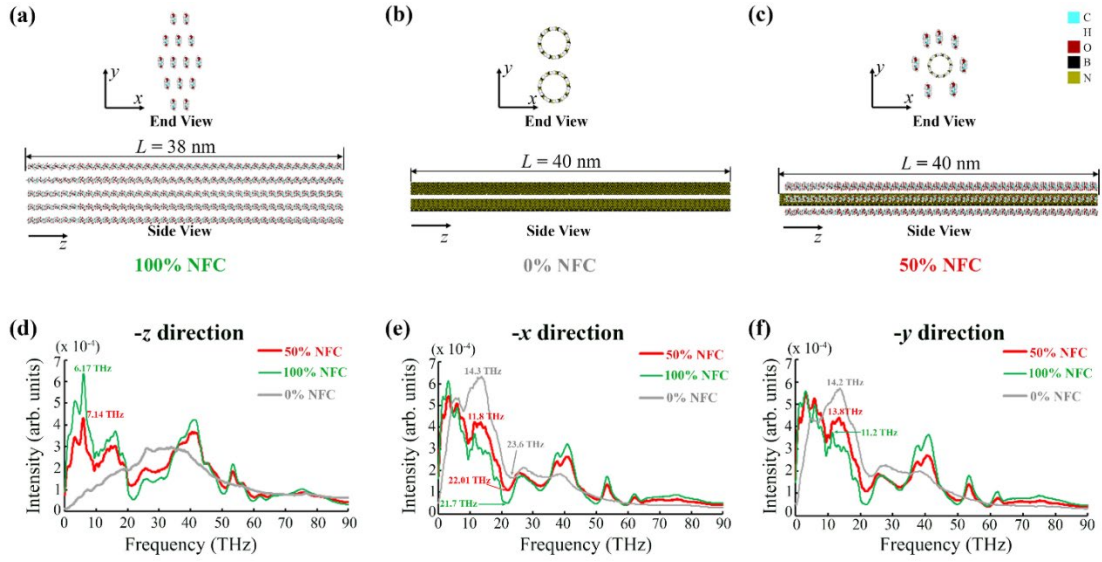


Figure 5.4 (a-c) Initial snapshots of the three models – (a) “100% NFC”, (b) “0% NFC” and (c) “50% NFC”, which are used to compute the total phonon vibrational density of states (DOS); (d-f) DOS plots along the (d) heat transfer direction ($-z$) and the out-of-plane (e) $-x$ and (f) $-y$ directions, revealing the effect on incorporation of BNNT on the pure NFC based (100% NFC) system. Intensity (arbitrary units) is denoted along the Y axis and frequency (THz) is plotted along X axis. Plot lines for the different models are color schemed. All the DOS plot lines in (d-f), obtained for the “100% NFC”, “0% NFC” and “50% NFC” models, by colors green, gray and red, respectively.

The mechanical properties of structures with the same constituent fiber lengths (NFC~38 nm and BNNT~40 nm) as those used to investigate thermal conductivity previously, are further examined. The objective is to assess the mechanical properties of the NFC/BNNT based hybrid in comparison to pure NFC and BNNT structures. In this study, four similar models are constructed: "0% NFC" (pure BNNT), "50% NFC" (NFC: BNNT=1:1 by weight), "60% NFC" (NFCBNNT=3:2 by weight), and "100% NFC" (pure NFC). The hybrid models are created with comparable weight contents as employed in experimental studies for related materials^{23,38–41} The “0% NFC”, “50% NFC”, “60% NFC” and “100% NFC” models contain 25760, 35238, 48014 and 44716

atoms, respectively. The initial simulation snapshots of three representative models “0% NFC”, “60% NFC” and “100% NFC” are demonstrated in Fig. 5.5a, Fig. 5.5c and Fig. 5.5e, respectively. The initial structures are placed starting randomly in a linear fashion (along tensile loading direction as indicated by red arrows in Figs. 5.5(a,c,e)). Periodic boundary conditions are applied across all dimensions to ensure that each molecule emerging from one end of the simulation box is mapped onto the opposite end. For the “0% NFC” model, there are four (10,10) BNNTs (Fig. 5.5a), each approximately 40 nm in length. The “50% NFC” and “60% NFC” (Fig. 5.5b) consist of 14 and 22 NFC molecular chains, with a length of ~ 38 nm, surrounded by two BNNTs each having length of ~ 40 nm. For the “100% NFC” model (Fig. 5.5c), there are 28 molecular chains of aligned NFCs, with a length of ~ 38 nm. The initial distance between each molecular chains and nanotubes before equilibration is kept consistent at 6 Å. Snapshots corresponding to tensile loading for the different models are presented in Fig. 5.5b, Fig. 5.5d and Fig. 5.5f for 0% NFC, 60% NFC and 100% NFC model, respectively. Consistent with previous findings,⁴² it is observed that the failure happens predominantly by inter-fiber sliding. The NFCs stick to the BNNTs in the hybrid due to strong interactions between them and are more mobile (protruding across the ends, as in Fig. 5.5d) than the BNNTs during the tensile deformation.

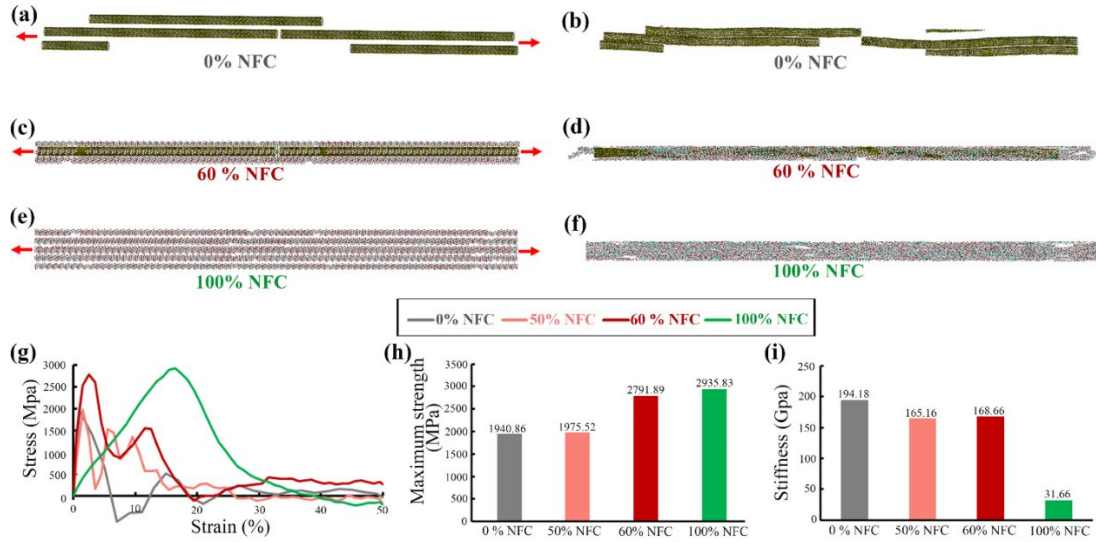


Figure 5.5 A comparison of mechanical properties (maximum strength, stiffness) with varying weight content of NFCs (“0% NFC”, “50% NFC”, “60% NFC” and “100% NFC”) in the NFC/BNNT models. Total weight content for each model is kept same; (a-f) Simulation snapshots of three representative models (“0% NFC” in (a,b); “60% NFC” in (c,d) and “100% NFC” in (e,f)) are shown before (a,c,e) and after (b,d,f) tensile deformations. Tensile loading directions are shown by red arrows in (a), (c) and (e); (g) Plots reporting the engineering stress (MPa)-strain (%) values for the four models (gray for “0% NFC”, light red for “50% NFC”, red for “60% NFC” and green for “100% NFC”); (h-i) Comparison of (h) maximum strength (in MPa) and (i) stiffness (in GPa) for the four models as obtained from the stress-strain plots, demonstrating the synergistic effect of NFC and BNNTs in enhancing the mechanical properties of the NFC-BNNT hybrid material.

An engineering stress-strain graph is plotted in Fig. 5.5g to confirm that NFCs play a dominant role in increasing the mechanical strength of the NFC/BNNT composite. Pure BNNTs exhibit the lowest maximum strength (“0% NFC” model; gray lines in Fig. 5.5g and Fig. 5.5h) at ~1940.86 MPa. On introducing NFC to 50% wt. content (total wt. remaining same as the “0% NFC” model), the maximum strength increased to ~1975.522 MPa (“50% NFC” model shown by “light red” lines in Fig. 5.5g and Fig. 5.5h). On further increasing the wt. content of NFCs to ~60%, the maximum strength

increased to ~ 2791.89 MPa (“60% NFC” model displayed by “dark red” lines in Fig. 5.5g and Fig. 5.5h). Notably, the structure with pure NFCs (“green” lines in Fig. 5.5g, Fig. 5.5h) demonstrated the highest maximum tensile strength at ~ 2935.83 MPa, which is comparable to recent modeling-based investigations.⁴³ The increase of maximum tensile strength due to the presence of NFCs in the composite is mainly because under tensile deformation, inter-fiber sliding occurs and the NFCs undergo repetitive events of intermolecular hydrogen bonds breaking and reforming. This delays the tensile failure in the resulting material. In contrast, structures based on pure BNNTs (“0% NFC” model) lack such morphology-dependent events, have a much faster failure rate and consequently lower tensile strength. This is further evident from the fact that in pure NFC (“100% NFC” model, green lines in Fig. 5.5g), the maximum strength is reached at a strain of $\sim 16\%$, in comparison to $\sim 1\%$ strain for “0% NFC” structure and at $\sim 1.5\%$ strain for the hybrid composites (“50% NFC” and “60% NFC” models). However, the stiffness (Fig. 5.5i) of pure NFCs (“100% NFC” model) is calculated to be ~ 31.66 GPa (comparable with experimental results ~ 23.9 GPa⁴⁴), which was much lower than that of pure BNNTs (~ 194.18 GPa as obtained from “0% NFC” model). In comparison to pure NFC structures, the stiffness of the hybrids was found to be much higher at 165.16 GPa and 168.66 GPa for the “50% NFC” and “60% NFC” structures, respectively. This indicates that the presence of BNNTs, which individually have higher stiffness ranging in the orders of GPa to TPa (~ 0.5 - 1.5 TPa⁴⁵⁻⁴⁷), imparts elevated stiffness to the hybrid. The NFCs adhere to the BNNTs in the hybrid materials, thereby increasing the stiffness of the composite compared to pure NFC-based structures. Hence, both BNNTs and NFCs play a mutually beneficial role in

improvement of mechanical properties. While BNNT contributes to increased stiffness, NFCs predominantly upgrades the strength, resulting in a high-strength and high-stiffness material. Therefore, the combination of NFC/BNNT serves as an ideal choice for applications requiring superior mechanical properties and enhanced thermal conductivity due to their synergistic effect in improving thermo-mechanical properties.

5.4 Conclusion

In summary, the fundamental understanding behind the role of boron nitride nanotubes incorporated into nanocellulose based materials to elevate thermal conductivity, is delineated. The thermal conductivity of pure nanocellulose structures, investigated using reverse molecular dynamics simulations, was found to be quite low at ~ 0.746 W/mK. On introducing boron nitride nanotubes by 50% wt. content in the nanocellulose/boron nitride composite, the thermal conductivity increased to ~ 24.38 W/mK. Furthermore, the phonon vibrational density of states for the composite were compared with pure boron nitride nanotube and pure cellulose structures having equivalent total weight, in a effort to identify the primary phonon vibrational modes driving the thermal transport in the nanocellulose based hybrid material. The individual roles of cellulose nanofibers and boron-nitride nanotubes in increasing mechanical properties (e.g., tensile strength, stiffness) of the derived hybrid material, are also discussed. In summary, the maximum tensile strength of the pure boron nitride nanotube structure (0% wt. content of nanocellulose) was observed to be lowest at ~ 1940.86 MPa. But the tensile strength increased to ~ 1975.522 MPa and ~ 2791.89 MPa when the nanocellulose wt. content in the composite increased to 50% and 60%, respectively, emphasizing on the vital role played by nanocellulose in improving the

mechanical strength of the hybrid material. The stiffness of the pure nanocellulose material, however, was much lower at ~31.66 GPa when compared with pure boron nitride nanotube (~194.18 GPa) structure. But for composites having 50% and 60% wt. content of nanocellulose, the stiffness was found to be 165.16 GPa and 168.66 GPa, respectively. This insinuates that while nanocellulose is playing a crucial role in increasing the mechanical strength, boron nitride nanotubes impart higher stiffness to the composite. This research is expected to encourage the materials science community fabricate composites based on cellulose and boron nitride nanotubes, and obtain novel, functional materials having increased thermal conductivity and superior mechanics. Such novel hybrids might be utilized in numerous lucrative future applications,^{48–56} pertaining to the domain of separators, flexible electronics, sensing and thermal management.

Chapter 6: Summary and significance of conducted research

6.1 Overview

This chapter summarizes the research outlined in this thesis with a focus on the general significance of the major findings. It is categorized into a few sections. Section 6.2 states the novelty of the two experimental research undertaken (as described in Chapter 1), which serves as a motivation for the rest of this thesis. Section 6.3 highlights the primary aim for including the state-of-the-art mechanics design strategies of cellulose-based materials, in Chapter 2. Section 6.4 reports the novelty of the molecular simulations that were applied to shed light on fundamental mechanisms influencing mechanical properties of cellulose/carbon-nanotube microfiber and elastic wood. Section 6.5 underlines the significance of the multi-scale coarse-grained scheme developed to study processes that transpire at length scales much higher than the nanometer-level. Section 6.6 outlines the significance of the investigation on the mechanics and thermal transport of cellulose nanofiber/boron-nitride hybrid. Section 6.7 educates readers on the logic behind shortlisting the idea of engineering intermolecular bonds to obtain programmable material properties, as one of the main avenues of future work.

6.2 Novelty of the experimental research presented in Chapter 1

The primary source of motivation for conducting the modeling-intensive research presented in this thesis came from the remarkable mechanical properties which we obtained in two novel cellulose-based functional materials. These materials were engineered wood (Section 6.2.1) and cellulose-graphite hybrid (Section 6.2.2).

6.2.1 Engineered wood (Super Wood) fabricated using top-down approach

Here, a ballistic impact testing set-up was designed to evaluate the ability of the densified engineered wood (Section 1.4.1) to withstand damage from crash loading. This was important because the eventual goal is to use this material in the body of green vehicles. If this can be made possible, the vehicle structure will be stronger, but its weight will be reduced appreciably. Subsequently, its fuel efficiency will also increase. That directly correlates with a drop in toxic emissions to the environment. But typically, crash testing in cars is done in big industrial facilities, which was not feasible (and affordable) for us to use on this prototype material. So, the set-up was designed in-house, such that projectiles could be fired on the material at speeds of 120-130 miles/hour, which is typically the speed at which car crashes occur. This low-cost, small-scale test demonstrated that the densified wood could indeed withstand impacts on the scale of crash-loading and has the potential to be implemented on larger-scales. The ballistic test thus played a pivotal role in enhancing this material's comprehensive research and development, which was eventually published in the journal *Nature*.

6.2.2 Cellulose-graphite hybrid made using bottoms-up approach

The novelty of the experimental research related to the fabrication of the cellulose-graphite hybrid (Section 1.4.2) lies in the meticulous steps of polymer formulation. Broadly, TEMPO oxidation treatment (details in Appendix III) of the source cellulosic pulp was done to chemically isolate the cellulose fibers by removing undesired components, such as hemicellulose and lignin. After this, the cellulose solution was subjected to homogenization to strip the thick cellulose fibrils into fibers having smaller diameters. If care was not taken to standardize the selective oxidation treatment, there

would be too much (or lack of) charges in the polymeric network, which can be verified through a Zeta Potential Analysis. Excessive charge will cause repulsion in the molecules and a lack of charge will make the cellulose ineffective to hybridize with graphite in the following step. Then the desired product with good mechanical properties cannot be attained. Furthermore, the pH during the chemical treatment must be monitored and balanced every 30 seconds to avoid an acidic solution, which can hydrolyze the cellulose molecular chains and decrease the degree of polymerization (DOP). For the final material to possess superior mechanical properties, molecular chains with higher DOP are desired. Once these steps were standardized, the cellulose solution was hybridized with graphite through centrifugation and ultrasonication. Then the resulting cellulose-graphite slurry was poured into a mold to dry, and then heat-pressed. The final material possessed high mechanical strength (>700 MPa) and toughness (~ 27.7 MJ/m³). The detailed engineering of the molecules regulated for preparing the slurry thus paved the way for a novel cellulose-graphite composite material. Lightweight, strong, and tough, sustainable materials such as this have great potential for applications in structural and construction industries. This research was published in the journal *Materials Today*.

6.3 Significance of state-of-art mechanics design strategies presented in Chapter 2

Chapter 2 was published as a progress report in the journal *Advanced Materials*. It is meant to be critical and visionary. Over 600 references were studied in detail, and then the applied mechanics design strategies from all of them were broadly categorized under the umbrella of a few common themes. Mechanics design strategies for both cellulose-based materials (structural alteration, alignment etc.) and composites

(interface engineering, topology engineering, structural engineering) were holistically explained, along with remarks emphasizing why these studies are crucial to the materials science community. The intention is to establish a knowledge base so that future researchers can educate themselves and then formulate their own research ideas.

6.4 Novelty of the research on cellulose-based materials using MD simulations included in Chapter 3

Chapter 3 contains our research using MD simulations to explain the remarkable mechanical properties in two different types of materials. They are cellulose/carbon-nanotube microfibers (Section 3.1) and elastic wood (Section 3.2). Section 3.1 shed insight on why the materials design strategies facilitating alignment in molecules of cellulose and functionalized carbon nanotube, help achieve better mechanical properties in the hybrid microfiber. The dominance of intermolecular hydrogen bonding that is demonstrated through this modeling-based research can later be extended to equivalent materials building blocks, too. Section 3.2 explains how the often-overlooked molecular water, along with the numerous small fibrils interconnecting the channels of elastic wood, aid in material recovery, after being subjected to compression. Materials such as strong microfiber, that are also electrically conductive, could have multiple potential applications in wearable electronics and textiles. This elastic wood is also a good insulator and can be implemented in future applications like artificial muscle and sensors. These research efforts were published in the journals *Small Methods* and *ACS Nano*, respectively.

Even though they are separate investigations, they eventually fit into the bigger picture constituting the development of next-generation devices and creating positive impact in society. One possible path can be as follows. Different companies, such as LTA Research and Hybrid Air Vehicles are now actively engaged in making giant airships. Airships were seldom used after the 1960s but are now coming back. The idea is to utilize them in disaster relief missions, where airplanes cannot penetrate and/or land. Their service can also be exploited in the tourism industry. The fact that they are lightweight, quiet and produce close to zero emissions makes them a very lucrative candidate for such humanitarian missions. Now the material for the outer covering of the airship needs to be a lightweight, strong textile material that can block UV rays. Cellulose based textile materials, such as the microfiber described in this section, can be a good candidate. In addition, the lifting gas for airships is typically Helium, the level of which is regularly monitored during flight by using a sensor. Insulating materials such as the ultra-compressible, elastic wood described here can be a good option for this kind of sensor. It is acknowledged that a balance of multiple other parameters (creep, stiffness, elevated temperature, stability, cost etc.) needs to be ticked off for their effective use as a unified whole. But hopefully, this example will provide the readers with a flavor of how these individual materials can complement each other to help a sustainable product come to life.

6.5 Novelty of the multi-scale coarse-grained model listed in Chapter 4

The novelty of the multi-scale coarse-grained scheme included in Chapter 4 and published in the journal *Cellulose*, lies in the fact that it can be utilized to analyze the failure mechanisms of cellulose nanopaper (Section 4.5) that are difficult to visualize

in experiments. Furthermore, the random network model that was built as a reasonable estimate of a cellulose nanopaper contains 267,696,576 atoms. Such a scale is cost prohibitive when only fully atomic simulations are applied. The versatility of the CG scheme has also been shown by using three models to demonstrate why mechanical properties of hybrid materials (combination of nano and micro-fibers) can be more appealing than equivalent materials mainly possessing just smaller (nano) or larger (micro) fibers. In real-world scenario any cellulosic material will contain fibers of various sizes ranging from nanometers (molecular chains) to micrometers (microfibrils). So, this scheme opens research pathways to study those kinds of practical systems which contain fibers having different sized diameters. Furthermore, this model can also be extended to address the practical application when surface of cellulose molecules is functionalized. The present CG scheme can be parametrized from an all-atomistic model, comprising of cellulose molecules and their functional groups. In contrast to a molecular cellulose chain at Level-1 in the present CG scheme, a molecular cellulose chain and its functional groups can represent the fundamental building blocks at Level-1 of the proposed CG-scheme. Then the model can be scaled up following a similar methodology starting from the functionalized molecular cellulose chain to the micron-level fibers. This extendibility makes this scheme a robust framework that enriches the mechanical design of cellulose-based materials by providing a qualitative guideline.

6.6 Novelty of research presented in Chapter 5

Cellulose nanofibers (NFCs) have emerged as a preferred choice for fabricating nanomaterials with exceptional mechanical properties, while Boron nitride nanotubes

(BNNTs) have long been favored in thermal management devices due to their superior thermal conductivity (k). In this study, k for a hybrid material based on NFCs and BNNTs is investigated through reverse non-equilibrium molecular dynamics simulations. The result is then compared with pure NFC and BNNT-based structures having equivalent total weight content to elucidate how the incorporation of BNNT fillers enhance k for the hybrid system. Furthermore, by computing the vibrational density of states from Fourier transform analysis of averaged mass-weighted velocity autocorrelation function, the fundamental phonon vibration modes responsible for driving thermal transport in NFC-based materials upon incorporating BNNTs, are identified. Additionally, molecular dynamics simulations are employed to demonstrate how both NFCs and BNNTs synergistically improve mechanical properties (e.g. tensile strength, stiffness) of the constituting hybrid structure. The overarching aim is to contribute towards engineered design of novel functional materials based on nanocellulose that exhibit a simultaneous improvement in crucial physical properties pertaining to thermal transport and mechanics.

6.7 Importance of the future work suggested in the following Chapter 7

So far, this thesis has proffered an in-depth discussion on how to refine the mechanics and fabricate cellulose-based, novel, sustainable materials. However, there are other materials which might also be suitable for selected applications related to mechanics, thermal stability, and electronics. The following Chapter 7 intends to branch out from cellulose and be an instructional report illustrating the readers on these other materials. The common link, however, is the method of engineering intermolecular bonds. In cellulose, discussions were governed by hydrogen bonds primarily. Now, the dialogue

in the following chapter has been extended to other kinds of intermolecular bonds (imine bonds, van der Waals forces, electrostatic interactions etc.), in addition to hydrogen bonding. The intermolecular bonds are significant because of lower bond energy in comparison to primary bonds (covalent bonds, ionic bond etc.). Also, they can form at a wide range of bond angles because of their ability to connect with neighboring molecules at all degrees of freedom across the surrounding three dimensions, a feature absent in primary bonds. Hence, programming material physical properties by engineering intermolecular bonds and designing futuristic, high-performance materials, is gaining a lot of prominence. This article has been published in *Journal of Applied Physics* and listed in the next chapter.

Chapter 7: Possible avenues for future work: Utilizing intermolecular bonding to obtain high-performance materials with programmable physical properties⁷

7.1 Introduction

Bonding between constituent atoms/molecules is crucial in designing engineering materials with desirable properties. Conventional material design strategies by leveraging primary bonding between constituent atoms are well established to design materials such as metals, ceramics, and alloys.^{1–9} Primary bonds can be broadly classified into three types: covalent bonds, ionic bonds, and metallic bonds. Covalent bonds usually occur between atoms of non-metals, such as carbon (Figure. 7.1a), where electrons are shared between neighboring atoms (e.g., the four electrons in the outermost valence shell of a carbon atom). To achieve the energetically favorable configuration (octet), a carbon atom may share those four electrons with one electron from the neighboring carbon atom and three electrons from each of the three surrounding hydrogen atoms, thus forming four different covalent bonds. Ionic bonds (Figure. 7.1b) occur when there is a large difference in electronegativity in neighboring atoms. For example, sodium (Na) possesses just one electron in its outermost shell, and to achieve the stable octet configuration, it donates this electron, thus becoming a positively charged cation (Na^+). On the other hand, chlorine (Cl) possesses seven

⁷ This chapter has been modified from the article which is published as: **A) U. Ray**, Z. Pang, T. Li, “Programming material properties by tuning intermolecular bonding”, *Journal of Applied Physics* 132 (21), 210703, 2022.

electrons in its outermost valence shell. It achieves the energetically favorable configuration by gaining that electron, thus becoming a negatively charged anion (Cl^-). An ionic bond is formed between Na^+ and Cl^- upon the transfer of the valence electron. Metallic bonds are formed when highly electrically conductive metals release their electrons from the inner valence band to the outer conduction band, thus becoming metallic cations (Figure. 7.1c), forming negatively charged free electrons (electron cloud) around them. This attraction between the positively charged metallic cation with the swarm of negatively charged electron clouds forms the metallic bond. Tuning the primary bonds between constituent atoms/molecules has been the focus of engineering materials design to achieve desired physical properties such as high strength, stiffness, toughness, thermal stability, etc. However, such desirable performances come at a price. The upper range for bond energy in primary bonds is relatively high at around 1000 kJ/mol (~ 1000 kJ/mol for covalent bonds, ~ 800 kJ/mol for ionic bonds, and ~ 850 kJ/mol for metallic bonds). On one hand, the high bond energy of primary bonds is the origin of many desirable physical properties of metals, ceramics, and alloys. But on the other hand, it also requires high temperature and enormous energy consumption in processing and manufacturing such materials, which often causes detrimental effects on the environment and poses challenges to sustainability and climate. For example, steel production releases more than 3 billion metric tons of carbon dioxide yearly, accounting for 8% of all human-made greenhouse gas emissions.

Intermolecular bonds, such as hydrogen bonds, van der Waals (vdW) forces, electrostatic interactions, imine bonds, etc., have relatively lower bond energy compared with primary bonds (Figure. 7.1d and 7.1f), the maximum value ranging

around ~ 470 kJ/mol (~ 1 - 190 kJ/mol for hydrogen bonds, ~ 5 - 200 kJ/mol for electrostatic interactions, ~ 1 - 50 kJ/mol for van der Waals forces, and 70 - 470 kJ/mol for imine bonds).¹⁰ So intermolecular bonds can readily form, break and reform under the influence of external forces when two compatible atoms or functional groups are in close proximity to each other. For example, a mechanically robust, self-healing, low-weight polymer can be designed by tuning the cross-linking density, which could rapidly heal multiple times without noticeable deformation.¹¹ This rapid healing is possible because the range of bond length in intermolecular bonds is much higher than the conventional primary bonds (Figure. 7.1d). In addition to the higher bond energy described above, since the range of bond length in primary bonds is smaller, their ability to reform and reconnect decreases considerably. Furthermore, primary bonds need to be formed at a specific range of bond angles in addition to the constraint already imposed by the relatively shorter bond length. Even when the atoms are within the bond length, a primary bond cannot form if the criteria related to the specific range of bond angle are not satisfied. However, intermolecular bonds can form at a wide range of bond angles^{12,13} because of their ability to reconnect at all degrees of freedom with the surrounding molecules across all three dimensions. As a result, unconventional material properties that were previously impossible using solely primary bonds can be realized by tuning intermolecular bonds. For example, the conflict between strength and toughness, which are conventionally two mutually exclusive mechanical properties, could be overcome in cellulose-based materials¹⁴⁻¹⁷ that can achieve both high strength and toughness through design strategies involving spatially dense intermolecular bonds present in the constituent cellulose molecular chains.¹⁸ A long-

standing quandary, the stiffness-toughness conflict, was also recently resolved through physical cross-linking in polymer, implementing a unique application of intermolecular interactions resulting in superb material physical properties.¹⁹ Thus, conceiving novel material design strategies to achieve unconventional yet desirable properties possess promising potential in designing next-generation high-performance materials, which asserts the need to explore the fundamental mechanism behind the strategies related to tuning of intermolecular bonds.

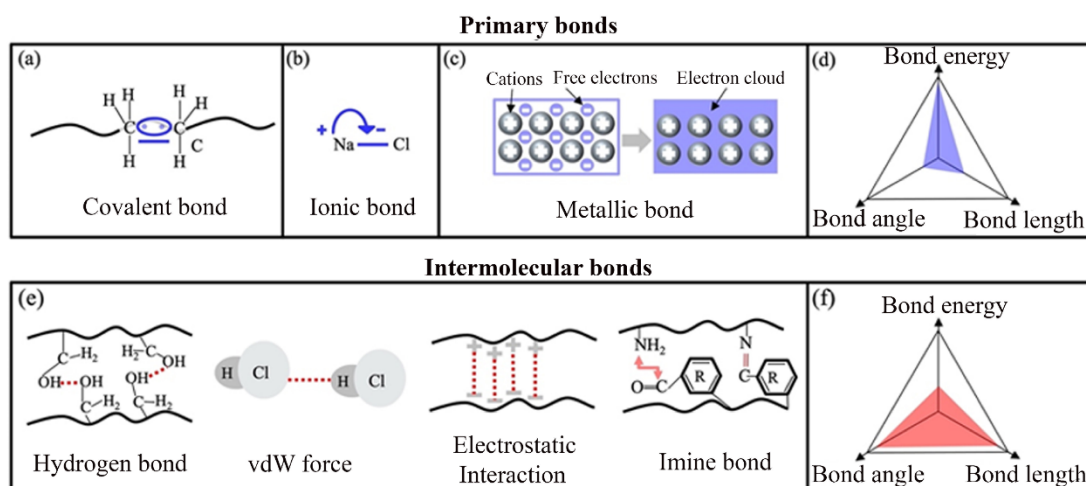


Figure 7.1 Comparison between primary bonds (a-d) and intermolecular bonds (e, f). (a) Covalent bond; (b) Ionic bond; (c) Metallic bond; (e) Selected types of intermolecular bonds such as hydrogen bond, van der Walls (vdW) force, electrostatic interaction, and dynamic imine bond. (d, f) Comparison between primary bonds and intermolecular bonds in terms of bond energy, bond angle, and bond length.

Intermolecular bonds can be broadly categorized into hydrogen bonding, vdW forces, electrostatic interactions, and some dynamic cross-linked bonds in between molecules, such as imine bonds, as illustrated in Figure. 7.1e. The term hydrogen bond was conceptualized as early as 1912²⁰ but imaging evidence of intermolecular hydrogen bonding was first obtained in 2013.²¹ A hydrogen bond is primarily a dipole-dipole

interaction which is formed when a hydrogen (H) is covalently bound to an atom or group having higher electronegativity. This will typically comprise elements such as oxygen (O), nitrogen (N), and fluorine (F). The atoms or groups containing these atoms are considered donors (Do), and the hydrogen covalently bonded to it is denoted by Do-H. When this group (Do-H) comes in proximity with another electronegative atom or groups having a lone pair of electrons (namely the acceptor denoted by Ac), this forms a hydrogen bond, denoted by Do-H---Ac, where the dashed line suggests the presence of hydrogen bond. For example, a hydrogen atom (-H) in a molecular chain (Figure. 7.1e, left schematic) can form hydrogen bonding with the electronegative Oxygen (-O) in a different (intermolecular hydrogen bonding) molecular chain. The energy and the geometry of the hydrogen bond can vary depending on the nature of Do and Ac. It has been proven to exist in DNA,^{22,23} chitosans,²⁴ proteins,²⁵ alcohols (e.g., ethanol, methoxymethane)^{26–28}, natural (e.g., cellulose^{29–31} and synthetic (e.g., nylon, aramid fibers^{32,33}) polymers.

Similar to hydrogen bonding, vdW forces also involve dipole-dipole interactions. However, they are weaker than hydrogen bonds and act between neutral molecules (e.g., HCl as in Figure. 7.1e titled “vdW force”). When neutral molecules come closer within a threshold distance, electrons of one molecule are pulled towards the nucleus of another, thus delocalizing them. When the neutral molecules are within a threshold distance, repulsion occurs, thus maintaining the intermolecular distance. During the vibration or motion of the molecule, this intermolecular interaction may disassociate, causing the electrons to be delocalized. Without vdW forces, molecules would simply drift away from each other, causing a gaseous phase. A prominent example of vdW

forces can be found in graphite, in which graphene layers are held together by weak vdW forces.^{34–36} Typically, vdW forces vary inversely with the distance between the interacting molecules.

Electrostatic interactions, another type of non-covalent intermolecular bonding³⁷ occurs when opposite charges (positive or negative) are separated either due to ionization or incorporation of another ionic species (Figure. 7.1e, schematic titled “Electrostatic interaction”). These interactions might be repulsive (between like charges) and attractive (between opposite charges). For example, metal organic frameworks (MOFs) are positively charged³⁸ when the pH of the solution is lesser than the point of zero charge (*pzc*). Hydrated H_3O^+ ions are present; thereby, the MOFs move towards the negatively charged toxic elements (TEs), resulting in attractive electrostatic interaction. However, when the pH of the solution is greater than *pzc*, the MOFs are negatively charged, whereas the TEs are positively charged, resulting in a repulsive electrostatic interaction. Electrostatic interactions can be much stronger than vdW force and hydrogen bonding. Similar to vdW force, electrostatic interactions are long-range, and the interaction decreases gradually with respect to the distance ($1/r^2$; r is the distance between two charged elements). The electrostatic force is the primary bonding between macromolecules such as MOFs, protein, RNA, DNA, and charged particles. Additionally, the electrostatic force is predominantly influenced by the water, salt concentration, and PH.

Other dynamic cross-linked intermolecular bonds can also occur in composites, and one such example is an imine bond. Imine bonds have bond energies lower than primary covalent bonds but higher than other intermolecular bonds, such as hydrogen

bonds, electrostatic interactions, and π - π stacking.¹⁰ Imine bonds (Figure. 1e, schematic titled “Imine bonds”) are formed through a reversible process when the nucleophilic addition of primary amine ($-\text{NH}_2\text{-R}$) takes place with the carbonyl group ($\text{O}=\text{C-R}$) present in a ketone or aldehyde functional group, followed by proton transfer and acid protonation which results in the formation of the iminium ion ($-\text{N}^+=\text{C-R}$) with the elimination of water. The final stage is the deprotonation of nitrogen to form imine bonds ($-\text{N}=\text{C-R}$), as shown in Figure. 7.1c (schematic titled “Imine bonds”). Some other types of dynamic cross-linked bonds also exist in the form of hydrazone bonds, disulfide bonds, and oxime bonds. These dynamic cross-linked bonds are widely used in materials requiring self-healing properties.^{39,40} For the scope of this review, since the discussion is based primarily on the influence of intermolecular bonds on major physical properties such as thermal stability and material mechanics, the focus of studies related to dynamic cross-linked bonds is primarily placed on imine bonds unless otherwise mentioned.

The rest of this review paper is organized as follows. Section 7.2 describes the corresponding material design strategies leveraging intermolecular bonding. Section 7.3 analyzes the influence of intermolecular bonding on thermal stability and mechanical properties. Section 7.4 describes the applications of the materials that have been fabricated by tuning the intermolecular bonding through the approaches that have been described in Section 7.3. Finally, Section 7.5 concludes with general remarks on the areas that require immediate focus related to this domain, along with the major challenges that call for further attention.

7.2 Material design strategies leveraging intermolecular bonding

Due to the weak and long-range force of these non-covalent bonding, the materials present an outstanding perspective to design and modify the intermolecular interactions, and tailor the properties of materials. Intercalation is the insertion of an ion or a molecule into materials with layered structures, thus increasing the layer spacing and consequently enhancing the physical properties of the bulk material.⁴¹ Typically, it is analyzed by diffraction techniques and/or by measuring electrical conductivity. A classic example of using ion intercalation techniques may be found in graphite. Pang *et al.*³⁵ inserted lithium (Li) ions in between the graphene layers of the bulk graphite and obtained around 7 times increase in the inter-graphene-layer friction than that present in the natural graphite. Seidl *et al.*⁴² analyzed in detail the reversible intercalation of solvated sodium (Na) ions into graphite which may aid in the development of future generation Na-based batteries. The strategies encompassing intercalation are not necessarily limited only to ions. They can also be extended to using polymers as the intercalating agents in metal dichalcogenides such as Molybdenum Disulfide (MoS_2), as demonstrated by Feng *et al.*⁴³ Here, various polymers (e.g., polyethyleneimine and polyethylene glycol) were intercalated into MoS_2 interlayers, thus expanding them. The expanded interlayer, acting as electrodes, had more active sites available for chemical reaction and allowed efficient diffusion of ions back and forth. As a result, the MoS_2 /N-doped carbon heteroagel exhibited ultrahigh capacitance and superior cycling stability. This might be beneficial for implementation in future energy storage devices, thus elevating the importance of novel intercalation strategies.

Another method of subjecting the molecules in a material to different modes of intermolecular bonding is through element or solution replacement and incorporation of functional groups. Element or solution replacement applies to oxidative/reductive chemical reactions by which one element in a molecule is replaced by another. In addition, this may also imply treating the precursor material through a series of experiments involving chemical treatments by alcohol/enzymes followed by sonication, homogenization, and/or centrifugation.^{31,44–47} For example, the TEMPO/NaBr/NaClO oxidation of native celluloses in water^{48,49} under suitable conditions will oxidize the C6-primary hydroxy groups ($-\text{CH}_2\text{OH}$) present on crystalline cellulose microfibril surfaces to sodium C6-carboxylate groups ($-\text{NaCOOH}$). As a result, there is more repulsion in the molecules which stabilizes the structure, and the resulting solution becomes well dispersed. This solution can be used as a precursor and, when hybridized with effective functional groups, may lead to the development of multiple promising high-tech materials used as filaments for osmotic energy conversion,⁵⁰ 3D printing ink,⁵¹ high-performance separators for lithium-ion batteries,⁵² biosensors for enzyme detection,⁵³ macrofibers for flexible supercapacitors,⁵⁴ and intelligent food packaging films.⁵⁵

Other strategies such as cross-linking⁵⁶ may also be incorporated to enhance the interfacial adhesion between the constituent molecules without significantly altering the chemical structure. This may be implemented to design the material topology by modifying the functional groups and fabricating high-performance functional materials. In addition, separate strategies such as physical and chemical cross-linking may also be used to develop engineered materials with superior physical properties.

Physical crosslinking is formed by ionic interactions or metal coordination or hydrogen bonding^{57,58} and is reversible in nature, i.e., they can be dissociated or associated depending on the external stimulus (e.g., heat). The structural morphology of a material may be designed so that physical cross-linking between neighboring is effectuated. For example, when cellulose molecular chains are involved in sliding relative to each other during tensile loading, it involves breaking and reforming physically crosslinked bonds. Chemical crosslinking is frequently used where molecules (cross-linkers) consisting of multiple reactive ends attach to the functional groups of neighboring polymeric molecules, thus introducing a covalent bond between them.^{59,60} They are much more stable than physical cross-linking and form a tight network by reducing the mobility of the chemically crosslinked molecular chains, which makes it difficult to sever the linked bonds. Sometimes a series of chemical and/or physical treatments may inflict a combination of a double network^{61–63} of both physical and chemical cross-linking, which also leads to improved physical properties in the material.

7.3 Influence of intermolecular bonding on the material physical properties

This section summarizes the effects of intermolecular bonds on various physical properties of materials, such as thermal stability, mechanical strength, toughness and stiffness.

7.3.1 Thermal Stability

Chemical and physical treatments for engineering the intermolecular bonding in composites can be an effective method to significantly improve their thermal stability, thus making it suitable in many large-scale industrial applications where high-

temperature material endurance is of prime importance. This subsection discusses the influence of various types of intermolecular bonding, such as hydrogen bonds and imine bonds, in significantly improving the thermal stability in composites for different material types such as hydrogels, aerogels, and composite films.

For example, a strategy of tuning the intermolecular bonds to increase the thermal stability of hydrogel can be envisioned by utilizing directed hydrogen bonding, along with hydrophobicity for polymers based on β -helical polyisocyanotriptides (TriPIC) as proposed by Yuan *et al.*⁶⁴ Synthetic polymers like TriPIC exhibit exceptionally high thermal stability owing to their structure, as shown in Figure. 7.2a. The central polyisocyanide backbone (bold red in Figure. 2a) possesses two amide groups adjacent to it, which forms two parallel intermolecular hydrogen bonding arrays A and B (Figure. 7.2a, top panel). During heating, the hydrogen bonding network A remains stable and shields the central backbone from water, thus forming a hydrophobic core. The second intermolecular hydrogen bonding network B gets stretched on heating, thus inflicting the central polymer backbone with a helical structure with enhanced stiffness. Heating beyond lower critical solution temperature dehydrates the oligo (ethylene glycol) tails, which results in bundle formation in the polymer network, rendering high thermal stability of the hydrogels for multiple hours at 80°C as validated by Figure. 7.2b. On heating using a rheometer, the storage modulus (G'), the ratio of applied stress to measured strain increases indicating enhanced gel stiffness, which further retains its value for over 10 hours at a high temperature of 80°C. For networks with different concentrations of the TriPIC polymer, the storage modulus was observed to prominently increase from the gelation temperature (bottom point of a sudden rise in

each curve in Figure. 7.2c indicating hydrogel formation) with the highest stiffness for the polymer network with maximum concentration (4 g L^{-1}) as shown in Figure. 7.2b. Polymers with different concentrations were much stiffer and retained its exceptional thermal stability at 80°C . This strain stiffening behavior is completely reversible in cooling the sample. Repeated thermal cycles have negligible effects on the other parameters, such as the mechanical properties of these hydrogels, further highlighting the effectiveness of this design principle. To shed further insights on how the bundle formation aids in thermal stability for these hydrogels, FTIR measurements were performed (Figure. 7.2d). The intermolecular hydrogen bonds formed by amides titled “A” had the maximum intensities for -C=O- during vibrations, indicating their probable role in protecting the central polymer backbone. In contrast, the intermolecular hydrogen bonds formed by amides titled “B” maintain the backbone helix and the structural stiffness, which in turn makes the structure thermally stable. The FTIR curves for variable temperatures (different colors, Figure. 7.2d) display a change in the -C=O- vibrations, indicating its adjustment to the ambient conditions to render superior thermal stability in the bulk composite. This innovative biological approach of utilizing hydrogen bonds and hydrophobic interactions is thus effective. It may replace conventional strategies of altering the electrostatic interactions of the surface for the material to be stable against excess thermal energy. Several other research investigations also report the advantages of intermolecular bonds in enhancing the thermal stability of the hydrogel class of materials, such as in Boron nitride/polyvinyl alcohol (PVA) hydrogel,⁶⁵ double-network PU-based hydrogels,⁶³ and in PVA-based hydrogels having nano fibrillated cellulose (NFC) aldehyde cross-linkers.⁶⁶

Besides hydrogels, engineering the intermolecular bonds to improve thermal stability has also been demonstrated in other soft materials, such as aerogel. For example, Song *et al.*⁶⁷ fabricated a cellulose carbon and reduced graphene oxide polydimethylsiloxane (PDMS) aerogel (CCA@rGO/PDMS) which showed exceptional thermal stability on increasing wt. % of cellulose in the cellulose carbon aerogel (CCA) from 2.24 wt. % to 3.95 wt. %. Here, cotton is dissolved in the cellulose solution (Figure. 7.2e) using intermolecular hydrogen bonding assisted assembly of cellulose and sodium hydroxide (NaOH)/ urea solution. Cellulose aerogels are thereby obtained through gelation and freeze-drying. The CCA@rGO are obtained through a sequence of steps involving vacuum impregnation, freeze-drying, and thermal annealing. Finally, the CCA@rGO/PDMS aerogel is prepared by pouring PDMS into the CCA@rGO mold followed by vacuum impregnation and natural cooling to room temperature. Different concentrations of CCA@rGO were impregnated in the PDMS solution to obtain CCA@rGO/PDMS aerogels with various cellulose concentrations. More cellulose wt. % may indicate more efficient self-assembly of the solution driven by spatially denser intermolecular hydrogen bonds. To obtain the glass transition temperature (T_g) of the different concentrations of CCA@rGO/PDMS aerogels, differential scanning calorimetry (DSC) curves were plotted (Figure. 7.2f). Here, T_g was obtained by the corresponding temperature of the trough of the curve. T_g gradually increases with an increase in loading of CCA@rGO. For loading of CCA@rGO at 3.05 wt. %, the T_g was ~5.7°C more than that of pure PDMS, which was fabricated without intermolecular hydrogen bonding assisted self-assembly. Since T_g indicates the phase alteration of a material from rigid solid to rubbery state, higher T_g signifies delay of the material

transformation to its rubbery state, which in turn decreases the weight loss % when that material is heated to higher temperatures, as shown in Figure. 7.2g. From the curves obtained in Figure. 7.2g, the heat resistance index (T_{HRI}) can be directly calculated using the formula $T_{HRI} = 0.49[T_5 + 0.6(T_{30}-T_5)]$. The temperatures T_5 and T_{30} correspond to a 5% and 30% loss in weight, respectively, and are marked in Figure. 7.2g by dashed black lines. From here, the CCA@rGO/PDMS aerogels with 3.05 wt. % of CCA@rGO were found to have a T_{HRI} of 178.3°C, which was much higher than CCA@rGO/PDMS aerogels having wt. % of 2.24 (172.4.9°C), 2.51(173.9°C) and 2.78 (175.7°C). This is because more loading of CCA@rGO might enrich the interfacial intermolecular bonding network between the matrix of CCA@rGO and PDMS, this restricting molecular chain movements on heating to high temperatures and thus enhancing thermal stability. Other literature suggesting the improvement of thermal stability due to the presence of intermolecular bonding mechanism has also been reported, such as but not limited to NFC aerogels cross-linking with diisocyanate, where the thermal stability at 500°C was improved significantly in comparison to the un-crosslinked aerogel,⁶⁸ when the char residues of both the samples were compared.

Like materials such as hydrogels and aerogels, intermolecular bonding has been found to play a decisive role in increasing the thermal stability of hard materials such as composite films, too. Shang *et al.*⁶⁹ prepared polydimethylsiloxane/boron nitride nanosheets (BNNS) based elastomer composites (PDMS/BNNS) with varying

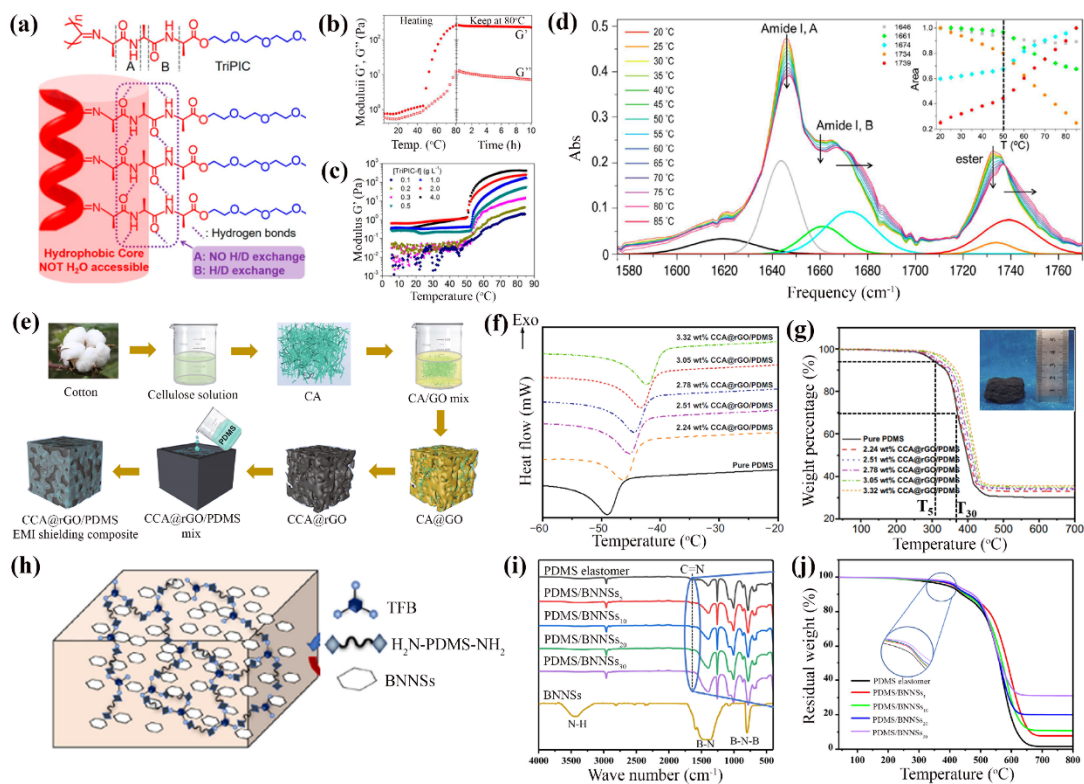


Figure 7.2: Role of intermolecular bonds in improving the thermal stability of (a-d) hydrogels ;(e-g) aerogels and (h-j) composite films. (a) A schematic of the molecular structure of hydrogels based on β -helical polyisocyanotriptides (TriPIC), clearly showing the central backbone (bold red) with two parallel intermolecular hydrogen bonding arrays A and B. (b) Linear rheological analysis (time sweep) when the TriPIC hydrogel is heated to 80°C and then conditioned at 80°C for 10 hrs, where G' and G'' are the storage and loss modulus, respectively. (c) Plots of G' with respect to temperature for different concentrations of the TriPIC hydrogel. (d) FTIR spectra of TriPIC hydrogel where the different colored lines represent each spectrum at different temperatures. (e) Schematic illustrating the fabrication process of cellulose carbon and reduced graphene oxide polydimethylsiloxane (PDMS) aerogel (CCA@rGO/PDMS). (f) Differential scanning calorimetry (DSC) curves to obtain the glass transition temperature (T_g) for different concentrations of CCA@rGO/PDMS aerogels. (g) Thermo gravimetric analysis (TGA) plots to evaluate T_5 and T_{30} (marked by dashed lines), which, along with T_g are used to compute the heat resistance index to determine the thermal stability of the aerogel. (h) Illustration of the molecular structure of polydimethylsiloxane (PDMS)/boron nitride nano sheets (BNNS) based elastomer composite film (PDMS/BNNS). (i) FTIR spectra comparison of the PDMS/BNNS for different contents. (j) TGA plots for PDMS/BNNS composite films.

of BNNS, with pure PDMS elastomer. (j) TGA plots of the PDMS/BNNS film for different contents of BNNS and pure PDMS elastomer. (a-d)⁶⁴ (e-g)⁶⁷ (h-j)⁶⁹

concentrations of BNNS such as 0%, 5%, 10%, 20%, and 30%. The resulting composite film contains multiple polymeric groups such as Polydimethylsiloxane (H₂N-PDMS-NH₂), 1,3,5-Triformylbenzene (TFB), and BNNS, the structures of which are shown in Figure. 7.2h. To investigate the presence of intermolecular bonds, FTIR spectra studies were conducted as shown in Figure. 7.2i. The two FTIR bands of BNNS at 812, 1370 and 3438 cm⁻¹ represent out-of-plane vibration in B-N-B, in-plane vibration of the ring due to stretching, and amino (N-H) group vibrations, respectively. Furthermore, for PDMS/BNNS composites, a peak at 1650 cm⁻¹, highlighted by dashed lines, was specifically present, representing the presence of dynamic imine bonds throughout the PDMS/BNNS composite films for all concentrations of BNNS. This polymer matrix, formed by the dynamic imine bonds in the PDMS, ensured homogenous dispersion of BNNS through the in-situ polymerization process during preparation. As a result, strong interfacial intermolecular bonding in the matrix provided an avenue to provide favorable thermal stability of the composite film. With the increase in the content of BNNS, the thermal stability of the composites increases, as shown in Figure. 7.2j. The T₅ of the pure BNNS is 392.7°C. However, the corresponding values when PDMS, enriched in dynamic imine bonds, were added increased to 411.8°C and 424.5°C for the composite having 5% and 30% wt. percent of BNNS. All the PDMS/BNNS composites for BNNS wt. % between 5 to 30% showed an exceptionally high thermal stability greater than 400°C. This enhanced thermal stability can be attributed to the higher heat stability of the BNNS, which in turn is stabilized in the polymer matrix due to the

synergistic interactions between the BNNS become PDMS facilitated by the dynamic imine bonds. Besides elevated thermal stability, the imine bonds are also responsible for making the material self-healing as on cooling, the aldehyde and amino groups diffuse in the damaged interface. They re-form the imine bonds when subjected to a condensation reaction. Such self-healing and thermally stable materials can be desirable in applications related to thermal management materials. In addition to imine bonds, intermolecular hydrogen bonds can also play a prominent role in improving the thermal stability of composite films. For example, Zhang *et al.*⁷⁰ increased the crosslinking density between polyurethanes and carboxymethyl chitosan in a bio-based film. This subsequently increased the hydrogen bonding between the functional groups. The glass transition temperature also increased, implying superior thermal stability of the film.

7.3.2 Mechanical Properties

Mechanical properties of various high-performance materials can also be tuned by engineering intermolecular bonding. Various strategies, such as forging intermolecular hydrogen bonds, tuning the vdW force and electrostatic interactions, and effectuating double cross-linking, for both hard (e.g., graphene-oxide nanosheets) and soft (e.g., hydrogels) materials are discussed here.

Hard materials such as graphene-oxide nanosheets, which are both mechanically strong and tough, generally two mutually exclusive properties, can be achieved by utilizing intermolecular hydrogen bond interactions between transition metallic carbides and polymers, as demonstrated by Shi *et al.*⁷¹ Here, Ti_3AlC_2 powder was gradually stirred

in a solution of water and hydrochloric acid (HCl), followed by heating, centrifugation, washing, and ultrasonication (Figure. 7.3a). The titanium carbide ($\text{Ti}_3\text{C}_2\text{X}$) nanosheet (NS) dispersion thus obtained possessed abundant -OH groups and was mixed with polypropylene (PP) latex at a 30:70 ratio by weight and stirred. The mixture was then subjected to an oxygen-free drying method to obtain a powder comprised of maleic anhydride-grafted isotactic polypropylene (MA-g-PP) and titanium carbide ($\text{Ti}_3\text{C}_2\text{X}$). Then, the powder was melt-blended with PP granules in a roller mill to obtain the PP/MA-g-PP/ $\text{Ti}_3\text{C}_2\text{X}$ NS nanocomposite. The MA-g-PP offers a plethora of active bonding sites facilitating intermolecular hydrogen bonding, which results in nanoconfinement in the resulting nanosheet, thus improving its mechanical performance. The tensile strength of the nanocomposite increased by 35.3%, and the toughness (ductility) increased by 674.6% (Figure. 7.3b), which was considerably higher than existing PP-based nanocomposites. The reason for the superior mechanical properties was primarily due to multiple active intermolecular hydrogen bonding sites in the 3D network of $\text{Ti}_3\text{C}_2\text{X}$ NS and the MA-g-PP. During stretching, the $\text{Ti}_3\text{C}_2\text{X}$ NS slid relative to each other, but the active intermolecular H-bonding forged between the intermediate layers restricted the sliding. Overcoming the dense H-bonds caused multiple slippages (Figure. 7.3c) at the interface, thus dissipating a large amount of energy during the entire loading process. Thus, the failure of the MA-g-PP polymeric chains was delayed resulting in enhanced tensile strength. Moreover, the tensile stretching at higher deformation enhanced the ductility without sacrificing the tensile strength. Similar observations of intermolecular hydrogen bonding playing a

predominant role in elevating strength and toughness have also been observed in other materials such as cellulose⁷² and spider silk.⁷³

Separate intermolecular bonding schemes utilizing a combination of electrostatic interactions and intermolecular hydrogen bonding have also been utilized so that the final developed material can possess extraordinary mechanical performance analogous to existing naturally occurring materials such as spider silk, which are already known to possess excellent mechanical properties. This was demonstrated in the artificial spider silk-like fiber formed by a combination of ion doping followed by twisting, as reported by Dou *et al.*⁷⁴ Here, vinyl-triethoxysilane and deionized water were stirred to obtain vinyl-functionalized silica nanoparticles (VSNPs) (Figure. 7.3d). Acrylic acid, ammonium persulfate, and metal salts (ZnCl₂, MgCl₂, etc.) were then added and stirred for a specific time, followed by degassing, to obtain polyacrylic acid crosslinked with VSNPs. A rod was then vertically dipped into the VSNP reaction mixture and quickly taken out, followed by drying at ambient temperature by holding at both ends, resulting in the solidified final fiber. The twisted fibers were produced by attaching both ends of the drawn non-dried fiber to a motor and a load at constant pressure. The fibers produced using this method displayed a high tensile strength (~895 MPa) and toughness (~370 MJ/m³) (pink stars, Figure. 7.3e), better than most synthetic and protein-based fibers and closely comparable to naturally occurring mechanically superior materials such as spider silk. Here a covalent network was formed due to the vinyl groups cross-linking in acrylic acid and/or functionalized silica nanoparticles, which was validated by NMR spectroscopy. In addition, intermolecular hydrogen bonding also formed in the active sites. Under tensile stretch, the polymeric chains

elongate, and the intermolecular hydrogen bonds unzip from one site in the chain and rezip in the adjacent available site, dissipating significant energy and causing an increase in the mechanical strength and toughness. Twisting aligned the polymeric chains to a greater extent contributing to the rise in mechanical performance. Furthermore, the cross-linking facilitated by the ions from salts (ZnCl_2) restricted the mobility of the polymeric chains, further elevating the strength, thus making these materials suitable for multiple applications where high energy dissipation and impact absorption are required.

Utilizing vdW forces and π - π stacking interactions, in addition to other intermolecular bonding mechanisms, are also prominent in graphene oxide (GO) based materials because GO is ideal for devising such strategies because it contains abundant oxygen-containing functional groups on its surface. Song *et al.*⁷⁵ developed an artificial nacre composed of GO nanosheets and benzene synthesized sulfonated styrene-ethylene/butylene-styrene (SSEBS) copolymer (Figure. 7.3f) using a vacuum-assisted filtration process. Here, π - π interactions exist between the GO nanosheets and benzene groups and the polystyrene chains in SSEBS. Intermolecular hydrogen bonding also exists between the -OH and -COOH groups of the GO nanosheets with the sulfonic groups in SSEBS. This caused the failure mechanism to progress in the proposed steps starting with the deformation of EB chains in SSEBS between the inter-layer spaces occupied by the GO NS. This was followed by further elongation of the chains till failure along with some proportion of partially slipped GO NS (Figure. 7.3g). The combined synergistic intermolecular bonding mechanisms comprised of H-bonds and π - π stacking interactions thus increased the interfacial stress transfer efficiency leading to

high energy dissipation, which caused a toughness (15.3 MJ/m^3) significantly higher than natural nacre and many other morphologically similar GO-based nanocomposites. Modeling-based studies predicting the mechanical properties as a function of graphene interlayer crosslinks have also been performed⁷⁶ to aid in the mechanistic design of GO-based sheets. Such models can predict the location of the maximum strain (e.g., at the edges) and how adjusting the cross-links through successful intermolecular bonding strategies (hydrogen, vdW, metal ions, etc.) can help improve the mechanical performance of the nanocomposite.

Another method of tuning the intermolecular bonds to obtain the superior mechanical properties of higher strength and toughness can also be realized by engineering the noncovalent interfaces of the hierarchical material architecture.^{77,78} Generally, this technique is inspired from the architecture of biological materials found in nature, such as wood, bone, conch shell and nacre.⁷⁹ All such materials consist of building blocks which spans across several length scales. The mechanics of these materials is largely dependent on the interfaces holding those building blocks together till deformation. These interfaces, when programmed efficiently, can lead to development of advanced materials with remarkable mechanical performance.⁸⁰ For example, natural nacre is known to have exceptional mechanical properties.^{81–83} Inspired from natural nacre, Zeng *et al.*⁸⁴ used a vacuum-assisted self-assembly method to fabricate artificial nacre-like papers comprised of noncovalent functionalized boron nitride nanosheets (NF-BNNSs) and PVA. In the ordered ‘brick-and-mortar’ arrangement obtained as a result, the long PVA molecular chains tuned the noncovalent interfaces by linking the NF-BNNSs through intermolecular hydrogen bonds. The resulting artificial nacre-like

paper demonstrated outstanding mechanical strength (125.2 MPa, similar to natural nacre) and 30% better toughness (2.37 MJ m^{-3}) than natural nacre. Theoretical studies on nacre-like composites by optimizing material compositions (volume fraction, aspect ratio, offset ratio) and resolving the conflicts related to mechanical properties in order to obtain better engineered, bio-inspired materials have also been demonstrated.⁸⁵ A combination of atomistic modeling and experimental investigation⁸⁶ also demonstrated superior strength and toughness in disc-shaped material molds made of silica-polymer composites. Here, the inorganic silica network was able to covalently bond with the polymer (polytetrahydrofuran (PTHF)) chains. This was because of the molecular structure of PTHF and presence of other organic silane coupling agents, such as glycidoxypentyl trimethoxysilane (GPTMS). The intermolecular bonding thus formed was crucial in increasing the strength of the hybrid by ~321% (0.32 MPa to 1.35 MPa) and toughness by 82 % (120 kPa to 219 kPa). All these above research efforts emphasize the effectiveness of tuning the noncovalent interfaces and fabricating synthetic materials with targeted mechanical performance.

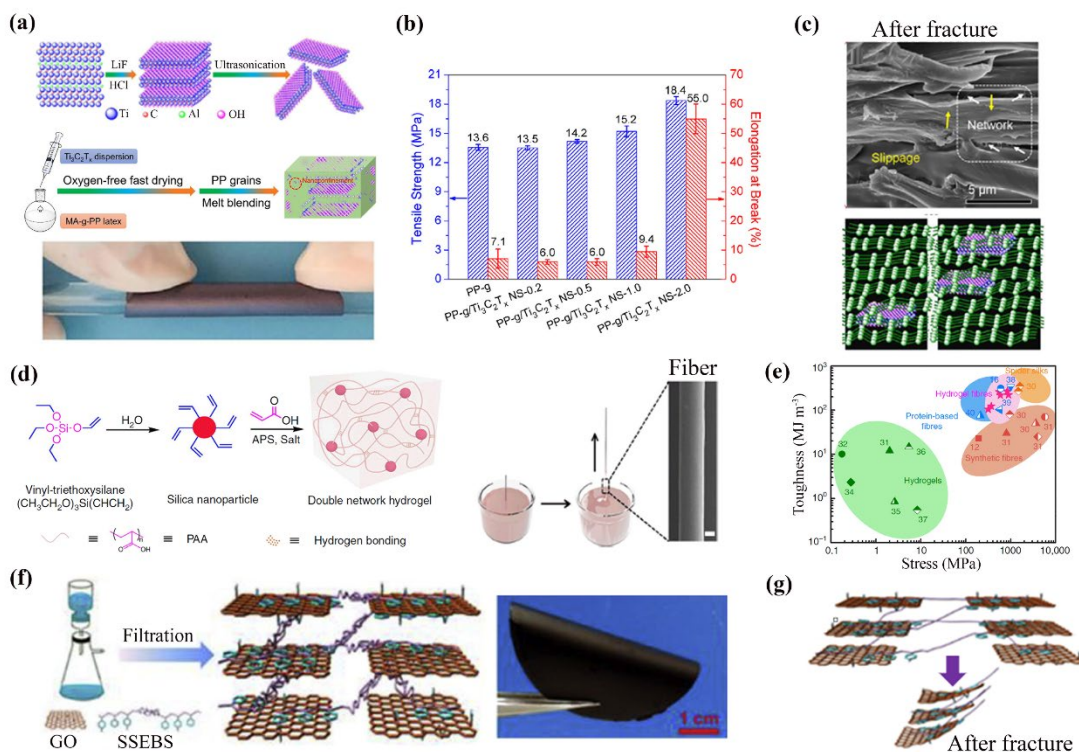


Figure 7.3 Role of intermolecular bonding in elevating the mechanical properties of hard materials such as (a-c) nanosheets; (d-e) fibers, and (f-g) artificial nacre. (a) Schematic representation to fabricate ultrathin titanium carbide ($\text{Ti}_3\text{C}_2\text{T}_x$)/polypropylene (PP) nanocomposites (PP/MA-g-PP/ $\text{Ti}_3\text{C}_2\text{T}_x$ NS) by utilizing intermolecular hydrogen bond interactions between transition metallic carbides and polymers, where MA-g-PP and NS stand for maleic anhydride-grafted isotactic polypropylene and nanosheet, respectively. (b) Mechanical performance (tensile strength in blue, elongation at break in red) of the nanocomposites for different weight content of $\text{Ti}_3\text{C}_2\text{T}_x$ and PP. (c) An SEM image (top) and model (bottom) of the multiple slippage sites of the nanocomposite on stretching. (d) Illustration showing the preparation of artificial spider silk-like fiber using vinyl-functionalized silica nanoparticles (VSNPs) to cross-link with polyacrylic acid, followed by vertical dip of a rod into the reaction mixture, concluding with quick drying by taking the rod out. (e) Plot showing the close comparison of the mechanical performance (toughness, tensile strength) of the artificial fiber with respect to other naturally occurring mechanically superior materials such as spider silk as well as synthetic fibers. (f) A schematic showing the fabrication process of an artificial nacre composed of graphene oxide (GO) nanosheets and benzene synthesized sulfonated styrene-ethylene/butylene-styrene (SSEBS) copolymer, using a vacuum-assisted

filtration process by facilitating the π - π interactions exist between the GO. Right panel shows a digital image of the nanocomposite material. (g) A molecular model showing the final stage of the proposed mechanism for fracture of this artificial nacre. (a-c)⁷¹ (d-e)⁷⁴ (f-g)⁷⁵

Apart from hard materials, soft materials such as hydrogels can also be fabricated by effective intermolecular bonding strategies. Hydrogels^{19,87} is a representative class of materials possessing a complex, three-dimensional network of polymeric chains with water occupying the molecular voids in between. Here, the molecular properties of water are retained as the polymer network mesh is much larger than individual molecules of water. The hydrophilic functional groups of the polymeric framework make it swell, a distinctive feature of hydrogels, and enable this material to have a high-water retention capacity. But the chemically induced cross-links among the constituent polymers restrict the dissolution of hydrogels in water. From a mechanistic standpoint, the brittle and tightly linked part of the network is primarily responsible for energy dissipation. In contrast, the ductile and loosely linked part helps conserve elasticity. Different novel cross-linking strategies are thus considered to render magnified mechanical stability to the hydrogel network,^{88,89} which has benefits in multiple applications. In one such study, Gong *et al.*⁶¹ reported a general method to combine different hydrophilic polymers to obtain a double network (DN) hydrogel with high mechanical strength (tensile strength up to 17.2 MPa, fracture strain up to 98%). For example, the first network of PAMPS and PAA was synthesized from methypropanesulfonic acid and a cross-linking agent (methylenebisacrylamide), followed by the synthesis of the second network in the presence of the first.⁹⁰ This investigation demonstrated that for two networks of polymers entangled with each other in a hydrogel, different parameters such as the molar ratio of the first network to

the second, the cross-linking density of the first (high cross-linking) concerning the second (loose cross-linking) network are of crucial importance to obtain a high mechanical strength hydrogel.

For this DN hydrogel⁶¹ comprising of a short-chain network of poly (1-acrylamido-2-methylpropane sulfonic acid) (PAMPS) and a long-chain network of polyacrylamide (PAAM) polymers, fatigue behavior was also studied by Zhang *et al.*⁹¹ During stretching, the short-chain network ruptures and dissipates energy. In contrast, the long-chain network contributed to the retention of the hydrogel elasticity for both types of prepared samples, cut and uncut (Figure. 7.4a). On application of a cycle of loading and unloading in the PAMPS/PAAM network, the PAMPS network broke. Still, the PAAM network was preserved (Figure. 7.4b). Cyclic load applied on uncut samples to check the stress-stretch curves revealed that the internal damage could accumulate through thousands of cycles before final failure. On application of cyclic loading on cut samples to study the fatigue crack propagation, it was observed that the crack travels cycle-wise when a stretch amplitude beyond a certain value was applied. The threshold for energy release rate, indicating when the crack starts propagating, was observed to be higher ($\sim 400 \text{ J/m}^2$) in PAAM networks having low-density cross-linkers and lower ($\sim 200 \text{ J/m}^2$) in PAAM networks having high-density cross-linkers, which was validated using the Lake-Thomas model. Such a study of fatigue behavior is essential for using hydrogels in applications where a large load needs to be sustained.

Novel design strategies to fabricate DN hydrogels with high self-recovery and improved fatigue resistance have also been demonstrated by incorporating ions in the second network, as reported by Chen *et al.*⁹² Here, a hybrid DN gel was fabricated

comprising physically cross-linked (via hydrogen bonding) Agar gel as the first network and chemically-physically cross-linked copolymer of acrylamide and acrylic acid (PMAAac) gel as the second network. The hybrid DN gel was soaked in Fe^{3+} solution at optimal conditions, and utilizing the strong intermolecular coordination bonding, Agar/PMAAac- Fe^{3+} DN gels were obtained (Figure. 7.4c). The mechanical properties of the obtained hybrid DN gel (strength ~ 1.55 MPa) were found to be much superior (Figure. 7.4d, top panel) than the gel without any ion intercalation or the gel that did not possess double network (PMAAac- Fe^{3+} gel, top panel of Figure. 7.4d), emphasizing the role of the coordination interactions to improve the mechanical properties in DN hydrogels. The hybrid DN gel even self-recovered almost 50% of its toughness around 1 minute after removal of loading (Figure. 7.4d, bottom panel), which can be attributed to the synergistic effect of intermolecular bonding (hydrogen bonds in the first network and coordination bonds in the second network) causing immense energy dissipation internally and thus delaying the fracture. Furthermore, manipulation of the second network content (AAc varied from 1 to 20 mol %) of the DN gel also demonstrated even higher mechanical strength (~ 8 MPa) and was subjected to six loading cycles; the hysteresis loops remained almost the same during the last four cycles. The latter phenomenon demonstrates its superior fatigue resistance due to the Fe^{3+} coordination bonding offering a higher withstanding capacity of larger stress, paving the path for applying these freely shapeable (Figure. 7.4d, side panel) double-network hydrogels in the development of strong and tough, shape-shifting next-generation soft materials.

Separate studies modifying the DN design strategies and forming a triple network (TN) supermacroporous hydrogel in the same manner by using the DN network (Figure. 7.4e) as the precursor have also been demonstrated,⁹³ which had a much higher compressive modulus (Figure. 7.4f) than double-network (DN) or single network (SN) hydrogels. Hydrogels having mesoscale networks containing constituent structures at different length scales (e.g., ionic bonds at the ~ 0.1 nm scale, transient polymer network at ~ 1 nm scale, permanent chemically cross-linked network at the ~ 10 nm scale, bicontinuous hard/soft phase at ~ 100 nm scale) have also been observed to be tough, self-healing and fatigue resistance as demonstrated by Li *et al.*⁹⁴ with detailed analysis on factors determining the rate (slow/fast) of crack propagation. Similar mechanistic analysis on the suppression of crack advance in other mesoscale network hydrogels has also been reported.^{95,96} Apart from this, numerous modeling studies including, but are not limited to, enriching the design of DN hydrogels with a focus on constitutive models⁹⁷ revealing the mechanism of damage, and also finite element models⁹⁸ studying the deformation regime near the crack tip of chemically and physically cross-linked PVA based hydrogel are also reported, that vividly elucidates the importance of utilizing features of intermolecular bonding on these novel soft materials.

Other soft materials, such as aerogels, have also exhibited superior mechanical performance due to the facilitation of intermolecular bonding. Aerogels are materials composed of a complex interconnected network of fibers confined together by diverse intermolecular bonding mechanisms. Aerogels are obtained from hydrogel as a starting material, then subjected to a series of physical/chemical treatments. For example, polyvinyl alcohol (PVA), phytic acid (PA), and montmorillonite (MMT) was used to

fabricate an aerogel utilizing both physical and chemical cross-linking design strategy.⁹⁹ The PVA, PA, and MMT were mixed in an aqueous suspension where the rich -OH groups in each of them were responsible for forming hydrogen bonding and thus enabling physical cross-linking (Figure. 7.4g). Then, the solution was freeze-dried by using a vacuum oven to obtain the final aerogel. The freeze-drying process enabled the esterification of PVA and PA, resulting in the chemical cross-linking (Figure. 7.4g). The resulting double network aerogel was ultralight ($0.078\text{--}0.103\text{ gm/cm}^3$) and possessed an ultrahigh compressive modulus ($\sim 41.9\text{ MPa}$) (Figure. 7.4h) when compared with similar single and double cross-linked aerogels. The ultralow density resulted in the aerogel standing on the flower petals lightly (Figure. 7.5h), while the ultra-strong bonding leads to the ultrahigh resistance against the crushing of a car ($\sim 1520\text{ kg}$) and bicycle tires ($\sim 75\text{ kg}$), as shown by SEM imaging in Figure. 7.5i. It should be noted that the optimal proportion of the elements in the double network is of prime importance to extract the best mechanical performance. A greater proportion of PA disrupted its ability to engage in excessive cross-linking, thus distorting the stable double cross-linked hydrogel network.

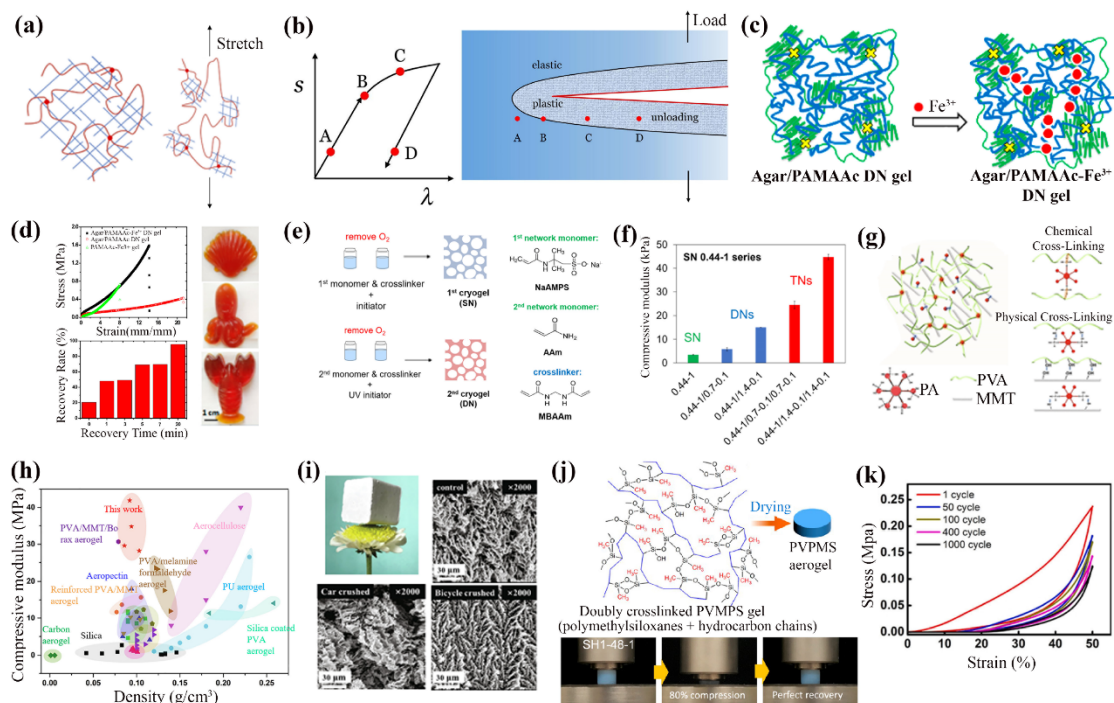


Figure 7.4 The role of intermolecular bonding in elevating the mechanical properties of soft materials such as (a-f) hydrogels and (g-k) aerogels. (a) Schematic of a double network (DN) hydrogel, a short-chain network of PAMPS, and a long-chain network of PAAM polymers. (b) Typical loading/unloading cycle of the hydrogel during stretching (left panel). Fatigue crack propagation on the application of cyclic loading (right panel). (c) Schematic of a hybrid DN gel composed of Agar gel in the first network and a chemically cross-linked copolymer of acrylamide and acrylic acid (PMAAAc) gel in the second network, soaked in Fe^{3+} solution. (d) Stress-strain plots show the superior mechanical strength of the hybrid DN gel (top panel) and the self-recovery characteristics (bottom panel). The side panel shows the digital images of the easily shapeable DN gel. (e) A schematic of the two-step process to fabricate DN cryogels. (f) Comparison of the compressive modulus values for the triple-network (TN) gel with the DN and single-network (SN) gels. (g) A schematic of the two-step process to fabricate a double-network aerogel using physical and chemical cross-linking of polyvinyl alcohol (PVA), phytic acid (PA), and montmorillonite (MMT). (h) Comparison of the ultra-high compressive modulus (MPa) of the aerogel (red star labeled “This work”) in this work with other similar single and double-network aerogels. (i) Top left image shows the ultra-light double network aerogel resting on a flower. The top right, bottom left, and bottom right are the SEM images after the aerogel is crushed under control, car and bicycle, (j) Schematic of a doubly crosslinked PVMPs gel (polymethylsiloxanes + hydrocarbon chains) and its transformation into a PVPMS aerogel through drying. (k) Stress-strain plots showing the mechanical properties of the aerogel after multiple cycles of compression and recovery.

respectively. (j) Schematic (top) of an aerogel structure comprised of polyvinylpolymethylsiloxane (PVPMS), prepared through a facile synthesis route involving radical polymerization and hydrolytic polycondensation. The bottom panel shows image evidence of the remarkable self-recovery characteristics of the aerogel. (k) Stress-strain plots of a GO-based aerogel infested with Cobalt ions, developed by facilitating coordination bond interactions (chemical cross-link) along with hydrogen bonding (physical cross-link) under multiple (till 1000) loading cycles. (a-b)⁹¹ (c-d)⁹² (e-f)⁹³ (g-i)⁹⁹ (j)¹⁰⁰ (k)¹⁰¹

Other design techniques effectuating enhanced intermolecular bonding by implementing double cross-linking have also been demonstrated by altering the modes of physical and chemical treatments. For example, polyvinylpolymethylsiloxane (PVPMS) aerogel was prepared through a facile synthesis route¹⁰⁰ involving radical polymerization and hydrolytic polycondensation (Figure. 7.4j), which enabled the double chemical cross-linking between polymethylsiloxanes and hydrocarbon chains, followed by drying using different methods such as ambient pressure drying or solar conduction drying. The transparent aerogel displayed extraordinary compression flexibility (till 80% strain without fracture with recovery to the original shape, as shown in Figure. 7.4j, bottom panel) and superior bending flexibility. These exquisite mechanical properties were primarily due to the hydrogen bonds in the -CH₃OH groups of the polymethylsiloxane skeleton, which aided in the recovery when compressed or bent, as well as the chemical cross-linking between the polymethylsiloxane skeleton and hydrocarbon chains, which increased the deformability under compression. This work shows significant progress in double cross-linked aerogels, which can be used in insulator applications in the near future. Apart from the above outstanding mechanical properties, the aerogel also presents us the high fatigue resistances. Zhang *et al.*¹⁰¹

demonstrated a double cross-linked hydrogel facilitating the coordination bond interactions (chemical cross-link) along with hydrogen bonding (physical cross-link). Here, hydrogen bonds formed between GO nanosheets, and coordination interactions inflicted by cobalt ions were applied in the resulting GO-polymer-based aerogel. The final aerogel possessed a high (0.506 MPa) compression modulus, 43% improvement of tensile modulus, and high fatigue resistances lasting over 1000 cycles (Figure. 7.4k). Such aerogels fabricated using relatively green, cheap, non-chemically toxic methods could be used as an insulating material in multiple applications proving the effectiveness of a successful intermolecular bonding scheme in aerogel like materials. Aerogels fabricated using such innovative mechanistic design strategies described above have already been found to be useful in multiple applications related to super elasticity, thermal insulation,^{102–105} heat stability,¹⁰¹ phase change materials,¹⁰⁶ biomedical industry,¹⁰⁷ wearable sensors,^{105,108–111} contaminant filters,^{62,112,113} some of which will be discussed in Section 7.4 below.

7.4 Applications

The enhanced properties fostered by engineering intermolecular bonding lead to multiple applications crucial to instigating the materials science community in designing next-generation materials.^{114,115} Some of those applications are categorized here primarily based on thermal and mechanical properties, which have been observed to improve significantly due to manipulation of the intermolecular bonding as reviewed above. Other applications based on properties related to electronics, sensing, optics, and biomedical uses are also briefly reviewed to demonstrate the versatility in materials development due to maneuvering intermolecular bonds.

Facilitating intermolecular bonding to tune thermal properties has been done in many materials, such as, but not limited to, $\text{Ti}_3\text{C}_2\text{T}_x$ MXene/Poly (vinyl alcohol) (PVA) composites.¹¹⁶ Here, the incorporation of PVA, forged hydrogen bonds between the MXene and PVA due to the presence of hydroxyl groups in the PVA and Ti-O bonds, as confirmed by spectroscopy. Thereby, the thermal stability significantly improved, as indicated by the reduction of the thermal coefficient from $-0.06271 \text{ cm}^{-1}/\text{K}$ to $-0.03357 \text{ cm}^{-1}/\text{K}$. Furthermore, the thermal conductivity of PVA based composite was higher ($\sim 47.8 \text{ W/mK}$) than many metals and most two-dimensional materials. Such nanocomposites may have novel future uses in battery and thermoelectric devices. Soft materials such as hydrogels based on polymers such as NFCs, contain spatially dense hydrogen bonding network between the NFCs and water,⁸⁹ and can be used as a raw material for biomimetic devices (Figure. 7.5a). When a double network hydrogel is fabricated based on NFCs and CNTs using wood as substrate, the NFC/CNT layer protected the wood substrate by localizing heat, thus acting as an effective thermal insulation layer, which can be considered as a future candidate for water purification, ionic conductors, and biomedical devices. Other soft materials such as double cross-linked aerogels¹⁰⁵ based on Polyvinylpolydimethylsiloxane show low thermal conductivities ($\sim 16.2 \text{ W/K}$), which are much lower than standard insulating materials such as stationary air (26 W/K), nanocellulose and chitosan aerogels ($22\text{-}30 \text{ W/K}$), polyurethane ($20\text{-}50 \text{ W/K}$), mineral wool ($35\text{-}80 \text{ W/K}$), etc., thus demonstrating their extraordinary thermal insulation performance.

Intermolecular bonding, if tuned appropriately, can result in mechanically strong and tough materials replicating natural materials. For example, Liao *et al.*¹¹⁷ demonstrated

strong (~ 1236 MPa) and tough (~ 137 J/gm) fibers with mechanical properties comparable to spider silk from yarn by electrospinning, stretching, and cross-linking using a minor amount of poly (ethylene glycol) bisazene. Techniques such as these, when applied to commercial polymers may be an effective method to design fibers with possible applications in satellite technology, biomedicine, and automobiles. A simple but sustainable two-step drawing process²⁴ using a chitosan and KOH/urea aqueous solution brought the inherent smaller fibers in closer proximity because of flow-induced alignment, thus increasing the spatial intermolecular hydrogen bond density and resulting in super stiff (~ 44.7 GPa) and strong (~ 878 MPa) chitosan filaments which could demonstrate vital applications as smart textiles such as lifting heavy weights (Figure. 7.5b). A combination of chemical cross-linking and intermolecular hydrogen bonding have also been exhibited to demonstrate high strength (13.7 MPa), toughness (11.8 MJ/m^3) and strain at break (91.8%) in hyperbranched polyester doped soy protein films²⁵ which could prove to be of great use in recyclable tissue engineering and packaging applications. This proves how various effective intermolecular bonding strategies can be extended for the bottoms-up design of multiple strong and tough materials with targeted properties, paving the way for application in many practical applications needing mechanically superior materials. Soft materials such as double cross-linked aerogel based on polyimide/reduced graphene oxide/cobalt have also been demonstrated¹⁰¹ to possess superior mechanical properties such as high modulus and high fatigue resistance which can prove very useful in applications as structural materials in buildings and pipelines as well as for thermal insulation materials (Figure. 7.5c). Polyimide (PI) based aerogels¹¹⁸ using amino-functionalized carbon nanotubes

as cross-linkers have been found to demonstrate mechanically strong (~ 2 MPa) aerogel materials where the compression modulus increased from 4.2 MPa in pristine PI based aerogels to ~ 47.3 MPa when intermolecular bonding strategy of cross-linking was adopted. The drastic increase of compression modulus aerogel by over 1100%, along with its high strength, indicates its applicability in lightweight, high-performance applications in the aerospace sector where strong materials providing superior thermal insulation are needed. Other soft materials such as cross-linked hydrogel inspired from natural substances such as mussels are already being manufactured with tunable mechanical properties such as stress, strain, Young's modulus, and toughness which could be very useful in wearable sensor applications used in smart textiles.¹¹⁹ Cross-linked hydrogels, when infested with different ions,¹²⁰ have also been observed to remarkably increase their mechanical properties (strength from ~ 50 kPa to ~ 15 MPa; toughness from ~ 0.0167 MJ/m³ to ~ 150 MJ/m³; elongation from $\sim 300\%$ to $\sim 2100\%$; modulus from ~ 24 kPa to ~ 140 kPa) manifesting the suitability of its usage in flexible electronics. Double network hydrogels have also found their applicability in many useful and life-saving biomedical applications to cure cancer cells.¹²¹

Tuning intermolecular bonds can also accelerate the enhancement of other lucrative properties of materials along with mechanical properties. Hydrogels can be used in artificial skins,¹²² human-machine interaction devices such as touchpads, and triboelectric generators to convert mechanical movement to electric current, widely used in pressure sensing electronics. Dynamic methylimidazolium chloride-based gels¹²³ (Figure. 7.5d) have also been designed to have tunable topological networks, reversible properties related to toughness, and electric conductivity along with adhesive

and self-healing properties, which may find their applications in artificial skins located in smart devices to detect the style of breathing and touch (Figure. 7.5e). Bi₂O₂Se as the layered structure is stacked through the electrostatic interaction (Figure. 7.5f). Recent research reveals that strain engineering can be utilized to modify this interlayer interaction and thus results in the conversion from semi-conductivity to metallicity.¹²⁴ All this enormous attention suitably proves the potential of intermolecular bond engineering to significantly alter various physical properties such as thermal stability and mechanics and emphasizes the urgent need to pursue research and development in this direction.

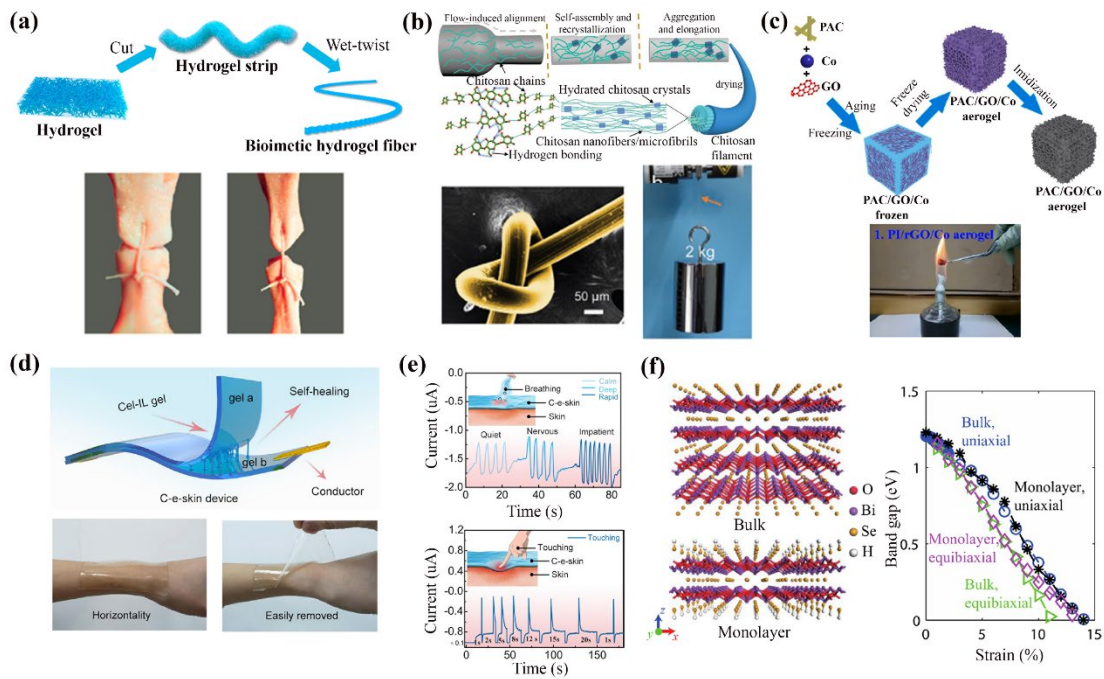


Figure 7.5 A few selected applications fostered by the enhanced material properties when the material structure is subjected to a greater degree of intermolecular bonding. (a) Biomimetic devices, (b) Smart textiles, (c) Structural and thermal insulation materials, (d-e) Artificial skins, and (f) Semiconductor devices. (a)⁸⁹ (b)²⁴ (c)¹⁰¹ (d-e)¹²³ (f)¹²⁴

7.5 Challenges and future perspectives

Despite the prominent interest in recent years in engineering intermolecular bonds and fabricating novel materials with superior physical properties, a few challenges related to intermolecular bonding strategies need to be addressed to foster research using these approaches. Some of the notable challenges posing as obstacles in this domain are discussed in this section.

For crystalline structures, it is a standard practice to compute phonon dispersion curves^{125,126} to identify whether the in-plane or out-of-plane vibrations of atoms are the dominant factors influencing thermal conductivity. A shift in the phonon spectra correlates with an increase or decrease in energy of the phonons in the bulk composite, which is directly related to the increase or decrease of the thermal conductivity of the material. However, to the best of our knowledge, this method is yet to be applied specifically to intermolecular bonded molecular regions, which could shed light on the fundamental reason for how intermolecular interactions lead to enhancement or weakening of the overall thermal conductivity values. Some studies¹²⁷ on strong/weak intermolecular hydrogen bond interactions between small, large, or continuous polymer blends affecting the thermal transport pathway could serve as a starting point in pursuing this research area which may enable obtaining targeted thermal conductivities. The molecular origin of various kinds of intermolecular interactions, bridging the bonding between molecules, affecting the phonon transport and thus the thermal conductivity of these structures is largely unknown, which, if possible, could help guide the thermal management of multiple beneficial devices.

The simultaneous improvement in strength and toughness is typically absent for traditional materials. But such a challenge has been addressed in some materials such as MXenes,¹²⁸ metal oxides,^{129,130} cellulose,¹⁸ dendrite composites^{131–133} and carbon-based composites^{130,134} by adopting different intermolecular bonding strategies. Applications of these strategies alter the material nano/micro-structure through different processes such as self-assembly, the introduction of anisotropy and/or chemically modified molecules or functional groups. These processes, along with the modifications they induce on the final mechanical properties, are well-documented. However, there is a lack of standardized experimental evidence that elucidates the mechanism of enhancement or weakening of the mechanical properties due to implementing these strategies. For example, an accurate, stepwise representation of a generalized failure mechanism in the resulting mechanically superior materials is still elusive. Furthermore, intercalated ions and molecules influence the enhancement of the mechanical properties, such as cellulose intercalated with water molecules¹³⁵ or polymers/graphene intercalated with ions.¹³⁶ Experimental results on increased mechanical strength by increasing the proportion of ions/molecules have also been demonstrated.¹³⁷ But there is still no research, to the best of our knowledge, which delineates the mechanism illustrating how this intercalation process evolves. Such knowledge may help identify the parameters that govern what ratio of intercalated ions/molecules best optimizes the mechanical properties. Without a proper understanding of a generalized mechanism, different intermolecular bonding techniques applied by various research groups lead to materials with diverse final

morphology. Such practice might make that specific material suitable for selected use but prohibits extending that study to multifaceted applications.

One of the unique features of successful intermolecular bonding is the development of large failure strain and remarkable thermal stability, as already discussed before. As a result, applications of such materials may become feasible in extreme environments caused by external factors such as, but not limited to, high temperature, pressure, or humidity. For example, a polyimide-based sensor,¹³⁸ comprised of ether and anhydride, could survive a wide spectrum of temperatures ranging from -150°C to 300°C and withstanding high deformations. It might make its applications possible for recording temperature in non-contact mode, a desirable feature for wireless temperature sensing. Similar other representative studies exist which elucidate how to achieve superlative electronic properties in extreme environments (e.g., flame, high pressure, and humidity).^{139–141} But the detailed process describing how the intermolecular bonding evolves in extreme environments and modifies the electronic properties is still unknown. Shedding light on this topic might be a great perspective for future researchers.

Another challenge that researchers should address is the large gap that exists in scaling up the bottoms-up design of tuning the intermolecular bonds towards bulk materials properties. Fundamental building blocks often have superior mechanical properties that are order of magnitudes higher than the bulk material. For example, isolated crystalline cellulose nanocrystals may have high strength (1.6-7.7 GPa)^{142,143} and stiffness (150 GPa),^{144–146} but natural wood that primarily contains cellulose has much lower strength (100MPa) and stiffness (few GPa).¹⁴⁷ Efforts are ongoing to correlate the molecular

properties with the bulk for materials such as, but not limited to, biomimetic polymers¹⁴⁸ and gel.¹⁴⁹ There, the force spectroscopy between functional groups have been demonstrated to agree reasonably well with the bulk mechanical properties, but these strategies are still far from being standardized. Furthermore, developing a prototype material in the lab often focuses on obtaining superior physical properties by overlooking other important aspects, such as a robust life cycle analysis of the entire process and wastage of chemicals or water. But neglecting these aspects might hinder the industrial-scale fabrication of these advanced materials.

Another significant hurdle that needs to be overcome, is scaling up the computational modeling framework and predict properties of advanced materials.¹⁵⁰ The nanoscale phenomenon become negligible at the continuum level, whereas continuum mechanics cannot consider the beneficial effects of microscale and molecular level. So, to capture all the properties dominated by structure and composition in the new material, a robust theoretical framework that incorporates multiscale mechanics and cross-scale modeling, is needed. There exist constraints to develop such as framework mainly because of the limitations on the existing computational capabilities.^{151,152} But when experimentation becomes unfeasible, computational materials modeling can be entrusted¹⁵³ to lead the research efforts. To that end, data-driven materials modeling techniques might be suitable.

Novel computational techniques such as machine learning (ML) aided materials discovery^{154–161} might provide another avenue to accelerate materials design by various intermolecular bonding strategies. For example, hydrogen bond donor and acceptor strengths¹⁶² in chloroform (CCl₄) were determined using ML methods with values quite

close to experiments, typically done using infrared spectroscopy techniques. This can prove to be a fast predictor by substituting experiments and avoiding repeated trial and error that wet lab experimental procedures typically entail, as well as significantly reducing the time taken for manually identifying useful hydrogen bond strength information after navigating previous literature. However, the hydrogen bond energy databases to train the ML models need to be expanded significantly to apply to other molecules beyond CCl_4 . Furthermore, unlocking the nature of chemical bonding between different molecules by evaluating how different molecules bind with each other could help realize how to control the strength of bonds by ML-based models. Some research on this domain has been done by applying the Bayesian learning-based model¹⁶³ to decipher how catalysts bind with different intermediate molecules leading to efficient catalytic processes and may have the potential to be extended to separate processes. There exist fertile opportunities for new materials development by tuning intermolecular bonds that call for collaborations among interdisciplinary researchers. Such collaborations will help in exploring the facile, unconventional strategy of programming materials properties by engineering intermolecular bonding. The rational materials design scheme obtained as a result, will help deliver unique materials and simultaneously reap multiple benefits for humanity, such as reducing energy consumption and diminishing carbon footprint.

Appendices

Appendix I: List of publications⁸

1. **U. Ray**, Z. Pang, T. Li, “Mechanics of cellulose nanopaper using a scalable coarse-grained modeling scheme”, *Cellulose* 28 (6), 3359-3372, 2021.
2. **U. Ray**, S. Zhu, Z. Pang, T. Li, “Mechanics design in cellulose-enabled high performance functional materials”, *Advanced Materials* 33 (28), 2002504, 2021.
3. **U. Ray**, S. Zhu, Z. Pang, T. Li, “Nanocellulose based Materials with Superior Mechanical Performance”, “Emerging Nanotechnologies in Nanocellulose” under Nanoscience and Technology book series, *Springer* 141-178, 2023.
4. **U. Ray**, Z. Pang, T. Li, “Programming material properties by tuning intermolecular bonding”, *Journal of Applied Physics* 132 (21), 210703, 2022.
5. Y. Li, H. Zhu (co-first), Y. Wang (co-first), **U. Ray (co-first)**, S. Zhu, J. Dai, C. Chen, K. Fu, S-H. Jang, D. Henderson, T. Li, L. Hu, “Cellulose-Nanofiber-Enabled 3D Printing of a Carbon-Nanotube Microfiber Network”, *Small Methods* 1(10), 1700222, 2017.
6. **U. Ray**, Z. Pang, T. Li, “Investigating thermal conductivity and mechanical properties of a hybrid material based on Cellulose nanofibers and Boron Nitride nanotube using molecular dynamics simulations”, *under preparation*.

⁸ For routinely updated list, please check [Google Scholar](#).

7. J. Song, C. Chen, S. Zhu, M. Zhu, J. Dai, **U. Ray**, Y. Li, Y. Kuang, Y. Li, N. Quispe, Y. Yao, A. Gong, U. H. Leiste, H. A. Bruck, J. Y. Zhu, A. Vellore, H. Li, M. L. Minus, Z. Jia, A. Martini, T. Li, L. Hu, “Processing bulk natural wood into a high-performance structural material”, *Nature* 554 (7691), 224-228, 2018.
8. Y. Zhou, C. Chen, S. Zhu, C. Sui, C. Wang, Y. Kuang, **U. Ray**, D. Liu, A. Brozena, U. H. Leiste, N. Quispe, H. Guo, A. Vellore, H. A. Bruck, A. Martini, B. Foster, J. Lou, T. Li, L. Hu, “A printed, recyclable, ultra-strong and ultra-tough graphite structural material” *Materials Today*, 30, 17-25, 2019.
9. X. Wang, Z. Pang, C. Chen, Q. Xia, Y. Zhou, S. Jing, R. Wang, **U. Ray**, W. Gan, C. Li, G. Chen, B. Foster, T. Li, L. Hu, “All Natural, degradable, rolled-up straws based on cellulose micro- and nano-hybrid fibers”, *Advanced Functional Materials*, 30 (22), 1910417, 2020.
10. R. Wang, C. Chen, Z. Pang, X. Wang, Y. Zhou, Q. Dong, M. Guo, J. Gao, **U. Ray**, Q. Xia, Z. Lin, S. He, B. Foster, T. Li, L. Hu, “Fabrication of Cellulose–Graphite Foam via Ion Cross-linking and Ambient-Drying”, *Nano Letters*, 14 (12), 16723-16734, 2022.
11. C. Chen, J. Song, J. Cheng, Z. Pang, W. Gan, G. Chen, Y. Kuang, H. Huang, **U. Ray**, T. Li, L. Hu, “Highly elastic hydrated cellulosic materials with durable compressibility and tunable conductivity”, *ACS Nano*, 14 (12), 16723-16734, 2020.

12. A. Fox, **U. Ray**, T. Li “Thermal conductivity of graphene grain boundaries along arbitrary in-plane directions: a comprehensive molecular dynamics study”, *Journal of Applied Physics*, 125(1), 015101, 2019.
13. A. Fox, **U. Ray**, T. Li “Strength of graphene grain boundaries under arbitrary in-plane tension”, *Carbon* 142, 388-400, 2019.

Appendix II: Python code to generate the random network model of Figure 4.6

```
import numpy as np
import numpy.ma as ma # Masked arrays
import numpy.random as rnd
import scipy.spatial as sp
from sklearn.neighbors import NearestNeighbors as nbh

import time
import io
start_time = time.time()

rnd.RandomState(19043)

pi = np.pi

# Define containing
# For 45 beads in each chain, number of chains will be 3267
# For 60 beads in each chain, number of chains will be 2400
# For 75 beads in each chain, number of chains will be 1960

XMIN, XMAX = 0, 60000 #67000
YMIN, YMAX = 0, 15000 #67000
ZMIN, ZMAX = 0, 1000

# Characteristics of chains
NUM_BEADS = 75
BEADS_DEFICIT = 25
MIN_NUM_BEADS = NUM_BEADS - BEADS_DEFICIT # 6 #USED ONLY
FOR CUT FIBRE CONDITION, 30
NUM_CHAINS = 394
MAX_CHAIN_MASS = NUM_BEADS * NUM_CHAINS

INTER_BEAD_DIST = 203.04

# Tolerances
SAME_CHAIN_TOLERANCE = 110.0
INTER_CHAIN_TOLERANCE = 110.0

# Varying boundary – Used to change the boundary conditions from periodic,
non-periodic etc.

VARYING_BDRY = False
CUT_FIBRE = True
plots = True
```

Create random chain

```
def create_chain (xmax, ymax, zmax, length):
    trans_mat = np.diag([xmax,ymax,zmax])
    r = INTER_BEAD_DIST
    rand_dir = rnd.uniform(-np.pi, np.pi)
    rand_start = rnd.uniform(0,1,3) @ trans_mat # Transforms from (0,1) to (0, MAX)
    x1 = rand_start[0] + np.arange(length) * r * np.cos(rand_dir)
    y1 = rand_start[1] + np.arange(length) * r * np.sin(rand_dir)
    z1 = rand_start[2] + np.zeros(length)
    chain = np.array([x1, y1, z1]).T
    return(chain)
```

Simulate based on required structure

```
CHAINS = []
CHAINS_MASS = 0 # For CUT_FIBRE
N = len(CHAINS)
nbrs = None
```

if CUT_FIBRE:

```
    while True:
        if N % 10 == 0:
            print(N)
            chain = create_chain(XMAX, YMAX, ZMAX, NUM_BEADS)
            c1 = ma.array(chain)
            c1[:,0] = ma.masked_outside(c1[:,0], 0, XMAX)
            c1[:,1] = ma.masked_outside(c1[:,1], 0, YMAX)
            if type(c1.mask) == np.ndarray:
                ind = np.argwhere(c1.mask.sum(axis=1)==0).flatten()
            else:
                ind = np.array(range(len(chain)))
            if len(ind) < MIN_NUM_BEADS:
                continue # Too small
            else:
                if N > 0: # have existing chains
                    d, i = nbrs.kneighbors(chain[ind,:])
                    if d.min() < INTER_CHAIN_TOLERANCE:
                        continue # Too close
                if CHAINS_MASS + len(ind) > MAX_CHAIN_MASS: # Stops the chain
                    growing
                    break
                CHAINS_MASS += len(ind)
                CHAINS.append(chain[ind,:])
```

```

        nbrs = nbh(n_neighbors = 1,
algorithm='ball_tree').fit(np.concatenate(CHAINS, axis=0))
        N = len(CHAINS)
        print("Number of chains = ", N)
        print("Total mass = ", CHAINS_MASS)

if ~CUT_FIBRE:
    while N < NUM_CHAINS:
        if N % 10 == 0:
            print(N)
            chain = create_chain(XMAX, YMAX, ZMAX, NUM_BEADS)
            if VARYING_BDRY:
                chain[:,0] = chain[:,0] % XMAX # Modulo operator
                chain[:,1] = chain[:,1] % YMAX # Modulo operator
            else:
                #if not np.all((chain > 0) * (chain < XMAX)):
                if not np.all((chain[:,0] > 0) * (chain[:,0] < XMAX)) & np.all((chain[:,1] > 0)
* (chain[:,1] < YMAX)):
                    continue # drop if crossing boundary
                if N > 0: # have existing chains
                    d, i = nbrs.kneighbors(chain)
                    if d.min() < INTER_CHAIN_TOLERANCE:
                        continue
                # dists = [sp.distance.cdist(chain, u).min() for u in CHAINS]
                # if np.array(dists).min() < INTER_CHAIN_TOLERANCE:
                #     continue # If chain is too close to others, drop.
                CHAINS.append(chain)
                nbrs = nbh(n_neighbors = 1, algorithm='ball_tree').fit(np.concatenate(CHAINS,
axis=0))
                N = len(CHAINS)

```

#

```

## Explanation: Once I have a set of chains, the nearest neighbors algorithm (nbh)
creates a hierarchical structure of the distances which is an efficient algorithm. It can
generate model fast. Or else, it may take hours. This structure also allows distances
from a candidate point to each point in the chains to be calculated very quickly. This
structure is computed once for a set of chains, so over the while loop I don't have to
recompute distances each time I have to test a new chain, when the old chain fails. ##

```

```

# The nbrs.kneighbors(chain) provides two outputs: euclidean distances (d) and
# the index (i) which is stating which point is the closest to the candidate point.
# We just need d here. Checking the minimum distance between all the beads in the
chain and all the beads already created is sufficient, which d.min() is doing.

```

```

chain_matrix = np.concatenate([np.array(v) for v in CHAINS], axis = 0)
#x1 = np.matrix(np.tile(np.arange(NUM_BEADS)+1, NUM_CHAINS)).reshape(-
1,1)
#x3 = np.matrix(np.repeat(np.arange(NUM_CHAINS)+1, NUM_BEADS)).reshape(-
1,1)
x1 = np.arange(chain_matrix.shape[0])[:,np.newaxis]+1
x3 = np.repeat(np.arange(len(CHAINS))+1, [len(u) for u in CHAINS])[:,np.newaxis]
x2 = x1
x4 = np.zeros((len(x1),1))

out = np.concatenate([x1,x2,x3,x4,chain_matrix], axis = 1)

np.savetxt('output.txt', out, fmt = ['%d','%d','%d','%d','%6f','%6f','%6f'])
#%6f is 6 decimal floating point
#%d is integer

```

Plots

```

if(plots):
    ## 3-D plots

    from mpl_toolkits import mplot3d
    import matplotlib.pyplot as plt

    fig = plt.figure()
    ax = plt.axes(projection='3d')
    ax.view_init(45,azim=None)
    ax.set_xlim(0,XMAX)
    ax.set_ylim(0, YMAX)
    ax.set_zlim(0, ZMAX)

    for v in CHAINS:
        ax.plot3D(v[:,0],v[:,1], v[:,2],'.')

    plt.show()

    ## 2-D plots

    fig, ax = plt.subplots()
    ax.set_xlim(0, XMAX)
    ax.set_ylim(0, YMAX)
    for v in CHAINS:
        plt.plot(v[:,0], v[:,1],'.')
        #plt.plot(v[:,0], v[:,1], linewidth=1)

```

#Parameters for creating the LAMMPS data file

```
Atoms = CHAINS_MASS
#Bonds = (NUM_BEADS-1)*NUM_CHAINS
#Angles = (NUM_BEADS-2)*NUM_CHAINS
#Dihedrals = (NUM_BEADS-3)*NUM_CHAINS
Bonds = np.array([len(u)-1 for u in CHAINS]).sum()
Angles = np.array([len(u)-2 for u in CHAINS]).sum()
Dihedrals = np.array([len(u)-3 for u in CHAINS]).sum()

Bond_Types = 1
Angle_Types = 1
Dihedral_Types = 1
Improper_Types = 0

Bead_Mass = 1470939.523

print(Atoms)
print(Bonds)
print(Angles)
print(Dihedrals)

#####
##
# Write LAMMPS data file

with open('data_random.txt','w') as fdata:
    # First line is a comment line
    fdata.write('LAMMPS data file - written for Random network\n')
    fdata.write(' {} atoms\n'.format(int(Atoms)))
    fdata.write(' {} bonds\n'.format(int(Bonds)))
    fdata.write(' {} angles\n'.format(int(Angles)))
    fdata.write(' {} dihedrals\n'.format(int(Dihedrals)))
    fdata.write(' {} impropers\n'.format(int(Improper_Types)))
    #fdata.write(' {} atom types\n'.format(int(NUM_CHAINS)))# Non cut- fiber
condition
    fdata.write(' {} atom types\n'.format(int(N)))
    fdata.write(' {} bond types\n'.format(int(Bond_Types)))
    fdata.write(' {} angle types\n'.format(int(Angle_Types)))
    fdata.write(' {} dihedral types\n'.format(int(Dihedral_Types)))
    fdata.write(' {} improper types\n'.format(int(Improper_Types)))
    fdata.write('\n')
```

```

#SPACE
#fdata.write(' Test\n')

    # Specify box dimensions
    fdata.write(' {} {} xlo xhi\n'.format(float(XMIN), float(XMAX)))
    fdata.write(' {} {} ylo yhi\n'.format(float(YMIN), float(YMAX)))
    fdata.write(' {} {} zlo zhi\n'.format(float(ZMIN), float(ZMAX)))
    fdata.write('\n')

#Mass section
fdata.write(' Masses\n')
fdata.write('\n')

#fdata.write('1\n')
#for beads in range(1, NUM_CHAINS+1, 1): #FOR NON CUT FIBER
CONDITION
    for beads in range(1, N+1, 1): #CUT FIBER condition
        #print(beads, Bead_Mass)
        #print(n, '\t', 1470939.523)
        fdata.write(' {} {} \n'.format(beads, float(Bead_Mass)))
    fdata.write('\n')

# Atoms section
fdata.write(' Atoms\n\n')

s = io.BytesIO()
np.savetxt(s, out, fmt = ['%d', '%d', '%d', '%d', '%.6f', '%.6f', '%.6f'])
fdata.write(s.getvalue().decode())
fdata.write('\n')

# Bonds section
fdata.write(' Bonds\n\n')

#chain_id, bead_count = np.unique(np.array(x3.flatten()))[0], return_counts=True)
#NON-CUT
    chain_id, bead_count = np.unique(np.array(x3.flatten()), return_counts=True)
    curr = 1
    id = 1
    for i, count in zip(chain_id, bead_count):

```

```

    for j in range(count - 1):
        fdata.write('{}\t1\t{}\t{}\tChain #\t{}\n'.format(id, curr, curr + 1, i))
        curr += 1
        id += 1
    curr += 1
    fdata.write('\n')

# Angles section
    fdata.write(' Angles\n\n')

    #chain_id, bead_count = np.unique(np.array(x3.flatten()))[0], return_counts=True)
#NON-CUT
    chain_id, bead_count = np.unique(np.array(x3.flatten()), return_counts=True)
    curr = 1
    id = 1
    for i, count in zip(chain_id, bead_count):
        for j in range(count - 2):
            fdata.write('{}\t1\t{}\t{}\t{}\tChain #\t{}\n'.format(id, curr, curr + 1, curr+2,
i))
                curr += 1
                id += 1
            curr += 2
        fdata.write('\n')

# Dihedrals section
    fdata.write(' Dihedrals\n\n')

    #chain_id, bead_count = np.unique(np.array(x3.flatten()))[0], return_counts=True)
#NON-CUT
    chain_id, bead_count = np.unique(np.array(x3.flatten()), return_counts=True)
    curr = 1
    id = 1
    for i, count in zip(chain_id, bead_count):
        for j in range(count - 3):
            fdata.write('{}\t1\t{}\t{}\t{}\t{}\tChain#\t{}\n'.format(id, curr, curr + 1,
curr+2, curr+3, i))
                curr += 1
                id += 1
            curr += 3

    print("--- %s seconds ---" % (time.time() - start_time))

```


Appendix III: Stepwise preparation of cellulose-graphite slurry

The graphite-cellulose hybrid composite material described in Section 1.4.2 was fabricated from a slurry, which was then poured into a mold and hot-pressed. The process of making the slurry consisted of three main steps as detailed in the following three sub-sections.

Step 1: TEMPO-Oxidation treatment

The TEMPO oxidation is a selective oxidation treatment which oxidizes the C6 carbon atom in the cellulose molecule to -COOH which stabilizes the molecular chain and isolates the cellulose fibers from the raw pulp (source- Alpen). The ingredients used in the chemical treatment are tabulated in Table A.3.1.

Table A.3.1 Ingredients used in the TEMPO-oxidation chemical treatment

Steps	Ingredient details
1) Buffer solution	8.48 gm Na_2CO_3 & 1.68 gm NaHCO_3 in 1000 ml DI water
2) NaBr solution	3.086 gm NaBr mixed with 300 ml of buffer solution
3) TEMPO solution	468.75 mg TEMPO mixed with 100 ml of buffer solution
4) Wood pulp	30gm pulp mixed with 900 ml of buffer solution.
5) NaClO required	65 ml
6) TEMPO process	Reduce the pH to 10.5 and then keep it constant around 10.48
7) Filtration	2-3 times

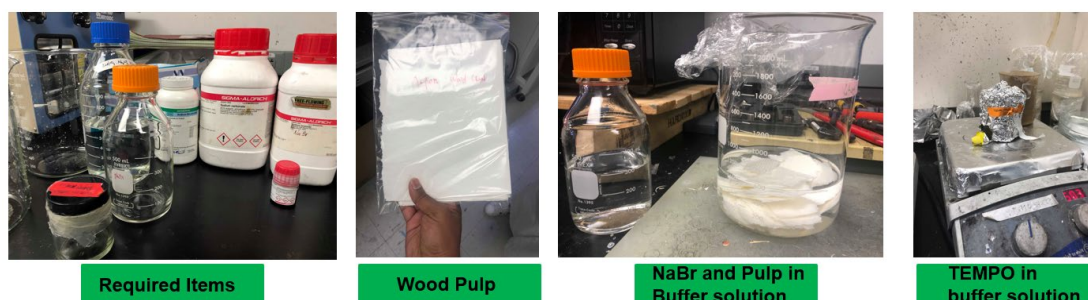


Figure A.3.1 Images showing necessary ingredients (Na_2CO_3 , NaHCO_3 , NaBr , Pulp, TEMPO) for preparation of the buffer solution before starting the TEMPO-oxidation.

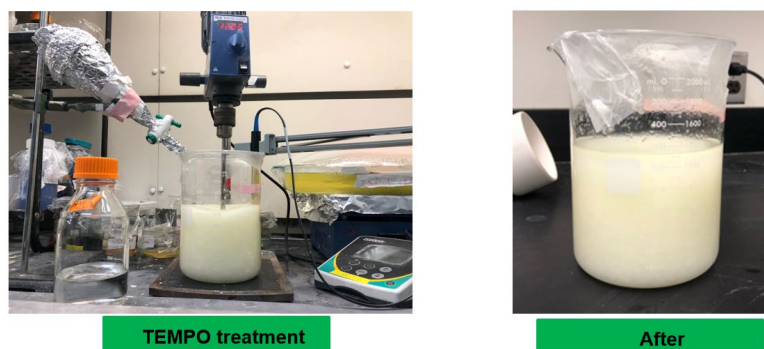


Figure A.3.2 The next step is the actual TEMPO treatment, where the pH is monitored and maintained ~ 10.48 by dropping NaOH dropwise. NaClO is also poured dropwise (1 drop in 6-8 seconds) to carry out the reaction. The entire process takes around 3 hours.

Step 2: Filtration and Homogenization

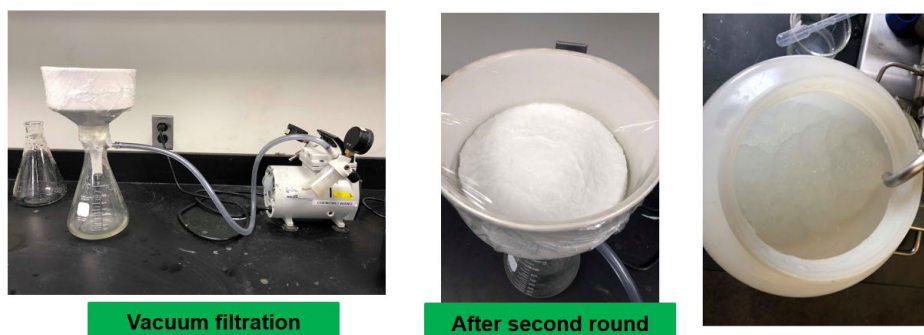


Figure A.3.3 Images after TEMPO treatment involving vacuum filtration (left and middle panels), followed by homogenization (using a Microfluidizer device) under a maintained pressure of 20000 psi (right panel).

Step 3: Ultrasonication and centrifugation to obtain cellulose-graphite slurry

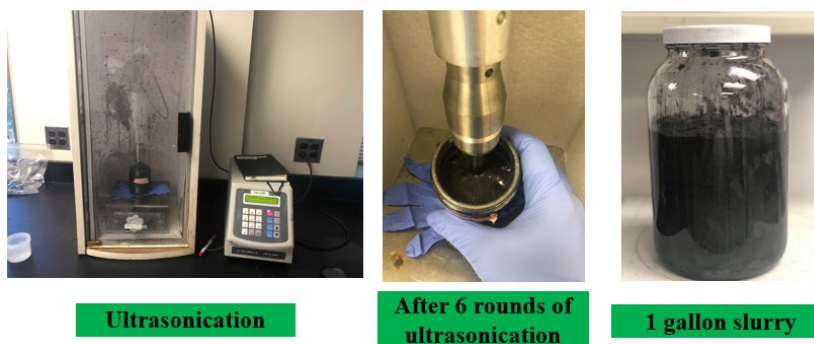


Figure A.3.4 The homogenized cellulose sample is mixed with commercial graphite powder and then ultrasonicated (left panel) around six times. This creates a uniform cellulose graphite dispersion (middle panel). Then the dispersion is subjected to centrifugation to remove the bulkier graphite flakes and the final slurry is obtained (right panel).

Appendix IV: Author Biography⁹




Upamanyu Ray conducted his doctoral research in the Department of Mechanical Engineering at the University of Maryland College Park, USA. His doctoral research centered around deciphering novel polymer sciences, with a focus on biopolymers such as cellulose. He is skilled in multi-scale materials modeling, along with experiments leading to fabrication and mechanical testing of advanced polymers. During his doctoral studies, he also spent around 4 years on a separate industry collaboration, where the team goal was to fabricate lightweight, strong cellulose-based functional materials. Prior to doctoral research, Upamanyu received his M.S and B.S. degrees, both in Mechanical Engineering, from Iowa State University (Ames, USA) and Jadavpur University (Kolkata, India), respectively.

Besides research, Upamanyu was a Teaching Assistant (TA) supporting the course instructor in designing/grading homework and labs, helping undergraduate/graduate students with coursework related problems, and guiding students in laboratories by acting as a Lab Instructor. The different courses where Upamanyu was in-charge as a TA were Applied Machine Learning for Engineering and Design, Introduction to Sensors, Electronics & Instrumentation, Engineering Mechanics, and Heat Transfer.

⁹ For correspondence, please connect on [LinkedIn](#).

Upamanyu has won different awards and honors during his stint as a doctoral student at the University of Maryland College Park (UMD). For example, he was the **finalist** (top 8 out of ~130) for the Dean's Dissertation Fellowship (May 2019). He was adjudged the **Best Speaker in Oral Presentation** (out of 123 speakers) at the "Graduate Research Appreciation Day" (April 2019). For his research activities, Upamanyu has earned the **Outstanding Graduate Research Assistant Award** (top 1%), conferred by the Clark School of Engineering of UMD (May 2019). To showcase research to the public, Upamanyu was an **Invited Speaker** at GradTerp Exchange (modeled on TEDx talks) organized by the Graduate School of UMD (October 2018). He has served the Graduate School by being part of the **search committee as a student representative**, to recruit their Assistant Dean (January 2022). As one of the top five TAs, Upamanyu has also served the Department of Mechanical Engineering at UMD by **co-leading the "TA Seminar Series"** to mentor first-time Teaching Assistants (August 2022-December 2022).



THE GRADUATE SCHOOL

Advancing graduate education.
Enhancing the graduate student experience.

[About](#) • [Admissions](#) • [Graduate Programs](#) • [Funding](#) • [Policies](#) • [Students](#) • [Faculty & Staff](#) • [Alumni & Friends](#)

HOME

GRADUATE SCHOOL WRITING CENTER

MEET THE FELLOWS

SHARE

Meet the Fellows

Writing Fellows are a select group of graduate students recommended by their departments for their demonstrated mastery of writing in their disciplines and their aptitude for peer review. Oral Communication Fellows are all advanced graduate students from the Communication Department. In ongoing training with the GSWC Director, fellows develop an understanding of writing and oral communication in the disciplines and theories of peer support, among other topics.

Learn more about the work our fellows do in this feature article, "[Meet the Writing Center Fellows](#)."

Director: [Linda Macri](#)

Writing Fellows

Ahana Mallick (Biological Sciences)	Natalie Cmosija (Environmental Health)	Courtney Douglass (Education)
Clark J. Lee (Public Health)	Melissa Sturges (Theatre, Dance & Performance Studies)	Kelsey Dutta (Engineering)
Upamanyu Ray (Engineering)	Kristina Kramarczuk (Education)	Danielle LaPlace (Women, Gender and Sexuality Studies)
Jared Strange (Theatre and Performance Studies)	Kathryn Thier (Communication)	Kristyn Lue (Education)
Rashe Alkhateeb (Education)	Lance Curtis (Mechanical Engineering)	Tony Febbri (Reliability Engineering in Systems Science)
Faith Sears (Teaching and Learning, Policy and Leadership)	Sahra Ibrahim (Maternal and Child Health)	Adway Petra (Electrical and Computer Engineering)
Erin Green (English)	Sam DiBella (Information Studies)	Lauren Samuelson (Public Policy)

GRADUATE SCHOOL WRITING CENTER

Request a Consultation

Apply to Be a Fellow

Cultural and Linguistic Awareness

Meet the Fellows

Oral Communication Consultations

Workshops, Retreats, and Write-Ins

Writing Groups

Using Sources

CONTACT INFORMATION

Graduate School Writing Center

5100B McKeldin Library
College Park, MD 20742
301-405-9871
gradwritingfellows@umd.edu
[@GradWritingCent](#)

Request a consultation
Spring Drop-In Hours: Wednesdays
and Thursdays, 12:00-3:00pm

Figure A.4.1 A snapshot (taken December 2022) including some details of the Writing Fellow cohort.

Another integral part of Upamanyu's academic service has been his role as a Writing Fellow at the [Graduate School Writing Center at UMD](#) for over 4 years. This is a competitive position where a cohort of ~20 people are selected. Some details on the cohort and their goals are included in Figure A.4.1. Upamanyu was the first graduate student from the Department of Mechanical Engineering at UMD to hold this position. At the Writing Center, Upamanyu's role was to lead writing workshops intermittently

and conduct weekly one-on-one consultations with two clients (4 hours) to revise their manuscripts, which would focus on diverse disciplines ranging from liberal arts, social sciences, and STEM related fields.

Bibliography

Chapter 1

1. Ritchie, R. O. The conflicts between strength and toughness. *Nat. Mater.* **10**, 817–822 (2011).
2. Hofmann, D. C. *et al.* Designing metallic glass matrix composites with high toughness and tensile ductility. *Nature* **451**, 1085–1090 (2008).
3. Evans, A. G. Perspective on the development. *J. Am. Ceram. Soc.* **73**, 187–206 (1990).
4. Launey, B. M. E. & Ritchie, R. O. On the Fracture Toughness of Advanced Materials. *Adv. Mater.* **21**, 2103–2110 (2009).
5. Lu, K., Lu, L. & Suresh, S. Strengthening Materials by Engineering Coherent Internal Boundaries at the Nanoscale. *Science*. **324**, 349–353 (2009).
6. Lu, L., Chen, X., Huang, X. & Lu, K. Revealing the Maximum Strength. *Science*. **323**, 607–611 (2009).
7. Lu, L., Shen, Y., Chen, X., Qian, L. & Lu, K. Ultrahigh Strength and High Electrical Conductivity in Copper. *Science*. **304**, 422–427 (2004).
8. Greer, J. R., Th, J. & Hosson, M. De. Plasticity in small-sized metallic systems: Intrinsic versus extrinsic size effect. *Prog. Mater. Sci.* **56**, 654–724 (2011).
9. Deng, C. & Sansoz, F. Near-Ideal Strength in Gold Nanowires Design. *ACS Nano* **3**, 3001–3008 (2009).
10. Zhu, T. & Li, J. Ultra-strength materials. *Prog. Mater. Sci.* **55**, 710–757 (2010).
11. Zhu, H. *et al.* Anomalous scaling law of strength and toughness of cellulose nanopaper. *PNAS* **112**, 8971–8976 (2015).
12. Moon, R. J., Martini, A., Nairn, J. & Youngblood, J. Cellulose nanomaterials

- review: structure, properties, and nanocomposites. *Chem. Soc. Rev.* **40**, 3941–3994 (2011).
13. Klemm, D. *et al.* Nanocelluloses: A New Family of Nature-Based Materials. *Angew. Chemie Int. Ed.* **50**, 5438–5466 (2011).
 14. Klemm, D., Heublein, B., Fink, H.-P. & Bohn, A. Cellulose : Fascinating Biopolymer and Sustainable Raw Material Angewandte. *Angew. Chemie Int. Ed.* **44**, 3358–3393 (2005).
 15. Khalil, H. P. S. A., Bhat, A. H. & Yusra, A. F. I. Green composites from sustainable cellulose nanofibrils: A review. *Carbohydr. Polym.* **87**, 963–979 (2012).
 16. Chinga-carrasco, G. Cellulose fibres , nanofibrils and microfibrils : The morphological sequence of MFC components from a plant physiology and fibre technology point of view. *Nanoscale Res. Lett.* **6**, 1–7 (2011).
 17. Lavoine, N., Desloges, I., Dufresne, A. & Bras, J. Microfibrillated cellulose – Its barrier properties and applications in cellulosic materials: A review. *Carbohydr. Polym.* **90**, 735–764 (2012).
 18. Isogai, A., Saito, T. & Fukuzumi, H. TEMPO-oxidized cellulose nanofiber. *Nanoscale* **3**, 71–85 (2011).
 19. Ahmed, M., Azizi, S., Alloin, F. & Dufresne, A. Review of Recent Research into Cellulosic Whiskers, Their Properties and Their Application in Nanocomposite Field. *Biomacromolecules* **6**, 612–626 (2005).
 20. Zhu, H. *et al.* Tin Anode for Sodium-Ion Batteries Using Natural Wood Fiber as a Mechanical Buffer and Electrolyte Reservoir. *Nano Lett.* **13**, 3093–3100

(2013).

21. Zhu, H., Fang, Z., Preston, C., Li, Y. & Hu, L. Environmental Science device applications. *Energy Environ. Sci.* **7**, 269–287 (2014).
22. Li, Y. *et al.* Hybridizing wood cellulose and graphene oxide toward high-performance fibers. *NPG Asia Mater.* **7**, e150 (2015).
23. Fang, Z. *et al.* Novel Nanostructured Paper with Ultrahigh Transparency and Ultrahigh Haze for Solar Cells. *Nano Lett.* **14**, 765–773 (2014).
24. Zhang, Q. *et al.* Nanocellulose-Enabled, All-Nanofiber, High-Performance Supercapacitor. *ACS Appl. Mater. Interfaces* **11**, 5919–5927 (2019).
25. Jia, C. *et al.* From Wood to Textiles: Top-Down Assembly of Aligned Cellulose Nanofibers. *Adv. Mater.* **30**, 1801347 (2018).
26. Klemm, D. *et al.* Nanocelluloses as Innovative Polymers in Research and Application. (Fig. 31, p87) *Adv Polym Sci* **205**, 49–96 (2006).
27. Nelson, K., Retsina, T., Lakovlev, M. & van Heiningen, A. in *Catalytic Materials: Nanofibers-From Research to Manufacture* 267–302 (2016).
28. Bajpai, P. *Pulp and Paper Industry: Chemical Recovery*. (2017).
29. Nelson, K. *Agenda 2020 Cellulose Nanomaterials Research Roadmap*. (2016).
30. Song, J. *et al.* Processing bulk natural wood into a high-performance structural material. *Nature* **554**, 224–228 (2018).
31. Zhou, Y. *et al.* A Printed, Recyclable, Ultra-Strong and Ultra-Tough Graphite Structural Material. *Materials. Today*, (2019).
32. Plimpton, S. Fast parallel algorithms for short-range molecular dynamics. *J. Comput. Phys.* **117**, 1–19 (1995).

33. Humphrey, W., Dalke, A. & Schulten, K. VMD: Visual Molecular Dynamics. *J. Mol. Graph.* **14**, 33–38 (1996).
34. Stukowski, A. Visualization and analysis of atomistic simulation data with OVITO – the Open Visualization Tool Visualization and analysis of atomistic simulation data with OVITO – the Open Visualization Tool. *Model. Simul. Mater. Sci. Eng.* **18**, 015012 (2010).
35. Shishehbor, M. & Zavattieri, P. D. Journal of the Mechanics and Physics of Solids Effects of interface properties on the mechanical properties of bio-inspired cellulose nanocrystal (CNC) -based materials. *J. Mech. Phys. Solids* **124**, 871–896 (2019).
36. Shishehbor, M., Dri, F. L., Moon, R. J. & Zavattieri, P. D. Journal of the Mechanics and Physics of Solids A continuum-based structural modeling approach for cellulose nanocrystals (CNCs). *J. Mech. Phys. Solids* **111**, 308–332 (2018).
37. Fan, B. & Maranas, J. K. Coarse-grained simulation of cellulose Ib with application to long fibrils. *Cellulose* **22**, 31–44 (2015).
38. Rudd, R. E. & Broughton, J. Q. Coarse-grained molecular dynamics and the atomic limit of finite elements. *Phys. Rev. B* **58**, 5893–5896 (1998).
39. Bond, P. J., Holyoake, J., Ivetac, A., Khalid, S. & Sansom, M. S. P. Coarse-grained molecular dynamics simulations of membrane proteins and peptides. *J. Struct. Biol.* **157**, 593–605 (2007).
40. Wang, Y., Jiang, W. E. I., Yan, T. & Voth, G. A. Understanding Ionic Liquids through Atomistic and Coarse-Grained Molecular Dynamics Simulations

- Multiscale Coarse-Graining Method. *Acc. Chem. Res.* **40**, 1193–1199 (2007).
41. Padding, J. & Briels, W. J. Time and length scales of polymer melts studied by coarse-grained molecular dynamics simulations. *J. Chem. Phys.* **117**, 925 (2002).
 42. Qin, X., Feng, S., Meng, Z. & Keten, S. Optimizing the mechanical properties of cellulose nanopaper through surface energy and critical length scale considerations. *Cellulose* **24**, 3289–3299 (2017).

Chapter 2

1. T. Li, M. Zhu, Z. Yang, J. Song, J. Dai, Y. Yao, W. Luo, G. Pastel, B. Yang, L. Hu, *Adv. Energy Mater.* **2016**, 6, 1601122.
2. A. . Bledzki, J. Gassan, *Prog. Polym. Sci* **1999**, 24, 221.
3. H. Zhu, W. Luo, P. N. Ciesielski, Z. Fang, J. Y. Zhu, G. Henriksson, M. E. Himmel, L. Hu, *Chem. Rev.* **2016**, 116, 9305.
4. M. Frey, G. Biffi, M. Adobes-vidal, M. Zirkelbach, Y. Wang, K. Tu, A. M. Hirt, K. Masania, I. Burgert, T. Keplinger, *Adv. Sci.* **2019**, 6, 1802190.
5. L. A. Berglund, I. Burgert, *Adv. Mater.* **2018**, 30, 1704285.
6. F. Jiang, T. Li, Y. Li, Y. Zhang, A. Gong, J. Dai, E. Hitz, W. Luo, L. Hu, *Adv. Mater.* **2018**, 30, 1.
7. E. Kontturi, P. Laaksonen, M. B. Linder, Nonappa, A. H. Gröschel, O. J. Rojas,

- O. Ikkala, *Adv. Mater.* **2018**, *30*.
8. B. Thomas, M. C. Raj, B. K. Athira, H. M. Rubiyah, J. Joy, A. Moores, G. L. Drisko, C. Sanchez, *Chem. Rev.* **2018**, *118*, 11575.
 9. Y. Zhou, C. Chen, S. Zhu, C. Sui, C. Wang, Y. Kuang, U. Ray, D. Liu, A. Brozena, U. H. Leiste, N. Quispe, H. Gui, A. Vellore, H. A. Bruck, A. Martini, B. Foster, J. Lou, T. Li, L. Hu, *Mater. Today* **2019**, *30*, 17.
 10. Y. Li, H. Zhu, Y. Wang, U. Ray, S. Zhu, J. Dai, C. Chen, K. Fu, S.-H. Jang, D. Henderson, T. Li, L. Hu, *Small Methods* **2017**, *1*, 1700222.
 11. J. Kim, G. Montero, Y. Habibi, J. P. Hinestroza, J. Genzer, S. Argyropoulos, Dimitris, O. J. Rojas, *Polym. Eng. Sci.* **2009**, 2054.
 12. X. Zeng, J. Sun, Y. Yao, R. Sun, J. Xu, C. Wong, *ACS Nano* **2017**, *11*, 5167–5178 Article.
 13. N. Song, D. Jiao, P. Ding, S. Cui, S. Tang, L. Shi, *J. Mater. Chem. C* **2016**, *4*, 305.
 14. M. M. Hamed, A. Hajian, A. B. Fall, K. Hkansson, M. Salajkova, F. Lundell, L. Wgberg, L. A. Berglund, *ACS Nano* **2014**, *8*, 2467.
 15. S. Wang, T. Li, C. Chen, W. Kong, S. Zhu, J. Dai, A. J. Diaz, E. Hitz, S. D. Solares, T. Li, L. Hu, *Adv. Funct. Mater.* **2018**, *28*, 1707491.
 16. N. Mittal, F. Ansari, K. G. V, C. Brouzet, P. Chen, P. T. Larsson, S. V Roth, F. Lundell, L. Wa, N. A. Kotov, L. D. Soderberg, *ACS Nano* **2018**, *12*, 6378.

17. J. Bras, D. Viet, C. Bruzzese, A. Dufresne, *Carbohydr. Polym.* **2011**, *84*, 211.
18. J. Song, C. Chen, S. Zhu, M. Zhu, J. Dai, U. Ray, Y. Li, Y. Kuang, Y. Li, N. Quispe, Y. Yao, A. Gong, U. H. Leiste, H. A. Bruck, J. Y. Zhu, A. Vellore, H. Li, M. L. Minus, Z. Jia, A. Martini, T. Li, L. Hu, *Nature* **2018**, *554*, 224.
19. Z. M. Ali, L. J. Gibson, *Soft Matter* **2013**, *9*, 1580.
20. K. Nelson, T. Retsina, M. Lakovlev, A. van Heiningen, in *Catal. Mater. Nanofibers-From Res. to Manuf.*, **2016**, 267–302.
21. T. Saito, R. Kuramae, J. Wohler, L. A. Berglund, A. Isogai, *Biomacromolecules* **2013**, *14*, 248.
22. R. M. A. Domingues, M. E. Gomes, R. L. Reis, *Biomacromolecules* **2014**, *15*, 2327.
23. S. Iwamoto, W. Kai, A. Isogai, T. Iwata, *Biomacromolecules* **2009**, *10*, 2571.
24. R. T. Olsson, M. A. S. Azizi Samir, G. Salazar-Alvarez, L. Belova, V. Ström, L. A. Berglund, O. Ikkala, J. Nogués, U. W. Gedde, *Nat. Nanotechnol.* **2010**, *5*, 584.
25. A. Šturcová, G. R. Davies, S. J. Eichhorn, *Biomacromolecules* **2005**, *6*, 1055.
26. F. J. Martin-Martinez, K. Jin, D. López Barreiro, M. J. Buehler, *ACS Nano* **2018**, *12*, 7425.
27. D. Lavanya, P. K. Kulkarni, M. Dixit, P. K. Raavi, L. N. V. Krishna, *Int. J. Drug*

Formul. Res. **2011**, 2, 19.

28. T. W. Crowther, H. B. Glick, K. R. Covey, C. Bettigole, D. S. Maynard, S. M. Thomas, J. R. Smith, G. Hintler, M. C. Duguid, G. Amatulli, M. N. Tuanmu, W. Jetz, C. Salas, C. Stam, D. Piotto, R. Tavani, S. Green, G. Bruce, S. J. Williams, S. K. Wiser, M. O. Huber, G. M. Hengeveld, G. J. Nabuurs, E. Tikhonova, P. Borchardt, C. F. Li, L. W. Powrie, M. Fischer, A. Hemp, J. Homeier, P. Cho, A. C. Vibrans, P. M. Umunay, S. L. Piao, C. W. Rowe, M. S. Ashton, P. R. Crane, M. A. Bradford, *Nature* **2015**, 525, 201.
29. E. Novaes, M. Kirst, V. Chiang, H. Winter-Sederoff, R. Sederoff, *Plant Physiol.* **2010**, 154, 555.
30. C. Plomion, A. Stokes, C. P. France, L. De Rhe, *Plant Physiol.* **2001**, 127, 1513.
31. H. Zhu, Z. Fang, C. Preston, Y. Li, L. Hu, *Energy Environ. Sci.* **2014**, 7, 269.
32. H. Zhu, Z. Jia, Y. Chen, N. Weadock, J. Wan, O. Vaaland, X. Han, T. Li, L. Hu, *Nano Lett.* **2013**, 13, 3093.
33. P. S. Mukherjee, K. G. Satyanarayana, *J. Mater. Sci.* **1986**, 21, 51.
34. S. R. D. Petroudy, in *Adv. High Strength Nat. Fibre Compos. Constr.*, Woodhead Publishing (Elsevier), **2017**, pp. 59–83.
35. A. K. Mohanty, M. Misra, L. T. Drzal, Eds. , *Natural Fibers, Biopolymers, and Biocomposites*, CRC Press, **2005**.
36. H. V. Scheller, P. Ulvskov, *Annu. Rev. Plant Biol.* **2010**, 61, 263.

37. Q. Liu, L. Luo, L. Zheng, *Int. J. Mol. Sci.* **2018**, *19*.
38. R. C. Sun, X. F. Sun, J. Tomkinson, in *Hemicellul. Sci. Technol.*, American Chemical Society, **2003**, pp. 2–22.
39. R. J. Moon, A. Martini, J. Nairn, J. Youngblood, *Chem. Soc. Rev.* **2011**, *40*, 3941.
40. J. Bidlack, M. Malone, R. Benson, *Proc. Oklahoma Acad. Sci.* **1992**, *72*, 51.
41. S. E. C. Whitney, M. G. E. Gothard, J. T. Mitchell, M. J. Gidley, *Plant Physiol.* **1999**, *121*, 657.
42. J. Pérez, J. Muñoz-Dorado, T. de la Rubia, J. Martínez, *Int. Microbiol.* **2002**, *53*.
43. X. Yang, F. Berthold, L. A. Berglund, *Biomacromolecules* **2018**, *19*, 3020.
44. C. Crestini, H. Lange, M. Sette, D. S. Argyropoulos, *Green Chem.* **2017**, *19*, 4104.
45. V. Pasangulapati, K. D. Ramachandriya, A. Kumar, M. R. Wilkins, C. L. Jones, R. L. Huhnke, *Bioresour. Technol.* **2012**, *114*, 663.
46. W. Fry, J. White, *Big Trees*, Stanford University Press, **1938**.
47. S. Iwamoto, A. N. Nakagaito, H. Yano, *Appl. Phys. A Mater. Sci. Process.* **2007**, *89*, 461.
48. T. Zimmermann, N. Bordeanu, E. Strub, *Carbohydr. Polym.* **2010**, *79*, 1086.

49. S. Josset, P. Orsolini, G. Siqueira, A. Tejado, P. Tingaut, T. Zimmermann, *Artic. Nord. Pulp Pap. Res. J.* **2014**, 29, 167.
50. A. Isogai, T. Saito, H. Fukuzumi, *Nanoscale* **2011**, 3, 71.
51. M. Pääkko, M. Ankerfors, H. Kosonen, A. Nykänen, S. Ahola, M. Österberg, J. Ruokolainen, J. Laine, P. T. Larsson, O. Ikkala, T. Lindström, *Biomacromolecules* **2007**, 8, 1934.
52. M. Henriksson, G. Henriksson, L. A. Berglund, T. Lindström, *Eur. Polym. J.* **2007**, 43, 3434.
53. G. Siqueira, H. Abdillahi, J. Bras, A. Dufresne, *Cellulose* **2010**, 17, 289.
54. S. H. Lee, W. S. Kim, T. H. Han, *Sci. Hortic. (Amsterdam)*. **2009**, 122, 77.
55. I. Filpponen, D. S. Argyropoulos, *Biomacromolecules* **2010**, 11, 1060.
56. D. Liu, T. Zhong, P. R. Chang, K. Li, Q. Wu, *Bioresour. Technol.* **2010**, 101, 2529.
57. Y. Habibi, L. A. Lucia, O. J. Rojas, *Chem. Rev.* **2010**, 110, 3479.
58. U. Romling, M. Y. Galperin, *Trends Microbiol* **2015**, 23(9), 545.
59. R. M. Brown, J. H. M. Willison, C. L. Richardson, *Proc. Natl. Acad. Sci. U. S. A.* **1976**, 73, 4565.
60. C. Castro, R. Zuluaga, J. L. Putaux, G. Caro, I. Mondragon, P. Gañán, *Carbohydr. Polym.* **2011**, 84, 96.

61. R. Jonas, L. F. Farah, *Polym. Degrad. Stab.* **1998**, 59, 101.
62. Z. Wu, H. Liang, L. Chen, B. Hu, S. Yu, *Acc. Chem. Res.* **2016**, 49, 96.
63. B. V. Mohite, S. V V. Patil, *Biotechnol. Appl. Biochem.* **2013**, 101.
64. M. Iguchi, S. Yamanaka, A. Budhiono, *J. Mater. SC* **2000**, 35, 261.
65. E. J. Foster, R. J. Moon, U. P. Agarwal, M. J. Bortner, J. Bras, S. Camarero-Espinosa, K. J. Chan, M. J. D. Clift, E. D. Cranston, S. J. Eichhorn, D. M. Fox, W. Y. Hamad, L. Heux, B. Jean, M. Korey, W. Nieh, K. J. Ong, M. S. Reid, S. Renneckar, R. Roberts, J. A. Shatkin, J. Simonsen, K. Stinson-Bagby, N. Wanasekara, J. Youngblood, *Chem. Soc. Rev.* **2018**, 47, 2609.
66. R. J. Moon, G. T. Schueneman, J. Simonsen, *Jom* **2016**, 68, 2383.
67. R. J. Moon, A. Martini, J. Nairn, J. Simonsen, J. Youngblood, *Cellulose Nanomaterials Review: Structure, Properties and Nanocomposites*, **2011**.
68. M. A. Hubbe, O. J. Rojas, L. A. Lucia, M. Sain, *BioResources* **2008**, 3, 929.
69. K. Lu, L. Lu, S. Suresh, *Science* **2009**, 324, 349.
70. L. Lu, X. Chen, X. Huang, K. Lu, *Science* **2009**, 323, 607.
71. L. Lu, Y. Shen, X. Chen, L. Qian, K. Lu, *Science* **2004**, 304, 422.
72. T. Zhu, J. Li, *Prog. Mater. Sci.* **2010**, 55, 710.
73. J. R. Greer, J. Th, M. De Hosson, *Prog. Mater. Sci.* **2011**, 56, 654.

74. C. Deng, F. Sansoz, *ACS Nano* **2009**, 3, 3001.
75. R. O. Ritchie, *Nat. Mater.* **2011**, 10, 817.
76. A. G. Evans, *J. Am. Ceram. Soc.* **1990**, 73, 187.
77. D. C. Hofmann, J. Suh, A. Wiest, G. Duan, M. Lind, M. D. Demetriou, W. L. Johnson, *Nature* **2008**, 451, 1085.
78. B. M. E. Launey, R. O. Ritchie, *Adv. Mater.* **2009**, 21, 2103.
79. H. Zhu, S. Zhu, Z. Jia, S. Parvinian, Y. Li, O. Vaaland, L. Hu, T. Li, *Proc. Natl. Acad. Sci.* **2015**, 112, 8971.
80. M. Hervy, A. Santmarti, P. Lahtinen, T. Tammelin, K. Y. Lee, *Mater. Des.* **2017**, 121, 421.
81. R. S. Rivlin, A. G. Thomas, *J. Polym. Sci.* **1953**, 10, 291.
82. R. Sinko, S. Mishra, L. Ruiz, N. Brandis, S. Keten, *ACS Macro Lett.* **2014**, 3, 64.
83. R. Sinko, S. Keten, *J. Mech. Phys. Solids* **2015**, 78, 526.
84. Q. Meng, B. Li, T. Li, X. Feng, *Eng. Fract. Mech.* **2018**, 194, 350.
85. Q. Meng, B. Li, T. Li, X. Feng, *J. Mech. Phys. Solids* **2017**, 103, 22.
86. Q. Meng, T. J. Wang, *Appl. Mech. Rev.* **2019**, 71, 040801.
87. S. jin Kim, J. Jang, *Fibers Polym.* **2013**, 14, 909.

88. H. Fukuzumi, T. Saito, A. Isogai, *Carbohydr. Polym.* **2013**, *93*, 172.
89. Z. Fang, B. Li, Y. Liu, J. Zhu, G. Li, G. Hou, J. Zhou, X. Qiu, *Matter* **2020**, *2*, 1000.
90. Y. Chen, B. Geng, J. Ru, C. Tong, H. Liu, J. Chen, *Cellulose* **2017**, *24*, 4831.
91. R. Mao, N. Meng, W. Tu, T. Peijs, *Cellulose* **2017**, *24*, 4627.
92. A. Kulachenko, T. Denoyelle, S. Galland, S. B. Lindström, *Cellulose* **2012**, *19*, 793.
93. M. Shishehbor, F. L. Dri, R. J. Moon, P. D. Zavattieri, *J. Mech. Phys. Solids* **2018**, *111*, 308.
94. M. Shishehbor, P. D. Zavattieri, *J. Mech. Phys. Solids* **2019**, *124*, 871.
95. M. Frey, D. Widner, J. S. Segmehl, K. Casdorff, T. Keplinger, I. Burgert, *ACS Appl. Mater. Interfaces* **2018**, *10*, 5030.
96. P. Navi, F. Heger, *MRS Bull.* **2004**, *29*, 332.
97. T. Li, Y. Zhai, S. He, W. Gan, Z. Wei, M. Heidarinejad, D. Dalgo, R. Mi, X. Zhao, J. Song, J. Dai, C. Chen, A. Aili, A. Vellore, A. Martini, R. Yang, J. Srebric, X. Yin, L. Hu, *Science* **2019**, *364*, 760.
98. M. Zhu, T. Li, C. S. Davis, Y. Yao, J. Dai, Y. Wang, F. AlQatari, J. W. Gilman, L. Hu, *Nano Energy* **2016**, *26*, 332.
99. C. Jia, C. Chen, Y. Kuang, K. Fu, Y. Wang, Y. Yao, S. Kronthal, J. Song, F. Xu,

- B. Liu, L. Hu, *Adv. Mater.* **2018**, *30*, 1801347.
100. G. Wimmers, *Nat. Rev. Mater.* **2017**, *2*, 1.
101. D. Huang, J. Wu, C. Chen, X. Fu, A. H. Brozena, Y. Zhang, P. Gu, C. Li, C. Yuan, H. Ge, M. Lu, M. Zhu, L. Hu, Y. Chen, **2019**, *1903270*, 1.
102. Z. Fang, H. Zhu, Y. Yuan, D. Ha, S. Zhu, C. Preston, J. Huang, L. Hu, *Nano Lett.* **2014**, *14*, 765.
103. Q. Zhu, Q. Yao, J. Sun, H. Chen, X. Weihua, *Carbohydr. Polym.* **2019**, 115609.
104. A. B. Reising, R. J. Moon, J. P. Youngblood, *J. Sci. Technol. For. Prod. Process.* **2012**, *2*, 32.
105. I. Diddens, B. Murphy, M. Krisch, M. Muller, *Macromolecules* **2008**, *41*, 9755.
106. M. Zhu, Y. Wang, S. Zhu, L. Xu, C. Jia, J. Dai, J. Song, Y. Yao, Y. Wang, Y. Li, D. Henderson, W. Luo, H. Li, M. L. Minus, T. Li, L. Hu, *Adv. Mater.* **2017**, *29*, 1606284.
107. H. Sehaqui, N. E. Mushi, S. Morimune, M. Salajkova, T. Nishino, L. A. Berglund, *ACS Appl. Mater. Interfaces* **2012**, *4*, 1043.
108. H. Qi, C. Chang, L. Zhang, *Green Chem.* **2009**, *11*, 177.
109. S. Wang, F. Jiang, X. Xu, Y. Kuang, K. Fu, E. Hitz, L. Hu, *Adv. Mater.* **2017**, *29*, 1702498.
110. K. Zhu, C. Qiu, A. Lu, L. Luo, J. Guo, H. Cong, F. Chen, X. Liu, X. Zhang, H.

- Wang, J. Cai, Q. Fu, L. Zhang, *ACS Sustain. Chem. Eng.* **2018**, 6, 5314.
111. J. Yao, S. Chen, Y. Chen, B. Wang, Q. Pei, H. Wang, *ACS Appl. Mater. Interfaces* **2017**, 9, 20330.
112. S. Vitta, V. Thiruvengadam, *Curr. Sci.* **2012**, 102, 1398.
113. K. M. O. Håkansson, A. B. Fall, F. Lundell, S. Yu, C. Krywka, S. V. Roth, G. Santoro, M. Kvik, L. Prah Wittberg, L. Wågberg, L. D. Söderberg, *Nat. Commun.* **2014**, 5:4018.
114. T. Pullawan, A. N. Wilkinson, S. J. Eichhorn, *Biomacromolecules* **2012**, 13, 2528.
115. S. Xu, D. Liu, Q. Zhang, Q. Fu, *Compos. Sci. Technol.* **2018**, 156, 117.
116. H. C. Kim, J. W. Kim, L. Zhai, J. Kim, *Cellulose* **2019**, 26, 5821.
117. A. W. Martinez, S. T. Phillips, G. M. Whitesides, *Anal. Chem.* **2010**, 82, 3.
118. A. W. Martinez, S. T. Phillips, G. M. Whitesides, *Proc. Natl. Acad. Sci.* **2008**, 105, 19606.
119. E. Carrilho, S. T. Phillips, S. J. Vella, A. W. Martinez, G. M. Whitesides, *Anal. Chem.* **2009**, 81, 5990.
120. Y. Lin, H. Ren, S. Gauza, Y. Wu, Y. Zhao, J. Fang, S. Wu, *J. Disp. Technol.* **2006**, 2, 21.
121. W. Xia, X. Qin, Y. Zhang, R. Sinko, S. Keten, *Macromolecules* **2018**, 51, 10304.

122. H. Tang, N. Butchosa, Q. Zhou, *Adv. Mater.* **2015**, 27, 2070.
123. Y. Li, H. Zhu, S. Zhu, J. Wan, Z. Liu, O. Vaaland, S. Lacey, Z. Fang, H. Dai, T. Li, L. Hu, *NPG Asia Mater.* **2015**, 7, e150.
124. A. Walther, J. V. I. Timonen, I. Díez, A. Laukkanen, O. Ikkala, *Adv. Mater.* **2011**, 23, 2924.
125. K. Oksman, Y. Aitomäki, A. P. Mathew, G. Siqueira, Q. Zhou, S. Butylina, S. Tanpichai, X. Zhou, S. Hooshmand, *Compos. Part A Appl. Sci. Manuf.* **2016**, 83, 2.
126. Z. Wan, C. Chen, T. Meng, M. Mojtaba, Y. Teng, Q. Feng, D. Li, *ACS Appl. Mater. Interfaces* **2019**, 11, 42808.
127. M. Salajkova, L. Valentini, Q. Zhou, L. A. Berglund, *Compos. Sci. Technol.* **2013**, 87, 103.
128. H. D. Huang, C. Y. Liu, L. Q. Zhang, G. J. Zhong, Z. M. Li, *ACS Sustain. Chem. Eng.* **2015**, 3, 317.
129. W. Luo, J. Hayden, S. H. Jang, Y. Wang, Y. Zhang, Y. Kuang, Y. Wang, Y. Zhou, G. W. Rubloff, C. F. Lin, L. Hu, *Adv. Energy Mater.* **2018**, 8, 1.
130. A. Hajian, S. B. Lindström, T. Pettersson, M. M. Hamed, L. Wågberg, *Nano Lett.* **2017**, 17, 1439.
131. A. Hajian, Z. Wang, L. A. Berglund, M. M. Hamed, *Adv. Electron. Mater.* **2019**, 5, 1.

132. S. S. Rahatekar, A. Rasheed, R. Jain, M. Zammarano, K. K. Koziol, A. H. Windle, J. W. Gilman, S. Kumar, *Polymer (Guildf)*. **2009**, *50*, 4577.
133. X. Wang, P. Wu, *ACS Appl. Mater. Interfaces* **2018**, *10*, 34311.
134. W. T. Cao, C. Ma, D. S. Mao, J. Zhang, M. G. Ma, F. Chen, *Adv. Funct. Mater.* **2019**, *29*, 1.
135. M. Naguib, M. Kurtoglu, V. Presser, J. Lu, J. Niu, M. Heon, L. Hultman, Y. Gogotsi, M. W. Barsoum, *Adv. Mater.* **2011**, *23*, 4248.
136. H. Abushammala, J. Mao, *Molecules* **2019**, *24*, 2782.
137. Y. Yanagisawa, Y. Nan, K. Okuro, T. Aida, *Science*. **2018**, *359*, 72.
138. N. Mittal, R. Jansson, M. Widhe, T. Benselfelt, K. M. O. Håkansson, F. Lundell, M. Hedhammar, L. D. Söderberg, *ACS Nano* **2017**, *11*, 5148.
139. D. Ye, X. Lei, T. Li, Q. Cheng, C. Chang, L. Hu, L. Zhang, *ACS Nano* **2019**, *13*, 4843.
140. J. Cai, L. Zhang, *Biomacromolecules* **2006**, *7*, 183.
141. D. Ye, Q. Cheng, Q. Zhang, Y. Wang, C. Chang, L. Li, H. Peng, L. Zhang, *ACS Appl. Mater. Interfaces* **2017**, *9*, 43154.
142. K. Li, P. Wei, J. Huang, D. Xu, Y. Zhong, L. Hu, L. Zhang, J. Cai, *ACS Sustain. Chem. Eng.* **2019**, *7*, 15974.
143. Z. Shi, J. Huang, C. Liu, B. Ding, S. Kuga, J. Cai, L. Zhang, *ACS Appl. Mater.*

Interfaces **2015**, 7, 22990.

144. B. Wang, J. G. Torres-Rendon, J. Yu, Y. Zhang, A. Walther, *ACS Appl. Mater. Interfaces* **2015**, 7, 4595.
145. H. L. Gao, R. Zhao, C. Cui, Y. B. Zhu, S. M. Chen, Z. Pan, Y. F. Meng, S.M. Wen, C. Liu, H. A. Wu, S. H. Yu, *National Science Review* **2019**, 7, 73-83.
146. M. Henriksson, L. A. Berglund, P. Isaksson, T. Lindström, T. Nishino, *Biomacromolecules* **2008**, 9, 1579.
147. S. Galland, F. Berthold, K. Prakobna, L. A. Berglund, *Biomacromolecules* **2015**, 16, 2427.
148. M. Özkan, M. Borghei, A. Karakoç, O. J. Rojas, J. Paltakari, *Sci. Rep.* **2018**, 8, 1.
149. M. Özkan, A. Karakoç, M. Borghei, J. Wiklund, O. J. Rojas, J. Paltakari, *Polym. Compos.* **2019**, 40, 4013.
150. A. G. Cunha, M. Lundahl, M. F. Ansari, L. Johansson, J. M. Campbell, O. J. Rojas, *ACS Appl. Nano Mater.* **2018**, 1, 5279.
151. M. J. Lundahl, A. G. Cunha, E. Rojo, A. C. Papageorgiou, L. Rautkari, J. C. Arboleda, O. J. Rojas, *Sci. Rep.* **2016**, 30695, 1.
152. K. J. De France, T. Hoare, E. D. Cranston, *Chem. Mater.* **2017**, 29, 4609.
153. E. M. Ahmed, *J. Adv. Res.* **2015**, 6, 105.

154. M. Mahinroosta, Z. Jomeh Farsangi, A. Allahverdi, Z. Shakoori, *Mater. Today Chem.* **2018**, 8, 42.
155. S. Liang, J. Wu, H. Tian, L. Zhang, J. Xu, *ChemSusChem* **2008**, 1, 558.
156. D. Zhao, J. Huang, Y. Zhong, K. Li, L. Zhang, J. Cai, *Adv. Funct. Mater.* **2016**, 26, 6279.
157. D. Ye, C. Chang, L. Zhang, *Biomacromolecules* **2019**, 20, 1989.
158. W. Kong, C. Wang, C. Jia, Y. Kuang, G. Pastel, C. Chen, G. Chen, S. He, H. Huang, J. Zhang, S. Wang, L. Hu, *Adv. Mater.* **2018**, 30, 1801934.
159. A. Sydney Gladman, E. A. Matsumoto, R. G. Nuzzo, L. Mahadevan, J. A. Lewis, *Nat. Mater.* **2016**, 15, 413.
160. H. Zhang, M. Yang, Q. Luan, H. Tang, F. Huang, X. Xiang, C. Yang, Y. Bao, *J. Agric. Food Chem.* **2017**, 65, 3785.
161. J. Song, C. Chen, Z. Yang, Y. Kuang, T. Li, Y. Li, H. Huang, I. Kierzewski, B. Liu, S. He, T. Gao, S. U. Yuruker, A. Gong, B. Yang, L. Hu, *ACS Nano* **2018**, 12, 140.
162. H. W. Liang, Q. F. Guan, Z. Z. Zhu, L. T. Song, H. Bin Yao, X. Lei, S. H. Yu, *NPG Asia Mater.* **2012**, 4.
163. C. Li, Z. Y. Wu, H. W. Liang, J. F. Chen, S. H. Yu, *Small* **2017**, 13, 1.
164. S. T. Nguyen, J. Feng, N. T. Le, A. T. T. Le, N. Hoang, V. B. C. Tan, H. M.

- Duong, *Ind. Eng. Chem. Res.* **2013**, 52, 18386.
165. Z. Y. Wu, C. Li, H. W. Liang, J. F. Chen, S. H. Yu, *Angew. Chemie Int. Ed.* **2013**, 52, 2925.
166. X. Yang, K. Shi, I. Zhitomirsky, E. D. Cranston, *Adv. Mater.* **2015**, 27, 6104.
167. G. Nystrom, A. Marais, E. Karabulut, L. Wågberg, Y. Cui, M. M. Hamed, *Nat. Commun.* **2015**, 6, 7259.
168. Z. Li, L. Zhong, T. Zhang, F. Qiu, X. Yue, D. Yang, *ACS Sustain. Chem. Eng.* **2019**, 7, 9984.
169. N. Lin, A. Gèze, D. Wouessidjewe, J. Huang, A. Dufresne, *ACS Appl. Mater. Interfaces* **2016**, 8, 6880.
170. D. Zhao, Y. Zhu, W. Cheng, G. Xu, Q. Wang, S. Liu, J. Li, C. Chen, H. Yu, L. Hu, *Matter* **2020**, 2, 1.
171. K. Hou, Y. Nie, I. Tendo Mugaanire, Y. Guo, M. Zhu, *Chem. Eng. J.* **2020**, 382, 122948.
172. M. C. Echave, R. M. A. Domingues, M. Gómez-Florit, J. L. Pedraz, R. L. Reis, G. Orive, M. E. Gomes, *ACS Appl. Mater. Interfaces* **2019**, 11, 47771.
173. B. Chen, Q. Zheng, J. Zhu, J. Li, Z. Cai, L. Chen, S. Gong, *RSC Adv.* **2016**, 6, 96518.
174. H. Orelma, A. Hokkanen, I. Leppänen, K. Kammiovirta, M. Kapulainen, A.

Harlin, *Cellulose* **2019**, 3.

175. A. Walther, J. V. I. Timonen, I. Díez, A. Laukkanen, O. Ikkala, *Adv. Mater.* **2011**, 23, 2924.
176. Y. Kuang, C. Chen, J. Cheng, G. Pastel, T. Li, J. Song, L. Hu, *Extrem. Mech. Lett.* **2019**, 29, 100463.
177. G. Chen, T. Li, C. Chen, C. Wang, Y. Liu, W. Kong, D. Liu, B. Jiang, S. He, Y. Kuang, L. Hu, *Adv. Funct. Mater.* **2019**, 29, 1.
178. C. Jia, F. Jiang, P. Hu, Y. Kuang, S. He, T. Li, C. Chen, A. Murphy, C. Yang, Y. Yao, J. Dai, C. B. Raub, X. Luo, L. Hu, *ACS Appl. Mater. Interfaces* **2018**, 10, 7362.
179. T. Li, X. Zhang, S. D. Lacey, R. Mi, X. Zhao, F. Jiang, J. Song, Z. Liu, G. Chen, J. Dai, Y. Yao, S. Das, R. Yang, R. M. Briber, L. Hu, *Nat. Mater.* **2019**, 18, 608.
180. H. Shaghaleh, X. Xu, S. Wang, *RSC Adv.* **2018**, 8, 825.
181. Z. Dai, V. Ottesen, J. Deng, R. M. L. Helberg, L. Deng, *Fibers* **2019**, 7, 1.
182. J. Torstensen, R. M. L. Helberg, L. Deng, Ø. W. Gregersen, K. Syverud, *Int. J. Greenh. Gas Control* **2019**, 81, 93.
183. L. Ansaloni, J. Salas-Gay, S. Ligi, M. G. Baschetti, *J. Memb. Sci.* **2017**, 522, 216.
184. D. Venturi, D. Grupkovic, L. Sisti, M. G. Baschetti, *J. Memb. Sci.* **2018**, 548,

263.

185. T. Li, J. Song, X. Zhao, Z. Yang, G. Pastel, S. Xu, C. Jia, J. Dai, C. Dai, A. Gong, F. Jiang, Y. Yao, T. Fan, B. Yang, L. Wågberg, R. Yang, L. Hu, *Sci. Adv.* **2018**, 4, 1.
186. C. Ye, *Appl. Opt.* **2006**, 45, 9092.
187. C. Chen, J. Song, C. Chen, J. Song, S. Zhu, Y. Li, Y. Kuang, J. Wan, D. Kirsch, *Chem* **2018**, 4, 544.
188. D. Ciolacu, C. Rudaz, M. Vasilescu, T. Budtova, *Carbohydr. Polym.* **2016**, 151, 392.

Chapter 3

1. Lee, J. *et al.* Conductive Fiber-Based Ultrasensitive Textile Pressure Sensor for Wearable Electronics. *Adv. Mater.* **27**, 2433–2439 (2015).
2. Shang, B. Y. *et al.* Large-Deformation, Multifunctional Artificial Muscles Based on Single-Walled Carbon Nanotube Yarns **. *Adv. Eng. Mater.* **17**, 14–20 (2015).
3. Ji, S. *et al.* High Dielectric Performances of Flexible and Transparent Cellulose Hybrid Films Controlled by Multidimensional Metal Nanostructures. *Adv. Mater.* **29**, 1700538 (2017).
4. Zhu, H. *et al.* Biodegradable transparent substrates for flexible organic-light-emitting diodes. *Energy Environ. Sci.* **6**, 2105–2111 (2013).
5. Nystrom, G. *et al.* Self-assembled three-dimensional and compressible

- interdigitated thin-film supercapacitors and batteries. *Nat. Commun.* **6**, 7259 (2015).
6. Ji, S. *et al.* Photo-patternable and transparent films using cellulose nano fi bers for stretchable origami electronics. *NPG Asia Mater.* **8**, e299 (2016).
 7. Kim, J. *et al.* Wearable smart sensor systems integrated on soft contact lenses for wireless ocular diagnostics. *Nat. Commun.* **8**, 1–8 (2017).
 8. Ahmad, S., Copic, D., George, C. & Volder, M. De. Hierarchical Assemblies of Carbon Nanotubes for Ultraflexible Li-Ion Batteries. *Adv. Mater.* **28**, 6705–6710 (2016).
 9. Lee, Y.-H. *et al.* Wearable Textile Battery Rechargeable by Solar Energy. *Nano Lett.* **13**, 5753–5761 (2013).
 10. Lee, S. *et al.* Ag Nanowire Reinforced Highly Stretchable Conductive Fibers for Wearable Electronics. *Adv. Funct. Mater.* **25**, 3114–3121 (2015).
 11. Sun, K. *et al.* 3D Printing of Interdigitated Li-Ion Microbattery Architectures. *Adv. Mater.* **25**, 4539–4543 (2013).
 12. Ota, H. *et al.* Application of 3D Printing for Smart Objects with Embedded Electronic Sensors and Systems. *Adv. Mater. Technol.* **1**, 1600013 (2016).
 13. Shin, S. R. *et al.* A Bioactive Carbon Nanotube-Based Ink for Printing 2D and 3D Flexible Electronics. *Adv. Mater.* **28**, 3280–3289 (2016).
 14. Zhu, C. *et al.* Supercapacitors Based on Three-Dimensional Hierarchical Graphene Aerogels with Periodic Macropores. *Nano Lett.* **16**, 3448–3456 (2016).
 15. Pan, S. *et al.* Novel Wearable Energy Devices Based on Aligned Carbon

- Nanotube Fiber Textiles. *Adv. Energy Mater.* **5**, 1401438 (2015).
16. Aleman, B., Reguero, V., Mas, B. & Vilatela, J. J. Strong Carbon Nanotube Fibers by Drawing Inspiration from Polymer Fiber Spinning. *ACS Nano* **9**, 7392–7398 (2015).
 17. Lekawa-raus, A., Patmore, J., Kurzepa, L., Bulmer, J. & Koziol, K. Electrical Properties of Carbon Nanotube Based Fibers and Their Future Use in Electrical Wiring. *Adv. Funct. Mater.* **24**, 3661–3682 (2014).
 18. Lu, W., Zu, M., Byun, J., Kim, B. & Chou, T. State of the Art of Carbon Nanotube Fibers: Opportunities and Challenges. *Adv. Mater.* **24**, 1805–1833 (2012).
 19. Sun, X., Chen, T. A., Yang, Z. & Peng, H. The Alignment of Carbon Nanotubes: An Effective Route To Extend Their Excellent Properties to Macroscopic Scale. *Acc. Chem. Res.* **46**, 539–549 (2013).
 20. Gui, W. *et al.* Aligned carbon nanotube / polymer composite fibers with improved mechanical strength and electrical conductivity †. *J. Mater. Chem.* **22**, 903–908 (2012).
 21. Koziol, K. *et al.* High-Performance Carbon Nanotube Fiber. *Science (80-.)*. **318**, 1892–1895 (2007).
 22. Jiang, C. *et al.* Macroscopic Nanotube Fibers Spun from Single-Walled Carbon Nanotube Polyelectrolytes. *ACS Nano* **8**, 9107–9112 (2014).
 23. Chen, T. *et al.* Nanotube Fibers for a Highly Efficient Solar Cell **. *Angew. Chemie Int. Ed.* **50**, 1815–1819 (2011).
 24. Li, Y. *et al.* Nanocellulose as green dispersant for two-dimensional energy

- materials. *Nano Energy* **13**, 346–354 (2015).
25. M. Hamed, M. *et al.* Highly Conducting, Strong Nanocomposites Based on Nanocellulose-Assisted Aqueous Dispersions of Single-Wall Carbon. *ACS Nano* **8**, 2467–2476 (2014).
 26. Walther, A., Timonen, J. V. I., Díez, I., Laukkanen, A. & Ikkala, O. Multifunctional High-Performance Biofibers Based on Wet-Extrusion of Renewable Native Cellulose Nanofibrils. *Adv. Mater.* **23**, 2924–2928 (2011).
 27. Cheng, Q., Wang, S. & Rials, T. G. Poly (vinyl alcohol) nanocomposites reinforced with cellulose fibrils isolated by high intensity ultrasonication. *Compos. Part A* **40**, 218–224 (2009).
 28. Li, Y. *et al.* Strong transparent magnetic nanopaper prepared by immobilization of Fe₃O₄ nanoparticles in a nano fibrillated cellulose network. *J. Mater. Chem. A* **1**, 15278–15283 (2013).
 29. Carlsson, D. O., Nyström, G., Zhou, Q., Berglund, L. A. & Strømme, M. Electroactive nanofibrillated cellulose aerogel composites with tunable structural and electrochemical properties †. *J. Mater. Chem.* **22**, 19014–19024 (2012).
 30. Li, Y. *et al.* Cellulose nano fibers enable paraffin encapsulation and the formation of stable thermal regulation nanocomposites. *Nano Energy* **34**, 541–548 (2017).
 31. Mattsson, T. R. *et al.* First-principles and classical molecular dynamics simulation of shocked polymers. *Phys. Rev. B* **81**, 054103 (2010).

Chapter 4

1. Moon, R. J., Martini, A., Nairn, J. & Youngblood, J. Cellulose nanomaterials review : structure , properties and nanocomposites. *Chem. Soc. Rev.* **40**, 3941–3994 (2011).
2. Kalia, S. *et al.* Cellulose-Based Bio- and Nanocomposites : A Review. *Int. J. Polym. Sci.* **2011**, 1–35 (2011).
3. Ioelovich, M. Cellulose as a nanostructured polymer: a short review. *BioResources* **3**(4), 1403–1418 (2008).
4. Dufresne, A. Cellulose nanomaterial reinforced polymer nanocomposites. *Curr. Opin. Colloid Interface Sci.* **29**, 1–8 (2017).
5. Klemm, D., Heublein, B., Fink, H.-P. & Bohn, A. Cellulose : Fascinating Biopolymer and Sustainable Raw Material Angewandte. *Angew. Chemie Int. Ed.* **44**, 3358–3393 (2005).
6. Chen, C. *et al.* Structure–property–function relationships of natural and engineered wood. *Nat. Rev. Mater.* (2020) doi:10.1038/s41578-020-0195-z.
7. Song, J. *et al.* Processing bulk natural wood into a high-performance structural material. *Nature* **554**, 224–228 (2018).
8. Li, T. *et al.* Wood Composite as an Energy Efficient Building Material : Guided Sunlight Transmittance and Effective Thermal Insulation. *Adv. Energy Mater.* **6**, 1601122 (2016).
9. Zhu, M. *et al.* Highly Anisotropic , Highly Transparent Wood Composites. *Adv. Mater.* **28**, 5181–5187 (2016).
10. Zhou, Y. *et al.* A Printed, Recyclable, Ultra-Strong and Ultra-Tough Graphite

- Structural Material. *Mater. Today* **30**, 17–25 (2019).
11. Sydney Gladman, A., Matsumoto, E. A., Nuzzo, R. G., Mahadevan, L. & Lewis, J. A. Biomimetic 4D printing. *Nat. Mater.* **15**, 413–418 (2016).
 12. Li, Y. (co-first) *et al.* Cellulose-Nanofiber-Enabled 3D Printing of a Carbon-Nanotube Microfiber Network. *Small Methods* **1**, 1700222 (2017).
 13. Jia, C. *et al.* From Wood to Textiles : Top-Down Assembly of Aligned Cellulose Nanofibers. *Adv. Mater.* **30**, 1801347 (2018).
 14. Zhu, H., Fang, Z., Preston, C., Li, Y. & Hu, L. Transparent paper: fabrications, properties, and device applications. *Energy Environ. Sci.* **7**, 269–287 (2014).
 15. Fang, Z., Hou, G., Chen, C. & Hu, L. Nanocellulose-based films and their emerging applications. *Curr. Opin. Solid State Mater. Sci.* **23**, 100764 (2019).
 16. Song, J. *et al.* Highly Compressible, Anisotropic Aerogel with Aligned Cellulose Nanofibers. *ACS Nano* **12**, 140–147 (2018).
 17. Zhang, Y. *et al.* High-capacity, low-tortuosity, and channel-guided lithium metal anode. *Proc. Natl. Acad. Sci. U. S. A.* **114**, 3584–3589 (2017).
 18. Zhang, Q. *et al.* Nanocellulose-Enabled, All-Nanofiber, High-Performance Supercapacitor. *ACS Appl. Mater. Interfaces* **11**, 5919–5927 (2019).
 19. Diaz, J. A. *et al.* Thermal conductivity in nanostructured films: From single cellulose nanocrystals to bulk films. *Biomacromolecules* **15**, 4096–4101 (2014).
 20. Shin, S. & Hyun, J. Matrix-Assisted Three-Dimensional Printing of Cellulose Nanofibers for Paper Microfluidics. *ACS Appl. Mater. Interfaces* **9**, 26438–26446 (2017).
 21. Czaja, W. K., Young, D. J., Kawecki, M. & Brown, R. M. The future prospects

- of microbial cellulose in biomedical applications. *Biomacromolecules* **8**, 1–12 (2007).
22. Svensson, A. *et al.* Bacterial cellulose as a potential scaffold for tissue engineering of cartilage. *Biomaterials* **26**, 419–431 (2005).
 23. Müller, F. A. *et al.* Cellulose-based scaffold materials for cartilage tissue engineering. *Biomaterials* **27**, 3955–3963 (2006).
 24. Li, T. *et al.* A radiative cooling structural material. *Science*. **364**, 760–763 (2019).
 25. Ray, U., Zhu, S., Pang, Z. & Li, T. Mechanics Design in Cellulose-Enabled High-Performance Functional Materials. *Adv. Mater.* **2002504**, 2002504(1–22) (2020).
 26. Meng, Q. & Wang, T. J. Mechanics of Strong and Tough Cellulose Nanopaper. *Appl. Mech. Rev.* **71**, 040801 (2019).
 27. Xia, W., Qin, X., Zhang, Y., Sinko, R. & Keten, S. Achieving Enhanced Interfacial Adhesion and Dispersion in Cellulose Nanocomposites via Amorphous Interfaces. *Macromolecules* **51**, 10304–10311 (2018).
 28. Sinko, R., Mishra, S., Ruiz, L., Brandis, N. & Keten, S. Dimensions of biological cellulose nanocrystals maximize fracture strength. *ACS Macro Lett.* **3**, 64–69 (2014).
 29. Sinko, R. & Keten, S. Traction – separation laws and stick – slip shear phenomenon of interfaces between cellulose nanocrystals. *J. Mech. Phys. Solids* **78**, 526–539 (2015).
 30. Wu, X., Moon, R. J. & Martini, A. Crystalline cellulose elastic modulus

- predicted by atomistic models of uniform deformation and nanoscale indentation. *Cellulose* **20**, 43–55 (2013).
31. Wu, X., Moon, R. J. & Martini, A. Tensile strength of I β crystalline cellulose predicted by molecular dynamics simulation. *Cellulose* **21**, 2233–2245 (2014).
 32. Zhu, H. *et al.* Anomalous scaling law of strength and toughness of cellulose nanopaper. *PNAS* **112**, 8971–8976 (2015).
 33. Fang, Z. *et al.* Novel Nanostructured Paper with Ultrahigh Transparency and Ultrahigh Haze for Solar Cells. *Nano Lett.* **14**, 765–773 (2014).
 34. Li, Y. *et al.* Hybridizing wood cellulose and graphene oxide toward high-performance fibers. *NPG Asia Mater.* **7**, e150 (2015).
 35. Wang, S. *et al.* Transparent , Anisotropic Biofilm with Aligned Bacterial Cellulose Nanofibers. *Adv. Funct. Mater.* **28**, 1707491(1–10) (2018).
 36. Wang, S. *et al.* Super-Strong , Super-Stiff Macrofibers with Aligned , Long Bacterial Cellulose Nanofibers. *Adv. Mater.* **29**, 1702498(1–8) (2017).
 37. Zhu, M. *et al.* Anisotropic , Transparent Films with Aligned Cellulose Nanofibers. *Adv. Mater.* **29**, 1606284(1–8) (2017).
 38. Fan, B. & Maranas, J. K. Coarse-grained simulation of cellulose Ib with application to long fibrils. *Cellulose* **22**, 31–44 (2015).
 39. Qin, X., Feng, S., Meng, Z. & Keten, S. Optimizing the mechanical properties of cellulose nanopaper through surface energy and critical length scale considerations. *Cellulose* **24**, 3289–3299 (2017).
 40. Shishehbor, M. & Zavattieri, P. D. Effects of interface properties on the mechanical properties of bio-inspired cellulose nanocrystal (CNC)-based

- materials. *J. Mech. Phys. Solids* **124**, 871–896 (2019).
41. Mehandzhiyski, A. Y. *et al.* A novel supra coarse-grained model for cellulose. *Cellulose* **27**, 4221–4234 (2020).
 42. Ahmed, M., Azizi, S., Alloin, F. & Dufresne, A. Review of Recent Research into Cellulosic Whiskers, Their Properties and Their Application in Nanocomposite Field. *Biomacromolecules* **6**, 612–626 (2005).
 43. Saito, T., Kuramae, R., Wohler, J., Berglund, L. A. & Isogai, A. An ultrastrong nanofibrillar biomaterial: The strength of single cellulose nanofibrils revealed via sonication-induced fragmentation. *Biomacromolecules* **14**, 248–253 (2013).
 44. Mao, R. *et al.* Modelling the elastic properties of cellulose nanopaper. *Mater. Des.* **126**, 183–189 (2017).
 45. Isaksson, P. & Hågg, R. Structural effects on deformation and fracture of random fiber networks and consequences on continuum models. *Int. J. Solids Struct.* **46**, 2320–2329 (2009).
 46. Goutianos, S., Mao, R. & Peijs, T. Effect of inter-fibre bonding on the fracture of fibrous networks with strong interactions. *Int. J. Solids Struct.* **136–137**, 271–278 (2018).
 47. Wang, X. *et al.* All-Natural, Degradable, Rolled-Up Straws Based on Cellulose Micro- and Nano-Hybrid Fibers. *Adv. Funct. Mater.* **30**, 1910417 (2020).
 48. Boda, D. & Henderson, D. The effects of deviations from Lorentz-Berthelot rules on the properties of a simple mixture. *Mol. Phys.* **106**, 2367–2370 (2008).
 49. Izvekov, S. & Voth, G. A. A multiscale coarse-graining method for biomolecular systems. *J. Phys. Chem. B* **109**, 2469–2473 (2005).

50. Rouhi, S. On the Mechanical Properties of the Graphdiyne Nanotubes: a Molecular Dynamics Investigation. *Brazilian J. Phys.* **49**, 654–666 (2019).
51. Mattsson, T. R. *et al.* First-principles and classical molecular dynamics simulation of shocked polymers. *Phys. Rev. B* **81**, 054103 (2010).
52. Ogawa, Y. Electron microdiffraction reveals the nanoscale twist geometry of cellulose nanocrystals. *Nanoscale* **11**, 21767–21774 (2019).
53. Srinivas, G., Cheng, X. & Smith, J. C. A solvent-free coarse grain model for crystalline and amorphous cellulose fibrils. *J. Chem. Theory Comput.* **7**, 2539–2548 (2011).
54. Moon, R. J., Martini, A., Nairn, J., Simonsen, J. & Youngblood, J. *Cellulose nanomaterials review: Structure, properties and nanocomposites*. *Chemical Society Reviews* vol. 40 (2011).
55. Buzio, R., Calvini, P., Ferroni, A. & Valbusa, U. Surface analysis of paper documents damaged by foxing. *Appl. Phys. A Mater. Sci. Process.* **79**, 383–387 (2004).
56. Koňas, P., Buchar, J. & Severa, L. Study of correlation between the fractal dimension of wood anatomy structure and impact energy. *Eur. J. Mech. A/Solids* **28**, 545–550 (2009).
57. Redinz, J. A. & Guimarães, P. R. C. The fractal nature of wood revealed by water absorption. *Wood Fiber Sci.* **29**, 333–339 (1997).
58. Fan, K., Hatzikiriakos, S. G. & Avramidis, S. Determination of the surface fractal dimension from sorption isotherms of five softwoods. *Wood Sci. Technol.* **33**, 139–149 (1999).

59. Zhu, S., Huang, Y. & Li, T. Extremely compliant and highly stretchable patterned graphene. *Appl. Phys. Lett.* **104**, (2014).
60. Szymanska-Chargot, M., Chylinska, M., Gdula, K., Koziol, A. & Zdunek, A. Isolation and characterization of cellulose from different fruit and vegetable pomaces. *Polymers (Basel)*. **9**, (2017).
61. Plimpton, S. Fast parallel algorithms for short-range molecular dynamics. *J. Comput. Phys.* **117**, 1–19 (1995).
62. Usov, I. *et al.* Understanding nanocellulose chirality and structure-properties relationship at the single fibril level. *Nat. Commun.* **6**, (2015).
63. Domingues, R. M. A., Gomes, M. E. & Reis, R. L. The potential of cellulose nanocrystals in tissue engineering strategies. *Biomacromolecules* **15**, 2327–2346 (2014).
64. Sehaqui, H., Zhou, Q., Ikkala, O. & Berglund, L. A. Strong and tough cellulose nanopaper with high specific surface area and porosity. *Biomacromolecules* **12**, 3638–3644 (2011).
65. Yousefi, H. *et al.* Comparative study of paper and nanopaper properties prepared from bacterial cellulose nanofibers and fibers/ground cellulose nanofibers of canola straw. *Ind. Crops Prod.* **43**, 732–737 (2013).
66. Motamedian, H. R., Halilovic, A. E. & Kulachenko, A. Mechanisms of strength and stiffness improvement of paper after PFI refining with a focus on the effect of fines. *Cellulose* **26**, 4099–4124 (2019).
67. Meng, Q., Li, B., Li, T. & Feng, X. A multiscale crack-bridging model of cellulose nanopaper. *J. Mech. Phys. Solids* **103**, 22–39 (2017).

68. Hou, Y. *et al.* Strengthening and Toughening Hierarchical Nanocellulose via Humidity-Mediated Interface. *ACS Nano* **15**, 1310–1320 (2020).
69. Guan, Q. F. *et al.* Lightweight, tough, and sustainable cellulose nanofiber-derived bulk structural materials with low thermal expansion coefficient. *Sci. Adv.* **6**, 1–9 (2020).

Chapter 5

1. U. Ray, S. Zhu, Z. Pang, and T. Li, *Adv. Mater.* **33**, 2002504 (2021).
2. U. Ray, S. Zhu, Z. Pang, T. Li, (2023). *Nanocellulose-Based Materials with Superior Mechanical Performance*. In: Hu, L., Jiang, F., Chen, C. (eds) *Emerging Nanotechnologies in Nanocellulose*. NanoScience and Technology. Springer, Cham. https://doi.org/10.1007/978-3-031-14043-3_5
3. K. Li, C.M. Clarkson, L. Wang, Y. Liu, M. Lamm, Z. Pang, Y. Zhou, J. Qian, M. Tajvidi, D.J. Gardner, H. Tekinalp, L. Hu, T. Li, A.J. Ragauskas, J.P. Youngblood, and S. Ozcan, *ACS Nano* **15**, 3646 (2021).
4. M.E. Lamm, K. Li, J. Qian, L. Wang, N. Lavoine, R. Newman, D.J. Gardner, T. Li, L. Hu, A.J. Ragauskas, H. Tekinalp, V. Kunc, and S. Ozcan, *Adv. Mater.* **33**, (2021).
5. T. Li, C. Chen, A.H. Brozena, J.Y. Zhu, L. Xu, C. Driemeier, J. Dai, O.J. Rojas, A. Isogai, L. Wågberg, and L. Hu, *Nature* **590**, 47 (2021).
6. A. Peterson, A.Y. Mehandzhiyski, L. Svenningsson, A. Ziolkowska, R. Kádár,

- A. Lund, L. Sandblad, L. Evenäs, G. Lo Re, I. Zozoulenko, and C. Müller, *Macromolecules* **54**, 3507 (2021).
7. H. Zhu, S. Zhu, Z. Jia, S. Parvinian, Y. Li, O. Vaaland, L. Hu, and T. Li, *PNAS* **112**, 8971 (2015).
 8. M.C. Jarvis, *Cellulose* **30**, 667 (2023).
 9. U. Ray, Z. Pang, and T. Li, *J. Appl. Phys.* **132**, 210703 (2022).
 10. K. Uetani and K. Hatori, *Sci. Technol. Adv. Mater.* **18**, 877 (2017).
 11. J.A. Diaz, Z. Ye, X. Wu, A.L. Moore, R.J. Moon, A. Martini, D.J. Boday, and J.P. Youngblood, *Biomacromolecules* **15**, 4096 (2014).
 12. X. Zeng, J. Sun, Y. Yao, R. Sun, J. Bin Xu, and C.P. Wong, *ACS Nano* **11**, 5167 (2017).
 13. W. Yang and J. Kim, *Ceram. Int.* **48**, 25284 (2022).
 14. R.-Y. Dong (董若宇), Y. Dong (董源), Q. Li, and C. Wan, *Int. J. Heat Mass Transf.* **148**, 119155 (2020).
 15. J.A. Diaz, X. Wu, A. Martini, J.P. Youngblood, and R.J. Moon, *Biomacromolecules* **14**, 2900 (2013).
 16. C. Zhi, Y. Bando, C. Tang, and D. Golberg, *Mater. Sci. Eng. R Reports* **70**, 92 (2010).
 17. D. Golberg, Y. Bando, C. Tang, and C. Zni, *Adv. Mater.* **19**, 2413 (2007).

18. J. Huang, Y. Guo, Y. Fan, and Y. Liang, *Mater. Res. Express* **7**, 0 (2020).
19. L. Wang, D. Han, J. Luo, T. Li, Z. Lin, and Y. Yao, *J. Phys. Chem. C* **122**, 1867 (2018).
20. C.J. Simonsen Ginestra, C. Martínez-Jiménez, A. Matatyaho Ya'akobi, O.S. Dewey, A.D. Smith McWilliams, R.J. Headrick, J.A. Acapulco, L.R. Scammell, M.W. Smith, D. V. Kosynkin, D.M. Marincel, C. Park, S.H. Chu, Y. Talmon, A.A. Martí, and M. Pasquali, *Nat. Commun.* **13**, 1 (2022).
21. C. Tang, Y. Bando, C. Liu, S. Fan, J. Zhang, X. Ding, and D. Golberg, *J. Phys. Chem. B* **110**, 10354 (2006).
22. C. Zhi, Y. Bando, T. Terao, C. Tang, H. Kuwahara, and D. Golberg, *Adv. Funct. Mater.* **19**, 1857 (2009).
23. X. Huang, C. Zhi, P. Jiang, D. Golberg, Y. Bando, and T. Tanaka, *Adv. Funct. Mater.* **23**, 1824 (2013).
24. T. Terao, C. Zhi, Y. Bando, M. Mitome, C. Tang, and D. Golberg, *J. Phys. Chem. C* **114**, 4340 (2010).
25. J.F. Khoury, J.C. Vitale, T.L. Larson, and G. Ao, *Nanoscale Adv.* **4**, 77 (2022).
26. C. Wang, P. Jagirdar, S. Naserifar, and M. Sahimi, *J. Phys. Chem. B* **120**, 1273 (2016).
27. M. Zhu, J. Li, J. Chen, H. Song, and H. Zhang, *Comput. Mater. Sci.* **164**, 108 (2019).

28. C. Fu, Q. Li, J. Lu, S. Mateti, Q. Cai, X. Zeng, G. Du, R. Sun, Y. Chen, J. Xu, and C.P. Wong, *Compos. Sci. Technol.* **165**, 322 (2018).
29. S. Plimpton, *J. Comput. Phys.* **117**, 1 (1995).
30. A.P. Thompson, H.M. Aktulga, R. Berger, D.S. Bolintineanu, W.M. Brown, P.S. Crozier, P.J. in 't Veld, A. Kohlmeyer, S.G. Moore, T.D. Nguyen, R. Shan, M.J. Stevens, J. Tranchida, C. Trott, and S.J. Plimpton, *Comput. Phys. Commun.* **271**, 108171 (2022).
31. K. Chenoweth, A.C.T. Van Duin, and W.A. Goddard, *J. Phys. Chem. A* **112**, 1040 (2008).
32. H.M. Aktulga, S.A. Pandit, A.C.T. Van Duin, and A.Y. Grama, *Prism NNSA Cent. Predict. Reliab. Integr. Surviv. Microsystems.* **34**, (2009).
33. R.S. Ambekar, A. Deshmukh, M.Y. Suárez-Villagrán, R. Das, V. Pal, S. Dey, J.H. Miller, L.D. Machado, P. Kumbhakar, and C.S. Tiwary, *ACS Appl. Mater. Interfaces* **12**, 45274 (2020).
34. F. Müller-plathe, *J. Chem. Phys.* **106**, 6082 (1997).
35. K. Uetani, T. Okada, and H.T. Oyama, *Biomacromolecules* **16**, 2220 (2015).
36. J. Huang, Y. Guo, Y. Fan, and Y. Liang, *Mater. Res. Express* **7**, (2020).
37. T. Luo, K. Esfarjani, J. Shiomi, A. Henry, and G. Chen, *J. Appl. Phys.* **109**, 074321 (2011).

38. K. Sato, H. Horibe, T. Shirai, Y. Hotta, H. Nakano, H. Nagai, K. Mitsuishi, and K. Watari, *J. Mater. Chem.* **20**, 2749 (2010).
39. C.Y. Zhi, Y. Bando, W.L. Wang, C.C. Tang, H. Kuwahara, and D. Golberg, *J. Nanomater.* **2008**, 1 (2008).
40. H. Zhu, Y. Li, Z. Fang, J. Xu, F. Cao, J. Wan, C. Preston, B. YANG, and L. Hu, *ACS Nano* **8**, 3606 (2014).
41. S. Kemalolu, G. Ozkoc, and A. Aytac, *Polym. Polym. Compos.* **31**, 1398 (2010).
42. U. Ray, Z. Pang, and T. Li, *Cellulose* **28**, 3359 (2021).
43. X. Zhang and S. Zhu, *Extrem. Mech. Lett.* **62**, 102035 (2023).
44. A. Kafy, H.C. Kim, L. Zhai, J.W. Kim, L. Van Hai, T.J. Kang, and J. Kim, *Sci. Rep.* **7**, 1 (2017).
45. X. Chen, L. Zhang, C. Park, C.C. Fay, X. Wang, and C. Ke, *Appl. Phys. Lett.* **107**, (2015).
46. H.M. Ghassemi, C.H. Lee, Y.K. Yap, and R.S. Yassar, *J. Appl. Phys.* **108**, 024314 (2010).
47. T. Li, Z. Tang, Z. Huang, and J. Yu, *Phys. E* **85**, 137 (2017).
48. M. Sathwane, M. Chhajed, C. Verma, K.K. Gaikwad, and P.K. Maji, *Polym. Compos.* **44**, 492 (2023).
49. Y. Lu, R. Zhao, L. Wang, and S. E, *Diam. Relat. Mater.* **136**, 109978 (2023).

50. C.H. Lee, S. Bhandari, B. Tiwari, N. Yapici, D. Zhang, and Y.K. Yap, *Molecules* **21**, (2016).
51. L. Yu, T. Gao, R. Mi, J. Huang, W. Kong, D. Liu, Z. Liang, D. Ye, and C. Chen, *Nano Res.* (2023).
52. D. Trache, A.F. Tarchoun, M. Derradji, T.S. Hamidon, N. Masruchin, N. Brosse, and M.H. Hussin, *Nanocellulose: From Fundamentals to Advanced Applications* (2020).
53. C. Chen, Y. Zhou, W. Xie, T. Meng, X. Zhao, Z. Pang, Q. Chen, D. Liu, R. Wang, V. Yang, H. Zhang, H. Xie, U.H. Leiste, W.L. Fournery, S. He, Z. Cai, Z. Ma, T. Li, and L. Hu, *Adv. Funct. Mater.* **33**, 1 (2023).
54. D. Nepal, S. Kang, K.M. Adstedt, K. Kanhaiya, M.R. Bockstaller, L.C. Brinson, M.J. Buehler, P. V. Coveney, K. Dayal, J.A. El-Awady, L.C. Henderson, D.L. Kaplan, S. Keten, N.A. Kotov, G.C. Schatz, S. Vignolini, F. Vollrath, Y. Wang, B.I. Yakobson, V. V. Tsukruk, and H. Heinz, *Nat. Mater.* **22**, 18 (2023).
55. M. Zhou, J. Wang, Y. Zhao, G. Wang, W. Gu, and G. Ji, *Carbon N. Y.* **183**, 515 (2021).
56. B. Thomas, M.C. Raj, B.K. Athira, H.M. Rubiyah, J. Joy, A. Moores, G.L. Drisko, and C. Sanchez, *Chem. Rev.* **118**, 11575 (2018).

Chapter 7

1. Lu, K., Lu, L. & Suresh, S. Strengthening Materials by Engineering Coherent

- Internal Boundaries at the Nanoscale. *Science*. **324**, 349–353 (2009).
2. Lu, L., Chen, X., Huang, X. & Lu, K. Revealing the Maximum Strength in Nanotwinned Copper. *Science*. **323**, 607–611 (2009).
 3. Zhu, T. & Li, J. Ultra-strength materials. *Prog. Mater. Sci.* **55**, 710–757 (2010).
 4. Lu, L., Shen, Y., Chen, X., Qian, L. & Lu, K. Ultrahigh Strength and High Electrical Conductivity in Copper. *Science*. **304**, 422–427 (2004).
 5. Ritchie, R. O. The conflicts between strength and toughness. *Nat. Mater.* **10**, 817–822 (2011).
 6. Evans, A. G. Perspective on the Development of High-Toughness Ceramics. *J. Am. Ceram. Soc.* **73**, 187–206 (1990).
 7. Hofmann, D. C. *et al.* Designing metallic glass matrix composites with high toughness and tensile ductility. *Nature* **451**, 1085–1090 (2008).
 8. Demetriou, M. D. *et al.* A damage-tolerant glass. *Nat. Mater.* **10**, 123 (2011).
 9. Launey, B. M. E. & Ritchie, R. O. On the Fracture Toughness of Advanced Materials. *Adv. Mater.* **21**, 2103–2110 (2009).
 10. Zhao, X. *et al.* Soft Materials by Design: Unconventional Polymer Networks Give Extreme Properties. *Chem. Rev.* **121**, 4309–4372 (2021).
 11. Yanagisawa, Y., Nan, Y., Okuro, K. & Aida, T. Mechanically robust, readily repairable polymers via tailored noncovalent cross-linking. *Science*. **359**, 72–76

(2018).

12. Nagy, P. I. *Competing intramolecular vs. Intermolecular hydrogen bonds in solution. International Journal of Molecular Sciences* vol. 15 (2014).
13. Ramasubbu, N., Parthasarathy, R. & Murray-Rust, P. Angular Preferences of Intermolecular Forces around Halogens Centers: Preferred Directions of Approach of Electrophiles and Nucleophiles around the Carbon-Halogen Bond. *J. Am. Chem. Soc.* **108**, 4308–4314 (1986).
14. Ray, U., Pang, Z. & Li, T. Mechanics of cellulose nanopaper using a scalable coarse-grained modeling scheme. *Cellulose* **28**, 3359–3372 (2021).
15. Ray, U., Zhu, S., Pang, Z. & Li, T. Mechanics Design in Cellulose-Enabled High-Performance Functional Materials. *Adv. Mater.* **33**, 2002504 (2021).
16. Li, T. EML Webinar Overview: Advanced materials toward a sustainable future—Mechanics design. *Extrem. Mech. Lett.* **42**, 101107 (2021).
17. Chen, Q., Chen, B., Jing, S., Liu, Y. & Li, T. Flaw sensitivity of cellulose paper. *Extrem. Mech. Lett.* **56**, 101865 (2022).
18. Zhu, H. *et al.* Anomalous scaling law of strength and toughness of cellulose nanopaper. *PNAS* **112**, 8971–8976 (2015).
19. Kim, J., Zhang, G., Shi, M. & Suo, Z. Fracture, fatigue, and friction of polymers in which entanglements greatly outnumber cross-links. *Science*. **216**, 212–216 (2021).

20. Gibb, B. C. The centenary (maybe) of the hydrogen bond. *Nat. Chem.* **12**, 665–667 (2020).
21. Zhang, J. *et al.* Real-space identification of intermolecular bonding with atomic force microscopy. *Science*. **342**, 611–614 (2013).
22. Guerra, C. F., Bickelhaupt, F. M., Snijders, J. G. & Baerends, E. J. The nature of the hydrogen bond in DNA base pairs: The role of charge transfer and resonance assistance. *Chem. - A Eur. J.* **5**, 3581–3594 (1999).
23. Guerra, C. F. & Bickelhaupt, F. M. Charge transfer and environment effects responsible for characteristics of DNA base pairing. *Angew. Chemie - Int. Ed.* **38**, 2942–2945 (1999).
24. Chen, Y. *et al.* Super-Strong and Super-Stiff Chitosan Filaments with Highly Ordered Hierarchical Structure. *Adv. Funct. Mater.* **31**, (2021).
25. Gu, W. *et al.* Multiple Hydrogen Bonding Enables Strong, Tough, and Recyclable Soy Protein Films. *ACS Sustain. Chem. Eng.* **8**, 7680–7689 (2020).
26. Mizuno, K., Miyashita, Y., Shindo, Y. & Ogawa, H. NMR and FT-IR studies of hydrogen bonds in ethanol-water mixtures. *J. Phys. Chem.* **99**, 3225–3228 (1995).
27. Lommerse, J. P. M., Price, S. L. & Taylor, R. Hydrogen bonding of carbonyl, ether, and ester oxygen atoms with alkanol hydroxyl groups. *J. Comput. Chem.* **18**, 757–774 (1997).

28. Vila, A., Mosquera, R. A. & Hermida-Ramón, J. M. AIM characterization of hydrogen bonds in dimers of methoxymethane. *J. Mol. Struct. THEOCHEM* **541**, 149–158 (2001).
29. Ye, D. *et al.* Ultrahigh Tough, Super Clear, and Highly Anisotropic Nanofiber-Structured Regenerated Cellulose Films. *ACS Nano* **13**, 4843–4853 (2019).
30. Fang, Z. *et al.* Novel Nanostructured Paper with Ultrahigh Transparency and Ultrahigh Haze for Solar Cells. *Nano Lett.* **14**, 765–773 (2014).
31. Henriksson, M., Berglund, L. A., Isaksson, P., Lindström, T. & Nishino, T. Cellulose nanopaper structures of high toughness. *Biomacromolecules* **9**, 1579–1585 (2008).
32. Navarro, E., Franco, L., Subirana, J. A. & Puiggali, J. Nylon 65 Has a Unique Structure with Two Directions of Hydrogen Bonds. *Macromolecules* **28**, 8742–8750 (1995).
33. Xu, R. *et al.* Preparation of High Strength and Toughness Aramid Fiber by Introducing Flexible Asymmetric Monomer to Construct Misplaced-Nunchaku Structure. *Macromol. Mater. Eng.* **306**, 2000814 (2021).
34. Bhimanapati, G. R. *et al.* Recent Advances in Two-Dimensional Materials beyond Graphene. *ACS Nano* **9**, 11509–11539 (2015).
35. Pang, Z. *et al.* Giant tunability of interlayer friction in graphite via ion intercalation. *Extrem. Mech. Lett.* **35**, 100616 (2020).

36. Wang, K., Li, H. & Guo, Y. Interfacial friction anisotropy in few-layer van der Waals crystals. *Materials (Basel)*. **14**, (2021).
37. Williams, L. . Molecular Interactions (aka Noncovalent Interactions, Intermolecular Forces) and the Behaviors of Biological Macromolecules. https://williams.chemistry.gatech.edu/structure/molecular_interactions/mol_int.html (2021).
38. Ramanayaka, S. *et al.* Performance of metal-organic frameworks for the adsorptive removal of potentially toxic elements in a water system: A critical review. *RSC Adv.* **9**, 34359–34376 (2019).
39. Deng, G., Tang, C., Li, F., Jiang, H. & Chen, Y. Covalent cross-linked polymer gels with reversible sol-gel transition and self-healing properties. *Macromolecules* **43**, 1191–1194 (2010).
40. Lin, F. *et al.* Peptide-functionalized oxime hydrogels with tunable mechanical properties and gelation behavior. *Biomacromolecules* **14**, 3749–3758 (2013).
41. Zhou, J. *et al.* Layered Intercalation Materials. *Adv. Mater.* **33**, 2004557 (2021).
42. Seidl, L. *et al.* Intercalation of solvated Na-ions into graphite. *Energy Environ. Sci.* **10**, 1631–1642 (2017).
43. Feng, N. *et al.* A polymer-direct-intercalation strategy for MoS₂/carbon-derived hetero-aerogels with ultrahigh pseudocapacitance. *Nat. Commun.* **10**, 1372 (2019).

44. Moon, R. J., Martini, A., Nairn, J. & Youngblood, J. Cellulose nanomaterials review : structure , properties and nanocomposites. *Chem. Soc. Rev.* **40**, 3941–3994 (2011).
45. Henriksson, M., Henriksson, G., Berglund, L. A. & Lindström, T. An environmentally friendly method for enzyme-assisted preparation of microfibrillated cellulose (MFC) nanofibers. *Eur. Polym. J.* **43**, 3434–3441 (2007).
46. Sehaqui, H., Allais, M., Zhou, Q. & Berglund, L. A. Wood cellulose biocomposites with fibrous structures at micro- and nanoscale. *Compos. Sci. Technol.* **71**, 382–387 (2011).
47. Pääkko, M. *et al.* Enzymatic hydrolysis combined with mechanical shearing and high-pressure homogenization for nanoscale cellulose fibrils and strong gels. *Biomacromolecules* **8**, 1934–1941 (2007).
48. Saito, T., Kimura, S., Nishiyama, Y. & Isogai, A. Cellulose nanofibers prepared by TEMPO-mediated oxidation of native cellulose. *Biomacromolecules* **8**, 2485–2491 (2007).
49. Isogai, A. & Zhou, Y. Diverse nanocelluloses prepared from TEMPO-oxidized wood cellulose fibers: Nanonetworks, nanofibers, and nanocrystals. *Curr. Opin. Solid State Mater. Sci.* **23**, 101–106 (2019).
50. Sheng, N. *et al.* TEMPO-Oxidized Bacterial Cellulose Nanofibers/Graphene Oxide Fibers for Osmotic Energy Conversion. *ACS Appl. Mater. Interfaces* **13**,

22416–22425 (2021).

51. Wei, J. *et al.* A 3D-printable TEMPO-oxidized bacterial cellulose/alginate hydrogel with enhanced stability via nanoclay incorporation. *Carbohydr. Polym.* **238**, 116207 (2020).
52. Huang, C. *et al.* TEMPO-oxidized bacterial cellulose nanofiber membranes as high-performance separators for lithium-ion batteries. *Carbohydr. Polym.* **230**, 115570 (2020).
53. Mackin, R. T. *et al.* Synthesis and characterization of TEMPO-oxidized peptide-cellulose conjugate biosensors for detecting human neutrophil elastase. *Cellulose* **29**, 1293–1305 (2022).
54. Sheng, N. *et al.* Polypyrrole@TEMPO-oxidized bacterial cellulose/reduced graphene oxide macrofibers for flexible all-solid-state supercapacitors. *Chem. Eng. J.* **368**, 1022–1032 (2019).
55. Wen, Y. *et al.* Development of intelligent/active food packaging film based on TEMPO-oxidized bacterial cellulose containing thymol and anthocyanin-rich purple potato extract for shelf life extension of shrimp. *Food Packag. Shelf Life* **29**, 100709 (2021).
56. Shabbir, H., Dellago, C. & Hartmann, M. A. A high coordination of cross-links is beneficial for the strength of cross-linked fibers. *Biomimetics* **4**, 1–20 (2019).
57. Li, C. H. & Zuo, J. L. Self-Healing Polymers Based on Coordination Bonds.

Adv. Mater. **32**, 1903762 (2020).

58. Cao, J., Li, J., Chen, Y., Zhang, L. & Zhou, J. Dual Physical Crosslinking Strategy to Construct Moldable Hydrogels with Ultrahigh Strength and Toughness. *Adv. Funct. Mater.* **28**, 1800739 (2018).
59. Wu, S. W. *et al.* Strengthening injectable thermo-sensitive NIPAAm-g-chitosan hydrogels using chemical cross-linking of disulfide bonds as scaffolds for tissue engineering. *Carbohydr. Polym.* **192**, 308–316 (2018).
60. Song, P. & Wang, H. High-Performance Polymeric Materials through Hydrogen-Bond Cross-Linking. *Adv. Mater.* **32**, 1901244 (2020).
61. Gong, J. P., Katsuyama, Y., Kurokawa, T. & Osada, Y. Double-network hydrogels with extremely high mechanical strength. *Adv. Mater.* **15**, 1155–1158 (2003).
62. Liu, L., Liu, Y., Tan, M., Che, N. & Li, C. Double-network cross-linked aerogel with rigid and super-elastic conversion: simple formation, unique properties, and strong sorption of organic contaminants. *Environ. Sci. Pollut. Res.* **28**, 42637–42648 (2021).
63. Zhang, Q. *et al.* A Novel Double-Network, Self-Healing Hydrogel Based on Hydrogen Bonding and Hydrophobic Effect. *Macromol. Chem. Phys.* **221**, 1900320 (2020).
64. Yuan, H. *et al.* Strategies to Increase the Thermal Stability of Truly Biomimetic

Hydrogels: Combining Hydrophobicity and Directed Hydrogen Bonding. *Macromolecules* **50**, 9058–9065 (2017).

65. Li, R. *et al.* Porous boron nitride nanofibers/PVA hydrogels with improved mechanical property and thermal stability. *Ceram. Int.* **44**, 22439–22444 (2018).
66. Zhu, L. *et al.* Highly temperature resistant cellulose nanofiber/polyvinyl alcohol hydrogel using aldehyde cellulose nanofiber as cross-linker. *Cellulose* **26**, 5291–5303 (2019).
67. Song, P. *et al.* Lightweight, Flexible Cellulose-Derived Carbon Aerogel@Reduced Graphene Oxide/PDMS Composites with Outstanding EMI Shielding Performances and Excellent Thermal Conductivities. *Nano-Micro Lett.* **13**, 91 (2021).
68. Jiang, F. & Hsieh, Y. Lo. Cellulose nanofibril aerogels: Synergistic improvement of hydrophobicity, strength, and thermal stability via cross-linking with diisocyanate. *ACS Appl. Mater. Interfaces* **9**, 2825–2834 (2017).
69. Shang, Z. *et al.* High thermal conductivity of self-healing polydimethylsiloxane elastomer composites by the orientation of boron nitride nano sheets. *Polym. Adv. Technol.* **32**, 4745–4754 (2021).
70. Zhang, W. *et al.* Semi-interpenetrating polymer networks prepared from castor oil-based waterborne polyurethanes and carboxymethyl chitosan. *Carbohydr. Polym.* **256**, 117507 (2021).

71. Shi, Y. *et al.* Interface engineering of MXene towards super-tough and strong polymer nanocomposites with high ductility and excellent fire safety. *Chem. Eng. J.* **399**, 125829 (2020).
72. Li, Y. (co-first) *et al.* Cellulose-Nanofiber-Enabled 3D Printing of a Carbon-Nanotube Microfiber Network. *Small Methods* **1**, 1700222 (2017).
73. Keten, S., Xu, Z., Ihle, B. & Buehler, M. J. Nanoconfinement controls stiffness, strength and mechanical toughness of B-sheet crystals in silk. *Nat. Mater.* **9**, 359–367 (2010).
74. Dou, Y. *et al.* Artificial spider silk from ion-doped and twisted core-sheath hydrogel fibres. *Nat. Commun.* **10**, 5293 (2019).
75. Song, P. *et al.* Super-tough artificial nacre based on graphene oxide via synergistic interface interactions of π - π stacking and hydrogen bonding. *Carbon N. Y.* **111**, 807–812 (2017).
76. Liu, Y., Xie, B., Zhang, Z., Zheng, Q. & Xu, Z. Mechanical properties of graphene papers. *J. Mech. Phys. Solids* **60**, 591–605 (2012).
77. Mahadevi, A. S. & Sastry, G. N. Cooperativity in Noncovalent Interactions. *Chem. Rev.* **116**, 2775–2825 (2016).
78. Chen, J., Peng, Q., Peng, X., Zhang, H. & Zeng, H. Probing and Manipulating Noncovalent Interactions in Functional Polymeric Systems. *Chem. Rev.* **122**, 14594–14678 (2022).

79. Jia, Z., Yu, Y. & Wang, L. Learning from nature: Use material architecture to break the performance tradeoffs. *Mater. Des.* **168**, 107650 (2019).
80. Barthelat, F., Yin, Z. & Buehler, M. J. Structure and mechanics of interfaces in biological materials. *Nat. Rev. Mater.* **1**, (2016).
81. Chen, S. M. *et al.* Superior Biomimetic Nacreous Bulk Nanocomposites by a Multiscale Soft-Rigid Dual-Network Interfacial Design Strategy. *Matter* **1**, 412–427 (2019).
82. Lai, Z. B. & Yan, C. Mechanical behaviour of staggered array of mineralised collagen fibrils in protein matrix: Effects of fibril dimensions and failure energy in protein matrix. *J. Mech. Behav. Biomed. Mater.* **65**, 236–247 (2017).
83. Le, T. Van, Ghazlan, A., Ngo, T., Nguyen, T. & Remennikov, A. A comprehensive review of selected biological armor systems – From structure-function to bio-mimetic techniques. *Compos. Struct.* **225**, 111172 (2019).
84. Zeng, X. *et al.* Artificial nacre-like papers based on noncovalent functionalized boron nitride nanosheets with excellent mechanical and thermally conductive properties. *Nanoscale* **7**, 6774–6781 (2015).
85. Zhou, L. C., Zhu, Y. B., He, Z. Z., Jin, X. & Wu, H. A. Multi-parameter structural optimization to reconcile mechanical conflicts in nacre-like composites. *Compos. Struct.* **259**, 113225 (2021).
86. Fan, W. *et al.* Resolving the Conflict between Strength and Toughness in

- Bioactive Silica-Polymer Hybrid Materials. *ACS Nano* **16**, 9748–9761 (2022).
87. *Self-Healing and Self-Recovering Hydrogels*. edited by C. Creton and O. Okay, Vol 285 (Springer, 2020).
88. GhavamiNejad, A., Ashammakhi, N., Wu, X. Y. & Khademhosseini, A. Crosslinking Strategies for 3D Bioprinting of Polymeric Hydrogels. *Small* **16**, 2002931 (2020).
89. Guan, Q. F. *et al.* Sustainable Cellulose-Nanofiber-Based Hydrogels. *ACS Nano* **15**, 7889–7898 (2021).
90. Jian Ping Gong *et al.* Synthesis of hydrogels with extremely low surface friction [4]. *J. Am. Chem. Soc.* **123**, 5582–5583 (2001).
91. Zhang, W. *et al.* Fatigue of double-network hydrogels. *Eng. Fract. Mech.* **187**, 74–93 (2018).
92. Chen, Q. *et al.* Improvement of Mechanical Strength and Fatigue Resistance of Double Network Hydrogels by Ionic Coordination Interactions. *Chem. Mater.* **28**, 5710–5720 (2016).
93. Sedlačik, T. *et al.* Preparation of Tough Double- And Triple-Network Supermacroporous Hydrogels through Repeated Cryogelation. *Chem. Mater.* **32**, 8576–8586 (2020).
94. Li, X. *et al.* Effect of mesoscale phase contrast on fatigue-delaying behavior of self-healing hydrogels. *Sci. Adv.* **7**, eabe8210 (2021).

95. Li, X. *et al.* Mesoscale bicontinuous networks in self-healing hydrogels delay fatigue fracture. *Proc. Natl. Acad. Sci. U. S. A.* **117**, 7606–7612 (2020).
96. McKinnon, D. D. *et al.* Measuring cellular forces using bis-aliphatic hydrazone crosslinked stress-relaxing hydrogels. *Soft Matter* **10**, 9230–9236 (2014).
97. Xiao, R., Mai, T. T., Urayama, K., Gong, J. P. & Qu, S. Micromechanical modeling of the multi-axial deformation behavior in double network hydrogels. *Int. J. Plast.* **137**, 102901 (2021).
98. Guo, J. *et al.* Fracture mechanics of a self-healing hydrogel with covalent and physical crosslinks: A numerical study. *J. Mech. Phys. Solids* **120**, 79–95 (2018).
99. Wang, H. *et al.* Double-cross-linked aerogels towards ultrahigh mechanical properties and thermal insulation at extreme environment. *Chem. Eng. J.* **399**, 125698 (2020).
100. Zu, G. *et al.* Transparent, Superflexible Doubly Cross-Linked Polyvinylpolymethylsiloxane Aerogel Superinsulators via Ambient Pressure Drying. *ACS Nano* **12**, 521–532 (2018).
101. Zhang, X., Li, W., Song, P., You, B. & Sun, G. Double-cross-linking strategy for preparing flexible, robust, and multifunctional polyimide aerogel. *Chem. Eng. J.* **381**, 122784 (2020).
102. Du, Y. *et al.* Reaction-Spun Transparent Silica Aerogel Fibers. *ACS Nano* **14**, 11919–11928 (2020).

103. Zhu, J., Hu, J., Jiang, C., Liu, S. & Li, Y. Ultralight, hydrophobic, monolithic konjac glucomannan-silica composite aerogel with thermal insulation and mechanical properties. *Carbohydr. Polym.* **207**, 246–255 (2019).
104. Zhang, J. *et al.* “Stiff–Soft” Binary Synergistic Aerogels with Superflexibility and High Thermal Insulation Performance. *Adv. Funct. Mater.* **29**, 1806407 (2019).
105. Zu, G., Kanamori, K., Maeno, A., Kaji, H. & Nakanishi, K. Superflexible Multifunctional Polyvinylpolydimethylsiloxane-Based Aerogels as Efficient Absorbents, Thermal Superinsulators, and Strain Sensors. *Angew. Chemie* **130**, 9870–9875 (2018).
106. Wang, B., Li, G., Xu, L., Liao, J. & Zhang, X. Nanoporous Boron Nitride Aerogel Film and Its Smart Composite with Phase Change Materials. *ACS Nano* **14**, 16590–16599 (2020).
107. Liu, Z., Ran, Y., Xi, J. & Wang, J. Polymeric hybrid aerogels and their biomedical applications. *Soft Matter* **16**, 9160–9175 (2020).
108. Wang, L., Zhang, M., Yang, B., Tan, J. & Ding, X. Highly Compressible, Thermally Stable, Light-Weight, and Robust Aramid Nanofibers/Ti₃AlC₂MXene Composite Aerogel for Sensitive Pressure Sensor. *ACS Nano* **14**, 10633–10647 (2020).
109. Zu, G., Kanamori, K., Nakanishi, K. & Huang, J. Superhydrophobic Ultraflexible Triple-Network Graphene/Polyorganosiloxane Aerogels for a

- High-Performance Multifunctional Temperature/Strain/Pressure Sensing Array. *Chem. Mater.* **31**, 6276–6285 (2019).
110. Hu, P. *et al.* Multifunctional Aramid Nanofiber/Carbon Nanotube Hybrid Aerogel Films. *ACS Nano* **14**, 688–697 (2020).
111. Zhu, J. *et al.* Facile and Green Strategy for Designing Ultralight, Flexible, and Multifunctional PVA Nanofiber-Based Aerogels. *Adv. Sustain. Syst.* **4**, 1900141 (2020).
112. Zhan, H. J. *et al.* Biomimetic Carbon Tube Aerogel Enables Super-Elasticity and Thermal Insulation. *Chem* **5**, 1871–1882 (2019).
113. Zhang, W. *et al.* 3D Space-Confined Pyrolysis of Double-Network Aerogels Containing In–Fe Cyanogel and Polyaniline: A New Approach to Hierarchically Porous Carbon with Exclusive Fe–Nx Active Sites for Oxygen Reduction Catalysis. *Small Methods* **1**, 1700167 (2017).
114. Dai, W. *et al.* Halogen Bonding: A New Platform for Achieving Multi-Stimuli-Responsive Persistent Phosphorescence. *Angew. Chemie* **134**, e202200236 (2022).
115. Wang, X. *et al.* Intermolecular Hydrogen-Bond-Assisted Solid-State Dual-Emission Molecules with Mechanical Force-Induced Enhanced Emission. *J. Org. Chem.* **87**, 8503–8514 (2022).
116. Liu, R. & Li, W. High-Thermal-Stability and High-Thermal-Conductivity

- Ti₃C₂T_x MXene/Poly(vinyl alcohol) (PVA) Composites. *ACS Omega* **3**, 2609–2617 (2018).
117. Liao, X. *et al.* Robust and Sustainable Polymeric Materials. *Science*. **366**, 1376–1379 (2019).
 118. Wang, Y. *et al.* Mechanically strong and tough polyimide aerogels cross-linked with amine functionalized carbon nanotubes synthesized by fluorine displacement reaction. *Compos. Sci. Technol.* **195**, 108204 (2020).
 119. Zhang, X., Chen, J., He, J., Bai, Y. & Zeng, H. Mussel-inspired adhesive and conductive hydrogel with tunable mechanical properties for wearable strain sensors. *J. Colloid Interface Sci.* **585**, 420–432 (2021).
 120. Wu, S. *et al.* Poly(vinyl alcohol) Hydrogels with Broad-Range Tunable Mechanical Properties via the Hofmeister Effect. *Adv. Mater.* **33**, 2007829 (2021).
 121. Suzuka, J. *et al.* Rapid reprogramming of tumour cells into cancer stem cells on double-network hydrogels. *Nat. Biomed. Eng.* **5**, 914–925 (2021).
 122. Yang, C. & Suo, Z. Hydrogel ionotronics. *Nat. Rev. Mater.* **3**, 125–142 (2018).
 123. Zhao, D. *et al.* A Dynamic Gel with Reversible and Tunable Topological Networks and Performances. *Matter* **2**, 1–14 (2020).
 124. Pang, Z. & Li, T. Mechanics and strain engineering of bulk and monolayer Bi₂O₂Se. *J. Mech. Phys. Solids* **157**, 104626 (2021).

125. Holland, M. G. Phonon scattering in semiconductors from thermal conductivity studies. *Phys. Rev.* **134**, (1964).
126. Chung, J. D., McGaughey, A. J. H. & Kaviani, M. Role of phonon dispersion in lattice thermal conductivity modeling. *J. Heat Transfer* **126**, 376–380 (2004).
127. Mu, L. *et al.* Molecular Origin of Efficient Phonon Transfer in Modulated Polymer Blends: Effect of Hydrogen Bonding on Polymer Coil Size and Assembled Microstructure. *J. Phys. Chem. C* **121**, 14204–14212 (2017).
128. Zhou, T. *et al.* Super-tough MXene-functionalized graphene sheets. *Nat. Commun.* **11**, 2077 (2020).
129. Zhang, Y. & Li, X. Bioinspired, Graphene/Al₂O₃ Doubly Reinforced Aluminum Composites with High Strength and Toughness. *Nano Lett.* **17**, 6907–6915 (2017).
130. Wang, L. & Chen, T. Simultaneously enhancing strength and toughness of graphene oxide reinforced ZK60 magnesium matrix composites through powder thixoforming. *Compos. Part A* **161**, 107097 (2022).
131. Yuan, D., Yang, X., Wu, S., Lü, S. & Hu, K. Development of high strength and toughness nano-SiCp/A356 composites with ultrasonic vibration and squeeze casting. *J. Mater. Process. Technol.* **269**, 1–9 (2019).
132. Ma, R., Li, W., Huang, M., Feng, M. & Liu, X. The reinforcing effects of dendritic short carbon fibers for rigid polyurethane composites. *Compos. Sci.*

- Technol.* **170**, 128–134 (2019).
133. Lu, Y. *et al.* Controllable additive manufacturing of gradient bulk metallic glass composite with high strength and tensile ductility. *Acta Mater.* **206**, 116632 (2021).
 134. Xie, W. & Wei, Y. Roughening for Strengthening and Toughening in Monolayer Carbon Based Composites. *Nano Lett.* **21**, 4823–4829 (2021).
 135. Hou, Y. *et al.* Strengthening and Toughening Hierarchical Nanocellulose via Humidity-Mediated Interface. *ACS Nano* **15**, 1310–1320 (2020).
 136. Wang, R. *et al.* Fabrication of Cellulose-Graphite Foam via Ion Cross-linking and Ambient-Drying. *Nano Lett.* **22**, 3931–3938 (2022).
 137. Sekhar, N. C. & Varghese, L. A. Mechanical, thermal, and rheological studies of phenolic resin modified with intercalated graphite prepared via liquid phase intercalation. *Polym. Test.* **79**, 106010 (2019).
 138. Cai, T. *et al.* Phosphorescence-Based Flexible and Transparent Optical Temperature-Sensing Skin Capable of Operating in Extreme Environments. *ACS Appl. Polym. Mater.* **3**, 2461–2469 (2021).
 139. Wang, J. *et al.* Multifunctional conductive cellulose fabric with flexibility, superamphiphobicity and flame-retardancy for all-weather wearable smart electronic textiles and high-temperature warning device. *Chem. Eng. J.* **390**, 124508 (2020).

140. Yang, K. *et al.* An anti-freezing/drying, adhesive and self-healing motion sensor with humidity-enhanced conductivity. *Polymer*. **214**, 123354 (2021).
141. Zhu, Y. *et al.* Developing flame-retardant lignocellulosic nanofibrils through reactive deep eutectic solvent treatment for thermal insulation. *Chem. Eng. J.* **445**, 136748 (2022).
142. Saito, T., Kuramae, R., Wohler, J., Berglund, L. A. & Isogai, A. An ultrastrong nanofibrillar biomaterial: The strength of single cellulose nanofibrils revealed via sonication-induced fragmentation. *Biomacromolecules* **14**, 248–253 (2013).
143. Domingues, R. M. A., Gomes, M. E. & Reis, R. L. The potential of cellulose nanocrystals in tissue engineering strategies. *Biomacromolecules* **15**, 2327–2346 (2014).
144. Iwamoto, S., Kai, W., Isogai, A. & Iwata, T. Elastic modulus of single cellulose microfibrils from tunicate measured by atomic force microscopy. *Biomacromolecules* **10**, 2571–2576 (2009).
145. Šturcová, A., Davies, G. R. & Eichhorn, S. J. Elastic modulus and stress-transfer properties of tunicate cellulose whiskers. *Biomacromolecules* **6**, 1055–1061 (2005).
146. Olsson, R. T. *et al.* Making flexible magnetic aerogels and stiff magnetic nanopaper using cellulose nanofibrils as templates. *Nat. Nanotechnol.* **5**, 584–588 (2010).

147. Song, J. *et al.* Processing bulk natural wood into a high-performance structural material. *Nature* **554**, 224–228 (2018).
148. Chung, J., Kushner, A. M., Weisman, A. C. & Guan, Z. Direct correlation of single-molecule properties with bulk mechanical performance for the biomimetic design of polymers. *Nat. Mater.* **13**, 1055–1062 (2014).
149. Xing, H. *et al.* Mechanochemistry of an Interlocked Poly[2]catenane: From Single Molecule to Bulk Gel. *CCS Chem.* **2**, 513–523 (2020).
150. Fish, J., Wagner, G. J. & Keten, S. Mesoscopic and multiscale modelling in materials. *Nat. Mater.* **20**, 774–786 (2021).
151. Gomes, C. P., Fink, D., van Dover, R. B. & Gregoire, J. M. Computational sustainability meets materials science. *Nat. Rev. Mater.* **6**, 645–647 (2021).
152. Zhou, S., Jin, K. & Buehler, M. J. Understanding Plant Biomass via Computational Modeling. *Adv. Mater.* **33**, 2003206 (2021).
153. Beckham, G. T., Bomble, Y. J., Bayer, E. A., Himmel, M. E. & Crowley, M. F. Applications of computational science for understanding enzymatic deconstruction of cellulose. *Curr. Opin. Biotechnol.* **22**, 231–238 (2011).
154. Wang, M., Wang, T., Cai, P. & Chen, X. Nanomaterials Discovery and Design through Machine Learning. *Small Methods* **3**, 1900025 (2019).
155. Elton, D. C., Boukouvalas, Z., Butrico, M. S., Fuge, M. D. & Chung, P. W. Applying machine learning techniques to predict the properties of energetic

- materials. *Sci. Rep.* **8**, 1–12 (2018).
156. Metcalf, D. P. *et al.* Approaches for machine learning intermolecular interaction energies and application to energy components from symmetry adapted perturbation theory. *J. Chem. Phys.* **152**, (2020).
157. Yang, Z., Yu, C. H., Guo, K. & Buehler, M. J. End-to-end deep learning method to predict complete strain and stress tensors for complex hierarchical composite microstructures. *J. Mech. Phys. Solids* **154**, 104506 (2021).
158. Schütt, K. T., Gastegger, M., Tkatchenko, A., Müller, K. R. & Maurer, R. J. Unifying machine learning and quantum chemistry with a deep neural network for molecular wavefunctions. *Nat. Commun.* **10**, 1–10 (2019).
159. Cole, D. J., Mones, L. & Csányi, G. A machine learning based intramolecular potential for a flexible organic molecule. *Faraday Discuss.* **224**, 247–264 (2020).
160. Gasparotto, P. & Ceriotti, M. Recognizing molecular patterns by machine learning: An agnostic structural definition of the hydrogen bond. *J. Chem. Phys.* **141**, 174110 (2014).
161. Hansen, K. *et al.* Machine learning predictions of molecular properties: Accurate many-body potentials and nonlocality in chemical space. *J. Phys. Chem. Lett.* **6**, 2326–2331 (2015).
162. Bauer, C. A., Schneider, G. & Göller, A. H. Machine learning models for

hydrogen bond donor and acceptor strengths using large and diverse training data generated by first-principles interaction free energies. *J. Cheminform.* **11**, 1–16 (2019).

163. Wang, S., Pillai, H. S. & Xin, H. Bayesian learning of chemisorption for bridging the complexity of electronic descriptors. *Nat. Commun.* **11**, 6132 (2020).